The effects of dust on the derived photometric parameters of disks and bulges in spiral galaxies

Bogdan Adrian Pastrav

A

D P

Jeremiah Horrocks Institute
University of Central Lancashire

May 2013

Declaration

The work presented in this thesis was carried out in the Jeremiah Horrocks Institute, University of Central Lancashire.

I declare that while registered as a candidate for the research degree, I have not been a registered candidate or enrolled student for another award of the University or other academic or professional institution.

I declare that no material contained in the thesis has been used in any other submission for an academic award and is solely my own work.

“Look up at the stars. Stay curious.

However difficult life may seem, there is always something you can do and succeed at.”

Stephen Hawking

Abstract

Spiral galaxies contain large amounts of interstellar dust, that absorbs and scatters their photons. This results in strong distortions and changes of their observed stellar images from what would be observed in the absence of the dust. Because of this the measured structural parameters of spiral galaxies, and indeed, knowledge of some of the most fundamental physical attributes of galaxies - their stellar distributions - is strongly biased.

I present here the results of a study to quantify the effects of dust on the derived photometric parameters of disks (old stellar disks and young stellar disks) and bulges in spiral galaxies: scale-lengths, axis-ratios, central surface-brightness, effective radii and Sérsic indices. The goal of this study is to provide corrections for dust effects to observers by following the procedures and algorithms they use to perform surface brightness photometry of real images of galaxies.

The changes in the derived photometric parameters from their intrinsic values (as seen in the absence of dust) were obtained by fitting simulated images of disks and bulges produced using radiative transfer calculations. The fits to the simulations were performed using GALFIT 3.0.2 data analysis algorithm and the fitted models were the commonly used infinitely thin disks described by exponential, general Sérsic and de Vaucouleurs distributions. The analysis was done firstly for disks and bulges seen in isolation (thus quantifying dust and projection effects) and subsequently for the same morphological

components seen together (thus quantifying the dust effects on bulge-disk decomposition). This is the first time a systematic and self-consistent quantification of these effects has been performed covering the whole parameter space and all photometric parameters of spiral galaxies and its constituent stellar components. The approach proposed here allows a clear separation of projection effects, dust effects and decomposition effects, through chain corrections.

For single morphological components, I find the young stellar disks to suffer the most severe variation in the photometric parameters due to dust effects. In this context I also present corrections for narrow line (Balmer line) images. Old stellar disks are also significantly affected by dust, in particular when fits are performed with exponential functions. The photometric parameters of bulges are to a lesser extent affected by dust. I also find that the variation of dust corrections with face-on dust opacity and inclination is similar for bulges with different intrinsic stellar emissivities (different Sérsic index), with differences manifesting only close to edge-on orientations of the disk. Dust corrections for bulges are found to be insensitive to the choice of the truncation radius and ellipticity of the bulge.

I find that dust effects on the photometric parameters of decomposed disks and bulges increase with the Sérsic index of bulge intrinsic volume stellar emissivity distribution and depend on the bulge-to-disk ratio for galaxies with bulge stellar emissivity described by higher Sérsic index functions.

All the numerical results are listed in the Appendices and made available to the scientific community.

Contents

Declaration **i**

Abstract **iii**

List of Publications **xxii**

Acknowledgements **xxiii**

1 Introduction **1**

2 The simulated images **10**

3 The method **19**

3.1 The general approach 19

3.2 The fitting procedure 25

4 Projection effects **31**

4.1 The Disk 32

4.1.1 Exponential fits to the disk 32

4.1.2 Sérsic fits to the disk 36

4.2 The Thin Disk 39

4.3 The Bulge 39

5 Dust Effects on Single Disks and Bulges 49

5.1 The Disk 50

5.1.1 Exponential fits to the disk 51

5.1.2 Sérsic fits to the disk 53

5.2 The Thin Disk 60

5.2.1 Exponential fits to the thin disk 60

5.2.2 Sérsic fits to the thin disk 64

5.3 The Bulge 67

5.4 Discussion 73

5.5 Application: the wavelength dependence of dust effects 76

6 Dust Effects on Decomposed Disks and Bulges 79

6.1 Galaxies with exponential bulges 80

6.1.1 Fits with exponential + variable-index Sérsic functions 80

6.1.2 Fits with two variable-index Sérsic functions 83

6.2 Galaxies with de Vaucouleurs bulges 84

6.3 Dust effects on single Sérsic fits of galaxies 85

6.4 Application: the inclination dependence of dust effects 86

7 Summary and Conclusions 101

A The corrections for projection effects 110

B The corrections for dust effects on single disks and bulges 113

C The corrections for dust effects on decomposed disks and bulges 146

D The corrections for dust effects on single Sérsic fits of galaxies 187

List of Tables

2.1 The parameters of the model. All length parameters are normalised to the B-band scalelength of the disk (from Tuffs et al. 2004). 14

2.2 Wavelength dependence of the scalelength of the disk normalised to its value in the B band (from Tuffs et al. 2004). 15

A.1 **Projection effects** $corr^{proj}$ on the derived photometric parameters of the **disk**: scale-lengths and central surface brightnesses. Results are listed as coefficients of polynomial fits a_k (Eq. 3.1.19) at different optical wavelengths, corresponding to the effective wavelength of B,V,I,J,K bands. 111

A.2 **Projection effects** $corr^{proj}$ on the derived axis ratios of the **disk**. Results are listed as coefficients of polynomial fits a_k and b_0 (Eq. 4.1.1.1) at different optical wavelengths, corresponding to the effective wavelength of B,V,I,J,K bands. 111

A.3 **Projection effects** $corr^{proj}$ on the derived photometric parameters of the **disk**: effective radius, central surface brightnesses and Sérsic index. Results are listed as coefficients of polynomial fits a_k (Eq. 3.1.19) at different optical wavelengths, corresponding to the effective wavelength of B,V,I,J,K bands. 112

A.4 **Projection effects** $corr^{proj}$ on the derived photometric parameters of the **bulge**: effective radius and Sérsic index. Results are listed as coefficients of polynomial fits a_0 (Eq. 3.1.19) for four different n_0^{sers} of the intrinsic volume stellar emissivity and two different truncation radii ($3R_0^{eff}$ and $10R_0^{eff}$). Results are independent of optical waveband. . . . 112

A.5 **Projection effects** $corr^{proj}$ on the derived effective radius of de Vaucouleurs **bulges**. Bulges are truncated at $3R_0^{eff}$. Results are listed as coefficients of polynomial fits a_0 (Eq. 3.1.19). Results are independent of optical waveband. 112

B.1 **Dust effects** $corr^{dust}$ on the derived scale-lengths and central surface brightnesses of the **disk**. Results are listed as coefficients of polynomial fits a_k (Eq. 3.1.19) at different τ_B^f, for B band. 114

B.2 **Dust effects** $corr^{dust}$, as in Table B.1, but in V band. 114

B.3 **Dust effects** $corr^{dust}$, as in Table B.1, but in I band. 115

B.4 **Dust effects** $corr^{dust}$, as in Table B.1, but in J band. 115

B.5 **Dust effects** $corr^{dust}$, as in Table B.1, but in K band. 116

B.6 **Dust effects** $corr^{dust}$ on the derived axis ratios of the **disk**. Results are listed as coefficients of polynomial fits a_0 and b_k (Eq. 5.1.1.1) at different τ_B^f and at the effective wavelength of the B band. 116

B.7 **Dust effects** $corr^{dust}$, as in Table B.6, but in V band. 117

B.8 **Dust effects** $corr^{dust}$, as in Table B.6, but in I band. 117

B.9 **Dust effects** $corr^{dust}$, as in Table B.6, but in J band. 118

B.10 **Dust effects** $corr^{dust}$, as in Table B.6, but in K band. 118

B.11 **Dust effects** *corr*^{dust} on the derived effective radius, central surface brightness, Sérsic index of the **disk**. Results are listed as coefficients of polynomial fits a_k (Eq. 3.1.19) at different τ_B^f, for B band. 119

B.12 **Dust effects** *corr*^{dust}, as in Table B.11, but in V band. 119

B.13 **Dust effects** *corr*^{dust}, as in Table B.11, but in I band. 120

B.14 **Dust effects** *corr*^{dust}, as in Table B.11, but in J band. 120

B.15 **Dust effects** *corr*^{dust}, as in Table B.11, but in K band. 121

B.16 **Dust effects** *corr*^{dust} on the derived photometric parameters of the **thin disk**: scale-lengths and central surface brightnesses. Results are listed as coefficients of polynomial fits a_k (Eq. 3.1.19) at different τ_B^f and at 912Å. 122

B.17 **Dust effects** *corr*^{dust}, as in Table B.16, but at 1350Å. 122

B.18 **Dust effects** *corr*^{dust}, as in Table B.16, but at 1500Å. 123

B.19 **Dust effects** *corr*^{dust}, as in Table B.16, but at 1650Å. 123

B.20 **Dust effects** *corr*^{dust}, as in Table B.16, but at 2000Å. 124

B.21 **Dust effects** *corr*^{dust}, as in Table B.16, but at 2200Å. 124

B.22 **Dust effects** *corr*^{dust}, as in Table B.16, but at 2500Å. 125

B.23 **Dust effects** *corr*^{dust}, as in Table B.16, but at 2800Å. 125

B.24 **Dust effects** *corr*^{dust}, as in Table B.16, but at 3600Å. 126

B.25 **Dust effects** *corr*^{dust}, as in Table B.16, but in B band. 126

B.26 **Dust effects** *corr*^{dust}, as in Table B.16, but in V band. 127

B.27 **Dust effects** *corr*^{dust}, as in Table B.16, but in I band. 127

B.28 **Dust effects** *corr*^{dust}, as in Table B.16, but in J band. 128

B.29 **Dust effects** *corr*^{dust}, as in Table B.16, but in K band. 128

B.30 **Dust effects** *corr*^{dust}, as in Table B.16, but for the $H\alpha$ line. 129

B.31 **Dust effects** $corr^{dust}$ on the derived photometric parameters of the **thin disk**: effective radius, central surface brightnesses and Sérsic index. Results are listed as coefficients of polynomial fits a_k (Eq. 3.1.19) at different τ_B^f and at 912Å. 130
B.32 **Dust effects** $corr^{dust}$, as in Table B.31, but at 1350Å. 130
B.33 **Dust effects** $corr^{dust}$, as in Table B.31, but at 1500Å. 131
B.34 **Dust effects** $corr^{dust}$, as in Table B.31, but at 1650Å. 131
B.35 **Dust effects** $corr^{dust}$, as in Table B.31, but at 2000Å. 132
B.36 **Dust effects** $corr^{dust}$, as in Table B.31, but at 2200Å. 132
B.37 **Dust effects** $corr^{dust}$, as in Table B.31, but at 2500Å. 133
B.38 **Dust effects** $corr^{dust}$, as in Table B.31, but at 2800Å. 133
B.39 **Dust effects** $corr^{dust}$, as in Table B.31, but at 3600Å. 134
B.40 **Dust effects** $corr^{dust}$, as in Table B.31, but in B band. 134
B.41 **Dust effects** $corr^{dust}$, as in Table B.31, but in V band. 135
B.42 **Dust effects** $corr^{dust}$, as in Table B.31, but in I band. 135
B.43 **Dust effects** $corr^{dust}$, as in Table B.31, but in J band. 136
B.44 **Dust effects** $corr^{dust}$, as in Table B.31, but in K band. 136
B.45 **Dust effects** $corr^{dust}$, as in Table B.31, but for the $H\alpha$ line. 137
B.46 **Dust effects** $corr^{dust}$ on the derived effective radius and Sérsic index of **exponential bulges**. Results are listed as coefficients of polynomial fits a_k (Eq. 3.1.19) at different τ_B^f, for B band. 138
B.47 **Dust effects** $corr^{dust}$, as in Table B.46, but in V band. 138
B.48 **Dust effects** $corr^{dust}$, as in Table B.46, but in I band. 139
B.49 **Dust effects** $corr^{dust}$, as in Table B.46, but in J band. 139
B.50 **Dust effects** $corr^{dust}$, as in Table B.46, but in K band. 140

B.51 **Dust effects** $corr^{dust}$ on the derived photometric parameters of **de Vaucouleurs bulges**: effective radius and Sérsic index. Results are listed as coefficients of polynomial fits a_k (Eq. 3.1.19) at different τ^f_B, for B band. 140

B.52 **Dust effects** $corr^{dust}$, as in Table B.51, but in V band. 141

B.53 **Dust effects** $corr^{dust}$, as in Table B.51, but in I band. 141

B.54 **Dust effects** $corr^{dust}$, as in Table B.51, but in J band. 142

B.55 **Dust effects** $corr^{dust}$, as in Table B.51, but in K band. 142

B.56 **Dust effects** $corr^{dust}$ on the effective radius of **de Vaucouleurs bulges**. Results are listed as coefficients of polynomial fits a_k (Eq. 3.1.19) at different τ^f_B and the effective wavelength of the B band. 143

B.57 **Dust effects** $corr^{dust}$, as in Table B.56, but in V band. 143

B.58 **Dust effects** $corr^{dust}$, as in Table B.56, but in I band. 144

B.59 **Dust effects** $corr^{dust}$, as in Table B.56, but in J band. 144

B.60 **Dust effects** $corr^{dust}$, as in Table B.56, but in K band. 145

C.1 **Dust effects** $corr^{B/D}$ on the derived photometric parameters of **decomposed disks** and **exponential bulges** ($B/D = 0.25$): disk scale-lengths, bulge effective radii and Sérsic indices. Results are listed as coefficients of polynomial fits a_k (Eq. 3.1.19) at different τ^f_B and at the effective wavelength of the B band. 147

C.2 **Dust effects** $corr^{B/D}$, as in Table C.1, but in V band. 148

C.3 **Dust effects** $corr^{B/D}$, as in Table C.1, but in I band. 149

C.4 **Dust effects** $corr^{B/D}$, as in Table C.1, but in J band. 150

C.5 **Dust effects** $corr^{B/D}$, as in Table C.1, but in K band. 151

C.6 **Dust effects** $corr^{B/D}$, as in Table C.1, but for $B/D = 0.5$. 152

C.7 **Dust effects** $corr^{B/D}$, as in Table C.1, but for $B/D = 0.5$, in V band. . . 153

C.8 **Dust effects** $corr^{B/D}$, as in Table C.1, but for $B/D = 0.5$, in I band. . . . 154
C.9 **Dust effects** $corr^{B/D}$, as in Table C.1, but for $B/D = 0.5$, in J band. . . . 155
C.10 **Dust effects** $corr^{B/D}$, as in Table C.1, but for $B/D = 0.5$, in K band. . . 156
C.11 **Dust effects** $corr^{B/D}$ on the derived photometric parameters of **decomposed disks** and **exponential bulges** ($B/D = 0.25$): disk and bulge bulge effective radii, disk and bulge Sérsic indices. Results are listed as coefficients of polynomial fits a_k (Eq. 3.1.19) at different τ_B^f and at the effective wavelength of the B band. 157
C.12 **Dust effects** $corr^{B/D}$, as in Table C.11, but in V band. 158
C.13 **Dust effects** $corr^{B/D}$, as in Table C.11, but in I band. 159
C.14 **Dust effects** $corr^{B/D}$, as in Table C.11, but in J band. 160
C.15 **Dust effects** $corr^{B/D}$, as in Table C.11, but in K band. 161
C.16 **Dust effects** $corr^{B/D}$, as in Table C.11, but for $B/D = 0.5$. 162
C.17 **Dust effects** $corr^{B/D}$, as in Table C.11, but for $B/D = 0.5$, in V band. . . 163
C.18 **Dust effects** $corr^{B/D}$, as in Table C.11, but for $B/D = 0.5$, in I band. . . 164
C.19 **Dust effects** $corr^{B/D}$, as in Table C.11, but for $B/D = 0.5$, in J band. . . 165
C.20 **Dust effects** $corr^{B/D}$, as in Table C.11, but for $B/D = 0.5$, in K band. . . 166
C.21 **Dust effects** $corr^{B/D}$ on the derived photometric parameters of **decomposed disks** and **de Vaucouleurs bulges** ($B/D = 0.25$): disk scalelengths, bulge effective radii and Sérsic indices. Results are listed as coefficients of polynomial fits a_k (Eq. 3.1.19) at different τ_B^f and at the effective wavelength of the B band. 167
C.22 **Dust effects** $corr^{B/D}$, as in Table C.21, but in V band. 168
C.23 **Dust effects** $corr^{B/D}$, as in Table C.21, but in I band. 169
C.24 **Dust effects** $corr^{B/D}$, as in Table C.21, but in J band. 170

C.25 **Dust effects** $corr^{B/D}$, as in Table C.21, but in K band. 171

C.26 **Dust effects** $corr^{B/D}$, as in Table C.21, but for $B/D = 0.5$. 172

C.27 **Dust effects** $corr^{B/D}$, as in Table C.21, but for $B/D = 0.5$, in V band. . . 173

C.28 **Dust effects** $corr^{B/D}$, as in Table C.21, but for $B/D = 0.5$, in I band. . . 174

C.29 **Dust effects** $corr^{B/D}$, as in Table C.21, but for $B/D = 0.5$, in J band. . . 175

C.30 **Dust effects** $corr^{B/D}$, as in Table C.21, but for $B/D = 0.5$, in K band. . . 176

C.31 **Dust effects** $corr^{B/D}$ on the derived photometric parameters of **decomposed disks** and **de Vaucouleurs bulges** ($B/D = 0.25$): disk and bulge bulge effective radii, disk and bulge Sérsic indices. Results are listed as coefficients of polynomial fits a_k (Eq. 3.1.19) at different τ^f_B and at the effective wavelength of the B band. 177

C.32 **Dust effects** $corr^{B/D}$, as in Table C.31, but in V band. 178

C.33 **Dust effects** $corr^{B/D}$, as in Table C.31, but in I band. 179

C.34 **Dust effects** $corr^{B/D}$, as in Table C.31, but in J band. 180

C.35 **Dust effects** $corr^{B/D}$, as in Table C.31, but in K band. 181

C.36 **Dust effects** $corr^{B/D}$, as in Table C.31, but for $B/D = 0.5$. 182

C.37 **Dust effects** $corr^{B/D}$, as in Table C.31, but for $B/D = 0.5$, in V band. . . 183

C.38 **Dust effects** $corr^{B/D}$, as in Table C.31, but for $B/D = 0.5$, in I band. . . 184

C.39 **Dust effects** $corr^{B/D}$, as in Table C.31, but for $B/D = 0.5$, in J band. . . 185

C.40 **Dust effects** $corr^{B/D}$, as in Table C.31, but for $B/D = 0.5$, in K band. . . 186

D.1 **Dust effects** $corr^{sS}$ on the derived sizes of galaxies with **exponential bulges** ($B/D = 0.25$), in B band. 188

D.2 **Dust effects** $corr^{sS}$, as in Table D.1, but in V band. 189

D.3 **Dust effects** $corr^{sS}$, as in Table D.1, but in I band. 189

D.4 **Dust effects** $corr^{sS}$, as in Table D.1, but in J band. 190

D.5 **Dust effects** $corr^{sS}$, as in Table D.1, but in K band. 190
D.6 **Dust effects** $corr^{sS}$, as in Table D.1, but for $B/D = 0.5$. 191
D.7 **Dust effects** $corr^{sS}$, as in Table D.1, but for $B/D = 0.5$, in V band. . . . 191
D.8 **Dust effects** $corr^{sS}$, as in Table D.1, but for $B/D = 0.5$, in I band. . . . 192
D.9 **Dust effects** $corr^{sS}$, as in Table D.1, but for $B/D = 0.5$, in J band. . . . 192
D.10 **Dust effects** $corr^{sS}$, as in Table D.1, but for $B/D = 0.5$, in K band. . . . 193

List of Figures

2.1 Schematic representation of the geometrical distributions of stellar and dust emissivity (taken from Popescu et al. 2011). 12

4.1 Major and minor axis **disk** profiles (**upper and middle rows**) and corresponding relative residuals, showing the deviations from pure exponentials due to projection effects (**lower row**). 43

4.2 Projection effects $corr^{proj}$ on the derived B band photometric parameters of **disks fitted with exponential fuctions** and with **Sérsic functions**: scale-lengths, axis-ratios, and central surface brightnesses. 44

4.3 Major and minor axis **disk** profiles (**upper and middle rows**) and corresponding relative residuals, showing the deviations from Sérsic functions due to projection effects (**lower row**). 45

4.4 The inclination dependence of the Sérsic index n_i^{sers} for the dustless images of the **disk** in the B band, for the case that the images are **fitted with a general Sérsic function** having n_i^{sers} as a free parameter. 46

4.5 The derived Sérsic index n_i^{sers} of the dust free images of the **bulge**, for bulges produced with volume stellar emissivities described by (deprojected) Sérsic functions having different Sérsic indices. 47

4.6 Projection effects $corr^{proj}$ on the derived effective radius of the **bulge**, for bulges produced with volume stellar emissivities described by (de-projected) Sérsic functions having different Sérsic indices. 48

5.1 Major and minor axis **disk** profiles (**upper and middle rows**) and corresponding relative residuals, showing the deviations from pure exponentials due to the combination of dust and projection effects (**lower row**). 56

5.2 Dust effects $corr^{dust}$ on the derived scale-length of **disks fitted with exponential functions**, as a function of inclination. 57

5.3 Dust effects $corr^{dust}$ on the derived central surface brightnesses of **disks fitted with exponential functions**, as a function of inclination. 57

5.4 Major and minor axis **disk** profiles (**upper and middle rows**) and corresponding relative residuals, showing the deviations from a general Sersic profile due to the combination of dust and projection effects (**lower row**). 58

5.5 **Left panels**: the inclination dependence of the derived Sérsic index for **disks fitted with Sérsic functions**, due to combined dust and projection effects. **Right panels**: The same but corrected for projection effects (Δn_i^{sers}). 59

5.6 Dust effects $corr^{dust}$ on the derived effective radius of **disks fitted with Sérsic functions**, as a function of inclination. 59

5.7 The face-on major axis profiles for the **thin disk** showing the deviations from pure exponentials due to dust effects. 61

5.8 Dust effects $corr^{dust}$ on the derived scale-length of **thin disks fitted with exponential functions**, as a function of inclination. 62

5.9 Same as in Fig. 5.8, for the optical bands and the $H\alpha$ line. 63

5.10 **Upper row**: the inclination dependence of the derived Sérsic index for the dusty images of **thin disks fitted with Sérsic functions**. **Lower row**: same, for the ratio between the apparent and intrinsic Sérsic effective radii, R_{app}^{eff} and R_i^{eff} respectively. 64

5.11 Same as in Fig. 5.10 top, for the the optical bands and the $H\alpha$ line. . . . 65

5.12 Same as in Fig. 5.10 bottom, for the the optical bands and the $H\alpha$ line. . 66

5.13 **Left**: The inclination dependence of the derived Sérsic index of **bulges** due to combined dust and projection effects, in B band, for simulations having the volume stellar emissivity described by different Sérsic index. **Right**: The same but corrected for projection effects (Δn_i^{sers}). 68

5.14 The inclination dependence of the derived Sérsic index of **bulges** due to dust effects only (corrected for projection effects), for bulges truncated at 3 effective radii (black curves) and at 10 effective radii (red curves). . 69

5.15 **Left**: Simulated images of **de Vaucouleurs bulges** in the B band, seen through the dust disks. 70

5.16 **Left panels**: the inclination dependence of the derived Sérsic index for the **exponential bulges** ($n_0^{sers} = 1$), due to combined dust and projection effects. **Right panels**: The same but corrected for projection effects (Δn_i^{sers}). 71

5.17 Dust effects $corr^{dust}$ on the derived effective radius of **exponential bulges** ($n_0^{sers} = 1$), as a function of inclination. 72

5.18 The inclination dependence of the derived Sérsic index of **bulges** due to dust effects only (corrected for projection effects), for spherical bulges (axis-ratios of 1.0) and for the standard bulges with axis-ratios of 0.6. . 75

5.19 The wavelength dependence of the Sérsic index (top) and effective radius (bottom) predicted to be measured on a disk population, due to the effect of dust only (black). Recent measurements from the GAMA survey are overplotted in red. 77

6.1 Simulated images of galaxies with **exponential bulges** and $B/D = 0.25$ (left column) and corresponding decomposed disks and bulges (middle and right columns). 81

6.2 Major- and minor- axis profiles of dusty galaxies (**upper and middle rows**) with $B/D = 0.25$, in the **B band**, and corresponding relative residuals (**lower row**). Fits are done with an **exponential** function (for the **disk** component) and a **variable-index Sérsic** function (for the **exponential bulge**). 90

6.3 Relative residuals between the **B-band** simulated image of a single disk and the corresponding decomposed disk, for $B/D = 0.25$ and $\tau_B^f = 4.0$, at inclinations $1 - cos(i) = 0.3, 0.7, 0.9$ ($i = 46, 73, 84$ degrees). 91

6.4 Dust effects $corr^{B/D}$ on the derived scale-length of decomposed **disks** for $B/D = 0.25$, as a function of inclination. An **exponential** (disk) plus a **variable index Sérsic** (bulge) distributions were used for image decomposition. 91

6.5 Dust effects $corr^{B/D}$ on the derived Sérsic index of decomposed **exponential bulges** for $B/D = 0.25$, as a function of inclination. An **exponential** (disk) and a **variable index Sérsic** (bulge) distributions were used for image decomposition. 92

6.6 Dust effects $corr^{B/D}$ on the derived effective radius of decomposed **exponential bulges** for $B/D = 0.25$, as a function of inclination. An **exponential** (disk) and a **variable-index Sérsic** (bulge) distributions were used for image decomposition. 92

6.7 Major- and minor- axis profiles of dusty galaxies (**upper and middle rows**) with $B/D = 0.25$, in the **B band**, and corresponding relative residuals (**lower row**). Fits are done with two **variable-index Sérsic** functions, one for the **disk** component and another one for the **exponential bulge** component. 93

6.8 Relative residuals between the **B-band** simulated image of a single disk and the corresponding decomposed disk, for $B/D = 0.25$ and $\tau^f_B = 4.0$, at inclinations $1 - cos(i) = 0.3, 0.7, 0.9$ ($i = 46, 73, 84$ degrees). 94

6.9 Dust effects $corr^{B/D}$ on the derived Sérsic index of decomposed **disks** for $B/D = 0.25$, as a function of inclination. Two variable Sérsic index functions were used for image decomposition. 94

6.10 Dust effects $corr^{B/D}$ on the derived effective radii of decomposed **disks** for $B/D = 0.25$, as a function of inclination. Two variable Sérsic index functions were used for image decomposition. 95

6.11 Dust effects $corr^{B/D}$ on the derived Sérsic index of decomposed **exponential bulges** for $B/D = 0.25$, as a function of inclination. Two variable Sérsic index functions were used for image decomposition. 95

6.12 Dust effects $corr^{B/D}$ on the derived effective radius of decomposed **exponential bulges** for $B/D = 0.25$, as a function of inclination. Two variable Sérsic index functions were used for image decomposition. . . 96

6.13 Dust effects $corr^{B/D}$ on the derived scale-length of decomposed **disks** for $B/D = 0.25$, as a function of inclination. An **exponential** (disk) plus a **variable index Sérsic** (bulge) distributions were used for image decomposition. 96
6.14 Dust effects $corr^{B/D}$ on the derived Sérsic index of decomposed **de Vaucouleurs bulges** for $B/D = 0.25$, as a function of inclination. An **exponential** (disk) and a **variable index Sérsic** (bulge) distributions were used for image decomposition. 97
6.15 Dust effects $corr^{B/D}$ on the derived effective radius of decomposed **de Vaucouleurs bulges** for $B/D = 0.25$, as a function of inclination. An **exponential** (disk) and a **variable-index Sérsic** (bulge) distributions were used for image decomposition. 97
6.16 Dust effects $corr^{sS}$ on the derived effective radius of galaxies fitted with **single Sérsic functions**, as a function of inclination. 98
6.17 Disk size-luminosity relation for a sample of galaxies selected from Simard et al. (2011). 99
6.18 Average inclination dependence of disk sizes for a sample of galaxies selected from Simard et al. (2011) (blue curve). Overplotted in black are the predictions of my model for a disk population. 99
6.19 Average inclination dependence of bulge effective radii for a sample of galaxies selected from Simard et al. (2011) (blue curve). Overplotted in black are the predictions of my model for a bulge population. 100

List of Publications

- *The effects of dust on the photometric parameters of decomposed disks and bulges*, **Pastrav, B. A.**, Popescu, C. C., Tuffs, R. J., Sansom, A. E., 2013, submitted to A&A

- *The effects of dust on the derived photometric parameters of disks and bulges in spiral galaxies*, **Pastrav, B. A.**, Popescu, C. C., Tuffs, R. J., Sansom, A. E., 2013, A&A 553, A80

- *GAMA/H-ATLAS: The dust opacity-stellar mass surface density relation for spiral galaxies*, Grootes, M. W., Tuffs, R. J., Popescu, C. C., **Pastrav, B.**, Andrae, E. et al. 2013, ApJ 766, 59

- *The effects of dust on the derived photometric parameters of disks and bulges in spiral galaxies*, **Pastrav, B. A.**, Popescu, C. C., Tuffs, R. J., Sansom, A. E., 2013, in "Molecular Gas, Dust, and Star Formation in Galaxies", Proceedings of the IAU, IAU Symposium 292, eds. Tony Wong & Juergen Ott, p. 290

- *Dust effects on the derived Sérsic indexes of disks and bulges in spiral galaxies*, **Pastrav, B. A.**, Popescu, C. C., Tuffs, R. J., Sansom, A. E., 2012, in "The Spectral Energy Distribution of Galaxies", Proceedings of the IAU, IAU Symposium 284, eds. Richard J. Tuffs & Cristina C. Popescu, p. 306

Acknowledgements

I would like to thank first and foremost to Dr. Cristina C. Popescu, for being an excellent supervisor, for all her patience she had with me these years. I would like to thank her for all her dedication and professionalism during our discussions. She has taught me so many things during my PhD. I would also like to thank her for all the other advices about life in general and for her careful listening whenever I had a problem.

Secondly, I would like to thank Dr. Richard J. Tuffs and Dr. Anne E. Sansom for their very useful scientific suggestions, advices and comments related to my project, and for their careful reading of my manuscript papers.
Thirdly, I would like to thank Dr. Tim Cawthorne, for all our friendly and enjoyable talks during lunches and for all the help given as a Research Degree Tutor.
I would also like to thank Dr. Giovanni Natale, for being a good friend and for all his useful advices.
I would like to thank Jeremiah Horrocks Institute, for the financial support, and especially to Dr. Gordon E. Bromage.

A special "Thank you" goes to my parents, for being so supportive these years, even though they missed me so much.

The effects of dust on the derived photometric parameters of disks and bulges in spiral galaxies

Bogdan Adrian Pastrav

June 27, 2013

Chapter 1

Introduction

Spiral galaxies are complex systems containing two primary, physically distinct morphological components: a disk and a classical / pseudo bulge. The classical bulge is a predominantly pressure-supported spheroidal component containing old stellar populations. As there is no cold interstellar medium associated with the spheroid, it is believed that there is no dust associated with this component. The pseudo-bulge is a kinematically cold (rotationally supported) disk-like component, showing signs of star formation, dust obscuration and containing old and young stellar populations. The disk is a flat, rotationally-supported component containing young, intermediate-age and old stellar populations, with star-formation activity mainly occurring in a system of spiral arms. Unlike the classical bulge, the disk is associated with a cold interstellar medium, and contains large amounts of dust. The dust in the disk has the effect of attenuating the stellar light from both the disk and the bulge (e.g. Tuffs et al. 2004, Driver et al. 2007).

Although the bimodal structure of spiral galaxies has long been known, the separate evolutionary history of these two morphological components, in terms of when and how they acquired their present-day stellar populations, is still poorly understood. One reason for this is that, observationally, it is difficult to trace the independent evolutionary history of disks and bulges, as this requires bulge-disk decompositions to be performed on higher resolution images of galaxies in large statistical samples. Such analyses have been lacking until recently, so that studies of decomposed bulges and disks have been mainly restricted to small samples of highly resolved local universe galaxies (e.g. Möllenhoff et al. 1999, Möllenhoff & Heidt 2001, Möllenhoff 2004, Fisher & Drory 2008, Fabricius et al. 2012).

However, in recent years, deep wide field spectroscopic and photometric surveys of galaxies (e.g. Sloan Digital Sky Survey - SDSS, York et al. 2000; The Galaxy and Mass Assembly - GAMA, Driver et al. 2011) have become available, providing us with large statistical samples of galaxies for which major morphological components can be resolved out to $z = 0.1$. This trend will continue into the future with the advent of new ground based surveys like The VST Atlas, The Kilo Degree Survey (KiDS; de Jong et al. 2012), the Dark Energy Survey (DES; The DES collaboration 2005), which will provide wide-field imaging surveys with sub-arcsec resolution, and will culminate in the wide-field diffraction-limited space-borne surveys done with EUCLID (Laureijs et al. 2010).

In parallel, automatic routines like GALFIT (Peng et al. 2002, Peng et al. 2010), GIM2D (Simard et al. 2002), BUDDA (Gadotti 2008) or MegaMorph (Häußler et al. 2013, Bamford et al. 2013) have been developed to address the need of fitting large number of images of galaxies with one dimensional (1D) analytic functions (radial profile functions, e.g. exponential, de Vaucouleurs and Sérsic functions, modified Ferrer or Nuker profiles) for the characterisation of the surface brightness distribution of their stellar components. These routines allow bulge-disk decomposition to be performed in a routine way, for large statistical samples of galaxies, as already done by Allen et al. (2006), Benson et al. (2007), Cameron et al. (2009), Gadotti (2009), Simard et al.

(2011), Lackner & Gunn (2012), Bruce et al. (2012), and Bernardi et al. (2012). In particular, Sérsic functions (Sersic 1968) are the most common distributions that have been used to describe and fit the observed profiles of galaxies and their constituent morphological components (e.g. Hoyos et al. 2011, Simard et al. 2011, Kelvin et al. 2012, Häußler et al. 2013). The derived Sérsic indices may then used (either by themselves or in combination with other photometric parameters) to classify galaxies as disk- or spheroid-dominated ones (e.g. Kelvin et al. 2012, Grootes et al. 2013). Bulge-to-disk ratios may be used similarly when bulge/disk decomposition is performed (Allen et al. 2006, Benson et al. 2007, Cameron et al. 2009, Gadotti 2009, Simard et al. 2011, Lackner & Gunn 2012, Bruce et al. 2012, Bernardi et al. 2012).

One potential problem with the interpretation of the results coming from Sérsic fits of galaxies or of their morphological components is that the measured Sérsic parameters differ from the intrinsic ones (as would be derived in the absence of dust). This happens because real galaxies, in particular spiral galaxies, contain large amounts of dust (e.g Stickel et al. 2000, Tuffs et al. 2002, Popescu et al. 2002, Stickel et al. 2004, Vlahakis et al. 2005, Driver et al. 2007, Dariush et al. 2011, Rowlands et al. 2012, Bourne et al. 2012, Dale et al. 2012, Grootes et al. 2013) and this dust changes their appearance from what would be predicted to be seen in projection based on only their intrinsic stellar distributions (e.g. Tuffs et al. 2004, Möllenhoff et al. 2006, Gadotti et al. 2010, Pastrav et al. 2013). Determining the changes due to dust is thus essential when characterising and classifying galaxies based on their fitted Sérsic indices (Pastrav et al. 2012, Pastrav et al. 2013). In addition it is, for a variety of reasons, essential to quantitatively understand and correct for the effects of dust on all photometric parameters derived from Sérsic fits, such as scale-lengths, effective radii, axis-ratios, surface-brightnesses, and integrated luminosities.

Knowledge of the scale-length of disks of galaxies is essential in understanding how these systems were assembled over cosmic time. If the disks of spiral galaxies grow from the inside out, as predicted by semi-analytical hierarchical models for galaxy formation (e.g. Mo et al. 1998), one would predict the stellar populations to be younger and have lower metallicity in the outer disk than in the inner disk, such that local universe galaxies should be intrinsically larger at the shorter wavelengths where light from the young stellar population is more prominent. For the same reason one would expect the intrinsic sizes of spiral disks to be larger at the current epoch than at higher redshift. Observationally, such predictions can be tested in two ways. One way is to compare the spatial distribution of the constituent stellar populations at different wavelengths, for local universe galaxies. Another way is to look for structural differences in galaxies observed at different cosmological epochs, at the same rest frame wavelength. Both methods require knowledge of the scale-length of disks, as measured at different wavelengths or at different redshifts (and therefore potentially for different dust opacities in disks). Since the effect of dust on the measured scale-lengths varies as a function of wavelength and disk opacity (e.g. Möllenhoff et al. 2006), it is imperative to quantify these effects on the derived scale-lengths. Accurate knowledge of the intrinsic scale-lengths of disks is also important when modelling the radiation fields in galaxies based on self-consistent calculations of the transfer of radiation in galaxy disks, since any scaling of solutions will depend on the surface area of the disk, and therefore on the square of the scale-length.

Another photometric parameter derived from surface-brightness photometry is the axis-ratio of the disk, which traditionally has been used as a proxy for estimating disk inclinations (Hubble 1926). Here again it is important to quantify the effects of dust on the derived ratios, in particular in studies that require precise knowledge of inclination, as for example in radiative transfer modelling of spiral disks and studies of the Tully-Fisher relation (Courteau & Rix 1999, Courteau et al. 2003, Bamford et al. 2006). In the future, high precision measurements of axis ratios of galaxies will be the main tool in quantifying the weak lensing effects in experiments aimed at understanding the nature of dark energy in the universe (Peacock 2008, Jouvel et al. 2011, Cimatti & Scaramella 2012) or at constraining modified gravitational theories (Martinelli et al. 2011). In these studies, even small systematic deviations introduced by dust could prove important when estimating weak lensing effects. This effect has not been yet quantified in the context of weak lensing.

Surface brightness measurements are an integral part of resolved studies of stellar populations, and quantitative corrections due to dust are required for a proper analysis which removes degeneracies due to dust. Studies of bulges in galaxies also require their effective radii and surface brightness distributions to be corrected for the effects of dust. This is because, although bulges themselves may be largely devoid of dust, they are seen through copious amounts of dust in the interstellar medium in the central regions of disks (Tuffs et al. 2004, Driver et al. 2007). Finally, measurements of scale-lengths and luminosities of narrow band images, like those of Balmer lines (e.g. $H\alpha$, $H\beta$) or of nebular lines (e.g. [OII] 3727, [OIII] 5007, [NI] 5199, [NII] 5754, [SiII] 4072, etc.) are also important in understanding the extent to which star-formation is distributed in galaxies (Koopmann & Kenney 2004a, Koopmann & Kenney 2004b), and again these studies will rely on proper corrections due to dust.

While a long list of reasons for the importance of proper dust corrections on the derived photometric parameters of galaxies can be still continued, I should only mention one last topic, namely that of scaling relations in galaxies (see Graham 2011 for a review on this topic). These relations are extremely important because they provide direct insights into the physical mechanisms of how galaxies assemble over cosmic time. Graham & Worley (2008) used the radiative transfer model of Popescu et al. (2000) and the predictions for dust corrections for brightness and scale-length of disks from Möllenhoff et al. (2006) to analyse the intrinsic (dust corrected) luminosity-size and (surface-brightness)-size relations for discs and bulges. Recently Grootes et al. (2013) found a strong relation between dust opacity and stellar surface mass density, a relation that was derived making use of dust corrections (obtained in this study and presented in Pastrav et al. 2013b, in prep.) calculated from simulations produced with radiative transfer models (Popescu et al. 2011). The work of Graham & Worley (2008) and the one of Grootes et al. (2013) demonstrated the crucial importance of proper dust corrections on the analysis of scaling relations for galaxies.

At this point one could ask the rhetorical question of why should I not try to do a proper job from the beginning, and fit images of galaxies with realistic surface distributions that already take into account the distortions due to dust. The first answer to this question is that no analytic functions exist to describe the complex modifications to surface brightness distributions induced by dust. Nonetheless, such modified surface brightness distributions can be calculated using radiative transfer codes, and indeed such simulations already exist in the literature (e.g. Tuffs et al. 2004, Popescu et al. 2011) or could be potentially produced. The problem is, however, that instead of fitting one or two analytic functions with a few free parameters, as usually done by the observers, one would need to find the best fit distribution from a large data set of simulations corresponding to all combinations of parameters describing dust effects. When knowing that even simple function fitting is computationally a difficult task when dealing with large samples of galaxies, it becomes immediately apparent that complex distribution fitting, though desirable, is computationally impractical. The goal of this study is therefore not to provide a better description of "nature", but to use realistic descriptions to provide observers with a means of correcting their simplistic - but necessary - approach to the quantification of the appearance of galaxies.

The approach of providing corrections due to dust is not new, and has been already used in the past to quantify these effects on the photometric parameters derived from surface brightness photometry, especially for disks (Byun et al. 1994, Evans et al. 1994, Cunow 2001, Möllenhoff et al. 2006, Gadotti et al. 2010). While there is overall consistency in the general trends found in these studies, the amplitude of the effects depend on the details of the geometrical model and/or of the optical properties of the grains used in the radiative transfer simulations, and, to some extent, on the fitting algorithm used to compare these simulations with the commonly used analytic functions. In some cases simplifying assumptions in the calculations of simulations can also account for differences in results (e.g. ignoring scattered light; Evans et al. 1994).

This work follows-on from the previous study from Möllenhoff et al. (2006), where the effects of dust were quantified on the derived photometric parameters of disks only, seen at low to intermediate inclinations. In keeping with the approach from Möllenhoff et al. (2006), I used simulations based on a model that can simultaneously account for both dust-attenuation in the ultraviolet (UV)/optical range and dust emission in the Mid-infrared (MIR)/Far-infrared (FIR)/submillimeter (sub-mm) range. Most of the simulations come from the library of Popescu et al. (2011), while additional simulations have been created for the purpose of this study. In particular, in this thesis I quantify the effects of dust on all morphological components of spirals, including bulges of different Sérsic indices and young stellar disks seen in the ultraviolet. I also consider corrections for photometric parameters on narrow-line imaging. Another goal of this study is to quantify the effects of dust when fits are done with general Sérsic functions with variable Sérsic indices, even for cases of exponential disks, since, as I am showing in this work, dust can even alter the type of function (the Sérsic index) that provides the best fits to dust-attenuated images. In addition, I disentangle here the dust effects from projection effects of the combined radial and vertical distribution of stellar emissivity, and give detailed corrections for both effects, to be used individually or in conjunction, as may better serve the purpose of observers. In this thesis I provide a comprehensive data set of corrections that cover the whole parameter space in dust opacity, inclination, and wavelength for all morphological components in spiral disks. These corrections describe the effect of dust on each morphological component taken individually, as seen through a common distribution of dust.

When more morphological components need to be decomposed (for bulge-decomposition purposes), dust may introduce an extra effect on the decomposition itself. This relates to the effect of dust on disks and bulges viewed in combination, attention to which was first drawn by Gadotti et al. (2010). This is also discussed in Pastrav et al. (2013b). This effect causes the decomposed attenuated disk and decomposed attenuated bulge to differ from the appearance of the real dust-attenuated disk and bulge. In other words the decomposed dust-attenuated disk in the presence of a bulge may be imperfectly subtracted and therefore differ from the dust-attenuated disk that would be fitted if the galaxy were to have no bulge. Conversely, the decomposed dust-attenuated bulge in the presence of a disk may also be imperfectly subtracted and differ from how it would appear in reality if it could be seen in the absence of the stellar disk. These artifacts are specific to routines that perform bulge-disk decomposition using simple analytical dust-less templates. However, this is the common practice, as it is the only feasible approach at present.

I describe and quantify this latter effect as well. I also disentangle this effect from projection effects and dust effects and give detailed corrections for decomposed disks and bulges, covering the same parameter space as the corrections provided for single morphological components. These corrections are given for two values of the bulge-to-disk ratio. All the aforementioned corrections are made publically available at the CDS database.

This thesis is organized as follows. In Chapter 2, I describe the stellar emissivity and dust distributions used in the simulations. The method and general approach used to fit the simulated images and to derive the apparent photometric parameters is explained in Sect. 3.1 of Chapter 3, while the technical details of the whole fitting process are presented in Sect. 3.2 of the same chapter. The projection effects are presented and discussed in Chapter 4, while in Chapter 5 I show and comment on the results for dust effects on the derived photometric parameters, for each morphological component. In the same chapter, in Sect. 5.4, I discuss the effect on the dust and projection corrections of changing some of the geometrical parameters of the model, while in Sect. 5.5, the predictions of the model are compared with recent observational data coming from the GAMA survey. The results for the dust effects on bulge-decomposition process are shown in Chapter 6 - for exponential bulges (Section 6.1) and de Vaucouleurs bulges (Section 6.2). The dust effects from Single Sérsic fits to the same simulated images of galaxies and the main results are presented in the same chapter, Section 6.3, while in Section 6.4 I compare the model predictions with recent observational data from the literature. Finally, in Chapter 7 I summarize the results and present my conclusions. All the corrections derived as a result of this study are listed in Appendices A,B,C and D.

Chapter 2

The simulated images

Since the philosophy of this thesis is to provide corrections to observers, the approach used here is to follow as closely as possible the procedures and algorithms observers use to perform surface brightness photometry of real images of galaxies. It is just that instead of using observations of galaxies I use simulations for which the input parameters describing the distributions of stellar emissivity and dust are known. By comparing the input values of the parameters describing the simulations with the values of the measured parameters describing simplified distributions, as used by the observers, I can then quantify the degree to which observers underestimate or overestimate the intrinsic parameters of galaxies, under the assumption that the simulations are a good representation of observed galaxies.

The simulations were produced as part of the large library of dust- and polycyclic aromatic hydrocarbon (PAH)-emission spectral energy distributions (SEDs) and corresponding dust attenuations presented in Popescu et al. (2011). The details of these calculations are described at length in Popescu et al. (2011). Here I only mention their main characteristics. All the simulations were calculated using a modified version of the ray-tracing radiative transfer code of Kylafis & Bahcall (1987), which includes a full treatment of anisotropic scattering, and the dust model from Weingartner & Draine (2001) and Draine & Li (2007), incorporating a mixture of silicates, graphites, and PAH molecules.

The simulations were produced separately for old stellar disks, bulges and young stellar disks, all seen through a common distribution of dust. The geometrical model of Popescu et al. (2011) consists of both a large scale distribution of diffuse dust and stars, as well as a clumpy component physically associated with the star forming complexes. For the purpose of this study only the large scale distribution of diffuse dust is considered, as it is this that affects the large-scale distribution of UV/optical light (Popescu & Tuffs 2005, Möllenhoff et al. 2006) determining the values of parameters typically used in fitting surface-brightness distributions (as listed in Chapter 3). A schematic representation of the geometrical model can be seen in Fig. 2.1.

The large scale distribution of stars and dust are approximated as continuous spatial functions of stellar emissivity and dust opacity, which are referred to as “diffuse” distributions. The old and young stellar populations are described by separate distributions in Popescu et al. (2011) model. Separate distributions are also considered for diffuse dust associated with these populations.

The old stellar population resides in a disk and a bulge, with its emissivity described by a double exponential (for the disk, in both radial and vertical directions) and a deprojected de Vaucouleurs (de Vaucouleurs 1948) distribution (for bulge), respectively:

$$\eta(\lambda, R, z) = \eta^{\rm disk}(\lambda, 0, 0) \exp\left(-\frac{R}{h_{\rm s}^{\rm disk}} - \frac{|z|}{z_{\rm s}^{\rm disk}}\right)$$

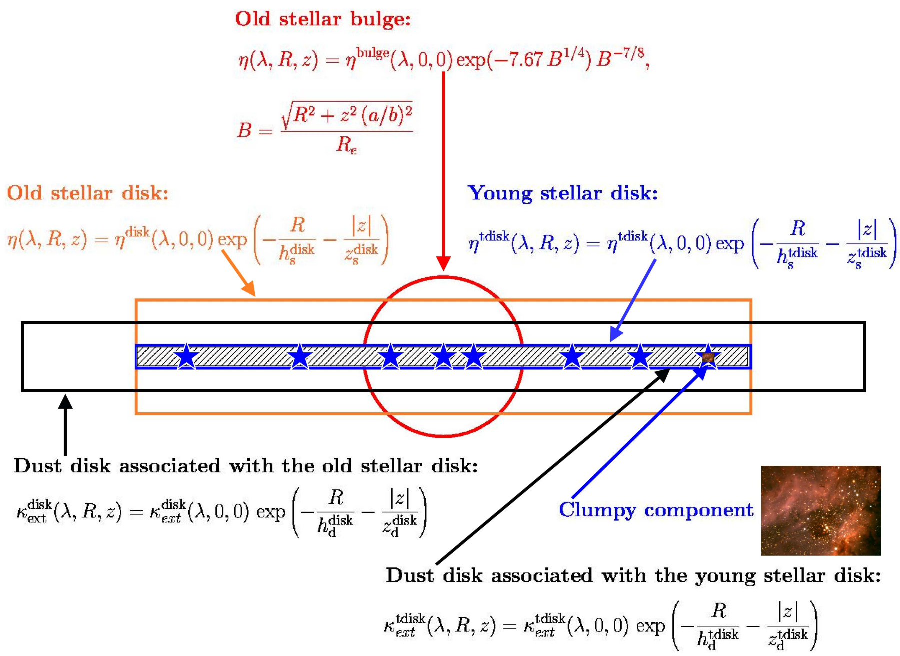

Figure 2.1: Schematic representation of the geometrical distributions of stellar and dust emissivity together with a mathematical prescription of the stellar emissivities and dust opacities used in the model. Here, and in the main body of the text the superscripts “disk”, “bulge” and “tdisk” are used for all the quantities respectively describing the disk (the old stellar disk plus the associated dust disk, also referred to as the “first dust disk”), the bulge and the thin disk (the young stellar disk plus the associated dust disk, also referred to as the “second dust disk”). Figure from Popescu et al. (2011).

$$+\,\eta^{\rm bulge}(\lambda, 0, 0)\exp(-7.67\,B^{1/4})\,B^{-7/8}, \tag{2.1}$$

$$B = \frac{\sqrt{R^2 + z^2\,(a/b)^2}}{R_{\rm e}}, \tag{2.2}$$

where R and z are the cylindrical coordinates, $\eta^{\rm disk}(\lambda, 0, 0)$ is the stellar emissivity at the centre of the disk, $h_{\rm s}^{\rm disk}$, $z_{\rm s}^{\rm disk}$ are the scalelength and scaleheight of the disk, $\eta^{\rm bulge}(\lambda, 0, 0)$ is the stellar emissivity at the centre of the bulge, $R_{\rm e}$ is the effective radius of the bulge, and a and b are the semi-major and semi-minor axes of the bulge.

The dust in the disk associated with the old stellar population is also described by a double exponential function (in both radial and vertical direction):

$$\kappa_{\rm ext}^{\rm disk}(\lambda, R, z) = \kappa_{\rm ext}^{\rm disk}(\lambda, 0, 0)\ \exp\left(-\frac{R}{h_{\rm d}^{\rm disk}} - \frac{|z|}{z_{\rm d}^{\rm disk}}\right), \quad (2.3)$$

where $\kappa_{\rm ext}^{\rm disk}(\lambda, 0, 0)$ is the extinction coefficient at the centre of the disk and $h_{\rm d}^{\rm disk}$ and $z_{\rm d}^{\rm disk}$ are the scalelength and scaleheight of the dust associated with the old stellar disk.

In a similar way, the young stellar population (the thin disk) and its associated dust disk are represented by exponential disk:

$$\eta^{\rm tdisk}(\lambda, R, z) = \eta^{\rm tdisk}(\lambda, 0, 0)\exp\left(-\frac{R}{h_{\rm s}^{\rm tdisk}} - \frac{|z|}{z_{\rm s}^{\rm tdisk}}\right) \quad (2.4)$$

$$\kappa_{\rm ext}^{\rm tdisk}(\lambda, R, z) = \kappa_{\rm ext}^{\rm tdisk}(\lambda, 0, 0)\ \exp\left(-\frac{R}{h_{\rm d}^{\rm tdisk}} - \frac{|z|}{z_{\rm d}^{\rm tdisk}}\right) \quad (2.5)$$

where $\eta^{\rm tdisk}(\lambda, 0, 0)$ is the stellar emissivity at the centre of the thin disk, $h_{\rm s}^{\rm tdisk}$ and $z_{\rm s}^{\rm tdisk}$ are the scalelength and scaleheight of the thin disk, $\kappa_{\rm ext}^{\rm tdisk}(\lambda, 0, 0)$ is the extinction coefficient at the centre of the thin disk and $h_{\rm d}^{\rm tdisk}$ and $z_{\rm d}^{\rm tdisk}$ are the scalelength and scaleheight of the dust associated with the young stellar disk (the thin disk).

The distributions of diffuse stellar emissivity and dust can also be described in terms of their amplitudes. The amplitudes of the two dust disks $\kappa_{\rm ext}^{\rm disk}$, $\kappa_{\rm ext}^{\rm tdisk}$ can be expressed in terms of the central face-on opacity in the B band, $\tau_{\rm B}^{\rm f,disk}$,$\tau_{\rm B}^{\rm f,tdisk}$, defined by:

$$\tau_{\rm B}^{\rm f,disk} = 2\,\kappa_{\rm ext}^{\rm disk}(\lambda_B, 0, 0)\, z_{\rm d}^{\rm disk} \quad (2.6)$$

$$\tau_{\rm B}^{\rm f,tdisk} = 2\,\kappa_{\rm ext}^{\rm tdisk}(\lambda_B, 0, 0)\, z_{\rm d}^{\rm tdisk} \quad (2.7)$$

Table 2.1: The parameters of the model. All length parameters are normalised to the B-band scalelength of the disk (from Tuffs et al. 2004).

$z_{\rm s}^{\rm disk}$	0.074
$h_{\rm d}^{\rm disk}$	1.406
$z_{\rm d}^{\rm disk}$	0.048
$h_{\rm s}^{\rm tdisk}$	1.000
$z_{\rm s}^{\rm tdisk}$	0.016
$h_{\rm d}^{\rm tdisk}$	1.000
$z_{\rm d}^{\rm tdisk}$	0.016
R_e	0.229
b/a	0.6
$\frac{\tau_{\rm B}^{\rm f,disk}}{\tau_{\rm B}^{\rm f,tdisk}}$	0.387

In order to minimise the number of free parameters, the ratio of these two opacities was fixed in Popescu et al. (2011) model to the value 0.387, found for their proto-type galaxy NGC 891. It is important to mention here that the attenuation-inclination relation predicted for this fixed ratio of opacities in the two dust disks was found to successfully reproduce the observed attenuation-inclination relation of a large and statistically complete sample of galaxies from the Millennium Galaxy Catalogue Survey (Driver et al. 2007). Thus, Popescu et al. adopted the total central face-on opacity in the B-band $\tau_{\rm B}^{\rm f}$ as a free parameter of the model:

$$\tau_{\rm B}^{\rm f} = \tau_{\rm B}^{\rm f,disk} + \tau_{\rm B}^{\rm f,tdisk} \tag{2.8}$$

All the geometrical parameters used in the model of Popescu et al. (2011) (and therefore for the simulated images) are listed in Table 2.1 and 2.2 (corresponding to Tables 1 and 2 from Tuffs et al. 2004), where all the length parameters describing the volume emissivity for stars and dust - scale-lengths, scale-heights and effective radii are normalised to B band scalelength of the disk, $h_{\rm s}^{\rm disk}(B) = h_{\rm s,ref}^{\rm disk} = 5670$, the fixed reference scalelength of the standard model galaxy, as derived for NGC 891.

Table 2.2: Wavelength dependence of the scalelength of the disk normalised to its value in the B band (from Tuffs et al. 2004).

	UV	B	V	I	J	K
h_s^{disk}	-	1.000	0.966	0.869	0.776	0.683

The relevant information for this study is that the old stellar disk component has a scalelength that decreases with increasing optical/near infrared-(NIR) wavelength, as given in Table 2.2 here (the same as Table 2 in Tuffs et al. 2004), while the scale-height remains constant over this wavelength range. Similarly, the effective radius of the bulge does not vary with optical/NIR wavelength. The bulge is an oblate ellipsoid with an axial ratio (thickness) of 0.6. For the purpose of testing the effects of changing the ellipticity of the bulge on the derived corrections, I also produced a few simulations for spherical bulges. The young stellar disk has a much smaller scaleheight than the older stellar disk (by a factor of 4.6), while its scalelength is constant over wavelength and is equal to that of the old stellar disk in the B band. The scalelength of the dust disk associated with the old stellar population is larger (by a factor of 1.4) than that of the corresponding stellar disk, while its scaleheight is smaller (by a factor of 1.5) than the scaleheight of the old stellar disk. By contrast, the young stellar disk spatially coincides with its associated dust disk (same scaleheights and lengths). The physical interpretation of this model and the way some of the geometrical parameters have been empirically constrained from data are also described in length in Tuffs et al. (2004) and Popescu et al. (2011).

Apart from these already existing simulations additional ones have been produced for the purpose of this study. These are simulations of bulges corresponding to general Sérsic functions (Sersic 1968) with various Sérsic indices. Since there is no exact analytical de-projection of Sérsic functions (approximate analytical expressions have been proposed, e.g. Baes & Gentile 2011, Baes & van Hese 2011), the simulations were created with volume emissivities that, for the case of untruncated distributions, will reproduce Sérsic distributions of various Sérsic indices.

All the simulated images have 34.54 pc/pixel. This linear resolution corresponds to 0.0066 of the B-band scalelength of the volume stellar emissivity. The high resolution of the simulated images matches the resolution of the optical images of NGC891, which was one of the galaxies used in the calibration of the model of Popescu et al. (2011). The disks were produced with a truncation radius at 5 exponential scalelength of the volume stellar emissivity. For bulges, I produced two sets of simulations, with truncations in volume stellar emissivity at 3 and 10 effective radii, respectively. The truncation at $3R_0^{\rm eff}$ was chosen as this avoids the problem of having a disk-bulge system dominated by the bulge light at high galactocentric radii for large values of the Sérsic index. The truncation at $10R_0^{\rm eff}$ is essentially representative of a bulge without any truncation, since at this galactocentric radius almost all the light inside the profile has been accounted for.

It is important to mention here that the true value of the truncation radius of bulges is unknown from observations. For a galaxy with a de Vaucouleurs bulge, a truncation of the bulge at 3 effective radii is enough to circumvent the above-mentioned problem. For galaxies with bulge volume stellar emissivities described by higher Sérsic indices, the truncation of the bulge would need to be at less than 3 effective radii. In other words, the truncation radius would depend in this case on the Sérsic index of the bulge. Overall, this is related to the fact that the intrinsic distribution of the bulge volume stellar emissivity is not known, and there is no physical interpretation attached to the Sérsic distribution that is used to described the projected stellar distribution (images) of bulges. The deprojected Sérsic distribution does not have an exact analytic formula due to the singularity in the centre, and therefore approximate formulae have been proposed to describe the volume stellar emissivity (e.g. Baes & Gentile 2011, Baes & van Hese 2011). In the Popescu et al. (2011) model is considered an analytic formula that, when integrated to infinity reproduces the Sérsic distribution of a 2D map. Nonetheless, if bulges are truncated, and one insists on preserving the same analytic formulation, one ends up with simulations that are not perfectly fitted by Sérsic distributions. As shown in Pastrav et al (2013), the shorter the truncation radius is the larger the deviation from the Sérsic distribution. I included this effect in the projection effects, although, unlike the case of the disk, this is a reverse problem. And, unlike the disk, it is unclear whether this is a real effect or just a limitation of our knowledge of the true 3D stellar distribution of bulges.

Here I note that the simulations for old stellar disks presented in this paper slightly differ from the disk simulations used in the previous study of Möllenhoff et al. (2006). This is due to the updates in the dust model used in Popescu et al. (2011), which included the incorporation of PAH molecules. Thus, though both the old dust model (from Popescu et al. 2000, as used in the simulations from Möllenhoff et al. 2006) and the new one can simultaneously account for the extinction and emission properties of the diffuse dust in the Milky Way, the relative contribution of scattering and absorption to the total extinction differ in the two models. This produces some small differences in the simulations.

For the purpose of quantifying the dust effects on bulge-disk decompositions, the simulated images of the old stellar disk and bulges were summed to create simulated images of galaxies, for each value of disk inclination, waveband and dust opacity considered here, and for different values of bulge-to-disk ratio, B/D. I considered both exponential and de Vaucouleurs bulges.

The simulations used in this work span the whole parameter space of the model of Popescu et al (2011). Thus, simulations were produced for 7 values of central face-on B band optical depth τ^f_B, 21 values for the disk inclination, 5 standard optical/NIR bands *B,V,I,J,K* (for disk, thin disk and bulge) and 9 far-UV (FUV) to near-UV (NUV) wavebands (for thin disk, corresponding to wavelengths of 912 Å, 1350 Å, 1500 Å, 1650 Å, 2000 Å, 2200 Å, 2500 Å, 2800 Å, and 3650 Å). The values of the dust opacity cover a wide range, from almost dustless to extremely optically thick cases, $\tau_B^f = 0.1, 0.3, 0.5, 1.0, 2.0, 4.0, 8.0$. The inclination values were chosen in such a way that $\triangle \cos(i) = 0.05$, with $1 - \cos(i) \in [0, 1]$, resulting in 21 values. I also considered two values of bulge-to-disk ratios, $B/D = 0.25, 0.5$ for the simulated images of galaxies used for the quantification of dust effects on bulge-disk decompositions. For each case, corresponding dustless simulations were produced to provide the reference point for quantifying the effects of dust and to also assess projection effects of the stellar distributions (see Chapter 3 - Sect. 3.1).

Chapter 3

The method

3.1 The general approach

Following the approach taken by observers on real images, all the simulated images were fitted with infinitely thin disks described by exponential (Eq. 3.1.1), Sérsic (Sersic 1968, Eq. 3.1.2), or de Vaucouleurs (de Vaucouleurs 1948, Eq. 3.1.3) distributions:

$$\Sigma(r) = \Sigma_0 \ \exp\left(-\frac{r}{r_{\rm s}}\right) \tag{3.1.1}$$

$$\Sigma(r) = \Sigma_0 \ \exp\left[-\kappa_{\rm n}(\frac{r}{r_{\rm e}})^{1/{\rm n}}\right] \tag{3.1.2}$$

$$\Sigma(r) = \Sigma_0 \ \exp\left[-\kappa_4(\frac{r}{r_{\rm e}})^{1/4}\right] , \tag{3.1.3}$$

where Σ_0 is the central surface brightness of the infinitely thin disk, r_s and r_e are the scale-length and effective radius[1] of the infinitely thin disk respectively, n is the Sérsic index, while κ_n is a normalisation variable, depending on n (e.g. Ciotti & Bertin 1999, Graham & Driver 2005). I use here the notations r_s and r_e only for the scale-length and effective radius of the infinitely thin fitting template. This should not be confused with the scale-length R_d and effective radius R^{eff} derived from fitting simulations produced from projecting 3D distributions of stellar emissivity.

From the formulation of the fitting functions it is clear that, even in the absence of dust, these simple distributions would differ from those of real galaxies due to the fact that they describe infinitely thin disks, while disks and bulges have a thickness. This means that in real life there would be an additional vertical distribution of stars superimposed on the corresponding radial distribution. This would produce isophotal shapes which are different from those predicted by an infinitely thin disk. I call these effects **projection effects**.

The approach adopted in this study is to separate projection effects from dust effects, and the latter from decomposition effects. Thus, I first derive the projection effects, by calculating the change between the intrinsic parameters of the volume stellar emissivity and those measured on dustless images. Subsequently, I derive the dust effects by calculating the change between the parameters measured on dustless and dusty images, respectively, for the same inclination and wavelength. So the total change in parameter values between the measured ones on dusty images and the corresponding parameters of the volume stellar emissivity can be written as a chain of corrections. In the case that the parameter is either the exponential scale-length R_d or the Sérsic effective radius R^{eff} of the surface-brightness distribution of the measured object, then the total correction

[1]such that half of the total flux is within r_e

can be written as

$$corr(A) \;=\; corr^{\rm proj}(A) * corr^{\rm dust}(A) \tag{3.1.4}$$

with

$$corr^{proj}(A) \;=\; \frac{A_{\rm i}}{A_0} \tag{3.1.5}$$

$$corr^{dust}(A) \;=\; \frac{A_{\rm app}}{A_{\rm i}}\,, \tag{3.1.6}$$

where A is either $R_{\rm d}$ or $R^{\rm eff}$, A_0 is the corresponding parameter describing the volume stellar emissivity (which I call *"intrinsic parameter of the volume stellar emissivity"*), $A_{\rm i}$ is the corresponding fitted parameter of the dustless simulated image (which I simply call *"intrinsic"* parameter), and $A_{\rm app}$ is the fitted parameter of the dust attenuated simulated image (which I call *"apparent"* parameter).

Eqs. 3.1.4, 3.1.5, and 3.1.6 also apply for the fitted axis-ratio Q, except that the meaning of the quantities defining $corr^{\rm proj}$ in Eq. 3.1.5 are different, since, as we will see in Sect. 4.1, it only makes sense to express corrections with respect to an infinitely thin disk case.

In the case that the fitted parameter is the Sérsic index $n^{\rm sers}$ the corrections are additive, since they are expressed as differences instead of ratios. The reason for this is that while the scalelength or axis ratio are extensive quantities, the Sérsic index is an intensive one. The corresponding formulas for them become:

$$corr(B) \;=\; corr^{\rm proj}(B) + corr^{\rm dust}(B)\,, \tag{3.1.7}$$

with

$$corr^{proj}(B) = B_{i} - B_{0} \quad (3.1.8)$$

$$corr^{dust}(B) = B_{app} - B_{i} \,. \quad (3.1.9)$$

Eqs. 3.1.7, 3.1.8, and 3.1.9 also apply for the fitted parameter surface-brightness, except that the term $corr^{proj}$ in Eq. 3.1.8 is again not taken with respect to the volume stellar emissivity. This is because surface-brightness is by definition a projected quantity (describing a surface). I define this correction with respect to the simulated image without dust (see Sect. 4.1).

One advantage of separating projection from dust effects is that this provides observers with a larger flexibility in using these corrections, according to different needs. In some cases observers may be only interested in the pure dust effects ($corr^{dust}$), in other cases the interest may be in deriving the intrinsic parameters of the volume stellar emissivity (e.g. $corr^{dust} * corr^{proj}$).

Another advantage of this approach is that it provides a more robust quantification of the dust effects. As I will show here, the term related to projection effects $corr^{proj}$ is affected by variations in the geometrical parameters of the volume stellar emissivity, including the truncation radius, while the term related to dust effects $corr^{dust}$ is relatively insensitive to such factors. This is true as long as both terms are derived on simulations produced with the same geometrical parameters: e.g. truncation radius.

Lastly, but equally important, the approach of chain corrections allows further corrections to be added to the formula, if more complex cases are considered. The best example of the generalisation of this formula is for multicomponent fits. Thus, when

I performed bulge-disk decomposition, an additional correction had to be calculated. This is the correction between the fitted parameters obtained from bulge-disk decomposition in the presence of dust, and the fitted parameters of the same bulge and disk, if they were to be observed alone through the same distribution of dust. Using the example from Eq. 3.1.4 and Eq. 3.1.7, I generalise these formulas for the case of bulge/disk decomposition:

$$corr(A) = corr^{\rm proj}(A) * corr^{\rm dust}(A) * corr^{\rm B/D}(A) \tag{3.1.10}$$

$$corr(B) = corr^{\rm proj}(B) + corr^{\rm dust}(B) + corr^{\rm B/D}(B)\,, \tag{3.1.11}$$

where the additional terms are

$$corr^{\rm B/D}(A) = \frac{A^{\rm B/D}_{\rm app}}{A_{\rm app}} \tag{3.1.12}$$

$$corr^{\rm B/D}(B) = B^{\rm B/D}_{\rm app} - B_{\rm app}\,. \tag{3.1.13}$$

I quantified the additional term $corr^{\rm B/D}$ for all photometric parameters, and related it to the dust and projection effects through equations Eqs. 3.1.10 and 3.1.11.

Bulge-disk decompositions were performed through multi-component fits of the simulated images with two distribution functions (one for each morphological component). I consider the following types of fits: i) fits with an infinitely thin exponential disk (Eq. 3.1.1) plus a variable-index Sérsic function (Eq. 3.1.2) for the disk and bulge component, respectively, and ii) fits with two variable-index Sérsic functions for both the disk and the bulge.

Thus, using Eqs. 3.1.10 and 3.1.11, the correction for the exponential scale-length of the decomposed disk fitted with an exponential function, $corr^{\mathrm{B/D}}(R)$, can be defined as

$$corr^{\mathrm{B/D}}(R_{\mathrm{d}}) = \frac{R^{\mathrm{B/D}}_{\mathrm{app,d}}}{R_{\mathrm{app,d}}}, \quad (3.1.14)$$

the correction for the effective radius of decomposed disks and bulges fitted with variable-index Sérsic functions, $corr^{\mathrm{B/D}}(R_{\mathrm{d}})$, as

$$corr^{\mathrm{B/D}}(R^{\mathrm{eff}}_{\mathrm{i}}) = \frac{R^{\mathrm{eff,B/D}}_{\mathrm{app,i}}}{R^{\mathrm{eff}}_{\mathrm{app,i}}}, \quad (3.1.15)$$

with i=d (disk) or b (bulge), and the correction for the corresponding Sérsic index, $corr^{\mathrm{B/D}}(n^{\mathrm{sers}})$, as

$$corr^{\mathrm{B/D}}(n^{\mathrm{sers}}_{\mathrm{i}}) = n^{\mathrm{sers,B/D}}_{\mathrm{app,i}} - n^{\mathrm{sers}}_{\mathrm{app,i}}, \quad (3.1.16)$$

again with i=d (disk) or b (bulge).

In addition to two-component fits to galaxies with two components, I also performed single Sérsic fits to the same simulated images. This part of the study was motivated by the fact that real images of galaxies are still being analysed by observers using global Sérsic fits to obtain their radial sizes. A more detailed motivation for this can be found in Sect. 6.3. Since the prime motivation for this is the derivation of disk sizes, I only give corrections ($corr^{\mathrm{sS}}(R_{\mathrm{gal}})$) as ratios between effective radii obtained from single Sérsic fits of dusty galaxies containing bulges, and the effective radii of corresponding dusty disks (derived from variable-index Sérsic fits to the pure disks with no bulges):

$$corr^{\mathrm{sS}}(R_{\mathrm{gal}}) = \frac{R^{\mathrm{eff}}_{\mathrm{app,gal}}}{R^{\mathrm{eff}}_{\mathrm{app,d}}}. \quad (3.1.17)$$

This isolates the effect of the bulge presence in constraining disk sizes from single Sérsic fits. The correction from Eq. 14 can be used in combination with the corrections for dust and projection effects on single disks (Eq. 3.1.4) to relate the effective radius of a disk derived from single Sérsic fits to the intrinsic effective radius of the stellar emissivity in the disk through the chain corrections:

$$corr = corr^{\text{proj}} * corr^{\text{dust}} * corr^{\text{sS}} \tag{3.1.18}$$

All corrections in this work are presented in terms of polynomial fits. Most of the fits are of the form:

$$corr(x) = \sum_{k=0}^{N} a_k\, x^k \quad \text{for} \quad 0 \leq x \leq 0.95\,, \tag{3.1.19}$$

where $x = 1 - \cos(i)$ and N has a maximum value of 5. In the case of the axis-ratio of disks Q, a combination of a polynomial and a constant was necessary, covering different ranges in inclination (see Sects. 4.1 and 5.1). Besides the inclination, the corrections depend also on wavelength, on τ_B^f, on B/D (only the 3rd term in the chain, $corr^{\text{B/D}}$) and on n_0^{sers} (for bulges).

3.2 The fitting procedure

For the fitting routine I used the commonly used GALFIT (version 3.0.2) data analysis algorithm (Peng et al. 2002, Peng et al. 2010). GALFIT uses a non-linear least squares fitting method, based on the Levenberg-Marquardt algorithm. Through this, the goodness of the fit is checked by computing the χ^2 between the simulated image (in the case of observations, the real galaxy image) and the model image (created by GALFIT, to fit the galaxy image). This is an iterative process, and the free parameters corresponding to each component are adjusted after each iteration in order to minimise the normalized (reduced) value of χ^2 (χ^2/N_{DOF}, with N_{DOF}= number of pixels − number of free parameters, being the number of degrees of freedom).

Since in my simulated images there is not any noise, I use as input to GALFIT a “sigma” image (error/weight image) which is constant for all pixels, except for points outside the physical extent of the images. The latter were set to a very high number, to act as a mask. This was necessary since the simulations are truncated in their volume stellar and dust emissivities while the fitting functions extend to infinity. I did not try to use the truncation functions from GALFIT, as this would only work properly for truncations done on surface stellar brightnesses. The simulated images have no background (by construction, unlike real images); this is why the sky value was set to zero during the fitting procedure, for all morphological components.

It is important to discuss here the effect that noise can produce on the resulting derived parameters of disks and bulges. Indeed noise in observed images will have an effect on the parameters recovered from fits of parametrised template functions of surface brightness distributions to the images. In general, the amplitude of noise fluctuations can either be uncorrelated with source structure (this is the case of background-dominated noise, such as commonly encountered for ground-based longer wavelength optical observations, where noise is dominated by atmospheric emission) or the amplitude of the fluctuations could be correlated with source brightness (this is the case for shot noise from photons from the source, which is generally the case for UV/optical space-based imaging). Even in the case of noise uncorrelated with source structure, one would expect, due to the way the likelihood function is constructed in GALFIT through the quadratic χ^2 function, that noise fluctuations will have more of an effect on the fitted amplitude of bright structures in galaxies with relatively low solid angles (for example the central regions of bulges) than on the fitted amplitude of extended low surface brightness (for example the outer regions of disks). Thus, one expects noise to induce a larger stochasticity in the recovered parameters for bulge luminosities than for disk luminosities. Furthermore, the fluctuations in the recovered parameters will be biased towards positive fluctuations, leading to a systematic positive bias to the fitted brightness of bright structures compared to the fitted brightness of faint structures. For this reason one expects the presence of noise in images to result in fits with larger B/D ratios when fitting a composite galaxy, or smaller disk scale lengths, when fitting a pure disk galaxy. These effects would be more pronounced for noise determined by the source rather than by the background.

To evaluate the effect of noise in this study one would therefore need to introduce a further dimensionality into the range of parameters fitted - namely the noise fluctuation per unit solid angle (expressed as a fraction of the solid angle scale as for example given by $h_{\rm s}^{\rm disk} * h_{\rm s}^{\rm disk}$ in the radiation transfer images and as a fraction of the luminosity of the structural component considered). In addition, source-based noise rather than background-limited noise would have to be considered in two separate cases. This would entail a huge increase in complexity which however is not warranted by the data. All present applications of morphological fits to galaxies in statistical samples are done for galaxies which in general have a very high S/N. For example the SDSS imaging survey is limited to about 23.5 mag. in integrated *r* magnitude which is about 7 mag. fainter than the typical SDSS samples used for fitting with GIM2D such as by Simard et al. (2011). It is therefore only for a small minority of very highly resolved galaxies in statistical blind surveys like SDSS, where structures approach the surface brightness limit, that we expect any appreciable effects. For such highly resolved sources however, one would normally use a dedicated imaging observation which recovers high S/N even on the extended outer disk (as in Möllenhoff et al. 1999, Möllenhoff & Heidt 2001, Möllenhoff 2004). For this reason the effect of noise fluctuations is not considered in the present work.

To fit the simulated images I used the exponential (“expdisk”), the Sérsic (“sersic”) and the de Vaucouleurs ("devauc") functions, as available in GALFIT. As explained in Sect. 3.1, these functions represent the distribution of an infinitely thin disk, and their mathematical description is given by Eqs. 3.1.1, 3.1.2, and 3.1.3.

Since the simulations were produced with high resolution and were not convolved with any instrumental point-spread-function (PSF), during the fitting procedure there was no need to use the PSF component available in GALFIT. It should however be noted that for lower resolution observations, where deconvolution from PSF is essential, an extra correction needs to be added to the corrections presented here. This is because the deconvolution itself is affected by dust. This effect will be analysed in future studies. Here I only note that such a correction, when available, could be simply added in my formulation of chain corrections. Eq. 3.1.4 and 3.1.7 would then become:

$$corr(A) = corr^{\rm proj}(A) * corr^{\rm dust}(A) * corr^{\rm PSF}(A) \tag{3.2.1}$$

$$corr(B) = corr^{\rm proj}(B) + corr^{\rm dust}(B) + corr^{\rm PSF}(B), \tag{3.2.2}$$

where the additional terms are

$$corr^{\rm PSF}(A) = \frac{A^{\rm PSF}_{\rm app}}{A_{\rm app}} \tag{3.2.3}$$

$$corr^{\rm PSF}(B) = B^{\rm PSF}_{\rm app} - B_{\rm app}. \tag{3.2.4}$$

The terms $A^{\rm PSF}_{\rm app}$ or $B^{\rm PSF}_{\rm app}$ represent the measured values of the photometric parameters A or B, which would be derived from fits done on dust-attenuated simulations convolved with PSFs. In this case the corrections will be a function of resolution.

Coming back to my fully sampled simulations, for the measurements presented in this work the free parameters of the fit for the individual components are: the X and Y coordinates of the centre of the galaxy in pixels, the integrated magnitude of the image, the scale-length $R_{\rm d}$ (for exponential)/ effective radius $R^{\rm eff}$ (for Sérsic and de Vaucouleurs functions), axis-ratios Q, and Sérsic index $n^{\rm sers}$ (for Sérsic function). The axis-ratio Q is defined as the ratio between the semi-minor and semi-major axis of the projected image. The position angle is the angle between the semi-major axis and the Y axis and it increases in counter clock-wise direction. For all the simulated images, the position angle was fixed to -90 (semi-major axis perpendicular to the Y axis).

The free parameters of the 2-component fits are: the Y coordinate of the centre of the galaxy in pixels (while this is a free parameter, in this case it is constrained to be the same for both the disk and the bulge component), the integrated magnitudes of the disk and bulge components, the scale-length (for exponential)/ effective radius (for Sérsic function), axis-ratios, and Sérsic index (for Sérsic function).

It is important to mention here that in most cases, the values of the input parameters one provides are not essential for GALFIT to derive the best fit parameters. If one inputs different input values, GALFIT will derive the same values, unless the input values are totally wrong and out of any expected range, which will cause the fitting routine to crash. I tested this by repeating the fitting procedure for a few cases with slightly different input parameter values. The results obtained for the best fit parameters were the same, the only difference being a few more iterations needed by GALFIT to derive the best fit parameters. Therefore, knowing the parameters that were used as input in the simulations, for most inclinations, at a given dust opacity and wavelength, I considered as input parameters in GALFIT average values that were well adjusted to determine GALFIT to produce the best fit after a minimum of iterations, without crashing. For the more extreme cases - close to edge-on inclinations and high values of τ_f^B - where the variation in the derived values of parameters (e.g. scalelengths/effective radii, integrated magnitudes, Sérsic indices) with inclination is larger, using the same input parameters as for lower inclination cases can cause GALFIT to crash or produce unreliable results/fits. In these cases, the fitting procedure is repeated considering as input parameters the values derived by GALFIT (as best fit parameters) for the previously fitted image (at previous inclination) before the crash. If this fails too, the input parameters are increased / decreased accordingly and the fit repeated until GALFIT derives the best fit parameters without crashing or outputting unreliable parameters (marked with "*" in the output log file).

Chapter 4

Projection effects

The main goal of this work, that of quantifying the changes due to dust on the derived photometric parameters of the main morphological components of spiral galaxies, is achievable due to the fact that, as mentioned before, the intrinsic parameters of the volume stellar emissivity are known, since they are input in the simulations. However, even in the absence of dust, the derived photometric parameters of the images measured from fitting infinitely thin disk distributions would differ from the intrinsic parameters of the volume stellar emissivity due to the thickness of real galaxies, which I call projection effects. Quantifying projection effects allows me to derive the change between the intrinsic parameters of the volume stellar emissivity and those measured on non-dusty images, which, subsequently, can be used to measure the changes between the parameters of the dustless and dusty images, respectively.

CHAPTER 4

4.1 The Disk

Disks are fairly thin objects; their vertical extent is significantly smaller than their radial extent (by a factor of 10 or so in the model; Tuffs et al. 2004). This means that projection effects will only start to be visible close to edge-on orientations, when the vertical distribution of stars becomes apparent.

4.1.1 Exponential fits to the disk

To quantify the projection effects I first fitted the dustless simulated images with an infinitely thin exponential disk, as available in GALFIT. To observe the accuracy of the fits, I analysed both the profiles and the relative residual maps, between the simulated and the fitted images. In the upper and middle rows of Fig. 4.1, major and minor axis profiles for the B band images are presented, for three orientations of the disk. At lower inclinations the exponential fits are a good representation of the profiles, while at higher inclinations deviations from a pure exponential start to appear due to the above-mentioned projection effects. In particular, these deviations can be seen in the central part of the disks - the flattening of the simulated profiles. At higher inclinations, projection effects produce deviations from a pure exponential also at intermediate radii, with stronger effects in the minor axis direction. For example, at an inclination of 84°, Fig. 4.1 (lower row, right panel) shows a deviation of up to 15% in the minor axis direction (the yellow wings; see also the corresponding double peak in the minor axis profile residuals in Fig. 4.1, second row). The black area that surrounds the disk, corresponding to very large relative residuals, appears because the simulated images are truncated, while the exponential fitted images extend to infinity (as explained in Sect. 3.2, I did not attempt to use the truncation features of GALFIT).

To understand the cause of all these deviations one needs to remember that what I try to do is to fit the projection of two exponential distributions (radial and vertical) with one single exponential, which will inevitably result in an imperfect fit. As long as the vertical extent of the disk will project within the predicted elliptical shape of the infinitely thin disk, meaning as long as the axis ratios of the measured isophotes will correspond to the predicted cos(i) inclination of the infinitely thin disk, the projected stellar distribution will be dominated by the radial exponential distribution of the disk, and the fit will accurately reproduce this radial distribution. At higher inclinations the vertical extent of the disk will increase the measured axis ratio of the projected elliptical isophotes (from the predicted cos(i) ratio). This means that the measured axis ratio will not be a good representation of the inclination of the disk. Moreover, the fit with an infinitely thin exponential disk will try to account for the extra thickness of the measured elliptical isophotes by trying to force a solution with a larger scale-length. This will produce the deviations from a pure exponential seen in the plots and will systematically overestimate the radial scale-length of the disk and underestimate the inclination of the disk on the basis of an infinitely thin disk approximation only.

The results of this analysis allow me to derive projection effects $corr^{\rm proj}$ on stellar disks using Eq. 3.1.5 for the exponential scale-length and axis-ratio and Eq. 3.1.8 for the central surface brightness. The inclination dependence of these corrections are shown in Fig. 4.2. As explained above, the disk scale-length is relatively insensitive to projection effects at low to intermediate inclinations (left panel, Fig. 4.2), while close to edge-on orientations it increases with inclination with respect to the radial scale-length of the volume stellar emissivity. It is important to mention here that the amplitude of these results slightly varies with the wavelength at which the measurements are taken. This happens because the simulations originate from a volume stellar emissivity having a varying radial scale-length with wavelength (for a fixed scale-height), as prescribed in the model of Popescu et al. (2011). Here only the results for the B band are shown, as the overall trend in the variation of the derived scale-lengths with inclination is the same for all wavebands. The results for all wavebands are given in the form of polynomial fits (Eq. 3.1.19), and are listed in Table A.1.

The deviation of the derived disk axis-ratios from the corresponding axis-ratio of an infinitely thin exponential disk ($corr^{\mathrm{proj}}(Q)$) is plotted in the middle panel of Fig. 4.2, as a function of inclination. As expected, at low inclination the thin disk approximation works very well, while at high inclination the vertical distribution of stars introduces an extra thickness, which cannot be taken into account by the infinitely thin approximation. To account for the steep increase in the measured axis ratio with respect to that of an infinitely thin disk, at high inclination, the measurements were fitted with a combination of a 5th order polynomial and a constant, of the form:

$$corr(x) = \begin{cases} \sum_{k=0}^{N} a_k\, x^k & \text{for} \quad 0 \le x \le 0.90 \\ b_0 & \text{for} \quad x = 0.95\,, \end{cases} \tag{4.1.1.1}$$

where $x = 1 - \cos(i)$. The coefficients of these polynomial fits are listed in Table A.2, for the *B, V, I, J, K* bands.

Here I also checked that the analytical formula used in Driver et al. (2007) [1] to account for the finite thickness of the disk is a good representation of the dependence of the measured axis ratios on inclination (see overplotted dashed line in Fig. 4.2, middle).

Finally, I looked at the distortions introduced by the projection effects on the derived central surface brightness ratios ($corr^{\mathrm{proj}}(SB)$). Here two measurements were considered. The first one is the measurement for the central pixel, where I calculated the ratio between the central surface brightness for the fitted dustless images of the old stellar

[1] $Q_i^2 = \cos^2(i) + q^2(1-\cos^2(i))$, with q being the ratio between the intrinsic scale-height and scale-length of the volume stellar emissivity of the disk, having different values for each optical band

disk and the central surface brightness for the corresponding simulated images, ΔSB_0 (Fig. 4.2, right). The ratios are expressed in magnitudes. A second measurement is to consider an average of the surface brightness over an elliptical aperture. This second measurement is necessary as a reference for measurements of surface brightness in simulations that include dust. As we will see in Sect. 5, dust introduces asymmetries in the surface-brightness distribution, therefore it only make sense to take an average measurement in the central region. Furthermore, in real observations central regions may be affected by resolution effects, which result in essentially an averaging of the signal. For this reason, the average central surface brightness ratio is defined as $\Delta SB_0 = -2.5log(F_{\rm i}/F_{\rm s})$: the ratio of the average central surface brightness ($F_{\rm i}$) of the fitted dustless disk images, and the average central surface brightness of the simulated dustless disk images ($F_{\rm s}$). Both $F_{\rm i}$ and $F_{\rm s}$ were calculated as an average over an elliptical aperture centred on the position of the geometrical centre of the simulated image, with a semi-major axis of $R_{\rm i}/10$ and an axis-ratio of $Q_{\rm i}$. In this case, the geometrical centre coincides with the coordinates of the intensity peak of the fitted image and of the simulated image.

As expected for the dustless case, the trends in the corrections for the central pixel ΔSB are the same as for the average ΔSB. These corrections are tabulated in Table A.1, in form of polynomial fits (Eq.3.1.19). Overall, the distortions in the surface brightness due to projection effects are negligible at face-on orientation and increase with inclination, producing up to 0.5 mag. difference for an edge-on galaxy. As already noted from Fig. 4.1, the derived surface brightness from the exponential fit is always brighter than the corresponding one in the simulated images, due to the flattening of their brightnesses in the central regions.

4.1.2 Sérsic fits to the disk

To quantify the deviation of the simulated images from pure exponentials I also fitted these images with a variable-index general Sérsic function, in order to see if a better fit to the images can be obtained. I followed the same approach as in the previous case, plotting major and minor axis profiles (Fig. 4.3, upper and middle rows) and generating relative residual maps (lower row, same figure) for various inclinations.

Overall the variable-index Sérsic functions provide better fits to the simulated images at higher inclinations than pure exponentials. Thus, the reduced-χ^2 shows a 63% decrease at an inclination of 73° and a 73% decrease at an inclination of 84°. This is a significant improvement in the goodness of the fit for the inclinations where projection effects play a role. In particular, one can see from the profiles in Fig. 4.3 that GALFIT tries to mimick the departure from exponentiality in the centre of the disks by fitting the simulated images with a Sérsic index lower than 1. This can also be seen from Fig. 4.4, where I plotted the inclination dependence of the derived Sérsic index of the fitted disk images. At high inclinations, the best fits correspond to output values for the Sérsic indices as low as 0.8.

As expected, at lower inclinations Sérsic fits recover the results from pure exponentials, since no projection effects are manifested by face-on disks. Thus, the reduced-χ^2 is similar for exponential and Sérsic fits. For example the reduced-χ^2 shows a 0.0004% decrease at an inclination of 46°. Similarly, the fitted Sérsic index is 1 (exponential) for face-on disks.

I fitted the variation of $n_{\rm i}^{\rm sers}$ index with inclination using a 4th order polynomial (Eq. 3.1.19). The fit for the B band is shown by the solid line in Fig. 4.4, while the coefficients of the fits in all wavebands are listed in Table A.3. By applying Eq. 3.1.8 for the specific case of the Sérsic index, the departure from exponentiality due to projection effects is defined as

$$\Delta n_{\rm i}^{\rm sers} = n_{\rm i}^{\rm sers} - n_{0}^{\rm sers}\,, \tag{4.1.2.1}$$

where $n_0^{\rm sers}$ is the Sérsic index of the volume stellar emissivity (for disks $n_0^{\rm sers} = 1$; exponential). From the definition, it follows that $\Delta n_{\rm i}^{\rm sers}$ varies with inclination from 0 to up to -0.2. Though Sérsic functions provide better fits to the disk images, in particular in the centre and at intermediate distances from the centre, they are poorer fits to the outer disks, where relative residuals can be high (e.g. 35-40% at 84°; see Fig. 4.3). The reason for this is that the surface brightness distribution in the outer parts is still decreasing according to an exponential distribution, while the fitted distribution - described by a Sérsic index less than 1.0 (mainly determined by the brightest pixels in the centre) is falling faster at large radii, thus underpredicting the luminosity profiles in the outer parts. However, outer disks of galaxies are in real life subject to additional truncation/anti-truncation effects, and may in any case require additional components to be fitted. I therefore conclude that variable index Sérsic functions are better representations of the disk images corresponding to pure exponential distributions of the volume stellar emissivity.

The resulting variation of the derived Sérsic effective radius $R_{\rm i}^{\rm eff}$ is compared with the corresponding derived exponential scale-length (from an exponential fit) by using the linear transformation $R_{\rm i}^{\rm eff} = 1.678 R_{\rm i}$ (which is exact only for $n^{\rm sers} = 1.0$) and by overplotting the variation of the equivalent intrinsic scale-length $R_{\rm i}$ in Fig. 4.2, with a red line (left panel). One can see an opposite trend in the two variations. At face-on inclinations both the exponential and the Sérsic fit are identical ($n^{\rm sers} = 1.0$). As the inclination increases the equivalent scale-length of the Sérsic fit decreases with respect to the radial scale-length of the volume stellar emissivity (while the intrinsic exponential scale-length increases). This is due to the decrease in the fitted Sérsic index with increasing inclination, resulting in an equivalent scale-length which is decreasingly smaller and smaller from the $R_i^{eff}/1.678$ transformation. The results of the polynomial fits (Eq. 3.1.19) to the $corr^{proj}(R^{eff})$ for all wavebands are listed in Table A.3.

Though the derived effective radius shows a different behaviour with inclination with respect to the exponential fit, the variation in axis ratios seems to be insensitive to whether the fit is done with an exponential or with a variable-index Sérsic function (see Fig. 4.2, middle panel). In other words the axis ratio seems to be a more robust quantity against projection effects. Irrespectively of the fitting function, the variation with inclination of Q_i only shows a departure from an infinitely thin disk variation, due to the vertical distribution of stars. The $corr^{proj}(Q)$ for the Sérsic fits are thus the same as for the exponential fits and the coefficients of the polynomial fits (Eq. 4.1.1.1) for all wavebands can be found in Table A.2.

Finally, the departure of the fitted central surface brightness from that of the simulated images is minimal in comparison with the exponential fit case (see right hand panel in Fig. 4.2), another proof that Sérsic fits are better representations of images corresponding to exponential distributions of volume stellar emissivity, especially in the central regions of the disks. The slight overestimation of the central surface brightnesses in the fit as compared to that of the simulations for the high inclinations can be also seen in the radial profiles from Fig. 4.3. The overall departure of the fit from the simulation is ± 0.1 mag, as compared to the 0.5 mag departure in the exponential fit. The coefficients of the polynomial fits (Eq.3.1.19) to $corr^{proj}(\Delta SB)$ for all wavebands are listed in Table A.3.

4.2 The Thin Disk

For the thin disk (young stellar disk), the projection effects are insignificant even at very high inclinations. This is due to the different geometry of the young stellar disk, with the ratio between the scale-height and the scale-length of the thin disk being very small (by a factor 60 or so in the model; Tuffs et al. 2004). In other words, the approximation of the infinite thin disk is a very good one for this stellar component.

4.3 The Bulge

The problem of projection effects on bulges is very different from that encountered in disks. The difference does not have an intrinsic, physical cause, but originates from the different way astrophysicists use to characterise the distribution of stellar emissivity in these two types of objects, and therefore in the two different ways the simulations used for this study are built. In disks the exact mathematical formulation of the stellar emissivity happens at the level of the volume emissivity, where we expect disks to be described by a double exponential, one for the radial distribution and one for the vertical distribution. When projecting this double exponential and fitting the resulting image with a single exponential distribution corresponding to an infinitely thin disk, we will obviously not be able to exactly fit the surface brightness distribution. So this will result in a projection effect. In bulges the situation is reversed. The exact mathematical formulation is for the surface brightness distribution of the images, as given by the Sérsic functions. By construction, the simulations were produced for a volume emissivity that, when projected, at any inclination, will reproduce the Sérsic function for the case of a bulge that extends to infinity. So by construction, the simulations incorporate the projection effects. The caveat is however that this is only true if bulges were to extend to infinity. Since in real life truncations must occur at some distance from the centre, distortions from the expected Sérsic distributions will occur too. So in my simulations I expect projection effects solely because of the missing light beyond the truncation radius. This would be a constant with inclination, as the missing light will always be the same at any given inclination. It will though strongly depend on the truncation radius, and on the type of Sérsic distribution considered (the Sérsic index).

Since real life bulges can be described by Sérsic functions characterized by different Sérsic indices, n_0^{sers}, and since real bulges could be either truncated, or could extend to high galactocentric radii (see Maltby et al. 2012), one needs to consider all these extra dimensions to the problem. Thus, I produced simulations of bulges with volume stellar emissivity corresponding to (de-projected) Sérsic functions with 4 different values of the Sérsic index $n_0^{sers} = 1, 2, 4, 8$. For each of these the bulges were truncated in the first case at 3 effective radii and in the second one at 10 effective radii. As mentioned in Chapter 2, the truncation at $3R_0^{eff}$ was chosen as this avoids the problem of having a disk-bulge system dominated by the bulge light at high galactocentric radii for large values of the Sérsic index. The truncation at $10R_0^{eff}$ is essentially representative of a bulge with no truncation at all, since at this galactocentric radius almost all the light inside the profile has been accounted for.

The results on projection effects of bulges are calculated using Eq. 3.1.8 and 3.1.5 for the derived Sérsic indices and corresponding effective radii, for different types of volume stellar emissivities (n_0^{sers}) and different truncations.

In Fig. 4.5 it can be seen that, as expected, the derived Sérsic index n_i^{sers} does not depend on inclination. This is true irrespective of the n_0^{sers} index of the corresponding volume stellar emissivity and of the truncation radius. For high values of the n_0^{sers} index ($n_0^{sers} = 8$) the constancy of n_i^{sers} with inclination is strongly affected by noise in the measurements. This is produced by insufficient spatial resolution in the radiative transfer calculations in the inner parts of these bulges. The simulations were optimised to properly sample the volume emissivity for bulges up to $n_0^{\rm sers} = 4$. For higher values of $n_0^{\rm sers}$, the steep rise in volume emissivity profiles near the centre would require even finer sampling, which would make these calculations prohibitively time consuming. For the purpose of this study the benefit of increasing the resolution in these simulations is limited, and instead I opted to fit all measurements with a 0th order polynomial function (a constant, Eq. 3.1.19). The results of the fits are overplotted in Fig. 4.5 and are listed in Table A.4.

From these results one can also see that the derived Sérsic index is always smaller than the Sérsic index corresponding to the volume stellar emissivity. This is because of the missing light outside the truncation radius. The difference between the Sérsic indices of the de-projected and projected distribution, $\Delta n_i^{\rm sers}$ increases (in absolute value) with increasing $n_0^{\rm sers}$, as seen in Fig. 4.5, due to the larger variation in the light intensity between the inner and outer radii for large values of $n_i^{\rm sers}$ (more peaky and steep profiles).

For the case of bulges truncated at $10R_0^{\rm eff}$, the fitted values of $n_i^{\rm sers}$ are closer to those of $n_0^{\rm sers}$, since in this case bulges are closer to a bulge which has its emissivity extending to infinity (where, as explained before, by construction $n_i^{\rm sers} = n_0^{\rm sers}$).

The constancy of projection effects with inclination is also visible in Fig. 4.6, for $corr^{\rm proj}(R^{\rm eff})$. As for the case of $ni^{\rm sers}$, I fitted the derived ratios with a constant, as listed in Table A.4. Fig. 4.6 also shows that the derived effective radius of truncated bulges decreases with increasing $n_i^{\rm sers}$. As expected, the decrease is minimal for bulges truncated at $10R_0^{\rm eff}$. Another aspect that can be noticed from this figure is that for any $n_0^{\rm sers}$ the effective radii for the bulges truncated at $10R_0^{\rm eff}$ are always higher than the ones for the bulges truncated at $3R_0^{\rm eff}$. This happens because in the former case more stellar emissivity will contribute to the corresponding Sérsic distribution than in the latter. Therefore, half of the total stellar emissivity will be enclosed in a larger region for bulges truncated at $10R_0^{\rm eff}$, with a corresponding higher effective radius.

Since in many cases bulges are fitted by observers with de Vaucouleurs functions, I considered this case as well, but only for de Vaucouleurs bulges ($n_0^{\rm sers} = 4$) truncated at $3R^{\rm eff}$. The results of the polynomial fits to the $n_{\rm i}^{\rm sers}$ are given in Table A.5 and are very similar to those obtained using Sérsic functions (for the same $n_0^{\rm sers}$ and truncation radius).

In the following chapter, when I quantify dust effects for bulges with different Sérsic functions and/or truncation, I apply Eq. 3.1.6 and 3.1.9, as well as the chain corrections from Eq. 3.1.4 and 3.1.7, by using dustless and dusty simulations with a common $n_0^{\rm sers}$ and truncation radius.

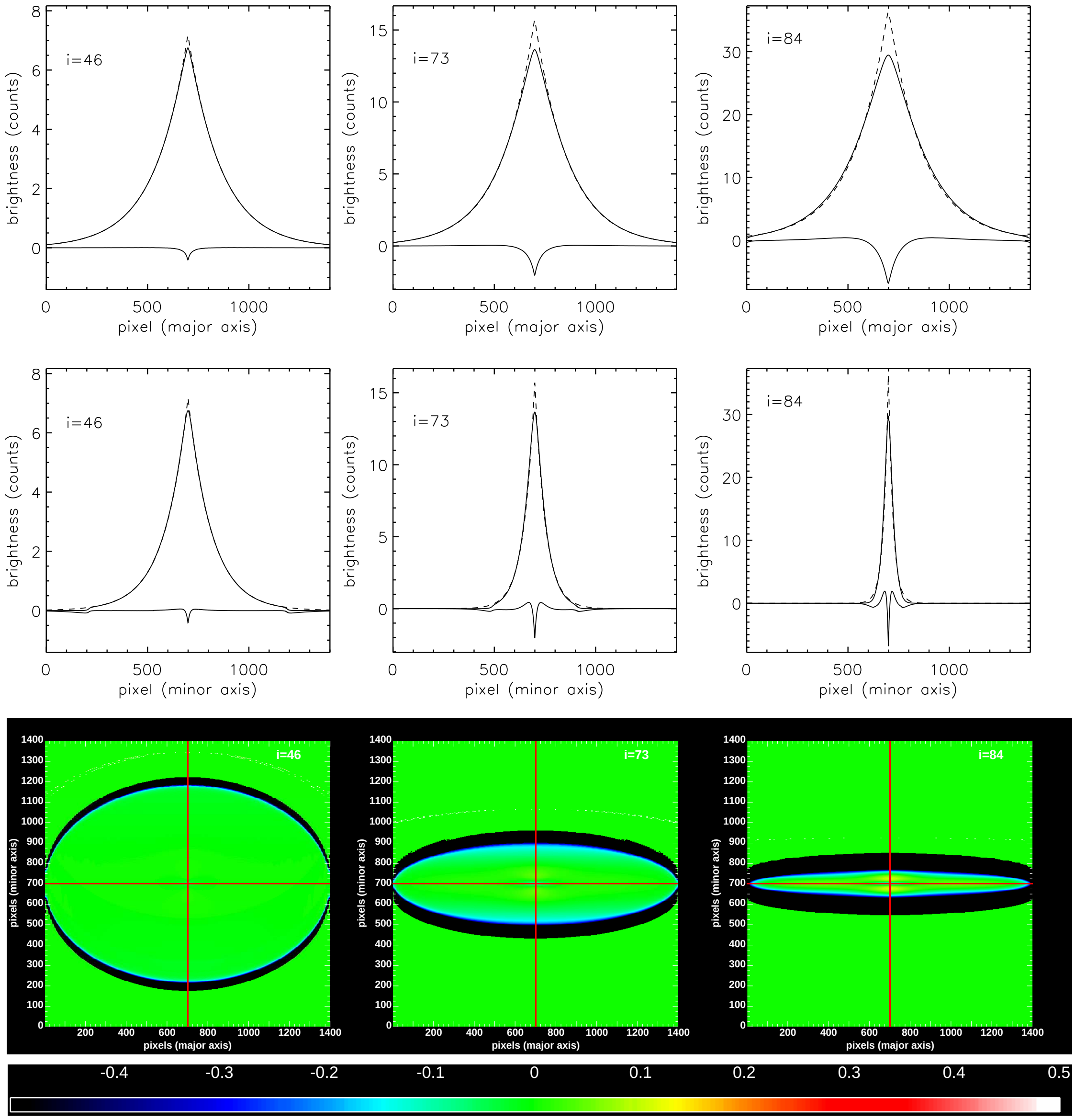

Figure 4.1: Major and minor axis **disk** profiles (**upper and middle rows**) showing the deviations from pure exponentials due to projection effects. Upper solid curves are for **B band** dust-free images, dashed curves are for corresponding exponential fits, while absolute residuals ($simulation - fit$) are represented by lower solid curves. The fits were done by fixing the position of the intensity peak of the fitted image to the geometrical centre of the map, which, in this case, corresponds to the intensity peak in the simulated image. The cuts were taken parallel and perpendicular to the major axis of the disk images, through their geometrical centres, at inclinations $1 - \cos(i) = 0.3, 0.7, 0.9$ ($i = 46°, 73°, 84°$). **Lower row**: Corresponding relative residuals ($\frac{simulation - fit}{simulation}$), at the same inclinations as the profiles. The red lines show **major and minor axis** cuts through the geometrical centre of each image.

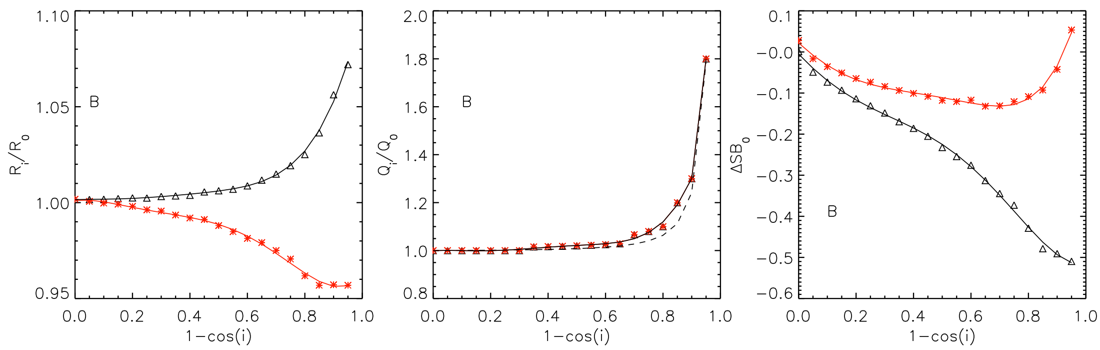

Figure 4.2: Projection effects $corr^{\rm proj}$ on the derived B band photometric parameters of **disks fitted with exponential functions** (black) and with **Sérsic functions** (red) : scale-lengths, axis-ratios, and central surface brightnesses. The symbols represent the measurements while the solid line are polynomial fits to the measurements. The plots represent the inclination dependence of: **left** - the ratio between the intrinsic scale-lengths, $R_{\rm i}$, and the intrinsic (radial) scale-length of the volume stellar emissivity, R_0; **middle** - the ratio between the intrinsic axis-ratio, $Q_{\rm i}$, and the axis-ratio of an infinitely thin disk, Q_0; with dashed line I overplotted the analytic formula from Driver et al. 2007, which is a modification of the *Hubble* formula from Hubble 1926, to take into account the thickness of the disk; **right** - the difference between the central surface brightness of the fitted images and of the corresponding simulated images, ΔSB_0, expressed in magnitudes. In the case of a Sérsic fit, $R_{\rm i}$ (left panel) is the equivalent intrinsic scale-length, calculated from the derived intrinsic Sérsic effective radius, $R_{\rm i}^{\rm eff}$, using the relation $R_{\rm i}^{eff} = 1.678 R_{\rm i}$ (which is an exact transformation only for $n^{\rm sers} = 1$).

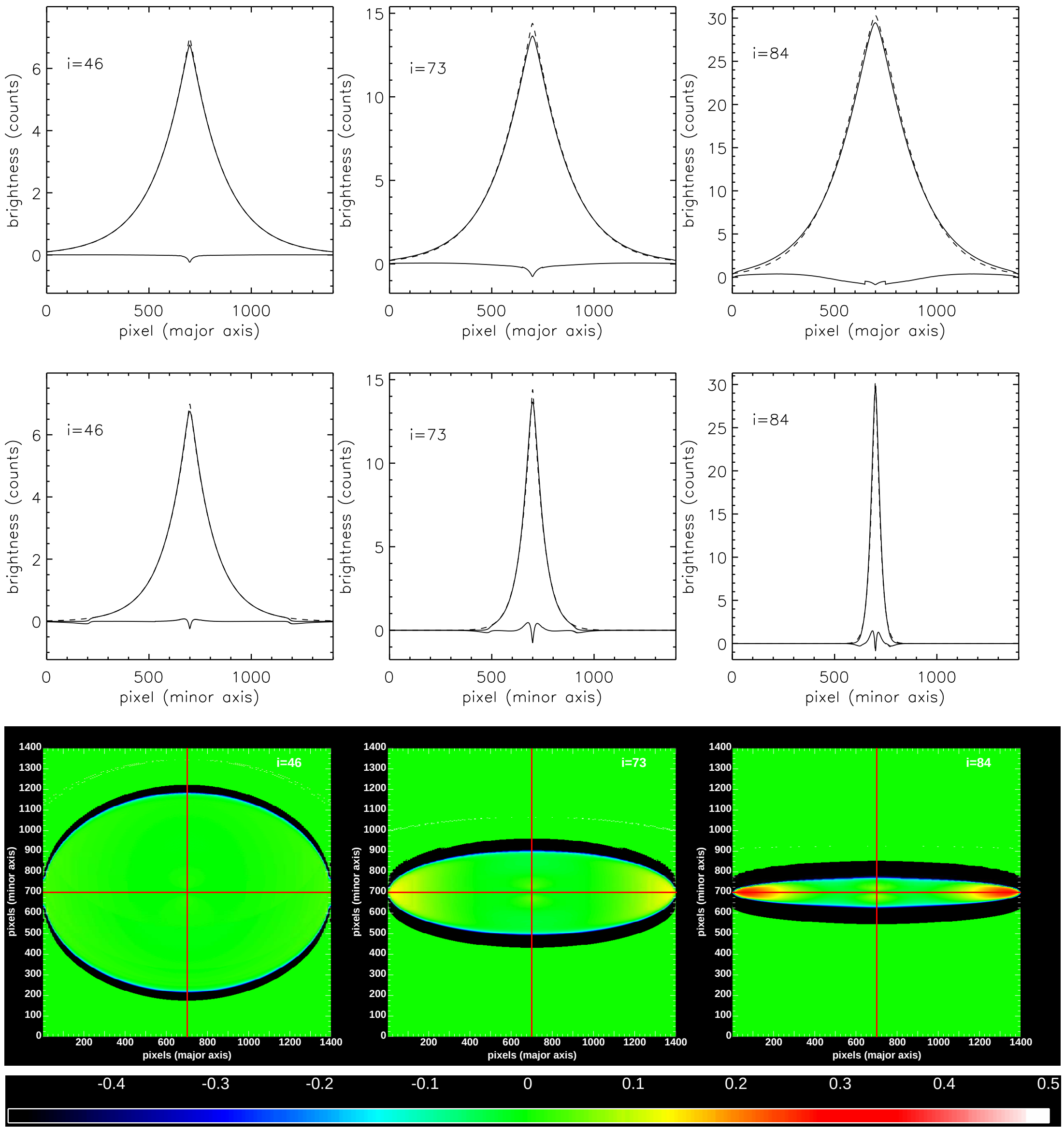

Figure 4.3: Major and minor axis **disk** profiles (**upper and middle rows**) showing the deviations from Sérsic functions due to projection effects. Upper solid curves are for **B band** dust-free images, dashed curves are for corresponding variable-index Sérsic fits, while absolute residuals (*simulation* − *fit*) are represented by lower solid curves. The fits were done by fixing the position of the intensity peak of the fitted image to the geometrical centre of the map. The cuts were taken parallel and perpendicular to the major axis of the dustless disk images, through their geometrical centres, at inclinations $1 - \cos(i) = 0.3, 0.7, 0.9$ ($i = 46°, 73°, 84°$). **Lower row**: Corresponding relative residuals ($\frac{simulation - fit}{simulation}$) at the same inclinations as the profiles. The red lines show major and minor axis cuts through the geometrical centre of each image.

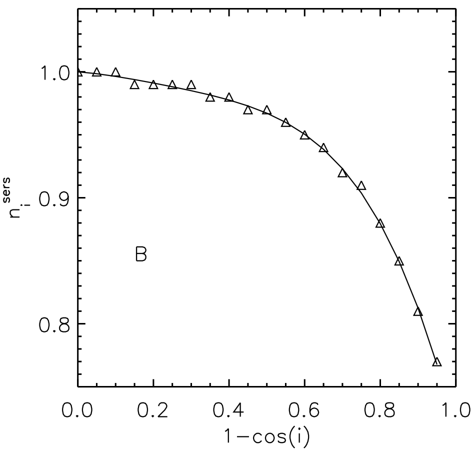

Figure 4.4: The inclination dependence of the Sérsic index n_i^{sers} for the dustless images (triangles) of the **disk** in the B band, for the case that the images are **fitted with a general Sérsic function** having n_i^{sers} as a free parameter. The solid line shows the polynomial fit to the measurements.

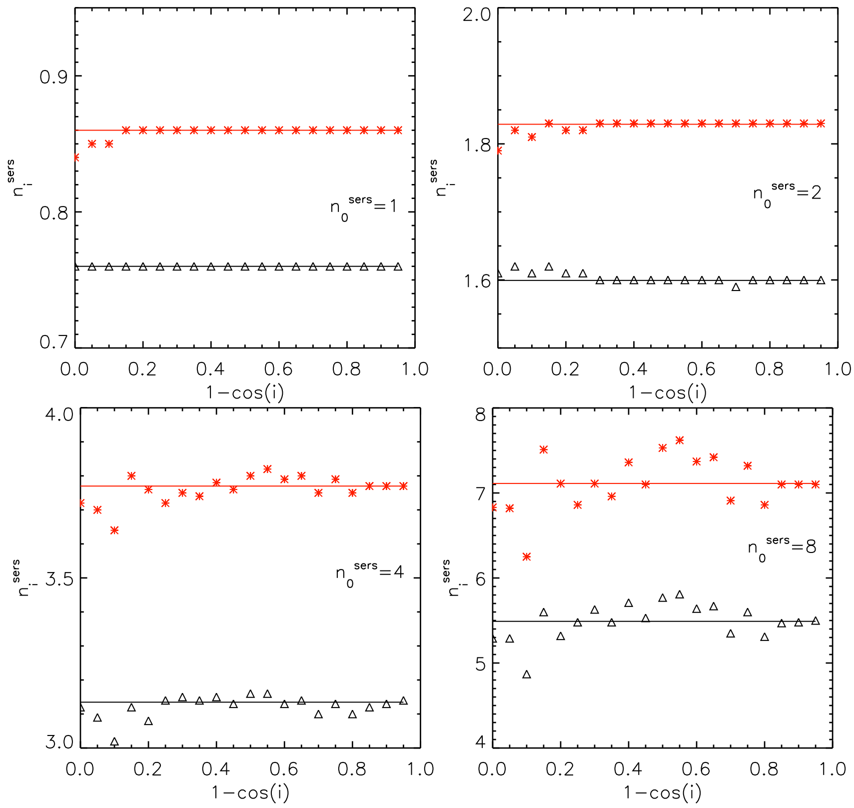

Figure 4.5: The derived Sérsic index n_i^{sers} of the dust free images of the **bulge**, for bulges produced with volume stellar emissivities described by (de-projected) Sérsic functions having different Sérsic indices. The symbols represent the measurements while the solid lines are polynomial fits to the measurements. The plots correspond to the bulge Sérsic index values $n_0^{sers} = 1.0, 2.0$ (upper row),$4.0, 8.0$ (lower row). The black curves correspond to bulges truncated at 3 R_0^{eff} while the red curves are for bulges truncated at 10 R_0^{eff}.

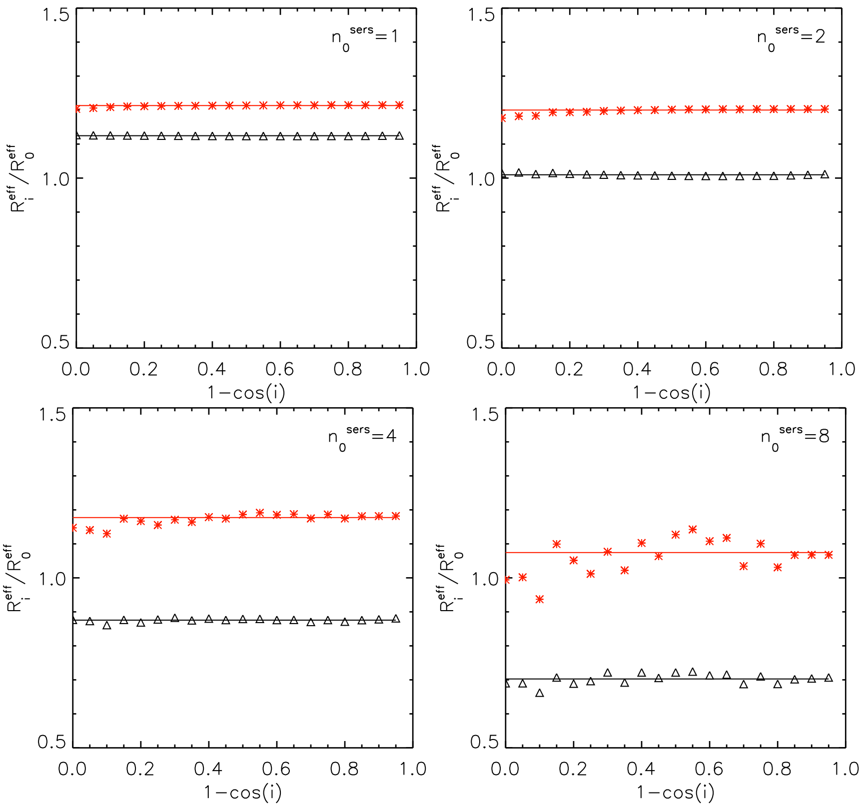

Figure 4.6: Projection effects $corr^{proj}$ on the derived effective radius of the **bulge**. The symbols represent the measurements while the solid lines are polynomial fits to the measurements. The plots represent the ratio between the intrinsic Sérsic effective radii, R_i^{eff}, and the corresponding volume stellar emissivity, R_0^{eff}. The plots correspond to bulges with volume stellar emissivity described by (de-projected) Sérsic functions having Sérsic index values $n_0^{sers} = 1.0, 2.0$ (upper row),$4.0, 8.0$ (lower row). The black curves correspond to bulges truncated at 3 R_0^{eff} while the red curves are for bulges truncated at 10 R_0^{eff}.

Chapter 5

Dust Effects on Single Disks and Bulges

The quantification of projection effects $corr^{\rm proj}$ allows the subsequent derivation of dust effects $corr^{\rm dust}$. To do this, the simulated dusty images of disks and bulges were fitted, in order to derive the apparent (dust affected) values for the photometric parameters. $corr^{\rm dust}$ were then derived using Eq. 3.1.6 and 3.1.9, by relating these apparent values of the photometric parameters with the corresponding intrinsic ones, determined from the previous analysis of projection effects. Dust effects were quantified for various values of the central B-band face-on dust optical depth τ^f_B.

In the previous work of Möllenhoff et al. (2006) a disentanglement between dust and projection effects was not attempted, nor an analysis of the simulations at high inclinations. As we will see in this section, the changes induced by dust in the values of the photometric parameters of spiral galaxies components, $corr^{\rm dust}$, are far more important than projection effects $corr^{\rm proj}$. I present here dust effects for each morphological component and discuss the results.

CHAPTER 5

5.1 The Disk

Dust affects the appearance of the galaxy disks because its opacity is higher in the central parts of the disks, and decreases exponentially with radius (e.g. Boissier et al. 2004, Popescu et al. 2005). As a consequence, the central parts of the disks will be more attenuated than the outer parts. This will alter the distribution of stellar emissivity as seen in the absence of dust.

Dust can also induce asymmetries in the surface brightness profiles, at high to edge-on inclinations. This happens because of the difference in the attenuation between the two halves of the disk (separated by the dust disk). At face-on and low inclinations, this effect is negligible, because at each radial position one sees the distribution of stellar emissivity through dust columns with the same scale-heights. At high inclinations, the half of the disk seen above the dust layer will suffer less attenuation than the half behind it. In addition, anisotropic scattering will also introduce asymmetries, which work in the same direction as the effect of absorption. This results in asymmetric minor axis profiles for inclined disks, with the half of the disk nearest to the observer appearing brighter. These asymmetries cannot be properly taken into account when fitting the images with symmetric analytical functions - exponential distribution and variable index Sérsic function.

Because of these dust-induced asymmetries for the simulated images, the position of the intensity peak will generally not coincide with the geometrical centre. As a consequence, better fits are provided when the position of the peak intensity is left as a free parameter. The asymmetries induced by dust are particularly visible for higher values of τ_B^f and at higher inclinations.

5.1.1 Exponential fits to the disk

When fitting disks with exponential functions a main problem, as mentioned before, is the appearance of dust-induced asymmetries at higher values of τ_B^f and i. A good illustration of this effect can be seen from the minor axis profiles in Fig. 5.1 (middle row, for τ_B^f = 4.0 case), where the position of the intensity peak is shifted with respect to the position of the geometrical centre, marked by the light green line. Also, in the corresponding residual maps on the lower row of Fig. 5.1 one can notice asymmetric residuals. For example, at 73° inclination the fit underpredicts the lower half of the simulated image with 10-15% (see the yellow lower feature in the residual maps) while at 84°, the residuals are as high as 30-35% (the lower yellow-red feature from Fig. 5.1; see also the minor axis profiles from the same figure, middle row, right panel).

It is also interesting to note that the residual maps exhibit a ring-like structure at intermediate inclinations (see the yellow ring in the middle row, left panel of Fig. 5.1). This feature appears because the fit underpredicts the simulated dusty images at intermediate radii (see also the left column of plots in Fig. 5.1) (first two rows), where both the fit and the simulated image contain only smooth (diffuse) distributions of stellar emissivity. In other words, dust can induce feature-like structures in the residual maps which have no connection with real structures like rings, spiral arms or clumpiness. In view of the fact that it is common practice to use residual maps in observations of galaxies to assess the degree of clumpiness of an object, or even to assess the morphological type (spiral type), a word of caution has to be added here - the reliability of the method is limited due to the above mentioned dust effects.

Fig. 5.2 shows the inclination dependence of the ratio between the apparent and intrinsic scale-lengths ($corr^{\mathrm{dust}}(R)$; Eq 3.1.6), for different values of the central face-on optical depth, τ_B^f. As previously found (e.g. Möllenhoff et al. 2006), the scale-length ratios increase with opacity and are always greater than 1. As noticed before from Fig. 5.1, this is due to the dust-induced flattening of the intrinsic stellar emissivity profiles. An additional feature of the plots for the B band is that, for low values of τ^f_B, there is a monotonic increase in scale-length with inclination, while at high opacities, when the disk becomes optically thick along all lines of sight (the opacity of the disk will be high even at large galactocentric radii), the increase flattens asymptotically (Fig. 5.2, left panel; see also Möllenhoff et al. 2006). However, this is not the case for the K band, where even at high τ^f_B one sees a monotonic increase in scale-length ratios with inclination (Fig. 5.2, right panel). This is because in the K band the disk is still optically thin along most of the lines of sight, at all inclinations. The results of the polynomial fits (Eq. 3.1.19) to $corr^{\rm dust}(R)$, for all opacities considered, are listed in Tables B.1 to B.5 for the *B, V, I, J, K* bands.

Fig. 5.3 shows the inclination dependence of the ratio between the apparent and intrinsic average central surface-brightness, expressed in magnitudes $\Delta SB{=}{-}2.5log(F_{\rm app}/F_{\rm i})$ ($corr^{\rm dust}(SB)$; Eq. 3.1.9). As already noted in Chapter 4 (Sect. 4.1), these are calculated as averages in elliptical apertures. $F_{\rm app}$ was calculated as an average over an elliptical aperture centred on the position of the geometrical centre of the fitted dusty images, with a semi-major axis of $R_{\rm app}/10$ and an axis-ratio of $Q_{\rm app}$.

The surface brightness ratios are always positive at any inclination and for all values of τ^f_B, meaning the apparent average central surface brightnesses are always fainter than the intrinsic ones. At high opacities, and close to edge-on inclinations, when the lines of sight pass through the longest columns of dust, the attenuation of central surface brightness is very strong (up to 8 mag. for the B band and up to 5 mag. for the K band at $\tau^f_B = 8.0$). As with $corr^{\rm dust}(R)$, the results of the polynomial fits (Eq. 3.1.19) to $corr^{\rm dust}(\Delta SB)$ for all opacities considered, are given in Tables B.1 to B.5 for the *B, V, I, J, K* bands.

The change in the disk axis-ratio due to dust ($corr^{\mathrm{dust}}(Q)$; Eq. 3.1.6) has been fitted by a combination of two polynomials, of the form:

$$corr(x) = \begin{cases} a_0 & \text{for} \quad 0 \leq x \leq x_1 \\ b_0 + b_1\, x_1 & \text{for} \quad x_1 \leq x \leq 0.95\,, \end{cases} \tag{5.1.1.1}$$

where $x = 1 - \cos(i)$ and $x_1 = 0.95$ for $\tau_B^f = 0.1, 0.3$, $x_1 = 0.90$ for $\tau_B^f = 0.5, 1.0, 2.0$ and $x_1 = 0.65$ for $\tau_B^f = 4.0, 8.0$. At low to intermediate inclinations, up to $1 - cos(i) = 0.65$, the derived axis-ratio in the presence of dust, Q_{app}, is the same as the intrinsic axis-ratio, Q_{i}, which, in turn, is the same as the axis ratio of the infinitely thin disk, $Q_0 = cos(i)$. It is only at higher inclinations and higher dust opacities that the dust starts to affect the derived axis-ratios, in the sense that the measured ratios are lower than the corresponding intrinsic values. This means that dust makes disks appear slightly thinner than they are in reality. Nonetheless, even at higher inclinations and dust opacities, the effects due to dust, $corr^{\mathrm{dust}}(Q)$, are smaller than projection effects, $corr^{\mathrm{proj}}(Q)$. Thus, the decrease in the axis ratio due to dust is at most 10%, while the increase in the intrinsic axis-ratio with respect to the axis-ratio of the infinitely thin disk is up to 50%. Overall, the correction from the $cos(i)$ term is dominated by the increase in the axis ratio due to the vertical distribution of stars. The resulting coefficients of the polynomial fits to $corr^{\mathrm{dust}}(Q)$ are given for all opacities considered in Tables B.6 to B.10 for *B, V, I, J, K* bands.

5.1.2 Sérsic fits to the disk

As with projection effects, to quantify the deviations of the simulated images from pure exponentials I also fitted the dusty disk images with general Sérsic functions. The corresponding major and minor axis profiles for $\tau_B^f = 4.0$ (as displayed in the upper and middle rows of Fig. 5.4 at three inclinations) show that overall general Sérsic functions are a better representation of the dusty disks. This can also be noticed from the residual maps (same figure, lower row) where the residuals are very low at most inclinations and radii. A reduced-χ^2 test for the case presented in Fig. 5.4 (B band and $\tau_B^f = 4.0$) shows a decrease of 94% in the reduced-χ^2 value at an inclination of 46° with respect to the exponential case. However, at higher inclinations the dust-induced asymmetries still remain, as both Sérsic and exponential are symmetric distributions. Correspondingly, the reduced-χ^2 shows a decreasing improvement in the goodness of the fit with increasing inclination, between the exponential and the Sérsic fit. Thus, the improvement in the goodness of the fit is only 42% for $i = 73°$ and reaches 1.9% at $i = 84°$.

The general trend for the derived Sérsic index is to decrease from the value $n_0^{\rm sers} = 1.0$ (characteristic for an exponential distribution) with the increase of τ_B^f and inclination, for lower values of τ_B^f (see Fig. 5.5, left panels). This comes as a result of the flattening in the central regions due to the higher attenuation at small galactocentric radii. For higher τ_B^f values the trend reverts, with $n_{\rm app}^{\rm sers}$ now increasing with inclination (see in particular the blue and red curves in the left panels from Fig. 5.5). This non-monotonic behaviour is caused by the fact that for larger τ_B^f the optically thick core increases in size, moving outwards towards large radii, flattening thus the profile amongst larger and larger radii. This will eventually revert to an exponential. The results of the polynomial fits to the $n_{\rm app}^{\rm sers}$, for all opacities considered, are listed in Tables B.11 to B.15 for the *B, V, I, J, K* bands.

Since the trends seen in the plots for $n_{\rm app}^{\rm sers}$ are due to both dust and projection effects, I correct for the latter by subtracting $corr^{\rm proj}(n^{\rm sers}) = \Delta n_{\rm i}^{\rm sers}$ - the corrections defined in Sect. 4.1.2, to the derived values of $n_{\rm app}^{\rm sers}$. The results are plotted in the right panels of Fig. 5.5. It is reassuring to notice that in the K band, after correcting for projection effects, the intrinsic value of 1 for the Sérsic index is recovered, for all inclinations except the edge-on ones, and for most values of dust opacities, except for the very high ones. It is also noticeable that at low inclinations the deviations from exponentiality are mainly due to dust effects while at higher inclinations, both dust and projection effects affect the derived Sérsic index. The resulting effective radius will always be larger than the corresponding one in the absence of dust, with the ratio of these two increasing with inclination, as noticed from Fig. 5.6. The coefficients of the polynomial fits are listed in the same tables as the n_{app}^{sers}.

The effects of dust on the derived axis ratios Q_{app}/Q_i are the same for the Sérsic and exponential fits, so the results are only listed once in the tables corresponding to the exponential fits.

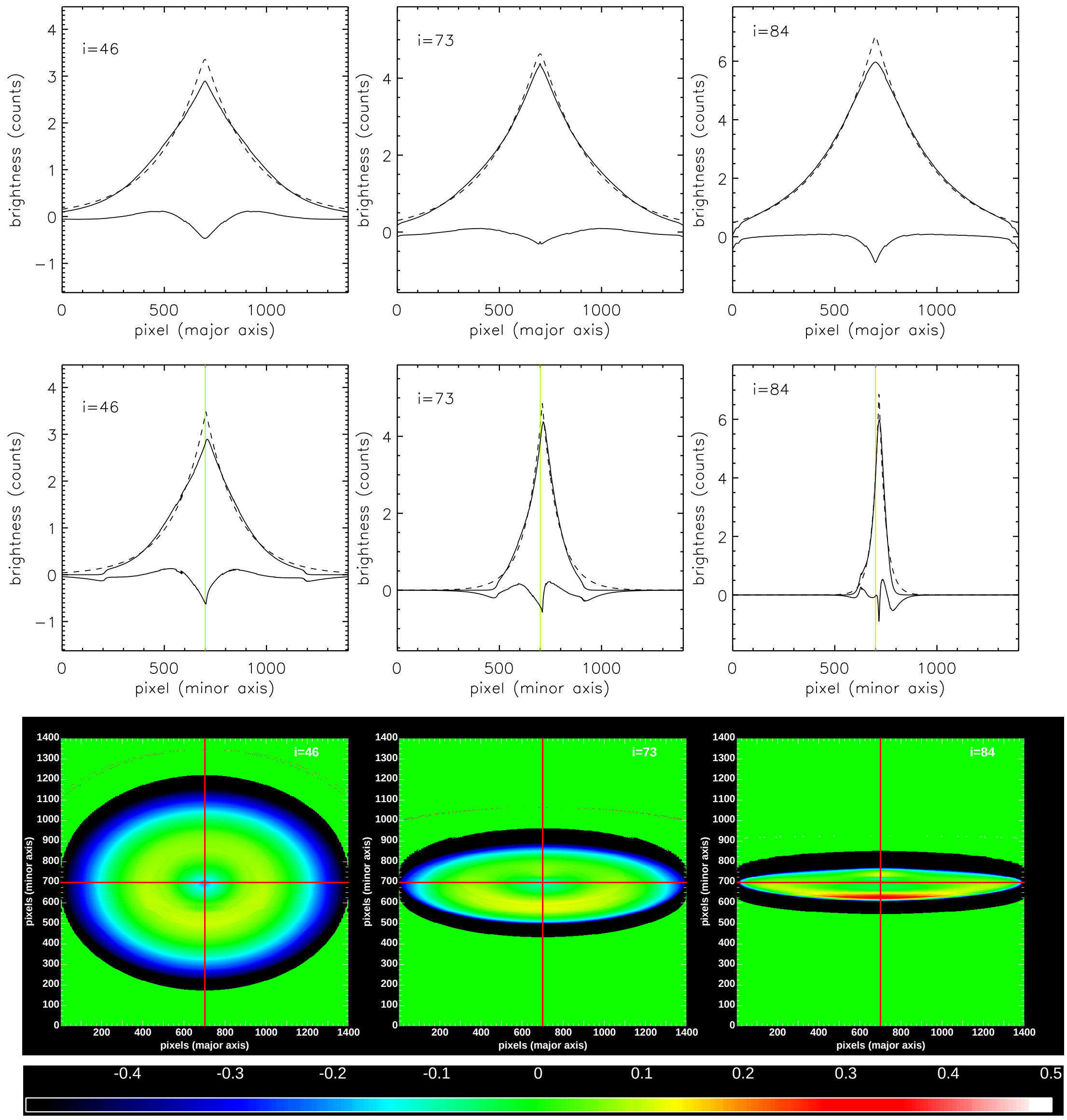

Figure 5.1: Major and minor axis **disk** profiles (**upper and middle rows**) showing the deviations from pure exponentials due to the combination of dust and projection effects. Upper solid curves are for **B band** dusty disk images, for $\tau_B^f = 4.0$, dashed curves are for corresponding exponential fits, while absolute residuals ($simulation - fit$) are represented by lower solid curves. The fits were done by letting the geometrical coordinates of the intensity peak as free parameters. The cuts were taken parallel and perpendicular with the major axis of the simulated dusty disk images, through the intensity peaks, at inclinations $1 - \cos(i) = 0.3, 0.7, 0.9$ ($i = 46°, 73°, 84°$). The light green line shows a cut through the geometrical centre of the image. **Lower row**: Corresponding relative residuals ($\frac{simulation - fit}{simulation}$), at the same inclinations and opacity as the profiles. The red lines show radial and vertical cuts through the geometrical centre of the image.

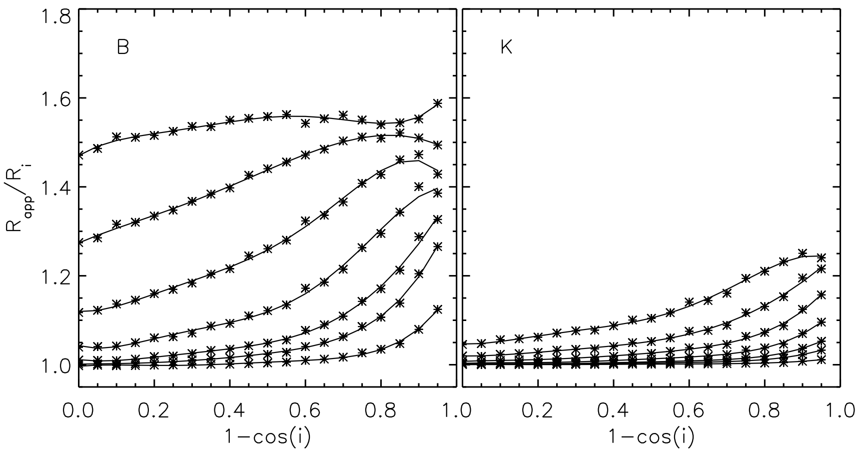

Figure 5.2: Dust effects $corr^{dust}$ on the derived scale-length of **disks fitted with exponential functions**. The symbols represent the measurements while the solid lines are polynomial fits to the measurements. The plots represent the ratio between the apparent and intrinsic scale-lengths R_{app} and R_i respectively, as a function of inclination $(1 - \cos(i))$, for B and K optical bands. From bottom to top, the curves are plotted for $\tau^f_B = 0.1, 0.3, 0.5, 1.0, 2.0, 4.0$, and 8.0.

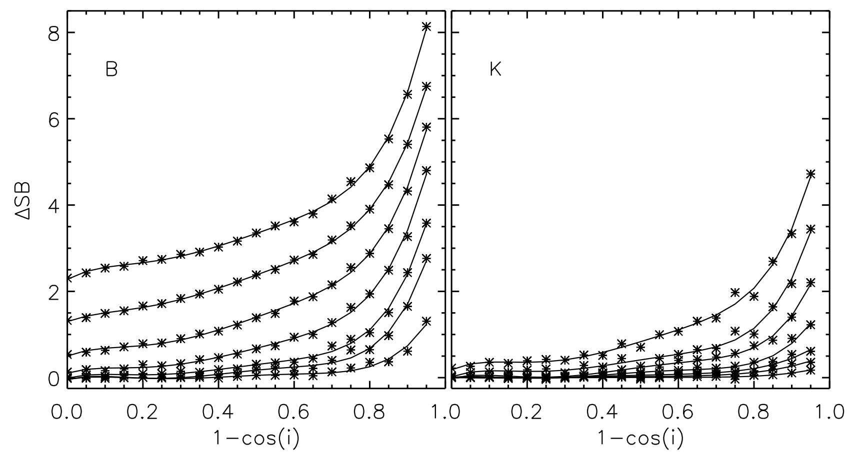

Figure 5.3: Dust effects $corr^{dust}$ on the derived central surface brightnesses of **disks fitted with exponential functions**. The symbols represent the measurements while the solid lines are polynomial fits to the measurements. The plots represent the difference between the apparent and intrinsic average central surface-brightness, ΔSB, expressed in magnitudes, versus inclination $(1 - \cos(i))$, for B and K optical bands. From bottom to top, the curves are plotted for $\tau^f_B = 0.1, 0.3, 0.5, 1.0, 2.0, 4.0$, and 8.0.

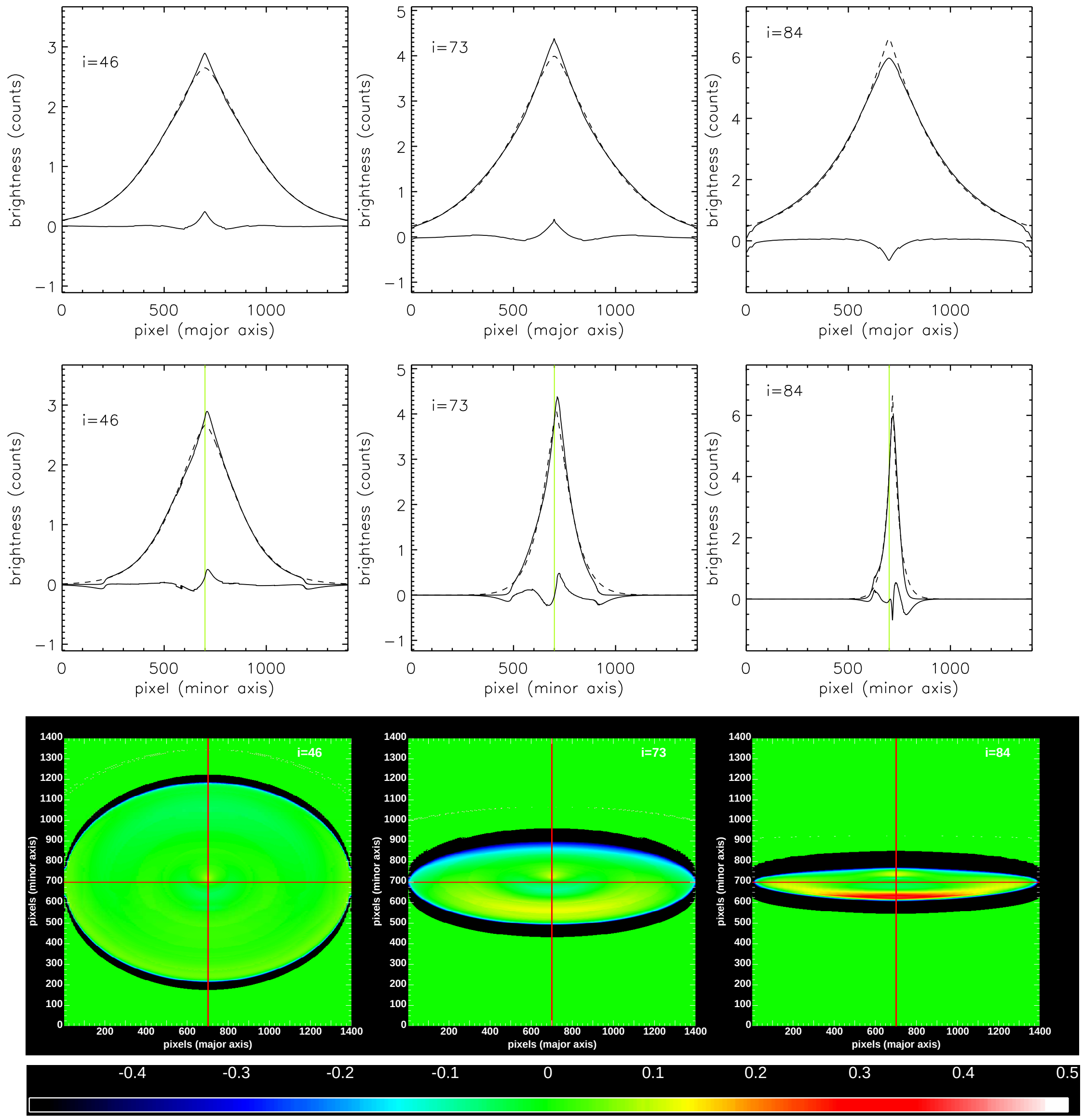

Figure 5.4: Major and minor axis **disk** profiles (**upper and middle rows**) showing the deviations from a general Sérsic profile due to the combination of dust and projection effects. Upper solid curves are for **B band** dusty disk images, for $\tau^f_B = 4.0$, dashed curves are for corresponding Sérsic fits, while absolute residuals ($simulation - fit$) are represented by lower solid curves. The fits were done by letting the geometrical coordinates of the intensity peak as free parameters. The cuts were taken parallel and perpendicular with the major axis of the simulated dusty disk images, through their intensity peaks, at inclinations $1 - \cos(i) = 0.3, 0.7, 0.9$ ($i = 46°, 73°, 84°$). The light green line shows a cut through the geometrical centre of the image. **Lower row**: Corresponding relative residuals ($\frac{simulation - fit}{simulation}$), at the same inclinations and opacity as the profiles. The red lines show radial and vertical cuts through the geometrical centre of the image.

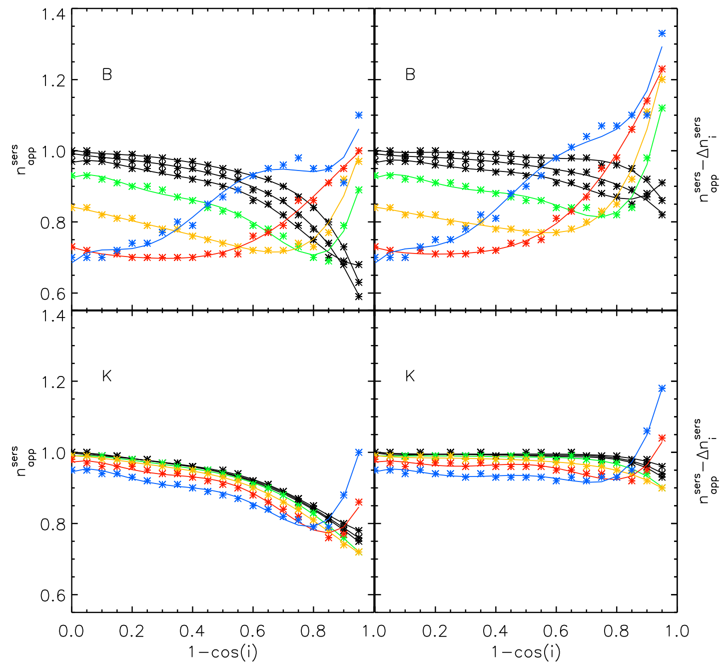

Figure 5.5: **Left panels**: the inclination dependence of the derived Sérsic index for **exponential disks fitted with Sérsic functions**, due to combined dust and projection effects. The symbols represent the measurements while the solid lines are polynomial fits to the measurements. **Right panels**: The same but corrected for projection effects ($\Delta n_i^{\rm sers}$). Upper panels are for the B band and lower panels are for the K band. The black curves are plotted for $\tau_B^f = 0.1, 0.3, 0.5$ (from top to bottom), while the other ones are for $\tau_B^f = 1.0$ (green), 2.0 (yellow), 4.0 (red), and 8.0 (blue).

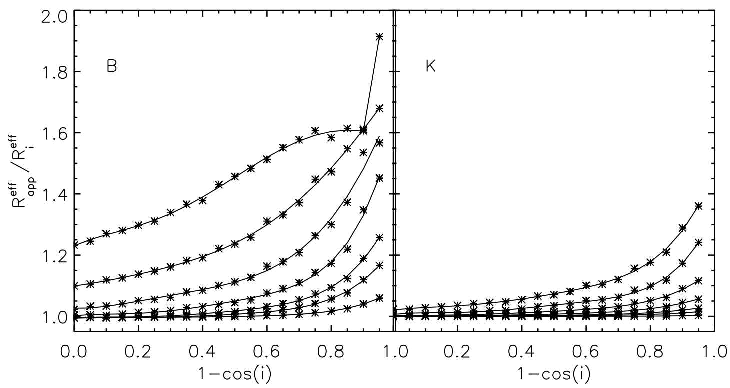

Figure 5.6: Dust effects $corr^{\rm dust}$ on the derived effective radius of **exponential disks fitted with Sérsic functions**. The symbols represent the measurements while the solid lines are polynomial fits to the measurements. The plots represent the ratio between the apparent and intrinsic Sérsic effective radii, $R_{\rm app}^{\rm eff}$ and $R_{\rm i}^{\rm eff}$ respectively, as a function of inclination $(1 - \cos(i))$, for B and K optical bands. From bottom to top, the curves are plotted for $\tau_B^f = 0.1, 0.3, 0.5, 1.0, 2.0, 4.0$, and 8.0.

5.2 The Thin Disk

The dust affects the perceived distribution of stellar emissivity in the young stellar disk in a stronger way than in the old stellar disk, as we will see in this section, although the overall trend is similar. This is because the young stellar disk is, in the model (Popescu et al. 2011), completely embedded in the dust distribution, and therefore suffers more attenuation effects than the old stellar disk. By contrast, as already noted in Sect. 4.2, projection effects are negligible for the thin disk, and therefore can be safely ignored.

The main application of my dust corrections on the derived photometric parameters of thin disks are for the UV range, as it is in this spectral range that the young stellar disk is prominent. In the optical range, the young stellar disk cannot be disentangled from the old stellar disk, based on optical images alone. Therefore, in the optical, the measured structural parameters are indicative of the old stellar disk. In analysing optical images of galaxies it is recommended to use dust corrections for the "disk" component. I nevertheless quantify dust corrections in the optical for the "thin disk" as well, as these are useful for deriving corrections for Balmer line/nebular line emission. Dust corrections on line emission can be derived by interpolating between the optical wavelengths tabulated in this paper. As an example, I only show dust corrections for the Hα line emission.

5.2.1 Exponential fits to the thin disk

In Fig. 5.7, major axis profiles for the dusty young stellar disk images are shown, for two UV bands, at face-on inclination. One can see that for intermediate values of the optical depth, even at face-on inclinations the profiles deviate from pure exponentials, as dust strongly alters the shape of the profile, making it extremely flat in the central

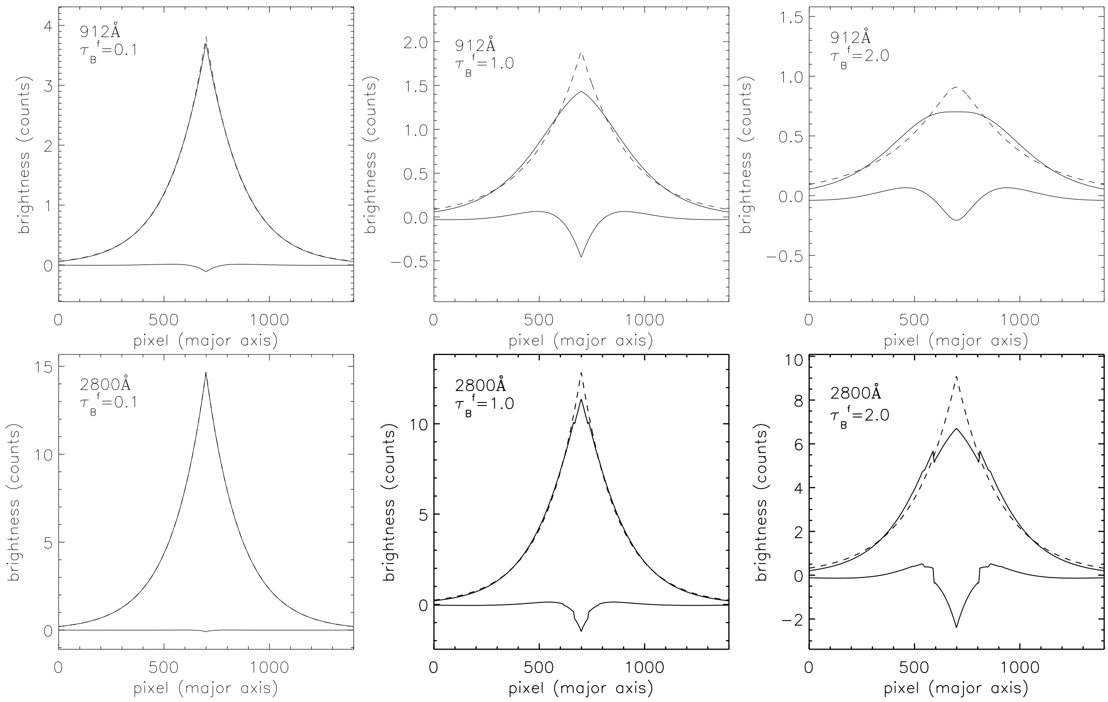

Figure 5.7: The face-on major axis profiles for the **thin disk** showing the deviations from pure exponentials due to dust effects. Upper solid curves are for the face-on dusty images, the corresponding exponential fits are represented by dashed curves, while the lower solid curves are for residuals. The upper row of plots corresponds to the 912 Å UV wavelength and $\tau_B^f = 0.1, 1.0, 2.0$ (from left to right), while the lower row of plots corresponds to the 2800 Å UV wavelength and same values of τ_B^f. The fits were done by letting the geometrical coordinates of the intensity peak as free parameters. The cuts were taken parallel with the major axis of the thin disk dusty images, through their intensity peaks.

part (see the third column plots in Fig. 5.7). In the central regions we can also observe high residuals between the simulated and the fitted profiles, another indication that the fits are imperfect. With increasing opacity and inclinations, the fits become more imperfect. At a certain point, exponential fits become completely inadequate to represent the surface-brightness distribution of thin disks. For this reason, I present here dust effects only at inclinations and opacity values for which an exponential profile is still a good representation of the stellar emissivity distribution in the young stellar disk. For example, in the UV range I present corrections only up to a dust opacity of $\tau_B^f = 2$.

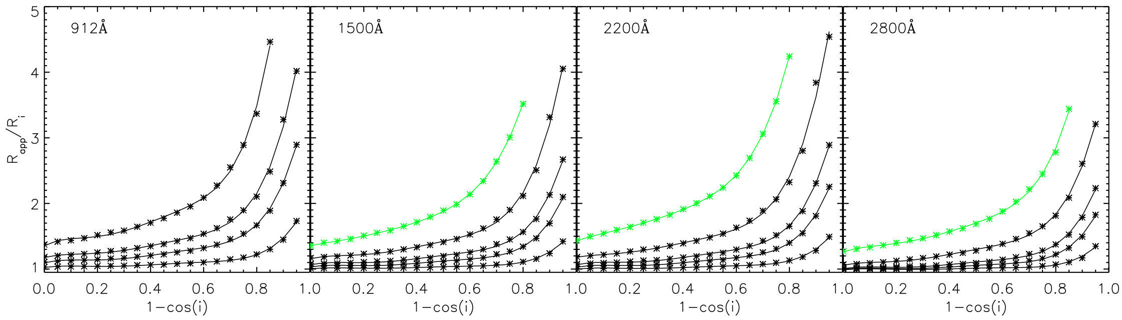

Figure 5.8: Dust effects $corr^{\mathrm{dust}}$ on the derived scale-length of **thin disks fitted with exponential functions**. The symbols represent the measurements while the solid lines are polynomial fits to the measurements. The plots represent the inclination dependence of the ratio between the apparent and intrinsic scale-lengths, R_{app} and R_{i} respectively. From left to right, the plots corresponds to increasing UV wavelengths: 912 Å, 1500 Å, 2200 Å, and 2800 Å. From bottom to top the black curves are plotted for $\tau_B^f = 0.1, 0.3, 0.5, 1.0$. The green curve corresponds to $\tau_B^f = 2.0$.

Fig. 5.8 shows the inclination dependence of the ratio between the apparent and intrinsic scale-lengths of the thin disk ($corr^{\mathrm{dust}}(R)$; Eq. 3.1.6), for different values of the B band central face-on optical depth, τ_B^f, for various UV wavelengths. As one can observe from these plots, the strongest distortion dust exerts over the stellar emissivity distribution is, as expected, at the shortest UV wavelengths. The dust effects decrease non-monotonically with increasing UV wavelength, due to the bump in the extinction curve at 2200 Å. Overall, the dust effects are quite severe for this morphological component in particular in the UV range.

But even in the optical range the thin disk is strongly affected by dust. This can be seen in Fig. 5.9, where I plotted the same quantities as in Fig. 5.8, this time for the longer optical wavelengths. The strong dust effects are due to the fact that, as mentioned before, the young stellar disk has a smaller scale-height than the old stellar disk, and therefore it has a stronger spatial coupling with the dust. By making a comparison between Fig. 5.2 on one hand (old stellar disk), and Fig. 5.9 (young stellar disk) on the other hand, one can see that, for the same wavelength and τ_B^f, the amplitude of the changes in the apparent scale-lengths is higher for the young stellar disk. It is noticeable however that the trend

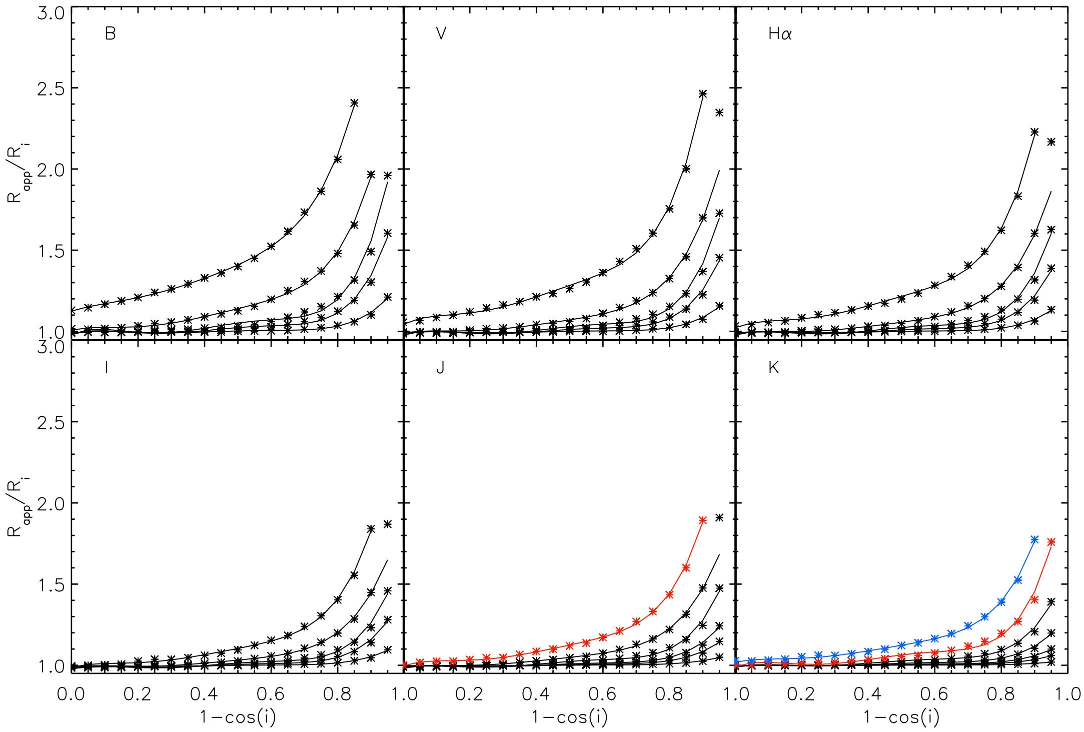

Figure 5.9: Same as in Fig. 5.8, for the optical bands and the $H\alpha$ line. From bottom to top the black curves are plotted for $\tau_B^f = 0.1, 0.3, 0.5, 1.0, 2.0$. The red curve corresponds to $\tau_B^f = 4.0$, while the blue one is for $\tau_B^f = 8.0$.

is similar for both stellar components.

In addition to the continuum optical emission I also show an example for the $H\alpha$ line (Fig. 5.9), as it is the young stellar disk component from where the recombination lines originate (the star forming regions). For other Balmer lines dust corrections can be obtained by interpolating the corrections for the thin disk between the relevant optical wavelengths. All the corrections $corr^{\rm dust}$, both in the UV range and in the optical, including those for the $H\alpha$ line, are listed in terms of coefficients of polynomial fits in Tables B.16 to B.30.

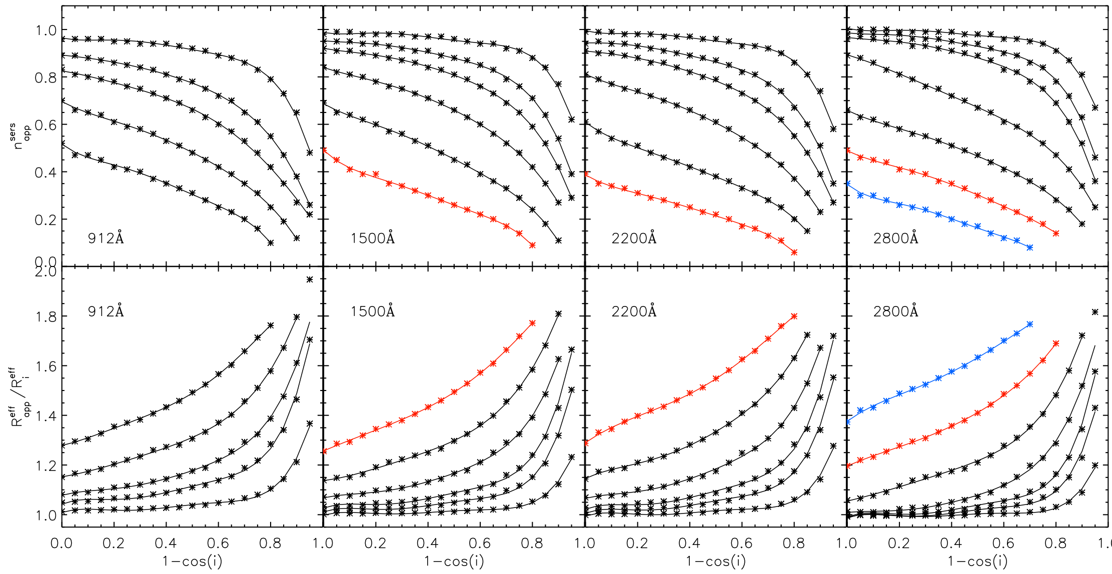

Figure 5.10: **Upper row**: the inclination dependence of the derived Sérsic index for the dusty images of **thin disks fitted with Sérsic functions**. **Lower row**: same, for the ratio between the apparent and intrinsic Sérsic effective radii, $R^{\rm eff}_{\rm app}$ and $R^{\rm eff}_{\rm i}$ respectively. The symbols represent the measurements while the solid lines are polynomial fits to the measurements. From left to right, the plots corresponds to increasing UV wavelengths: 912 Å, 1500 Å, 2200 Å, and 2800 Å. The black curves are plotted for $\tau^f_B = 0.1, 0.3, 0.5, 1.0, 2.0$ (from top to bottom, in this order for the upper row and in reverse order for the lower row). The red curve corresponds to $\tau^f_B = 4.0$, while the blue one is for $\tau^f_B = 8.0$.

5.2.2 Sérsic fits to the thin disk

As in the case of the old stellar disk, in order to quantify the deviations of the stellar emissivity profiles from pure exponentials I also performed Sérsic fits for the thin disk images. In Fig. 5.10, the inclination dependence of the derived Sérsic index (upper row) and the Sérsic effective radii ratios (lower row) are displayed, for the same UV wavelengths chosen when fitting with an exponential. Even for low values of τ^f_B, at high inclinations the effects of dust are important and increase towards shorter wavelengths. At higher values of τ^f_B the deviations of the derived Sérsic indices from its exponential value can be dramatic, with values going down to $n^{\rm sers}_{\rm app} = 0.5$ (gaussian) or even lower,

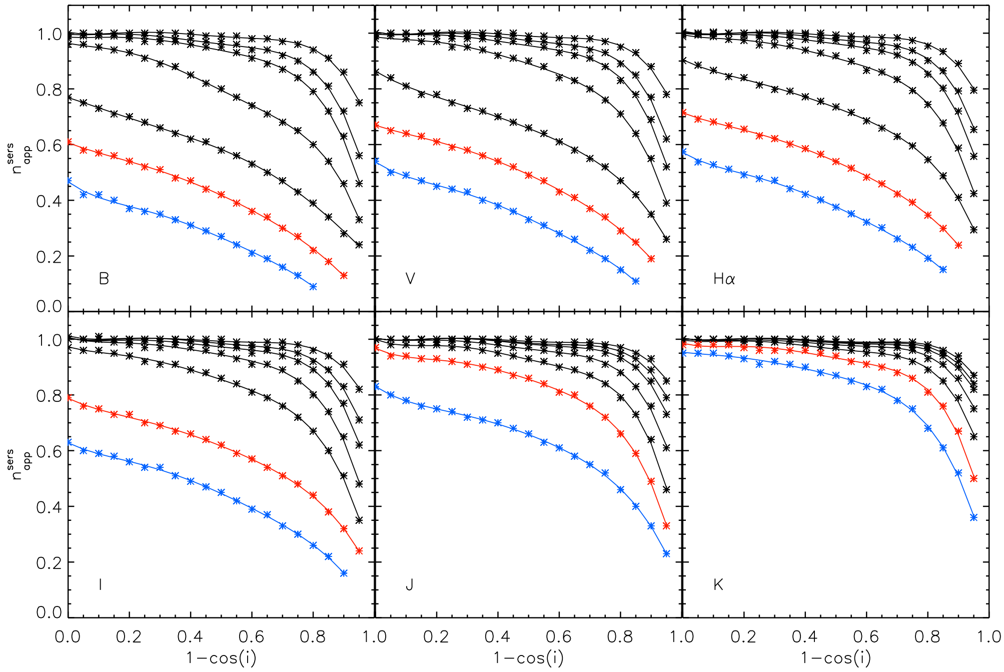

Figure 5.11: Same as in Fig. 5.10 top, for the the optical bands and the $H\alpha$ line.

to $n^{\rm sers}_{\rm app} \approxeq 0.1$. Since there are no significant projection effects ($\Delta n^{\rm sers}_{\rm i} \approxeq 0$) for the thin disk (as mentioned in Sect. 4.2), the deviations of the Sérsic index from an exponential are in this case caused only by the dust effects. At high inclinations and for extremely opaque thin disks, even Sérsic fits become poor representations of the profiles, therefore these cases were omitted from the plots in Fig. 5.10.

In the optical range I proceeded in a similar way to the UV range, by fitting variable Sérsic index functions to the simulated images of the young stellar disk. In Figs. 5.11 and 5.12 I show the corresponding Sérsic index and effective radii ratios variation as a function of inclination for various optical bands and also for the $H\alpha$ line. By comparing the derived Sérsic indices for the old stellar disk (Fig. 5.5, right hand panel) and the young stellar disk (Fig. 5.11), at the same wavelength, τ^f_B and inclination one notices that the dust-induced changes in the derived Sérsic index are higher in the latter case. The reason for this is, as noted in Sect. 5.2.1, that the old stellar disk has a larger scale-height than the young stellar disk, with stars above the associated dust disk. As the

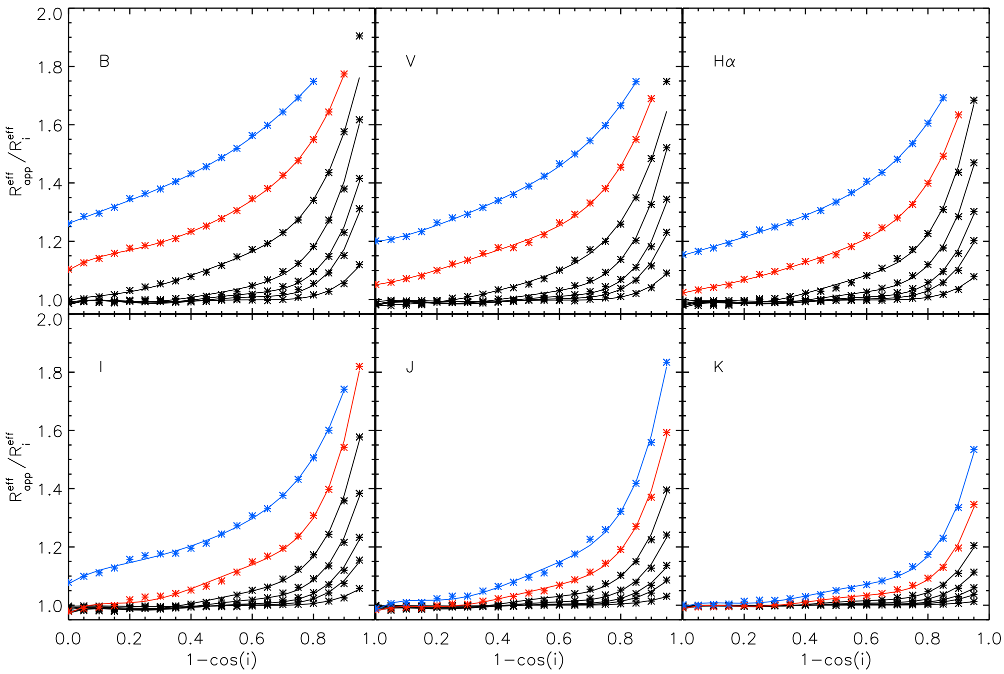

Figure 5.12: Same as in Fig. 5.10 bottom, for the the optical bands and the $H\alpha$ line.

attenuation is stronger and subsequently the surface brightness distribution flatter for the young stellar disk, the derived Sésic indices will be systematically lower than the ones characterising the surface brightness distribution of the old stellar disk. It can also be seen that for high values of τ^f_B (τ^f_B = 4.0, 8.0) the trend for the two morphological components is not the same. Thus, for the old stellar disk the derived Sérsic index increases with increasing inclination, while for the young stellar disk an opposite trend is observed.

The analysis of the dust effects on the derived thin disk axis-ratios ($corr^{\rm dust}(Q)$; Eq. 3.1.6) shows that these are negligible, therefore I do not present these. All the other results on $corr^{\rm dust}$, both in the UV and in the optical range, including the $H\alpha$ line are listed in terms of coefficients of polynomial fits in Tables B.31 to B.45.

5.3 The Bulge

The analysis of the effect of dust on bulges is the most novel aspect of this study, as, unlike disks, there is very little work based on radiation transfer simulations on this topic. As for the case of dustless bulges, I used simulations of dusty bulges with volume stellar emissivity distributions described by de-projected Sersic functions, having various Sérsic indices, $n_0^{\mathrm{sersic}} = 1, 2, 4, 8$. The bulges are seen through the dust distribution in the disk, but no disk stellar emissivity is included in these simulations. Accordingly, for each of these cases I used as fitting functions variable-index Sérsic distributions. For the case of $n_0^{\mathrm{sersic}} = 4$, de Vaucouleurs functions were also used to fit the simulations. I considered simulations for bulges truncated at 3 and 10 effective radii, respectively.

We have already seen in Sect. 4.3 that projection effects $corr^{\mathrm{proj}}$ on bulges strongly depend on the intrinsic Sérsic index of the volume stellar emissivity n_0^{sers}, and on the presence or not of a truncation radius. So it is important to assess whether dust effects $corr^{\mathrm{dust}}$ also have these extra dimensions in parameter space.

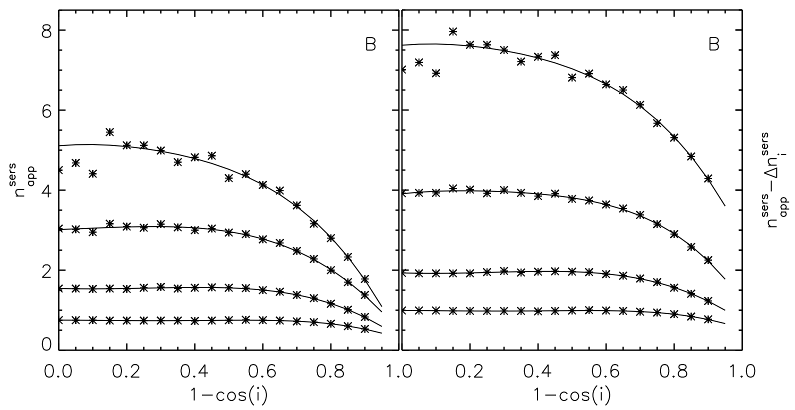

Figure 5.13: **Left**: The inclination dependence of the derived Sérsic index of **bulges** due to combined dust and projection effects, in B band, for simulations having the volume stellar emissivity described by different Sérsic index, $n_0^{\mathrm{sersic}} = 1, 2, 4, 8$ (from bottom to top curve), and $\tau_B^f = 1.0$. The symbols represent the measurements while the solid lines are polynomial fits to the measurements. **Right**: The same but corrected for projection effects ($\Delta n_i^{\mathrm{sers}}$).

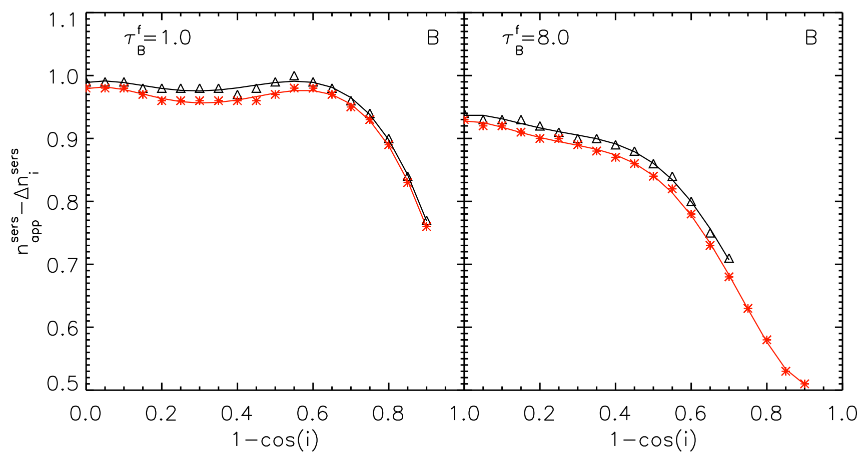

Figure 5.14: The inclination dependence of the derived Sérsic index of **bulges** due to dust effects only (corrected for projection effects), for bulges truncated at 3 effective radii (black curves) and at 10 effective radii (red curves). The symbols represent the measurements while the solid lines are polynomial fits to the measurements. Results are for the B band and for simulations corresponding to volume stellar emissivity described by a (de-projected) Sérsic function with $n_0^{sers} = 1$. Left panel is for $\tau_B^f = 1.0$ and right panel is for $\tau_B^f = 8.0$

First, I tested whether the corrections depend on the choice of the Sérsic index used as input in the simulations (n_0^{sers}). To do this I analysed bulges produced with 4 different values of the Sérsic indices, $n_0^{sersic} = 1, 2, 4, 8$, for the same $\tau_B^f = 1.0$, for bulges truncated at $3R_0^{eff}$, and at different inclinations. Subsequently, these bulges were fitted with variable-index Sérsic functions. The variation of the derived Sérsic indices with inclination is displayed in Fig. 5.13. After correcting for projection effects (right panel in Fig. 5.13), we see that for low to intermediate inclinations the variation of the derived Sérsic index (n_{app}^{sers}) with inclination does not depend on the input Sérsic index in the simulation, n_0^{sers}. In particular for this value of τ_B^f, I broadly recover the values of the parameter n_0^{sers}. It is only for high value of n_0^{sers} and closer to edge-on inclinations that the measured Sérsic index starts to drop significantly from its intrinsic value. As mentioned in Sect. 4.3, the noisier curves at $n_0^{sers} = 8$ are not due to real physical effects, but are inherent to the limited resolution of the radiative transfer calculations for this high value of Sérsic index. As a result of these tests done for simulations with different

$n_0^{\rm sers}$, I decided that, because the differences are small, to only consider dust effects for two different values of the Sérsic index, $n_0^{\rm sers} = 1.0$ (exponential bulge) and $n_0^{\rm sers} = 4.0$ (de Vaucouleurs bulge).

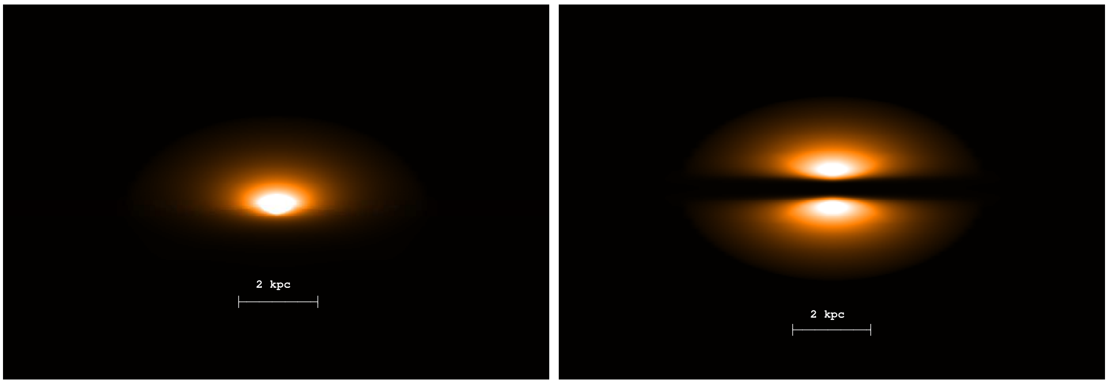

Figure 5.15: **Left**: Simulated image of a **de Vaucouleurs bulge (spheroidal)** in the B band, truncated at $3\,R_0^{\rm eff}$ seen through the dust disks, having $\tau_B^f = 4.0$, and inclined at $i = 73°$. **Right**: Same for $\tau_B^f = 1.0$ and $i = 90°$. The size of both images corresponds to 15.16×15.20 kpc. In both cases, no stellar emissivity is included in the disk - pure bulge case.

Secondly, I tested whether truncation radius affects dust corrections $corr^{\rm dust}$. In Fig. 5.14, the effect of dust for bulges truncated at $3\,R_0^{\rm eff}$ and at $10\,R_0^{\rm eff}$ is displayed, for two values of τ_f^B. This test indicates that, unlike for the projection effects, truncation radius does not affect the results on dust effects. Therefore there was no need to present the dust corrections as a function of truncation radius.

When performing the fit to simulations, one of the main problems was related to the dust-induced asymmetries in the surface brightness distribution profiles at high inclinations (of the dust disk) and large values of τ_B^f. As an illustration of this effect I show in Fig. 5.15 two simulated dusty bulge images, one at 73° inclination (left) and one edge-on (right). It is easily noticeable from the image on the left, that a bulge observed in the B band, at 73° inclination, for $\tau_B^f = 4.0$, would have half of its image obscured by dust. This issue produces difficulties when fitting such images with a symmetrical analytic function like a Sérsic distribution. Similar problems can arise for bulges seen at edge-on inclinations, where the dust lanes block the bulge stellar emissivity in the plane of the disk [1] (see right panel of Fig. 5.15 for an edge-on orientation). For this reason it is not feasible to perform Sérsic fits for bulges at high inclinations and high τ_B^f.

To quantify the dust effects on the bulge photometric parameters, I fitted both exponential ($n_0^{\rm sersic} = 1$) and de Vaucouleurs ($n_0^{\rm sersic} = 4$) bulges with variable-index Sérsic functions. I plotted the inclination dependence of the Sérsic index only for the values of τ_B^f and at inclinations for which the derived fit was reasonable. These values were chosen by thoroughly analysing for each case the relative residuals, radial and vertical profiles and/or the fitted images. The combined dust and projection effects on the Sérsic index of exponential bulges can be seen in the left panels from Fig. 5.16, for B and K bands. For large values of τ_B^f the distortions in the derived Sérsic index are strong, with observed trends looking similar, and with $n_{\rm app}^{\rm sersic}$ decreasing with inclination and τ_B^f. For example, for $\tau_B^f = 4.0$, $i = 78°$, $n_{\rm app}^{\rm sersic}$ decreases to 0.45. The decrease of the measured Sérsic index of bulges with increasing opacity and inclination has also been found by Gadotti et al. (2010), though a direct comparison is not possible, since the latter trends were derived from bulges obtained from bulge/disk decomposition, which, beside the effects of dust also contain the effect of dust on the bulge/disk decomposition itself, what I call in this study $corr^{\rm B/D}$, as given by Eq. 3.1.12 and 3.1.13.

Since the trends seen in my plots for $n_{\rm app}^{\rm sersic}$ of exponential bulges are due to both dust and projection effects, I corrected for the latter by subtracting $\Delta n_{\rm i}^{\rm sers}$ - the corrections defined in Sects. 4.1 and 4.3, to the derived values of $n_{\rm app}^{\rm sers}$. The results are plotted in the right panels of Fig. 5.16. The derived values of Sérsic index are now closer to the values of the $n_0^{\rm sersic}$ parameter input in the simulations. At very high inclinations and large values of τ_B^f the deviations in the B band are still very important. The plots also show that at all inclinations the deviations from the intrinsic distributions are due to

[1] I remind the reader that no disk stellar emissivity is included in these simulations

both dust and projection effects, with projection effects being constant with inclination (see Fig. 4.5). For low values of τ^f_B and up to $1 - cos(i) = 0.7$ inclination, the shifts from value 1 observed in the left column plots of Fig. 5.16 are mainly due to projection effects, which in turn are due to truncation effects.

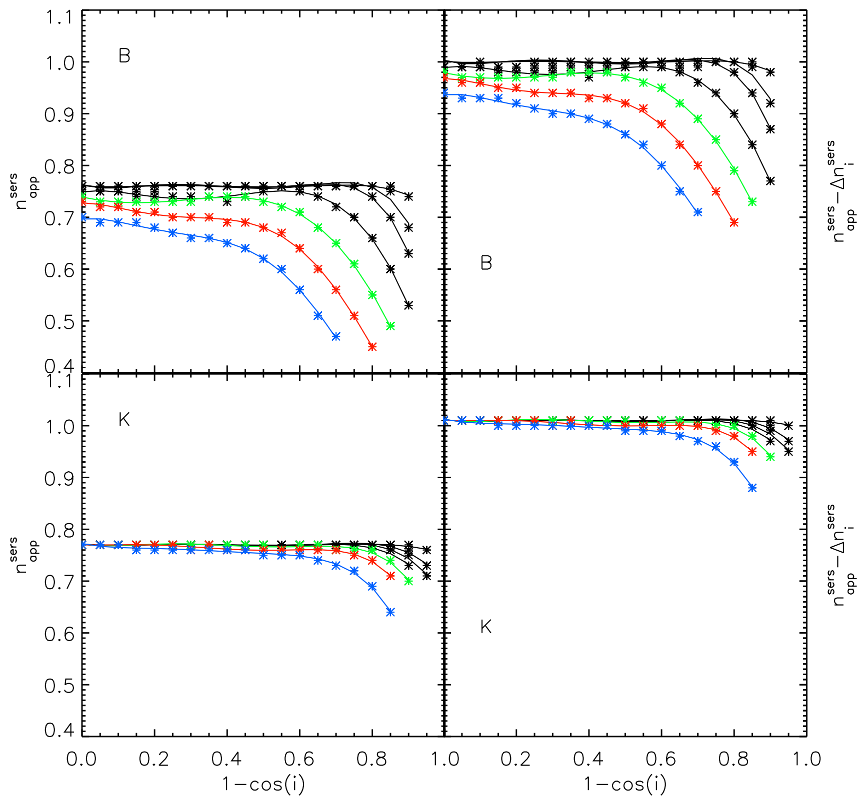

Figure 5.16: **Left panels**: the inclination dependence of the derived Sérsic index for the **exponential bulges** ($n_0^{\rm sers} = 1$), due to combined dust and projection effects. The symbols represent the measurements while the solid lines are polynomial fits to the measurements. **Right panels**: The same but corrected for projection effects ($\Delta n_{\rm i}^{\rm sers}$). Upper panels are for the B band and lower panels are for the K band. From top to bottom, the curves are plotted for $\tau^f_B = 0.1, 0.3, 0.5, 1.0$ (black), 2.0 (green), 4.0 (red), and 8.0 (blue).

In Fig. 5.17 I show the inclination dependence of the ratio between the apparent and intrinsic bulge effective radii of exponential bulges, for different values of τ^f_B. The effect of dust on the effective radii is small, even for large values of τ^f_B, and has a weak dependence on inclination.

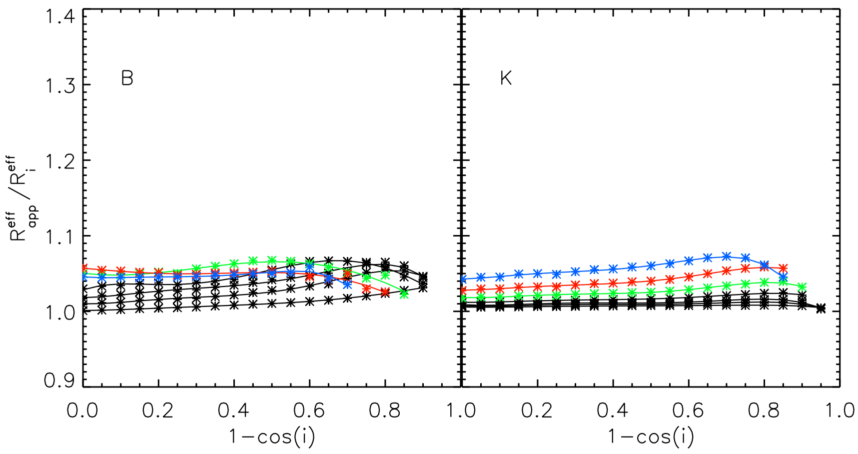

Figure 5.17: Dust effects $corr^{dust}$ on the derived effective radius of **exponential bulges** ($n_0^{sers} = 1$). The symbols represent the measurements while the solid lines are polynomial fits to the measurements. The plots represent the ratio between the apparent and intrinsic Sérsic effective radius, R^{eff}_{app} and R^{eff}_{i} respectively, versus inclination $(1 - \cos(i))$, for B and K optical bands. From bottom to top, the curves are plotted for $\tau^f_B = 0.1, 0.3, 0.5, 1.0$ (black), 2.0 (green), 4.0 (red), and 8.0 (blue).

Overall, looking at the effects dust has on bulge photometric parameters, we noticed an overestimation of the effective radii and an underestimation of the Sérsic indices, when fitting bulges with variable-index Sérsic functions. The overestimation of the effective radii is more pronounced for de Vaucouleurs bulges than for exponential bulges, while the underestimation of the Sérsic indices is more pronounced for exponential bulges than for de Vaucouleurs bulges. In particular at high inclination and opacities the ratio of the apparent to intrinsic effective radius increases with inclination for de Vaucouleurs bulges and decreases with inclination for exponential bulges.

All the corrections $corr^{dust}$ for both exponential and de Vaucouleurs bulges are presented in form of coefficients of polynomial fits in Tables B.46 to B.55. For de Vaucouleurs bulges, the fits at higher inclinations were quite poor, therefore I restricted my measurements to inclinations of up to $1 - cos(i) = 0.7$. Consequently, only the flat trend with inclination was recovered. Therefore, as a word of caution, I note here that highly inclined, high Sérsic index bulges cannot be properly fitted with symmetric analytic functions like Sérsic or de Vaucouleurs distributions. In this respect, I caution observers that fitting Sérsic functions to bulges in images of highly inclinded galaxies (in particular the ones with high S/N) will not produce reliable results. The solution for these cases is to fit the images with simulated images produced by radiative transfer calculations. In addition, I present results for de Vaucouleurs fits to de Vaucouleurs bulges (constrained Sérsic functions). These are listed in Tables B.56 to B.60.

5.4 Discussion

The corrections presented in this study, both for projection and dust effects, assume a fixed geometry for the underlying components of spiral galaxies. In particular the relative ratios between scalelengths and scaleheights of stars and dust are fixed to the reproducible trends found from modelling edge-on galaxies with radiative transfer calculations, as described at length in Tuffs et al. (2004) and Popescu et al. (2011). Nonetheless, one can expect some scatter from these trends, and a logical question to ask is to what extent the corrections presented in this thesis are affected by such a variation. While it is beyond the scope of this study to quantify this variation, as indeed the whole power and reliability of the calculations based on radiative transfer calculations rely on the existence of these constant trends in geometrical parameters, I shall discuss some simple plausible variations from these trends and consequences for the dust and projection effects.

One geometrical parameter that could vary is the thickness of the old stellar disk relative to its scale-length. As long as the ratio of the scale-height of the stellar disk to the dust disk remains the same, the dust corrections will not change much. However, there will be a visible effect on the projection effects. In particular this can be seen from my already existing calculations at various optical/NIR wavelengths, since the geometrical model assumes that the scalelength of the stellar disk decreases with increasing wavelength, which is the same, from the point of view of projection effects, as having a thicker stellar disk with increasing wavelength. The main effect is the departure from the $cos(i)$ law of an infinitely thin disk (see Sect. 4.1 and Fig. 4.2). Because the stellar disk has a larger scaleheight, the departure from the infinitely thin approximation starts at lower inclinations, and the amplitude of the effect is more pronounced. Thus, $corr^{\mathrm{proj}}(Q)$, the ratio between the intrinsic axis-ratio Q_{i}, and the axis-ratio of an infinitely thin disk, Q_0, will increase (at higher inclinations) for galaxies having a thicker stellar disk. Consequently, the overestimation of the exponential scalelength of the disk will start at lower inclinations, and the amplitude of the effect will increase for thicker stellar disks ($corr^{\mathrm{proj}}(R)$ will increase). When fitting thicker stellar disks with Sérsic functions, the underestimation of the Sérsic index will also be larger. Overall thicker stellar disks will produce the same trends for projection effects, but with a larger amplitude of the effect.

A more complex problem to address is when an increase in thickness of the stellar disk is also accompanied by an increase in the ratio between the scale-height of stars and that of dust. This will produce not only changes in projection effects but also changes in the dust corrections. An extreme case of such a change can be seen from the differences in dust corrections between the "thin disk" and the "disk". The stellar emissivity in the thin disk is completely embedded in the dust disk, while the disk has a layer of stars extending above the dust layer. Consequently, the dust corrections are less severe for the disk than for the thin disk. Thus, when fitting a galaxy having a larger ratio of the scale-height of stars-to-dust, one obtains smaller corrections for $corr^{\mathrm{dust}}(R)$, $corr^{\mathrm{dust}}(R^{\mathrm{eff}})$, and $\Delta n^{\mathrm{sersic}}$, for the same dust opacity and inclination.

In the case of bulges there are only two parameters defining the geometry: the effective

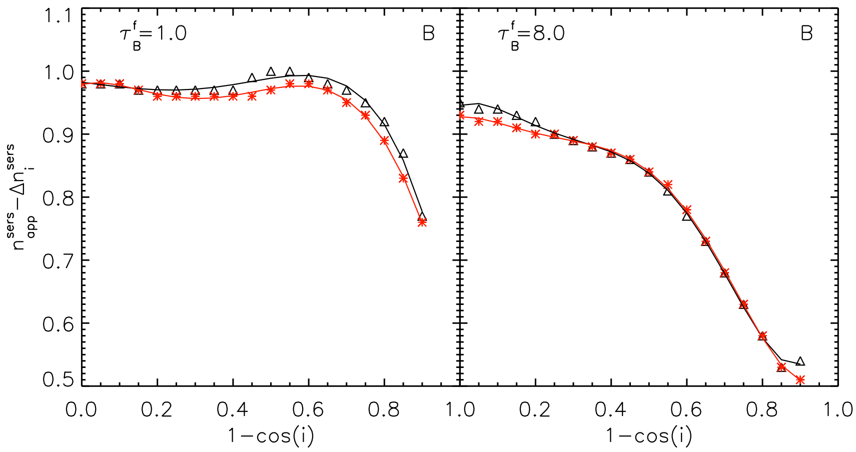

Figure 5.18: The inclination dependence of the derived Sérsic index of **bulges** due to dust effects only (corrected for projection effects), for spherical bulges (axis-ratios of 1.0; black curves) and for the standard bulges with axis-ratios of 0.6 (red curves). The symbols represent the measurements while the solid lines are polynomial fits to the measurements. Results are for the B band and for simulations corresponding to volume stellar emissivity described by a (de-projected) Sérsic function with $n_0^{\rm sers} = 1$. Left panel is for $\tau_B^f = 1.0$ and right panel is for $\tau_B^f = 8.0$

radius and the ellipticity of the bulge. The effective radius in the model was taken to be much smaller than the radial scalelength of the stellar disk (and of the dust disk). Essentially much of the stellar light from the bulge is strongly attenuated by the higher optical depth in the centre of the disks. As long as the size of the bulge remains within these constraints, not much change in the dust corrections are foreseen due to changes in the radial distribution. It is more likely that any effects would be due to changes in the vertical distribution affecting the amount of stars seen above the dust layer. This can be caused by either a larger effective radius of the bulge, or by a more spherical bulge. I tested the latter effect by producing a few simulations for bulges with axis ratios equal to unity (spherical bulge). In Fig. 5.18 I show the results for exponential bulges, for two cases of dust opacity, $\tau_B^f = 1.0$ and $\tau_B^f = 8.0$. The curves showing the inclination dependence of the corrected (for projection effects) Sérsic index are very similar for both spherical (black curves) and ellipsoidal bulges (red curves), for both optically thin and optically thick cases. I therefore conclude that the ellipticity of the bulge does not significantly affect the corrections for dust effects of the derived structural parameters of bulges.

This has also consequences for the modelling of pseudo-bulges. Pseudo-bulges are considered to be flatter systems, and have smaller sizes than classical bulges. My conclusions regarding the relative insensitivity of dust corrections on the ellipticity and effective radius of the bulge means that the corrections derived here are also valid for pseudo-bulges.

5.5 Application: the wavelength dependence of dust effects

One important application of my modelling is the prediction of the wavelength dependence of the effects of dust. Recent observational work (Kelvin et al. 2012, Häußler et al. 2013) has shown that for a population of disk dominated galaxies there is a distinctive trend of increasing Sérsic index and effective radius with increasing wavelength. In the case of Kelvin et al. (see the red curves in Fig. 5.19) the results have been obtained using single-Sérsic fits to 167600 galaxies measured independently in the *ugrizYJHK* bandpasses using reprocessed Sloan Sky Survey Data Release Seven and UKIRT Infrared Deep Sky Survey Large Area Survey imaging data available from the Galaxy and Mass Assembly Survey (GAMA; Driver et al. 2011). The measured galaxies have been further divided into early-type and late-type galaxies, according the the K-band Sérsic index/u-r color relation. For the late-type galaxies their averaged trends are compared with the predictions of my models (black curves in Fig. 5.19). For this purpose I considered the $corr^{\rm dust}$ obtained for disks simulations with $\tau_B^f = 4.0$ and for an average inclination of 60°. The choice of $\tau_B^f = 4.0$ was motivated by the analysis of the attenuation-inclination relation by Driver et al. (2007), who found an average dust opacity for local universe disk galaxies of $\tau_B^f = 3.8$. A similar average value for comparable stellar masses was also found by Grootes et al. (2013). Also, radiative transfer analysis of the UV to FIR SEDs of individual edge-on galaxies by Misiriotis et al. (2001) and Popescu et al. (2004) found similar values for τ_B^f.

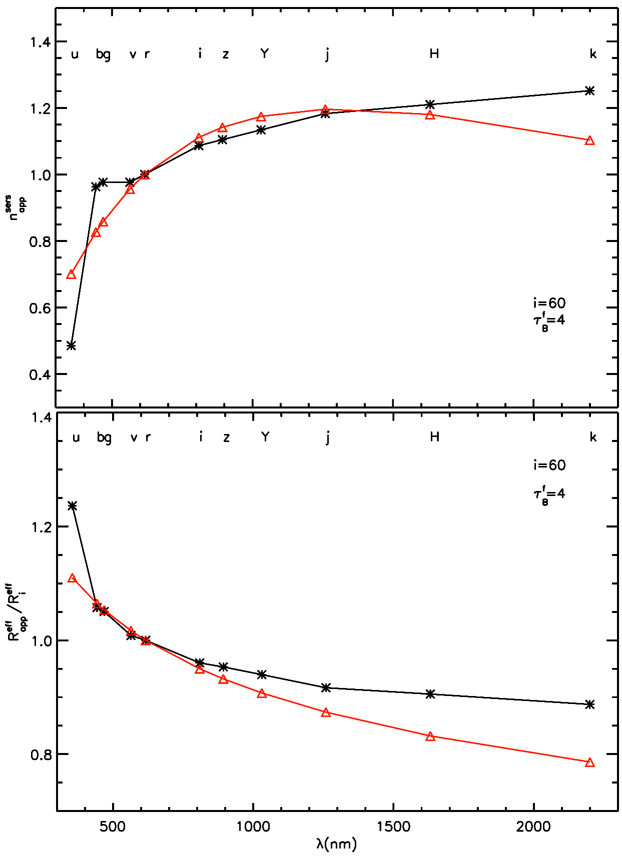

Figure 5.19: The wavelength dependence of the Sérsic index (top) and effective radius (bottom) predicted to be measured on a disk population, due to the effect of dust only (black). The recent measurements from the GAMA survey, from Kelvin et al. (2012), are overplotted in red. All the plots are normalised to the corresponding measurement in the r band.

The comparison between data and model predictions for effective radii indicates that in both cases there is a trend of decreasing radius with increasing wavelength, with the data showing a more pronounced decrease than the models. This could potentially indicate that, in addition to the dust effects, there is an intrinsic stellar gradient, with disks being smaller at longer than at shorter wavelengths, as predicted from theories of disk growth from inside out. This preliminary result would need to be followed up with more accurate determinations of disk sizes, which are performed on bulge/disk decomposition. The caveat of this interpretation is that, although a population of disk dominated galaxies has been isolated in Kelvin et al. (2012), one cannot exclude contamination with bulges in late-type spirals. This would bias the results towards smaller effective radii at longer wavelengths, where bulges are more prominent (see also Häußler et al 2013), resulting in the same qualitative trend as the effect of intrinsic stellar gradients. Thus, a quantitative interpretation of these trends are still awaiting for more accurate determinations of disk sizes and disk opacities.

The comparison between data and model predictions for Sérsic indices shows again that dust effects can account for most of the trends shown in the data, with a small difference towards the K band. As before, I mention that a quantitative comparison of these trends would require disk measurements obtained from bulge-disk decomposition on higher resolution data.

In the future, higher resolution data could allow selection of pure disk samples, thus excluding any contamination from bulges in late-type spirals. This would allow further tests of my theoretical results. In addition, further tests can be refined by selecting subsamples of low and high inclination galaxies.

Chapter 6

Dust Effects on Decomposed Disks and Bulges

In this section I present and discuss the effects of dust on the process of decomposing galaxy images and therefore on the photometric parameters of decomposed disks and bulges. Using Eqs. 3.1.14, 3.1.15, 3.1.16 I relate this new set of measured photometric parameters to those obtained in Chapter 5 (the apparent values from fitting individual components) in order to quantify $corr^{\mathrm{B/D}}$, the dust effects on bulge-disk decompositions. These effects are quantified for various values of τ_B^f, optical wavebands and two values of bulge-to-disk ratios, B/D, and measured for galaxies with exponential bulges (Sect. 6.1) and de Vaucouleurs bulges (Sect. 6.2).

One of the main problems to be dealth with when doing bulge-disk decomposition of dusty galaxies is the dust-induced asymmetries in the surface-brightness distributions, in particular at higher inclinations. These asymmetries are present in both the dust-attenuated disk and bulge, as described previously in Chapter 5 (see also Pastrav et al. 2013), and because of them, the position of the intensity peak does not coincide with the geometrical centre of the image. In addition, the position of the peak intensity of each dust attenuated component is shifted differently from the geometrical centre. Therefore the combined image will have a peak intensity which will coincide neither with the geometrical centre, nor with the true position of the peak intensity of either disk or bulge. As a consequence, the resulting bulges and disks will be imperfectly subtracted when performing bulge-disk decomposition with simple analytic templates, irrespective of the combination of functions used to fit the composite systems (exponential plus Sérsic or Sérsic plus Sérsic). As the tests with the intensity peaks of disk and bulge left as free parameters resulted in poorer fits than the case where the intensity peaks are free but constrained to be the same for both morphological components, I opted for the latter when performing bulge-disk decomposition.

6.1 Galaxies with exponential bulges

6.1.1 Fits with exponential + variable-index Sérsic functions

The first type of fit performed on the two-component simulated galaxies consists of an exponential plus a variable-index Sérsic function for the disk and bulge component, respectively. Examples of bulge-disk decomposition performed in this way are given in Fig. 6.1.

I also show examples of resulting fits in the form of major and minor axis profiles (upper and middle rows) and relative residuals (bottom row) in Fig. 6.2. One can see the aforementioned asymmetries about the major axis, which increase with increasing inclination of the disk. The blue region in the outer disk in the residual maps is due to the fact that the simulations are truncated while the fits extend to infinity.

Another effect which affects the decomposition is the flattening of the radial profiles in

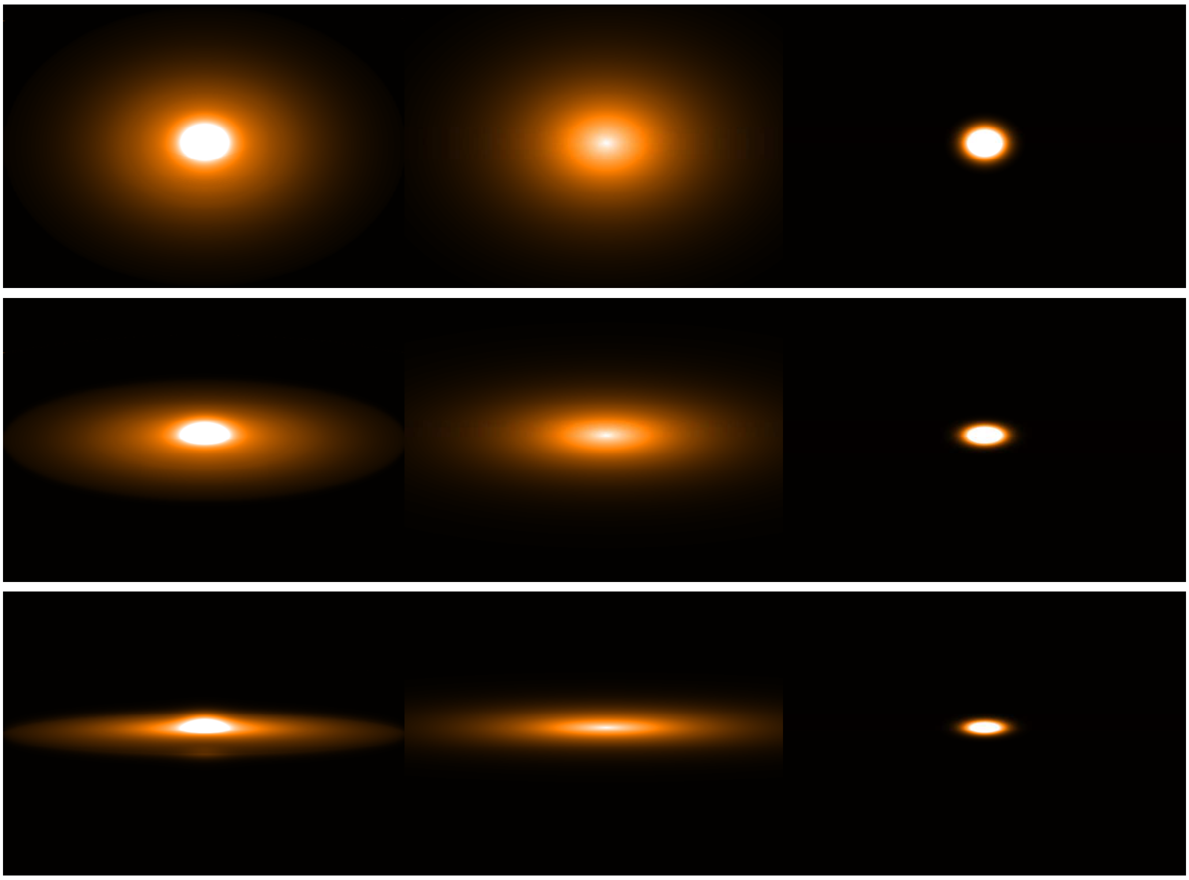

Figure 6.1: Simulated images of galaxies with **spheroidal exponential bulges** and $B/D = 0.25$ (left column) and corresponding decomposed disks and bulges (middle and right columns). The bulge-disk decomposition fit was done with an **exponential plus a variable index Sérsic** function, at inclinations $1 - cos(i) = 0.3, 0.7, 0.9$ ($i = 46°$ (first row), $73°$ (second row) and $84°$ (third row)), for $\tau^f_B = 4.0$.

the inner regions of dust attenuated disks, in particular for higher values of dust opacity, as already discussed in Chapter 5 (see also Pastrav et al. 2013). When such disks exist in isolation (without a bulge) and are fitted with an exponential function, the depression of the surface-brightness in the centre of disks results in a fit with an exponential model having a larger scalelength than the intrinsic one. However, in the presence of a bulge, the flattening of the disk profile in the centre is incorrectly compensated by stellar light from the bulge. This can be seen in Fig. 6.3, where I plot examples of relative residuals between the simulated single dusty disks and corresponding decomposed disks. The blue region in the centre (for $i = 46°$ and $73°$) is due to the exponential form of the decomposed disk which rises above the flattened central region of the simulated attenuated single disk. At lower dust opacities, when the flattening of the disk is small and happens within one effective radius of the bulge, the fitting routine will transfer enough light from the bulge to reasonably compensate for the flattening of the disk. Therefore the derived scalelength is closer to (or slightly smaller than) the intrinsic scalelength of the disk (measured at the same inclination in the absence of dust). At higher optical depth, however, when the disk is optically thick up to large radii, beyond the effective radius of the bulge, there is still a transfer of light from the bulge to the disk, but not enough to compensate for the more pronounced flattening. Therefore, to account for the remaining depression in the surface-brightness, the routine will tend to overestimate the scale-length of the decomposed disk (with respect to the dustless case), as in the case of a single disk analysis. However, the overestimation will be smaller than in the case of a single disk. To conclude, the derived scalelength of a decomposed disk is close to the intrinsic one at smaller opacities and is overestimated at higher opacities. I note here that this effect is not visible in Fig. 6.3, since the outer regions of the disks in the residual maps are dominated by the difference between the truncated simulation and the untruncated model. However, in all cases the derived scale-lengths of decomposed disks will be smaller than the derived scale-lengths in the absence of a bulge (see Fig. 6.4).

Conversely, the decomposed bulge will be slightly more extended than in reality, since light from the bulge has been transferred to the simulated disk, resulting in a larger effective radius than in the case of a pure attenuated bulge (see Fig. 6.6). As expected, the corrections $corr^{\mathrm{B/D}}$ are larger in the B band than in the K band. The derived Sérsic index of bulges seems to be more robust to the decomposition process (see Fig. 6.5), even in B band. The results from Figs. 6.4 to 6.6 are for a $B/D = 0.25$. The same analysis performed on simulations having $B/D = 0.5$ show very little differences in the results, indicated that $corr^{\mathrm{B/D}}$ is relatively insensitive to the exact value of the bulge-to-disk ratio.

6.1.2 Fits with two variable-index Sérsic functions

For bulge-disk decomposition performed with two variable-index Sérsic functions there is an extra free parameter for fitting the disk component, which results in less transfer of light from the bulge to the disk, and therefore in a solution which is closer to single disk and single bulge cases. Examples of resulting fits in the form of major- and minor-axis profiles (upper and middle rows) and relative residuals (bottom row) are presented in Fig. 6.7. In this case, a more robust decomposition is obtained, which can be noticed from Fig. 6.8, for the decomposed disks.

As shown in Chapter 5 (see also Pastrav et al. 2013), the flattening of the central parts of single disks due to attenuation is fitted with a Sérsic index having a lower value than the intrinsic one. When a bulge is also present, GALFIT will find a solution with a slightly larger Sérsic index than for the single disk (see Fig. 6.9), because light transfer from the bulge still occurs for all opacities. However, as for the Sérsic fits of single disks (see Sect. 5.1.2), the Sérsic index will also decrease with increasing opacity, just with a small offset from the single disk case. Because of this the derived effective radii will be close (or slightly smaller) to the ones derived for single disks, as shown in Fig.6.10.

Since a fraction of the light from the bulge is transferred to the disk, their profiles will be less peaky than in the case of single bulges. However, because the transfer fraction is small, this results in only a small overestimate of the effective radii (see Fig. 6.12). The derived Sérsic index of the bulge is relatively insensitive to the existence of a disk, meaning the solution is very close to that derived for single bulges (see Fig. 6.11).

The results presented in Figs. 6.9 to 6.12 are for $B/D = 0.25$. A similar analysis performed on simulations made with $B/D = 0.50$ shows that a more prominent bulge does not significantly change the results on $corr^{\mathrm{B/D}}$. Thus, irrespectively of the fitting functions (exponential plus Sérsic or Sérsic plus Sérsic) bulge-disk decompositions of systems containing exponential bulges are robust against the exact value of B/D ratio.

All the corrections obtained for both exponential plus Sérsic fits as well as for two variable Sérsic functions are given in Tables C.1 to C.20 from Appendix C.

6.2 Galaxies with de Vaucouleurs bulges

In the case of de Vaucouleurs bulges the results for $corr^{\mathrm{B/D}}$ show several differences from the case of exponential bulges. Firstly, the amplitude of the corrections is larger for any given inclination and opacity. This means that for higher Sérsic indices the decomposition between disk and bulge starts to be biased. Secondly, the trends are noisier for the extreme cases and less well defined. Finally, unlike systems with exponential bulges, the results depend on the B/D ratio, with the amplitude of the corrections increasing for larger B/D values.
Examples of plots with the corrections are shown in Figs. 6.13-6.15 for disk scale-lengths, bulge effective radii and Sérsic indices, corresponding to exponential+Sérsic fits. In the case of a fit performed with two Sérsic functions, as the parameters are less constrained during the fitting procedure, this results in even noisier and less defined results. I therefore caution the reader that these results are less reliable, especially for high values of τ^f_B, for the derived bulge effective radii and Sérsic indices.
All the corrections obtained for both exponential plus Sérsic fits as well as for two variable Sérsic functions are given in Tables C.21 to C.40 from Appendix C.

6.3 Dust effects on single Sérsic fits of galaxies

This part of my study is motivated by the fact that single Sérsic fits are commonly used in image analysis (e.g. Hoyos et al. 2011, Simard et al. 2011, Kelvin et al. 2012, Lackner & Gunn 2012, Bruce et al. 2012, Bernardi et al. 2012, Häußler et al. 2013). This is usually done for large sample of galaxies with marginal resolution, where morphological components cannot be clearly separated/distinguished, or where a two-component fit is not a significant improvement over a single Sérsic fit.

I show here that the derived effective radius of a composite galaxy fitted with single Sérsic functions is strongly underestimated. This can be seen in Fig. 6.16, where the effect is visible for both the B and the K bands. The strongest effect appears for the optically thinner cases, where the bulge is biasing the general solution of the fit. For galaxies with higher optical depth the attenuation due to dust is flattening the profiles in the centre of the galaxy, making the effect of bulges less pronounced, and therefore bringing the results of single Sérsic fits closer to the real effective radius of the disk. The effects strongly depend on the B/D parameter, with higher values of the B/D resulting in a stronger underestimation of galaxy effective radii, for the same inclination and dust opacity (see the differences between the upper and lower plots in Fig. 6.16, for both bands). All the corrections obtained for single Sérsic fits of galaxies with exponential bulges are given in Tables D.1 to D.10 from Appendix D.

6.4 Application: the inclination dependence of dust effects

One important application of my modelling is the prediction for the inclination dependence of the effects of dust on the derived scale-lengths of disks. To compare my predictions with observations I used the photometric data derived by Simard et al. (2011) for galaxies from the Legacy area of the Sloan Digital Sky Survey (SDSS) Data Release 7. In total, Simard et al. performed bulge-disk decompositions in g and r bands for $1,123,718$ galaxies using three different type of fits: an exponential disk plus a de Vaucouleurs bulge, an exponential disk plus a Sérsic bulge and a single Sérsic fit. I used the measurements in r band for exponential scale-lengths derived from fits with an exponential disk plus a Sérsic bulge. From these I selected only the measurements for which these fits represent a significant improvement over a single Sérsic fit, as listed by Simard et al. I also selected galaxies with redshifts $z \leq 0.08$ from the resulting sample. This gave me a sample of 117833 galaxies. From this, galaxies with $B/D < 0.35$ were further selected. This criterion was applied to ensure a higher probability of selecting a sample of bonafide spiral disks. This left me with a sample of 38555 galaxies with measured exponential disk sizes, integrated magnitudes and inclinations. Since the inclinations listed in Simard et al. (2011) are not corrected for projection effects (due to the vertical distribution of stars), I re-calculated these by applying the corrections $corr^{\rm proj}$ from my model, as listed in Chapter 4 - Sect. 4.1 (see also Pastrav et al. 2013).

In Fig. 6.17 I show the size-luminosity relation for this sample, as plotted with black stars. A well defined correlation can be seen, with more luminous galaxies having larger sizes. I also plotted with red crosses the data corresponding to galaxies with disk inclinations $1 - \cos(i) > 0.8$. It is interesting to see that the red points occupy only the brighter part of the correlation, with most of the points having disk magnitudes brighter than −17. No red points exist for the very faint end of the correlation. This suggest that the galaxies with the smaller axis-ratios are biased towards more luminous galaxies, which, according to size-luminosity correlation, are also bigger (more extended) galaxies. I made similar tests for the other bins in inclinations, where I found no bias. Because of this I decided to exclude the galaxies with $1-\cos(i) > 0.8$ and only compare the prediction of my model with data for inclinations in the range $1 - cos(i) < 0.8$. This left me with a sample of 33770 galaxies.

To compare the model predictions with the data I derived the average exponential scale-length for each bin in inclination, where the bins were taken to be $\Delta\cos(i) = 0.05$. For the model predictions I considered the whole chain of corrections

$$corr(\mathrm{R_d}) = \mathrm{corr}^{\mathrm{proj}}(\mathrm{R_d}) * \mathrm{corr}^{\mathrm{dust}}(\mathrm{R_d}) * \mathrm{corr}^{\mathrm{B/D}}(\mathrm{R_d}) \tag{6.4.1}$$

where R_d is the exponential (radial) scale-length of the stellar disk, $corr^{\mathrm{proj}}(R_\mathrm{d})$ are the projection effects listed in Chapter 4-Sect. 4.1, $corr^{\mathrm{dust}}(R_\mathrm{d})$ are the effects of dust on the scale-length of disks seen in isolation, as listed in Chapter 5 - Sect. 5.1, and $corr^{\mathrm{B/D}}(R_\mathrm{d})$ are the effects of dust on the scale-length of disks seen in combination with a bulge, as derived in Chapter 6 - Subsect. 6.1.1. As in Sect. 5.5, the corrections for an average population of spiral galaxies were calculated for $\tau_B^f = 4.0$. The choice for this value of dust opacity was motivated by the analysis of the attenuation-inclination relation by Driver et al. (2007), who found an average dust opacity for local universe disk galaxies of $\tau_B^f = 3.8$. A similar average value for comparable stellar masses was also found by Grootes et al. (2013). Moreover, radiative transfer analysis of the UV to FIR SEDs of individual edge-on galaxies by Misiriotis et al. (2001) and Popescu et al. (2004) found similar values for τ_B^f.

In Fig. 6.18, I present the comparison of my model predictions with the data from Simard et al. (2011). Overall, the data show the same monotonic increase in disk sizes with inclination as predicted by the model. While this indicates that on average my model predictions can account for the trends seen in the data, a more detailed analysis of the inclination dependence of disk sizes would require both a more accurate determination of disk scale-lengths and an analysis done on an object-by-object case. From the point of view of the data, a more accurate determination of scale-lengths would require higher resolution images, as will soon become available from VISTA/VST. From the point of view of the analysis, corrections to each data point should be applied, according to the dust opacity of each galaxy. This, in turn, requires determination of τ_B^f. For galaxies with available panchromatic integrated luminosity densities, determination of τ_B^f can be obtained by using the library of radiative transfer model SEDs of Popescu et al. (2011), the same model that was used here to derive the dust corrections. Since the fits to the SEDs need to be scaled according to the size of the disk, this becomes an iterative problem to solve. The use of this approach allows for a self-consistent determination of both intrinsic parameters of galaxies derived from global measurements and structural parameters derived from images. For galaxies without measurements of integrated dust luminosities, the dust opacity can be derived solely from optical data, using the method of Grootes et al. (2013), which was calibrated by using the same radiative transfer model of Popescu et al. (2011), again allowing for a self-consistent analysis of both integrated quantities and structural properties.

Using the same sample of 33770 galaxies considered for the above comparison, I used the same approach, this time to study the inclination dependence of bulge effective radii. I derived the average bulge effective radius for each bin in inclination, while for the model predictions I considered again the whole chain of corrections:

$$corr(\mathrm{R_b^{eff}}) = \mathrm{corr^{proj}}(\mathrm{R_b^{eff}}) * \mathrm{corr^{dust}}(\mathrm{R_b^{eff}}) * \mathrm{corr^{B/D}}(\mathrm{R_b^{eff}}) \qquad (6.4.2)$$

where R_b^{eff} is the effective radius of the stellar bulge. In Fig. 6.19, I present the comparison of my model predictions with the data from Simard et al. (2011) for the bulge effective radii. As one can see, unlike disks, the model predictions for the total dust corrections do not exhibit a strong dependence with inclination for the effective radius of the bulge. Therefore one does not expect any trend for this range of inclinations, which overall can be seen in the data (blue curve).

As the photometric data derived by Simard et al. (2011) are only available in *g* and *r* bands (data available from other studies are likewise available in maximum two wavebands), a study of the dependence of disk sizes/bulge effective radii with wavelength is not be possible at this point.

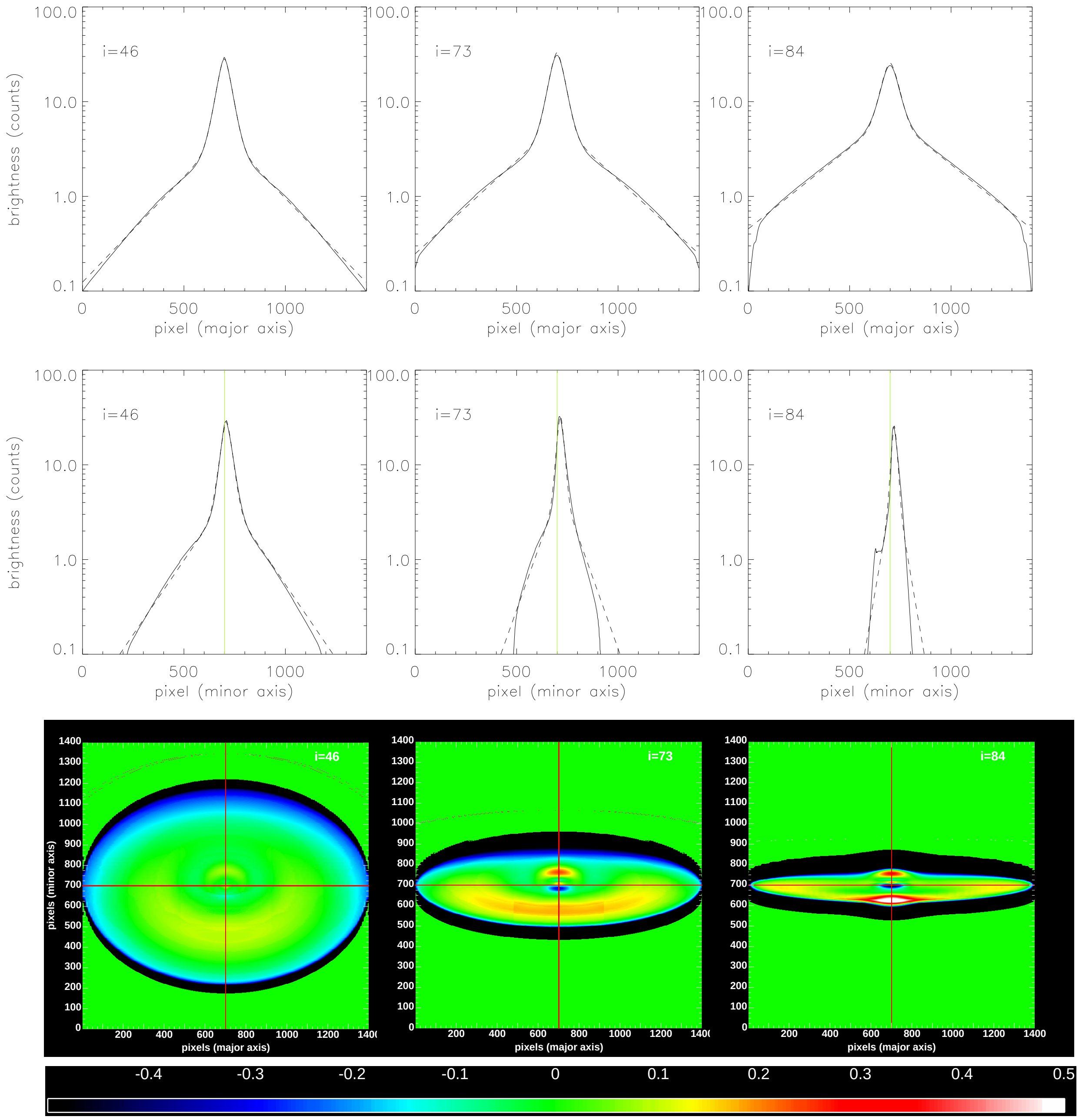

Figure 6.2: Major- and minor- axis profiles of dusty galaxies (**upper and middle rows**) with $B/D = 0.25$, and $\tau_B^f = 4.0$, in the **B band**. Fits are done with an **exponential** function (for the **disk** component) and a **variable-index Sérsic** function (for the **exponential bulge**). Solid and dashed curves are for simulations and corresponding fits, respectively. The cuts were taken parallel and perpendicular to the major axis of the simulated image, through the intensity peak, at inclinations $1 - cos(i) = 0.3, 0.7, 0.9$ ($i = 46°, 73°, 84°$). The light green line shows a cut through the geometrical centre of the image. **Lower row**: Corresponding relative residuals ($\frac{simulation-fit}{simulation}$), at the same inclination and opacity as the profiles. The red lines show radial and vertical cuts through the geometrical centre of the image.

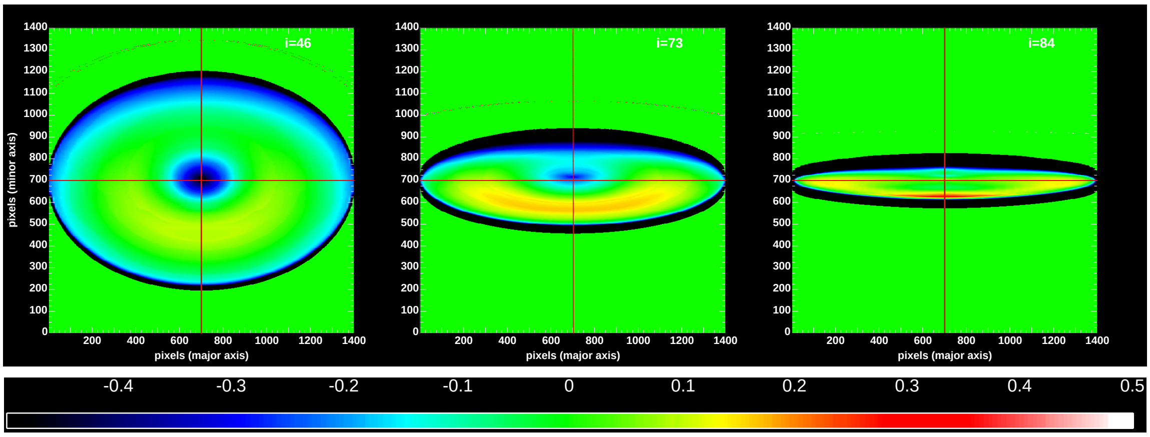

Figure 6.3: Relative residuals between the **B-band** simulated image of a single disk and the corresponding decomposed disk ($\frac{simulation-fit}{simulation}$), for $B/D = 0.25$ and $\tau^f_B = 4.0$, at inclinations $1 - cos(i) = 0.3, 0.7, 0.9$ ($i = 46, 73, 84$ degrees). The red lines show radial and vertical cuts through the geometrical centre of the image.

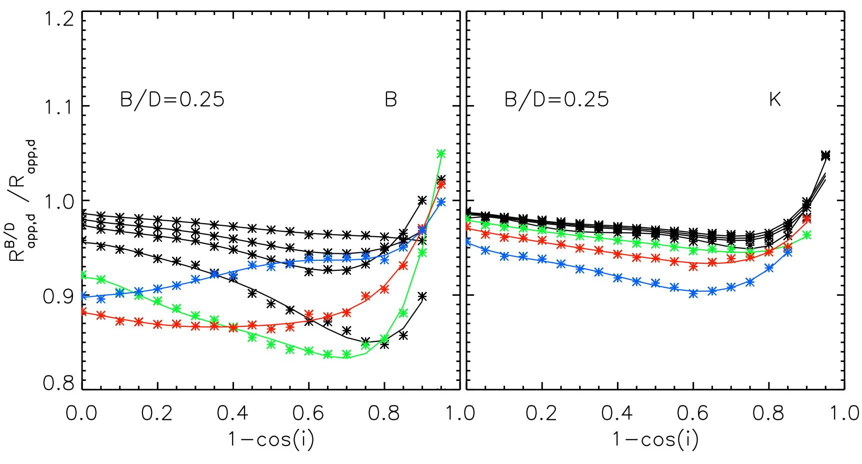

Figure 6.4: Dust effects $corr^{\mathrm{B/D}}$ on the derived scale-length of decomposed **disks** for $B/D = 0.25$. The symbols represent the measurements while the solid lines are polynomial fits to the measurements. The plots represent the ratio between the scale-lengths of apparent decomposed and single disks, $R^{\mathrm{B/D}}_{\mathrm{app,d}}$ and $R_{\mathrm{app,d}}$, respectively, as a function of inclination ($1 - cos(i)$), for B and K optical bands. An **exponential** (disk) plus a **variable index Sérsic** (bulge) distributions were used for image decomposition. The black curves are plotted for $\tau^f_B = 0.1, 0.3, 0.5, 1.0$ (from top towards the bottom), while the other curves correspond to $\tau^f_B = 2.0$ (green), 4.0 (red), and 8.0 (blue).

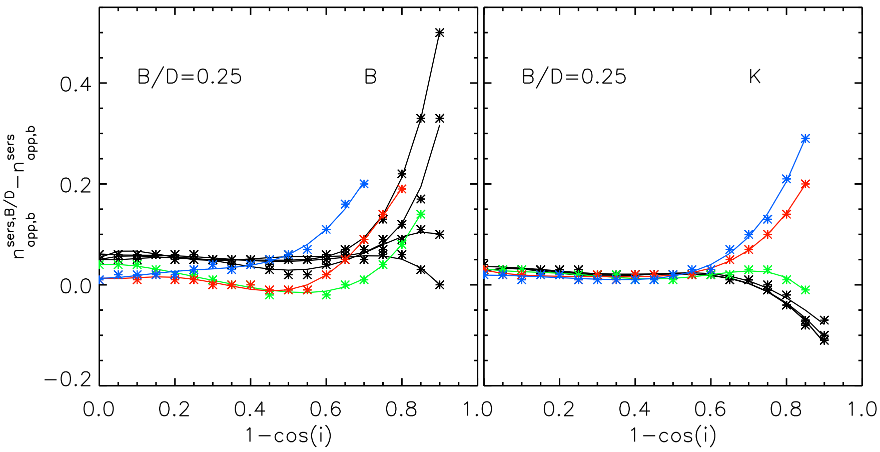

Figure 6.5: Dust effects $corr^{\mathrm{B/D}}$ on the derived Sérsic index of decomposed **exponential bulges**, for $B/D = 0.25$. The symbols represent the measurements while the solid lines are polynomial fits to the measurements. The plots represent the difference between the derived Sérsic index of decomposed and single bulges, $n^{\mathrm{sers,B/D}}_{\mathrm{app,b}}$ and $n^{\mathrm{sers}}_{\mathrm{app,b}}$, respectively, as a function of inclination ($1-cos(i)$), for B and K optical bands. An **exponential** (disk) and a **variable index Sérsic** (bulge) distributions were used for image decomposition. The black curves are plotted for $\tau^f_B = 0.1, 0.3, 0.5, 1.0$, while the other curves correspond to $\tau^f_B = 2.0$ (green), 4.0 (red), and 8.0 (blue).

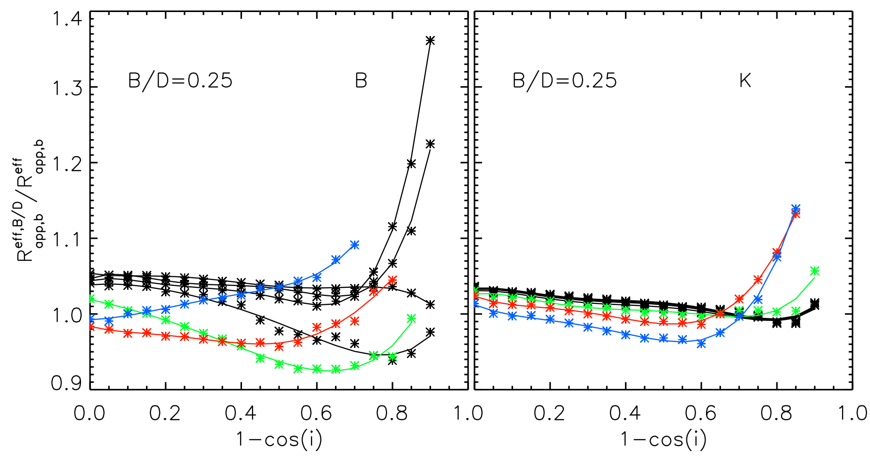

Figure 6.6: Dust effects $corr^{\mathrm{B/D}}$ on the derived effective radius of decomposed **exponential bulges** for $B/D = 0.25$. The symbols represent the measurements while the solid lines are polynomial fits to the measurements. The plots represent the ratio between the effective radii of apparent decomposed and single bulges, $R^{\mathrm{eff,B/D}}_{\mathrm{app,b}}$ and $R^{\mathrm{eff}}_{\mathrm{app,b}}$ respectively, as a function of inclination ($1 - cos(i)$), for B and K optical bands. An **exponential** (disk) and a **variable-index Sérsic** (bulge) distributions were used for image decomposition. The black curves are plotted for $\tau^f_B = 0.1, 0.3, 0.5, 1.0$, while the other curves correspond to $\tau^f_B = 2.0$ 2.0 (green), 4.0 (red) and 8.0 (blue).

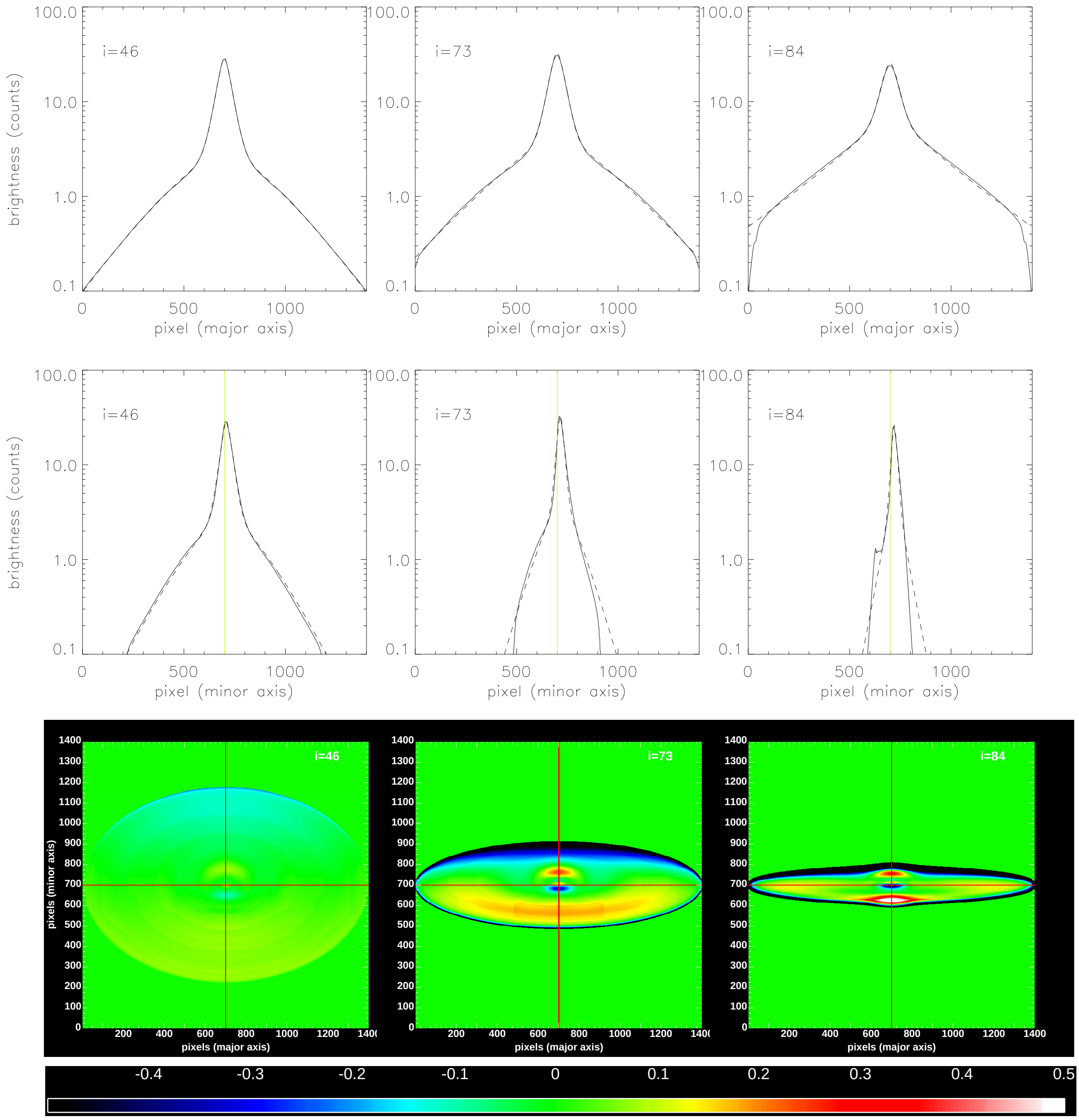

Figure 6.7: Major- and minor- axis profiles of dusty galaxies (**upper and middle rows**) with $B/D = 0.25$, and $\tau_B^f = 4.0$, in the **B band**. Fits are done with two **variable-index Sérsic** functions, one for the **disk** component and another one for the **exponential bulge**. Solid and dashed curves are for simulations and corresponding fits, respectively. The cuts were taken parallel and perpendicular to the major axis of the simulated image, through the intensity peak, at inclinations $1 - cos(i) = 0.3, 0.7, 0.9$ ($i = 46°, 73°, 84°$). The light green line shows a cut through the geometrical centre of the image. **Lower row**: Corresponding relative residuals ($\frac{simulation-fit}{simulation}$), at the same inclination and opacity as the profiles. The red lines show radial and vertical cuts through the geometrical centre of the image.

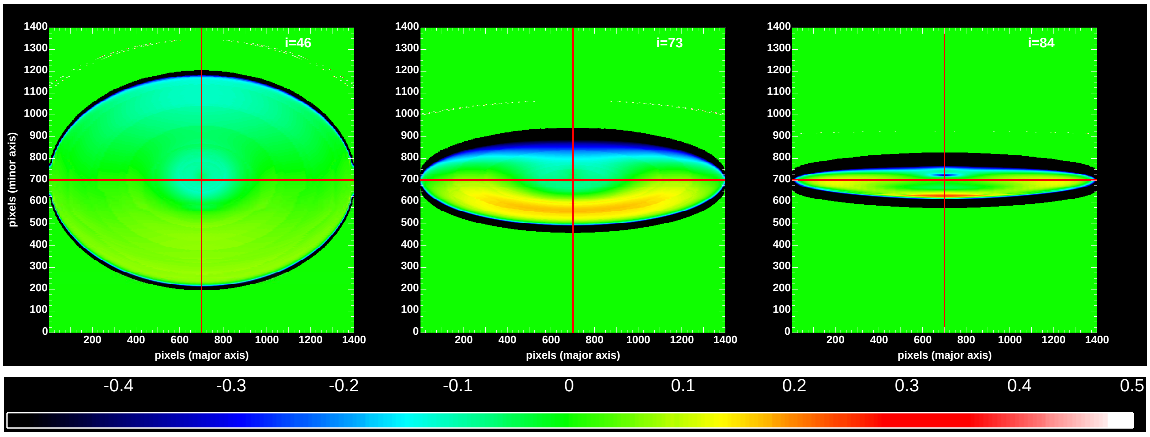

Figure 6.8: Relative residuals between the **B-band** simulated image of a single disk and the corresponding decomposed disk ($\frac{simulation-fit}{simulation}$), for $B/D = 0.25$ and $\tau^f_B = 4.0$, at inclinations $1 - cos(i) = 0.3, 0.7, 0.9$ ($i = 46, 73, 84$ degrees). The red lines show radial and vertical cuts through the geometrical centre of the image.

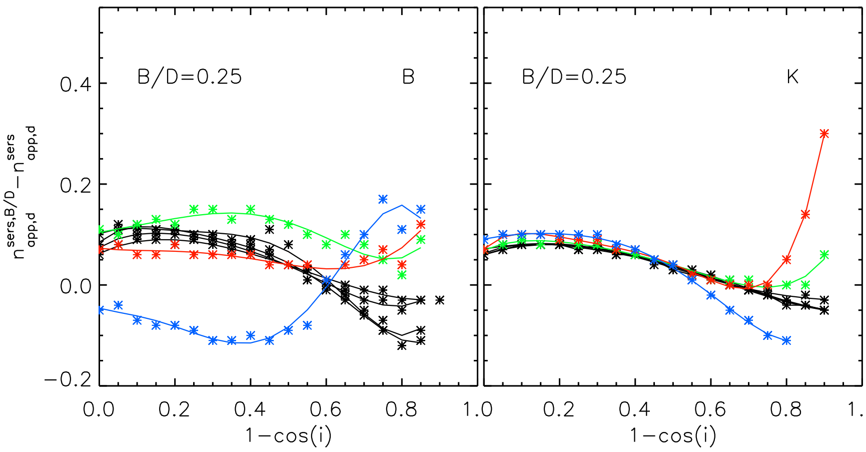

Figure 6.9: Dust effects $corr^{\mathrm{B/D}}$ on the derived Sérsic index of decomposed **disks**, for $B/D = 0.25$. The symbols represent the measurements while the solid lines are polynomial fits to the measurements. The plots represent the difference between the derived Sérsic index of decomposed and single disks, $n^{\mathrm{sers,B/D}}_{\mathrm{app,d}}$ and $n^{\mathrm{sers}}_{\mathrm{app,d}}$, respectively, as a function of inclination ($1 - cos(i)$), for B and K optical bands. Two variable Sérsic index functions were used for image decomposition. The black curves are plotted for $\tau^f_B = 0.1, 0.3, 0.5, 1.0$, while the other curves correspond to $\tau^f_B = 2.0$ (green), 4.0 (red), and 8.0 (blue).

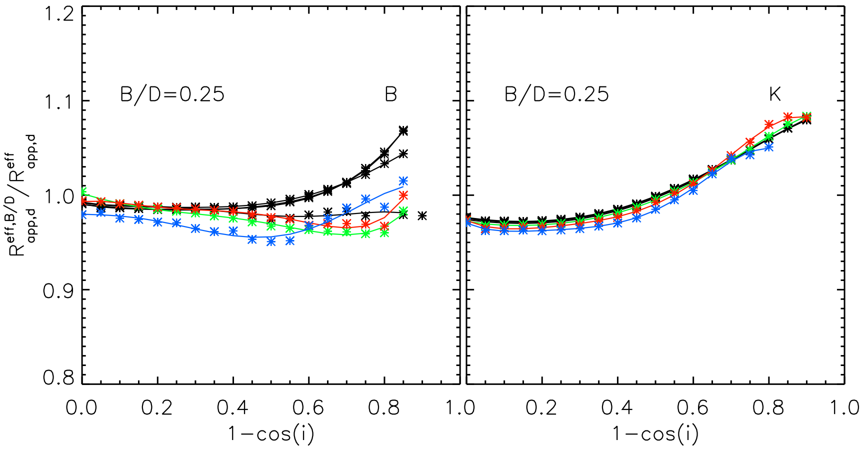

Figure 6.10: Dust effects $corr^{\mathrm{B/D}}$ on the derived effective radii of decomposed **disks** for $B/D = 0.25$. The symbols represent the measurements while the solid lines are polynomial fits to the measurements. The plots represent the ratio between the effective radii of the apparent decomposed and single disk, $R^{\mathrm{eff,B/D}}_{\mathrm{app,d}}$ and $R^{\mathrm{eff}}_{\mathrm{app,d}}$, respectively, as a function of inclination $(1 - cos(i))$, for B and K optical bands. Two variable Sérsic index functions were used for image decomposition. The black curves are plotted for $\tau^f_B = 0.1, 0.3, 0.5, 1.0$, while the other curves correspond to $\tau^f_B = 2.0$ (green), 4.0 (red), and 8.0 (blue).

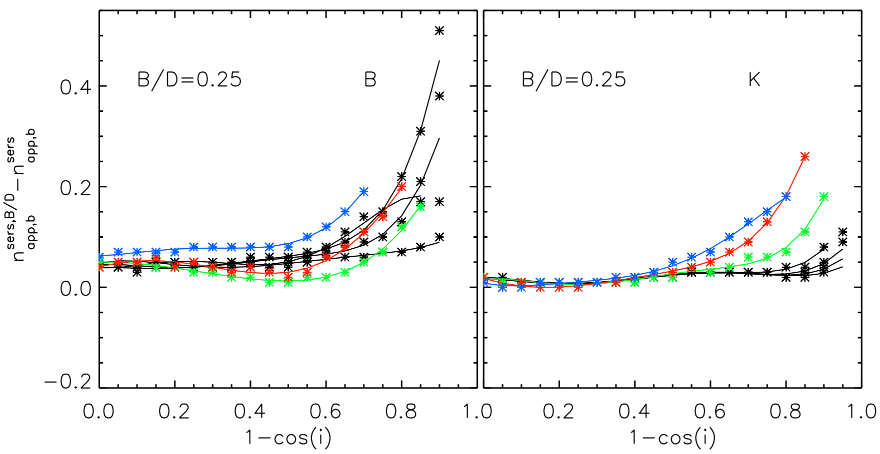

Figure 6.11: Dust effects $corr^{\mathrm{B/D}}$ on the derived Sérsic index of decomposed **exponential bulges**, for $B/D = 0.25$. The symbols represent the measurements while the solid lines are polynomial fits to the measurements. The plots represent the difference between the derived Sérsic index of decomposed and single bulges, $n^{\mathrm{sers,B/D}}_{\mathrm{app,b}}$ and $n^{\mathrm{sers}}_{\mathrm{app,b}}$, respectively, as a function of inclination $(1 - cos(i))$, for B and K optical bands. Two variable Sérsic index functions were used for image decomposition. The black curves are plotted for $\tau^f_B = 0.1, 0.3, 0.5, 1.0$, while the other curves correspond to $\tau^f_B = 2.0$ (green), 4.0 (red), and 8.0 (blue).

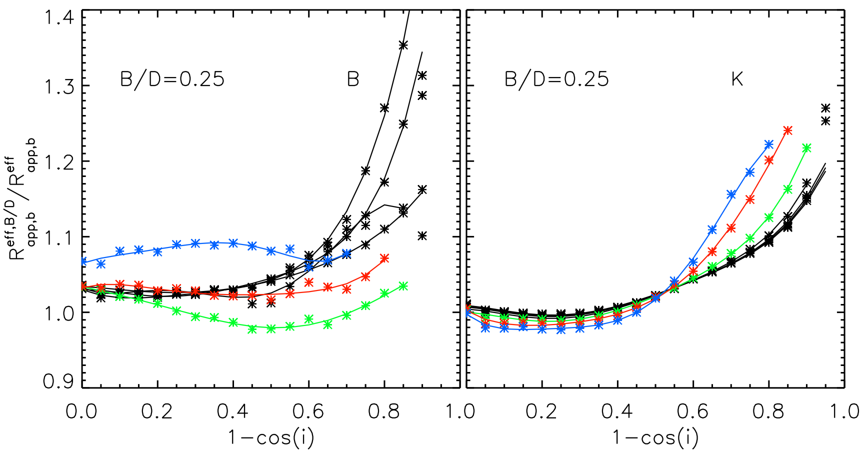

Figure 6.12: Dust effects $corr^{B/D}$ on the derived effective radius of decomposed **exponential bulges** for $B/D = 0.25$. The symbols represent the measurements while the solid lines are polynomial fits to the measurements. The plots represent the ratio between the effective radii of apparent decomposed and single bulges, $R^{eff,B/D}_{app,b}$ and $R^{eff}_{app,b}$ respectively, as a function of inclination $(1 - cos(i))$, for B and K optical bands. Two variable Sérsic index functions were used for image decomposition. The black curves are plotted for $\tau^f_B = 0.1, 0.3, 0.5, 1.0$, while the other curves correspond to $\tau^f_B = 2.0$ (green), 4.0 (red), and 8.0 (blue).

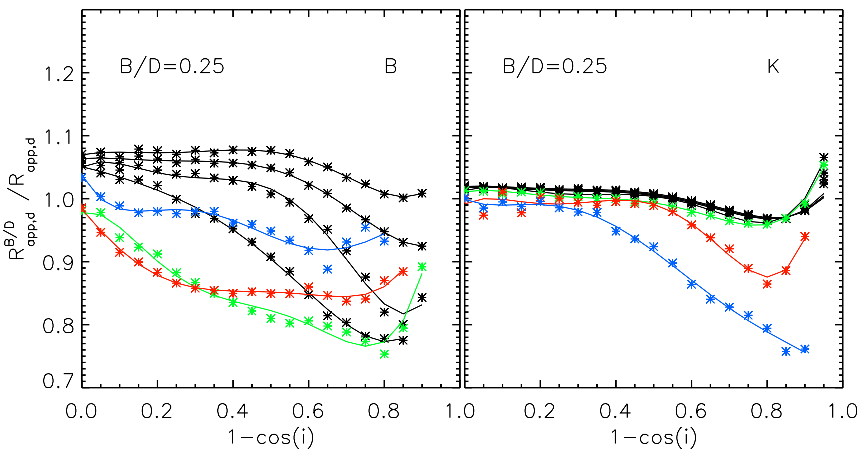

Figure 6.13: The ratio between the scale-lengths of the apparent (with dust) decomposed galaxy disks (with **de Vaucouleurs bulges**, $B/D = 0.25$), $R^{B/D}_{app,d}$, and the scale-lengths of apparent single disk images, $R_{app,d}$, as a function of inclination (1-cos(i)), for the B and K optical bands. An exponential (disk) and a variable index Sérsic (bulge) distributions were used for image decomposition. The black curves are plotted for $\tau^f_B = 0.1, 0.3, 0.5, 1.0$ (black), while the other curves correspond to $\tau^f_B = 2.0$ (green), 4.0 (red) and 8.0 (blue).

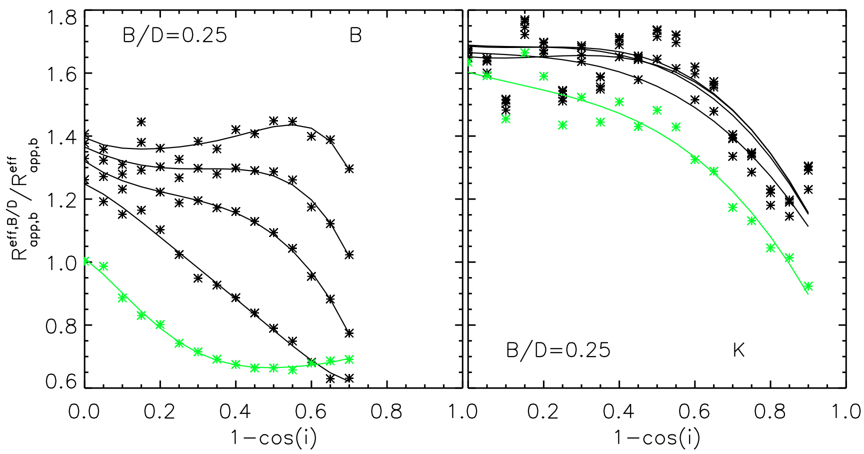

Figure 6.14: The ratio between the effective radii of the apparent (with dust) decomposed **de Vaucouleurs** galaxy bulges ($B/D = 0.25$), $R^{\rm eff,B/D}_{\rm app,b}$, and the effective radii of apparent single bulge images, $R^{\rm eff}_{\rm app,b}$, as a function of inclination (1-cos(i)), for the B and K optical bands. An exponential (disk) and a variable index Sérsic (bulge) distributions were used for image decomposition. From top to bottom, the curves are plotted for $\tau^f_B = 0.1, 0.3, 0.5, 1.0$ (black) and 2.0 (green).

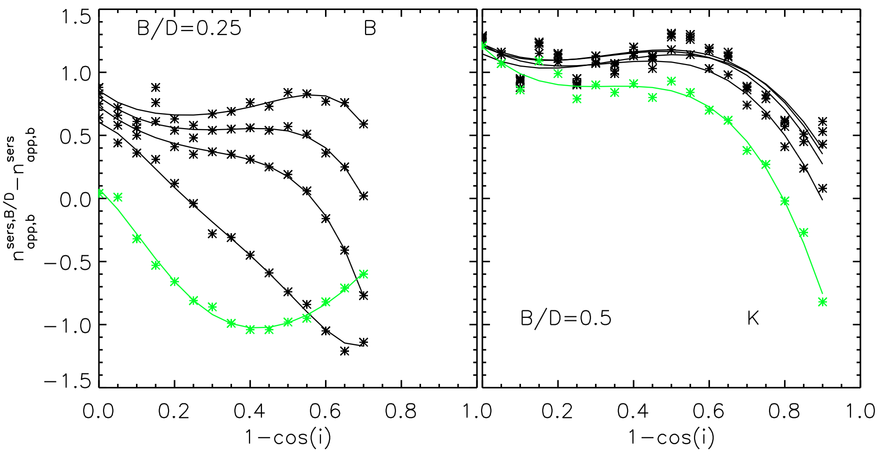

Figure 6.15: The difference between the derived Sérsic index of the decomposed **de Vaucouleurs** galaxy bulges ($B/D = 0.25$), $n^{\rm sers,B/D}_{\rm app,b}$, and the derived Sérsic index of the dusty single bulge images, $n^{\rm sers}_{\rm app,b}$. An exponential (disk) and a variable index Sérsic (bulge) distributions were used for image decomposition. From top to bottom, the curves are plotted for $\tau^f_B = 0.1, 0.3, 0.5, 1.0$ (black) and 2.0 (green).

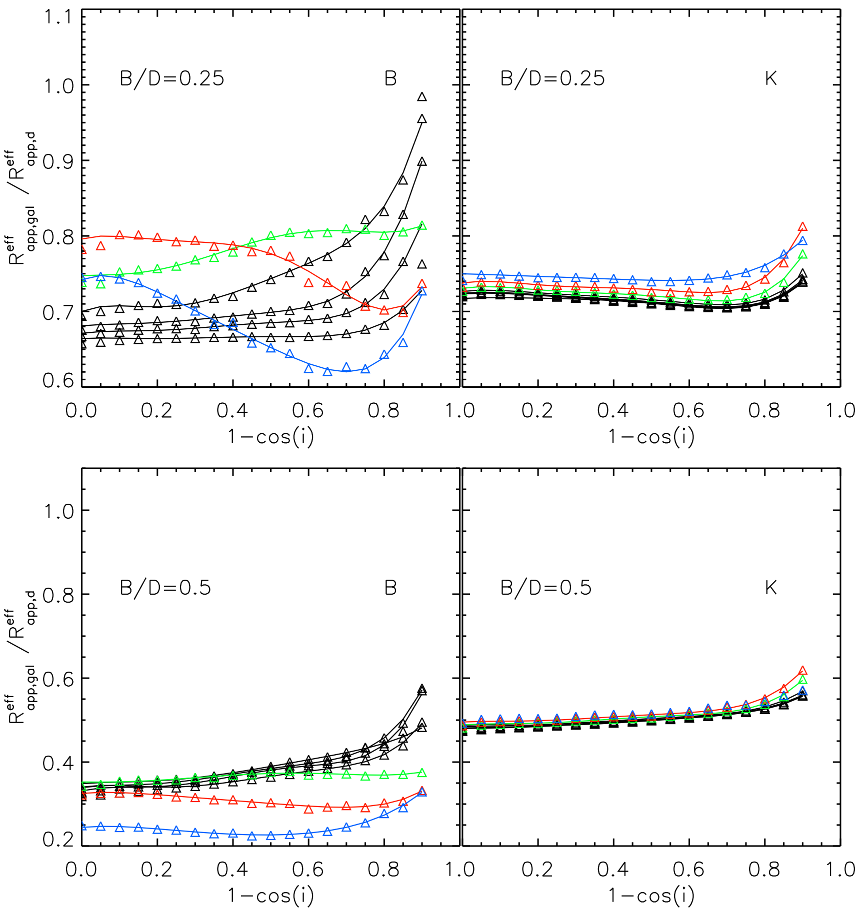

Figure 6.16: Dust effects $corr^{sS}$ on the derived effective radius of galaxies fitted with **single Sérsic functions**. The symbols represent the measurements while the solid lines are polynomial fits to the measurements. The plots represent the ratio between the effective radius of a bulge+disk system and a single disk, R^{sS}_{app} and $R_{app,d}$, respectively, as a function of inclination ($1 - cos(i)$), for the B and K optical bands and two values of B/D (0.25 - upper row; 0.5 - lower row). The black curves are plotted for τ^f_B = 0.1, 0.3, 0.5, 1.0 (from the bottom towards the top), while the other curves are for τ^f_B = 2.0 (green), 4.0 (red), and 8.0 (blue).

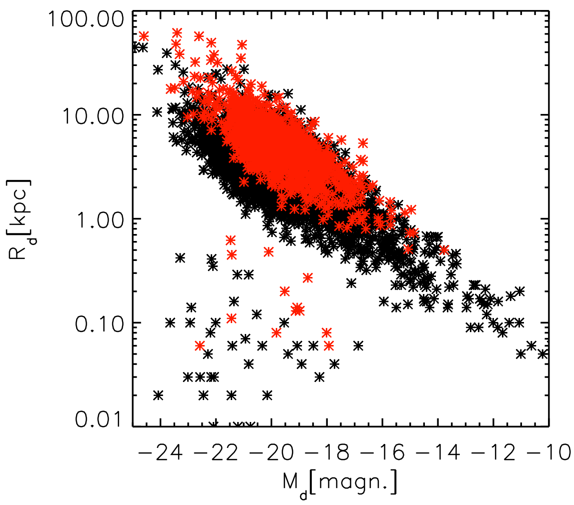

Figure 6.17: Disk size-luminosity relation for a sample of galaxies selected from Simard et al. (2011). Galaxies with inclinations $1 - \cos(i) > 0.8$ are overplotted as red crosses.

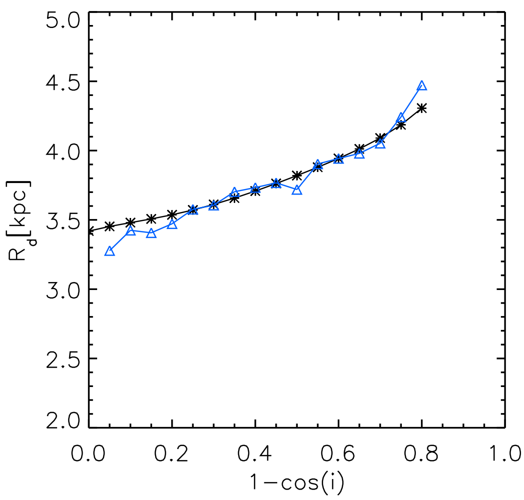

Figure 6.18: Average inclination dependence of disk sizes for a sample of galaxies selected from Simard et al. (2011) (blue curve). Overplotted in black are the predictions of my model for a disk population, scaled to the averaged disk size derived from the data, at $1 - \cos(i) = 0.6$.

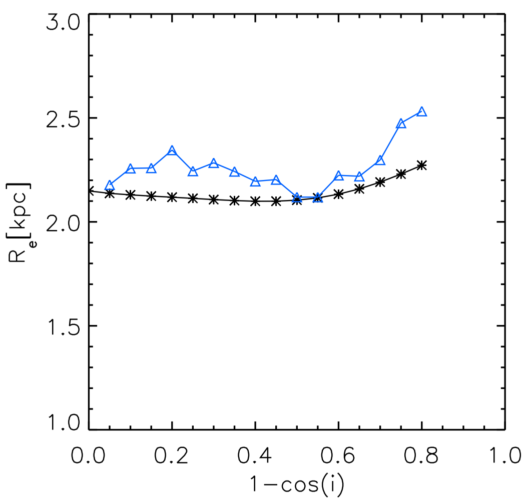

Figure 6.19: Average inclination dependence of bulge effective radii for a sample of galaxies selected from Simard et al. (2011) (blue curve). Overplotted in black are the predictions of my model for a bulge population, scaled to the averaged bulge effective radius derived from the data, at $1 - \cos(i) = 0.6$.

Chapter 7

Summary and Conclusions

In this thesis I presented the results of a study to quantify the effects of dust on the derived photometric parameters of disks and bulges in spiral galaxies. In my approach I followed the same path observers do, but instead of real images I used simulated ones, produced by radiative transfer techniques.

The simulations were produced as part of the large library of dust and PAH emission SEDs and corresponding dust attenuations presented in Popescu et al. (2011). All the simulations were calculated using a modified version of the ray-tracing radiative transfer code of Kylafis & Bahcall (1987), which includes a full treatment of anisotropic scattering. The simulations were produced separately for old stellar disks, bulges, and young stellar disks, all seen through a common distribution of dust.

The intrinsic volume stellar distributions were described by exponential functions in both radial and vertical directions for the disks and by de-projected de Vaucouleurs functions for the bulges. The corresponding dust distributions were described by double (radial and vertical) exponential functions for the two dust disks of the model. Apart from these already existing simulations additional ones have been produced for the purpose of this study. These are simulations of bulges corresponding to general Sérsic functions with various Sérsic indices.

I fitted the simulated images of disks and bulges with 1D analytic functions available in GALFIT, the same ones observers use when fitting real galaxy images (exponentials/-variable index Sérsic functions or de Vaucouleurs distributions). I showed that, even in the absence of dust, these simple distributions would differ from those of real galaxies due to the fact that they describe infinitely thin disks, while disks and bulges have a thickness. I called these effects **projection effects**.

The approach adopted in this study was to first separate projection from dust effects, while in the second stage the latter were separated from dust effects on bulge-disk decompositions. Thus, I first derived the projection effects, by calculating the change between the intrinsic parameters of the volume emissivity and those measured on dustless images. Subsequently, I derived the dust effects by calculating the change between the parameters measured on dustless and dusty images, respectively, for the same inclination and wavelength. The total change in parameter values between the measured ones on dusty images and the corresponding parameters of the volume stellar emissivity was written as a chain of corrections (Eq. 3.1.4, 3.1.5, 3.1.6 or Eq. 3.1.7, 3.1.8, 3.1.9). Finally, I quantified the dust + projection effects on bulge-disk decompositions by considering the following types of fits: i) fits with an infinitely thin exponential plus a variable-index Sérsic function for the disk and bulge component, respectively, and ii) fits with two variable-index Sérsic functions for both the disk and the bulge.
The dust effects on bulge-disk decompositions were derived by calculating the change between the parameters measured on decomposed disks and bulges and the ones measured on single dusty disks and bulges. These were connected to the previous changes (due to dust and projection effects) by adding another term in the chain of corrections

(Eq. 3.1.10, 3.1.11 or Eq. 3.1.12, 3.1.13).

I showed that one advantage of this approach is that it provides a more robust quantification of the dust effects. In particular I showed that the term related to projection effects is affected by variations in the geometrical parameters of the volume stellar emissivity, including the truncation radius, while the term related to dust effects is relatively insensitive to such factors.

The main results on the dust effects on **single disks and bulges** are as follows:

Disks

- The derived scale-length of dusty disks fitted with exponential functions is always greater than that obtained in the absence of dust, with the amplitude of the effect increasing with the central face-on dust opacity τ^f_B of the disk and with inclination, and with decreasing wavelength. The increase is very small for low values of τ^f_B or longer wavelengths, steepens for intermediate values of τ^f_B or higher inclinations, and flattens again for very high values of τ^f_B and shorter wavelengths.

- The derived central surface-brightness of dusty disks fitted with exponential functions is always fainter than that obtained in the absence of dust, with the amplitude of the effect increasing with τ^f_B of the disk and with inclination, and with decreasing wavelength.

- At low to intermediate inclinations, up to $1 - cos(i) = 0.65$, the derived axis-ratio in the presence of dust is the same as the intrinsic axis-ratio, which, in turn, is the same as the axis ratio of the infinitely thin disk, $cos(i)$. It is only at higher inclinations and higher dust opacities that the dust starts to affect the derived axis-ratios, in the sense that the measured ratios are lower than the corresponding intrinsic values. This means that dust makes disks appear slightly thinner than they are in reality. Nonetheless, even at higher inclinations and dust opacities, the effects due to dust are smaller than projection effects. Overall, the correction from the $cos(i)$ term is dominated by the increase in the axis ratio due to the vertical distribution of stars.

- The derived Sérsic index of dusty disks fitted with Sérsic functions is, for a broad range of τ^f_B and inclinations, smaller than that obtained in the absence of dust. The trend is for the Sérsic index to decrease with increasing inclination and τ^f_B. Only at very high opacities ($\tau^f_B = 4.0$ and 8.0) and close to the edge-on view is the derived Sérsic index larger than that obtained in the absence of dust, and the trend with inclination is reversed. At low inclinations the deviations from exponentiality are mainly due to dust effects while at higher inclinations, both dust and projection effects affect the derived Sérsic index.
- The derived effective radius of disks fitted with Sérsic functions is always greater than that obtained in the absence of dust, with the amplitude of the effect increasing with τ^f_B of the disk and with inclination, and with decreasing wavelength.
- The effects of dust on the derived axis ratios are the same for the Sérsic and exponential fits.

Thin Disks

- The trends in the derived scale-length and effective radius of thin disks fitted with exponential and Sérsic functions, respectively, are similar to those obtained for disks. However, the amplitude of the effect is more pronounced, even when the comparison is done at the same optical wavelength. In the UV range the trend with wavelength is non-monotonic, due to the bump in the extinction curve at the 2200 Å. The derived Sérsic index is always smaller than that obtained in the absence of dust, and has a monotonic decrease with increasing inclination and τ_B^f.

- I also showed corrections for the $H\alpha$ line, both for the case of exponential and Sérsic fits.

Bulges

- The effects of dust do not seem to strongly depend on the exact value of the Sérsic index corresponding to the intrinsic volume stellar emissivity, $n_0^{\rm sers}$. Only at very high values of $n_0^{\rm sers}$ and close to the edge-on view do the effects of dust start to deviate from the trends seen at lower $n_0^{\rm sers}$.
- The effects of dust are completely insensitive to the truncation radius of the bulge, in strong contrast to projection effects, which critically depend on the choice of truncation radius.
- The effects of dust are also insensitive to the ellipticity of the bulge. In particular spherical or ellipsoidal bulges seem to require the same corrections for the effects of dust.
- Dust does not significantly change the derived Sérsic index of bulges, for a wide range of τ_B^f and inclinations. Only at very high τ_B^f and close to the edge-on view is the derived Sérsic index of bulges smaller that that obtained in the absence of dust (the Sérsic index is underestimated). The trend is for the Sérsic index to decrease with inclination and τ_B^f.
- Similarly, dust only induces small changes in the derived effective radius of bulges. The radii are higher than that obtained in the absence of dust. The trend is for the

effective radius to increase with τ_B^f.

- The overestimation of the effective radii is more pronounced for de Vaucouleurs bulges than for exponential bulges, while the underestimation of the Sérsic indices is more pronounced for exponential bulges than for de Vaucouleurs bulges.

In the optical range, where both a disk and a thin disk are emitting, I recommend the following. For correcting the structural parameters of optical images in broad-band continuum light, dust corrections for the "disk" (and "bulge") component should be used. The corrections for the thin disk in the optical should only be used for correcting narrow-band optical images of line emission (Balmer or nebular lines), by interpolating between the optical wavelengths tabulated here (except for the Hα line, for which corrections are already explicitly listed in the tables). The main application of my dust corrections for the thin disk is for UV broad-band imaging, where this morphological component dominates the bolometric output and appearance of the spiral galaxy images.

I used the derived corrections for single disks to compare my model predictions for the wavelength dependence of dust effects with similar trends seen in recent observational data coming from the GAMA survey (Kelvin et al. 2012). The results of this comparison for Sérsic indices and effective radii show that dust effects can account for most of the trends seen in the data, with some additional room for intrinsic gradients in the stellar populations.

The main results for dust effects on **decomposed disks and bulges** are the following:

Galaxies with exponential bulges

- The derived scale-length of a decomposed disk (obtained from fits of type i. - an infinitely thin exponential plus a variable-index Sérsic function for the disk and bulge component) is smaller than the derived scale-length of a single disk (in the absence of a bulge).

- The derived effective radius of a decomposed bulge (obtained from fits of type i.) is larger than the effective radius of a single bulge (in the absence of a disk).
- The derived Sérsic index of a decomposed bulge (obtained from fits of type i.) is similar to that obtained in the absence of a disk.
- The derived effective radius of a decomposed disk (obtained from fits of type ii. - fits with two variable-index Sérsic functions for both the disk and the bulge) is closer to the single disk solution (in the absence of a bulge).
- The derived effective radius of a decomposed bulge (obtained from fits of type ii.) is slightly larger than the effective radius of a single bulge (in the absence of a disk).
- The corrections $corr^{\mathrm{B/D}}$ are relatively insensitive to the exact value of the B/D.

Galaxies with de Vaucouleurs bulges

- The amplitude of the corrections $corr^{\mathrm{B/D}}$ is larger than in the case of systems with exponential bulges.
- The results strongly depend on the exact value of the B/D.
- The trends with inclination are noisier than in the case of systems with exponential bulges.

The predictions for the inclination dependence of disk sizes were compared with observational data from a sample selected from Simard et al. (2011). I showed that on average the model can account for the trends seen in the data. I would also recommend that for more detailed studies of disk sizes, an analysis on an object-by-object case should be involved, in conjunction with determinations of disk opacities. Self-consistent determinations of both intrinsic disk sizes and dust opacities can be obtained using the library of model SEDs of Popescu et al. (2011) or the method of Grootes et al. (2013), since these have been obtained with the same radiative transfer model that was used to derived the corrections presented in this work.

All the corrections derived here are based on high resolution simulated images. With decreased resolution I expect these corrections to change. In future work I will quantify the effect of resolution on the derived corrections, both for single disks and bulges, as well as for decomposed components by degrading the resolution of the existing simulated images, and performing new fits. I will then compare the derived photometric parameters obtained for different resolutions with those obtained on higher resolution images. As already mentioned in Chapter 3.2, this will provide a new set of corrections, which can be used in the chain correction approach. For the derived scale-length or effective radius of disks I will also use a cross-calibration method. This would imply fitting the integrated panchromatic SEDs of galaxies imaged at lower resolution with the modelling tool of Popescu et al. (2011), whereby the size of the disk will be a free parameter of the fit. The derived size of the disk will be then compared with the size directly measured on the optical images, using surface-brightness photometry analysis, and corrected for the effects of dust and projection effects using the corrections derived in this thesis on higher resolution simulations. Any discrepencies between the two measures will give us the corrections due to resolution.
Another extension of this study would be the quantification of dust effects on barred galaxies, which would require the production of simulated images of composite systems containing bars in addition to bulges and disks, and then perform bulge-bar-disk decompositions. I expect changes in the derived photometric parameters of the bulges

due to the presence of a bar.

All the corrections derived as a result of this study, for all opacities considered and at different wavelengths, are listed in the tables given in the Appendices as follows: projection effects - **Appendix A**; dust effects on single disks and bulges - **Appendix B**; dust effects on decomposed disks and bulges - **Appendix C**; dust effects on single Sérsic fits of galaxies - **Appendix D**. The corrections are provided in form of coefficients of polynomial fits to the corrections as a function of inclination.
The combined set of corrections derived as a result of the study presented in this thesis provides a useful and easy to apply tool kit that can be used by observers on real images to accurately recover the intrinsic photometric parameters of disks and bulges in spiral galaxies.

Appendix A

The corrections for projection effects

Table A.1: **Projection effects** $corr^{proj}$ on the derived photometric parameters of the **disk**: scale-lengths and central surface brightnesses. Results are listed as coefficients of polynomial fits a_k (Eq. 3.1.19) at different optical wavelengths, corresponding to the effective wavelength of B,V,I,J,K bands.

Disk (exponential fits)

	$\frac{R_i}{R_0}$	ΔSB_0
B		
a_0	1.000	-0.005
a_1	0.005	-0.736
a_2	-0.055	0.863
a_3	0.352	0.825
a_4	-0.699	-4.004
a_5	0.497	2.542
V		
a_0	1.000	-0.006
a_1	0.010	-0.740
a_2	-0.101	0.703
a_3	0.508	1.524
a_4	-0.915	-5.095
a_5	0.603	3.116
I		
a_0	1.000	-0.005
a_1	0.026	-0.917
a_2	-0.239	1.789
a_3	0.970	-1.652
a_4	-1.547	-1.135
a_5	0.912	1.390
J		
a_0	1.000	-0.004
a_1	0.032	-1.102
a_2	-0.292	2.813
a_3	1.164	-4.469
a_4	-1.817	2.233
a_5	1.047	-0.017
K		
a_0	1.000	-0.004
a_1	0.037	-1.230
a_2	-0.310	3.120
a_3	1.232	-4.717
a_4	-1.902	1.986
a_5	1.089	0.336

Table A.2: **Projection effects** $corr^{proj}$ on the derived axis ratios of the **disk**. Results are listed as coefficients of polynomial fits a_k and b_0 (Eq. 4.1.1.1) at different optical wavelengths, corresponding to the effective wavelength of B,V,I,J,K bands.

Disk (exponential fits)

	$\frac{Q_i}{Q_0}$
B	
a_0	1.000
a_1	0.062
a_2	-1.076
a_3	5.554
a_4	-10.067
a_5	6.219
b_0	1.800
V	
a_0	1.000
a_1	0.112
a_2	-1.403
a_3	6.462
a_4	-11.075
a_5	6.591
b_0	1.800
I	
a_0	1.000
a_1	0.354
a_2	-3.917
a_3	15.437
a_4	-24.016
a_5	13.120
b_0	1.800
J	
a_0	1.000
a_1	0.199
a_2	-1.876
a_3	7.766
a_4	-12.960
a_5	7.765
b_0	2.000
K	
a_0	1.000
a_1	0.456
a_2	-4.612
a_3	17.689
a_4	-27.146
a_5	14.786
b_0	2.200

Table A.3: **Projection effects** $corr^{proj}$ on the derived photometric parameters of the **disk**: effective radius, central surface brightnesses and Sérsic index. Results are listed as coefficients of polynomial fits a_k (Eq. 3.1.19) at different optical wavelengths, corresponding to the effective wavelength of B,V,I,J,K bands.

Disk (Sérsic fits)

	$\frac{R_i}{R_0}$	ΔSB_0	n_i^{sers}
B			
a_0	1.000	0.022	1.000
a_1	0.019	-0.641	-0.023
a_2	-0.368	0.893	-0.180
a_3	1.259	1.228	0.459
a_4	-1.840	-4.709	-4.709
a_5	0.891	3.375	0.000
V			
a_0	1.000	0.022	1.000
a_1	0.024	-0.671	-0.041
a_2	-0.429	1.030	-0.057
a_3	1.479	0.897	0.141
a_4	-2.162	-4.321	-4.321
a_5	1.059	3.205	0.000
I			
a_0	1.000	0.026	1.000
a_1	0.046	-0.906	-0.067
a_2	-0.625	2.819	0.060
a_3	2.139	-4.731	-0.117
a_4	-3.098	3.214	3.214
a_5	1.539	-0.355	0.000
J			
a_0	1.000	0.032	1.000
a_1	0.065	-1.163	-0.112
a_2	-0.794	4.633	0.369
a_3	2.681	-10.149	-0.824
a_4	-3.848	10.273	10.273
a_5	1.921	-3.636	0.000
K			
a_0	1.000	0.035	1.000
a_1	0.057	-1.297	-0.146
a_2	-0.809	5.376	0.530
a_3	2.825	-12.078	-1.220
a_4	-4.138	12.662	12.662
a_5	2.110	-4.729	0.000

Table A.4: **Projection effects** $corr^{proj}$ on the derived photometric parameters of the **bulge**: effective radius and Sérsic index. Results are listed as coefficients of polynomial fits a_0 (Eq. 3.1.19) for four different n_0^{sers} of the intrinsic volume stellar emissivity and two different truncation radii ($3R_0^{eff}$ and $10R_0^{eff}$). Results are independent of optical waveband.

Bulge (Sérsic fits)

$3R_0^{eff}$	n_0^{sers}	$\frac{R_i^{eff}}{R_0^{eff}}$	n_i^{sers}
a_0	1	1.124	0.760
a_0	2	1.009	1.604
a_0	4	0.875	3.123
a_0	8	0.702	5.490
$10R_0^{eff}$	n_0^{sers}	$\frac{R_i^{eff}}{R_0^{eff}}$	n_i^{sers}
a_0	1	1.212	0.860
a_0	2	1.200	1.829
a_0	4	1.177	3.760
a_0	8	1.061	7.112

Table A.5: **Projection effects** $corr^{proj}$ on the derived effective radius of de Vaucouleurs **bulges**. Bulges are truncated at $3R_0^{eff}$. Results are listed as coefficients of polynomial fits a_0 (Eq. 3.1.19). Results are independent of optical waveband.

Bulge (de Vaucouleurs fits)

	$\frac{R_i}{R_0}$
a_0	0.870

Appendix B

The corrections for dust effects on single disks and bulges

Table B.1: **Dust effects** *corr*^{dust} on the derived scale-lengths and central surface brightnesses of the **disk**. Results are listed as coefficients of polynomial fits a_k (Eq. 3.1.19) at different τ_B^f, for B band.

Disk (exponential fits); B band

	$\frac{R_{app}}{R_i}$	ΔSB
$\tau_B^f = 0.1$		
a_0	0.997	-0.038
a_1	0.085	1.616
a_2	-0.812	-15.360
a_3	2.937	52.673
a_4	-4.296	-73.834
a_5	2.274	36.932
$\tau_B^f = 0.3$		
a_0	1.001	-0.043
a_1	0.021	2.361
a_2	-0.179	-23.824
a_3	1.204	86.724
a_4	-2.266	-126.152
a_5	1.577	65.145
$\tau_B^f = 0.5$		
a_0	1.011	-0.010
a_1	-0.109	2.286
a_2	1.185	-20.803
a_3	-3.211	76.489
a_4	3.783	-113.419
a_5	-1.257	60.717
$\tau_B^f = 1.0$		
a_0	1.043	0.106
a_1	-0.251	2.702
a_2	3.103	-22.735
a_3	-9.716	84.285
a_4	13.274	-122.295
a_5	-6.060	64.497
$\tau_B^f = 2.0$		
a_0	1.120	0.501
a_1	-0.056	3.620
a_2	2.405	-26.334
a_3	-7.737	95.612
a_4	11.398	-135.142
a_5	-5.750	69.357
$\tau_B^f = 4.0$		
a_0	1.274	1.300
a_1	0.372	3.307
a_2	-0.613	-19.225
a_3	1.889	73.647
a_4	-1.905	-108.615
a_5	0.457	58.097
$\tau_B^f = 8.0$		
a_0	1.470	2.278
a_1	0.529	4.961
a_2	-2.545	-30.875
a_3	7.470	104.631
a_4	-9.944	-146.070
a_5	4.658	75.259

Table B.2: **Dust effects** *corr*^{dust}, as in Table B.1, but in V band.

Disk (exponential fits); V band

	$\frac{R_{app}}{R_i}$	ΔSB
$\tau_B^f = 0.1$		
a_0	0.996	-0.066
a_1	0.077	1.918
a_2	-0.736	-18.401
a_3	2.634	63.155
a_4	-3.826	-88.001
a_5	2.003	42.994
$\tau_B^f = 0.3$		
a_0	0.997	-0.115
a_1	0.073	3.761
a_2	-0.660	-34.873
a_3	2.661	118.192
a_4	-4.140	-164.147
a_5	2.383	81.037
$\tau_B^f = 0.5$		
a_0	1.001	-0.099
a_1	-0.008	3.738
a_2	0.190	-35.218
a_3	-0.030	123.256
a_4	-0.528	-175.160
a_5	0.753	88.595
$\tau_B^f = 1.0$		
a_0	1.022	-0.027
a_1	-0.190	2.530
a_2	2.232	-22.728
a_3	-6.798	84.104
a_4	9.033	-122.926
a_5	-3.910	65.082
$\tau_B^f = 2.0$		
a_0	1.074	0.249
a_1	-0.162	2.492
a_2	2.843	-19.569
a_3	-9.104	76.479
a_4	13.040	-112.807
a_5	-6.337	60.324
$\tau_B^f = 4.0$		
a_0	1.194	0.855
a_1	0.212	4.148
a_2	0.534	-30.259
a_3	-1.796	113.208
a_4	3.296	-164.003
a_5	-2.042	84.867
$\tau_B^f = 8.0$		
a_0	1.380	1.802
a_1	0.454	5.040
a_2	-1.699	-34.958
a_3	5.204	123.917
a_4	-6.930	-175.264
a_5	3.124	89.385

Table B.3: **Dust effects** *corr*^{dust}, as in Table B.1, but in I band.

Disk (exponential fits); I band	$\frac{R_{app}}{R_i}$	ΔSB
$\tau_B^f = 0.1$		
a_0	0.998	-0.040
a_1	0.043	1.170
a_2	-0.405	-10.802
a_3	1.465	35.834
a_4	-2.135	-48.074
a_5	1.120	22.735
$\tau_B^f = 0.3$		
a_0	0.995	-0.094
a_1	0.080	2.791
a_2	-0.687	-26.681
a_3	2.541	92.471
a_4	-3.763	-129.647
a_5	2.042	64.046
$\tau_B^f = 0.5$		
a_0	0.996	-0.116
a_1	0.072	3.692
a_2	-0.518	-35.113
a_3	2.039	121.962
a_4	-3.126	-170.856
a_5	1.818	84.483
$\tau_B^f = 1.0$		
a_0	1.003	-0.123
a_1	-0.004	3.955
a_2	0.503	-34.541
a_3	-1.433	119.722
a_4	1.789	-168.466
a_5	-0.516	84.852
$\tau_B^f = 2.0$		
a_0	1.029	0.005
a_1	-0.080	3.910
a_2	1.822	-32.885
a_3	-6.159	115.346
a_4	8.943	-161.037
a_5	-4.232	81.347
$\tau_B^f = 4.0$		
a_0	1.098	0.354
a_1	0.080	4.626
a_2	1.136	-33.132
a_3	-4.122	114.623
a_4	6.840	-158.173
a_5	-3.731	79.565
$\tau_B^f = 8.0$		
a_0	1.238	1.101
a_1	0.350	5.451
a_2	-0.927	-37.437
a_3	2.791	131.221
a_4	-3.132	-183.944
a_5	1.049	93.035

Table B.4: **Dust effects** *corr*^{dust}, as in Table B.1, but in J band.

Disk (exponential fits); J band	$\frac{R_{app}}{R_i}$	ΔSB
$\tau_B^f = 0.1$		
a_0	0.999	-0.003
a_1	0.025	-0.387
a_2	-0.230	3.483
a_3	0.816	-9.873
a_4	-1.165	10.686
a_5	0.597	-3.568
$\tau_B^f = 0.3$		
a_0	0.998	-0.032
a_1	0.063	0.599
a_2	-0.555	-5.416
a_3	1.962	19.556
a_4	-2.794	-28.555
a_5	1.441	14.989
$\tau_B^f = 0.5$		
a_0	0.998	-0.053
a_1	0.087	1.439
a_2	-0.727	-14.406
a_3	2.566	53.389
a_4	-3.646	-78.165
a_5	1.895	39.884
$\tau_B^f = 1.0$		
a_0	1.000	-0.069
a_1	0.103	2.379
a_2	-0.700	-21.841
a_3	2.431	77.446
a_4	-3.396	-111.134
a_5	1.823	56.793
$\tau_B^f = 2.0$		
a_0	1.010	-0.027
a_1	0.072	2.777
a_2	0.025	-24.235
a_3	-0.289	85.624
a_4	0.722	-121.744
a_5	-0.234	62.772
$\tau_B^f = 4.0$		
a_0	1.039	0.065
a_1	0.072	3.090
a_2	0.739	-20.816
a_3	-3.223	71.558
a_4	5.601	-99.585
a_5	-2.951	51.943
$\tau_B^f = 8.0$		
a_0	1.110	0.502
a_1	0.264	3.961
a_2	-0.326	-25.968
a_3	0.093	90.053
a_4	1.546	-123.285
a_5	-1.428	62.387

Table B.5: **Dust effects** $corr^{dust}$, as in Table B.1, but in K band.

Disk (exponential fits); K band

	$\frac{R_{app}}{R_i}$	ΔSB
$\tau_B^f = 0.1$		
a_0	1.000	-0.002
a_1	0.007	0.177
a_2	-0.064	-1.737
a_3	0.241	6.099
a_4	-0.356	-8.839
a_5	0.189	4.587
$\tau_B^f = 0.3$		
a_0	1.001	0.005
a_1	0.017	-0.201
a_2	-0.163	0.870
a_3	0.638	-0.106
a_4	-0.962	-2.692
a_5	0.517	2.674
$\tau_B^f = 0.5$		
a_0	1.001	0.008
a_1	0.023	-0.141
a_2	-0.232	-0.302
a_3	0.928	5.527
a_4	-1.414	-11.720
a_5	0.769	7.566
$\tau_B^f = 1.0$		
a_0	1.003	0.010
a_1	0.037	0.796
a_2	-0.338	-11.017
a_3	1.371	44.350
a_4	-2.107	-66.118
a_5	1.167	33.936
$\tau_B^f = 2.0$		
a_0	1.008	-0.013
a_1	0.032	2.251
a_2	-0.212	-22.720
a_3	1.037	81.245
a_4	-1.713	-113.686
a_5	1.057	56.193
$\tau_B^f = 4.0$		
a_0	1.020	0.021
a_1	-0.016	3.379
a_2	0.508	-28.283
a_3	-1.456	96.856
a_4	1.871	-135.716
a_5	-0.672	68.721
$\tau_B^f = 8.0$		
a_0	1.047	0.183
a_1	-0.031	4.151
a_2	1.244	-33.590
a_3	-4.392	113.511
a_4	6.612	-153.092
a_5	-3.251	75.245

Table B.6: **Dust effects** $corr^{dust}$ on the derived axis ratios of the **disk**. Results are listed as coefficients of polynomial fits a_0 and b_k (Eq. 5.1.1.1) at different τ_B^f and at the effective wavelength of the B band.

Disk (exponential fits) B band

	$\frac{Q_{app}}{Q_i}$
$\tau_B^f = 0.1$	
a_0	1.000
b_0	–
b_1	–
$\tau_B^f = 0.3$	
a_0	1.000
b_0	–
b_1	–
$\tau_B^f = 0.5$	
a_0	1.000
b_0	0.888
b_1	–
$\tau_B^f = 1.0$	
a_0	1.000
b_0	0.888
b_1	–
$\tau_B^f = 2.0$	
a_0	1.000
b_0	0.888
b_1	–
$\tau_B^f = 4.0$	
a_0	1.000
b_0	1.202
b_1	-0.317
$\tau_B^f = 8.0$	
a_0	1.000
b_0	1.202
b_1	-0.317

Table B.7: **Dust effects** *corr*^{dust}, as in Table B.6, but in V band.

Disk (exponential fits) V band	
	$\frac{Q_{app}}{Q_i}$
$\tau_B^f = 0.1$	
a_0	1.000
b_0	–
b_1	–
$\tau_B^f = 0.3$	
a_0	1.000
b_0	–
b_1	–
$\tau_B^f = 0.5$	
a_0	1.000
b_0	–
b_1	–
$\tau_B^f = 1.0$	
a_0	1.000
b_0	0.888
b_1	–
$\tau_B^f = 2.0$	
a_0	1.000
b_0	0.888
b_1	–
$\tau_B^f = 4.0$	
a_0	1.000
b_0	1.185
b_1	-0.285
$\tau_B^f = 8.0$	
a_0	1.000
b_0	1.152
b_1	-0.259

Table B.8: **Dust effects** *corr*^{dust}, as in Table B.6, but in I band.

Disk (exponential fits) I band	
	$\frac{Q_{app}}{Q_i}$
$\tau_B^f = 0.1$	
a_0	1.000
b_0	–
b_1	–
$\tau_B^f = 0.3$	
a_0	1.000
b_0	–
b_1	–
$\tau_B^f = 0.5$	
a_0	1.000
b_0	–
b_1	–
$\tau_B^f = 1.0$	
a_0	1.000
b_0	–
b_1	–
$\tau_B^f = 2.0$	
a_0	1.000
b_0	–
b_1	–
$\tau_B^f = 4.0$	
a_0	1.000
b_0	1.263
b_1	-0.380
$\tau_B^f = 8.0$	
a_0	1.000
b_0	1.173
b_1	-0.277

Table B.9: **Dust effects** *corr*^{dust}, as in Table B.6, but in J band.

Disk (exponential fits) J band	$\frac{Q_{app}}{Q_i}$
$\tau_B^f = 0.1$	
a_0	1.000
b_0	–
b_1	–
$\tau_B^f = 0.3$	
a_0	1.000
b_0	–
b_1	–
$\tau_B^f = 0.5$	
a_0	1.000
b_0	–
b_1	–
$\tau_B^f = 1.0$	
a_0	1.000
b_0	–
b_1	–
$\tau_B^f = 2.0$	
a_0	1.000
b_0	–
b_1	–
$\tau_B^f = 4.0$	
a_0	1.000
b_0	1.115
b_1	-0.283
$\tau_B^f = 8.0$	
a_0	1.000
b_0	1.180
b_1	-0.285

Table B.10: **Dust effects** *corr*^{dust}, as in Table B.6, but in K band.

Disk (exponential fits) K band	$\frac{Q_{app}}{Q_i}$
$\tau_B^f = 0.1$	
a_0	1.000
b_0	–
b_1	–
$\tau_B^f = 0.3$	
a_0	1.000
b_0	–
b_1	–
$\tau_B^f = 0.5$	
a_0	1.000
b_0	–
b_1	–
$\tau_B^f = 1.0$	
a_0	1.000
b_0	–
b_1	–
$\tau_B^f = 2.0$	
a_0	1.000
b_0	–
b_1	–
$\tau_B^f = 4.0$	
a_0	1.000
b_0	–
b_1	–
$\tau_B^f = 8.0$	
a_0	1.000
b_0	1.155
b_1	-0.234

Table B.11: **Dust effects** $corr^{dust}$ on the derived effective radius, central surface brightness, Sérsic index of the **disk**. Results are listed as coefficients of polynomial fits a_k (Eq. 3.1.19) at different τ_B^f, for B band.

Disk (Sérsic fits); B band

	$\frac{R_{app}}{R_i}$	ΔSB	n_{app}^{sers}
$\tau_B^f = 0.1$			
a_0	0.995	-0.063	1.002
a_1	0.044	2.372	-0.182
a_2	-0.345	-22.131	1.211
a_3	1.120	74.180	-4.537
a_4	-1.560	-101.264	6.691
a_5	0.833	48.914	-3.684
$\tau_B^f = 0.3$			
a_0	0.994	-0.048	0.992
a_1	0.056	2.415	-0.132
a_2	-0.496	-21.653	0.417
a_3	1.898	74.819	-1.545
a_4	-2.891	-104.905	2.127
a_5	1.672	53.047	-1.365
$\tau_B^f = 0.5$			
a_0	0.995	0.003	0.967
a_1	0.065	2.920	0.247
a_2	-0.613	-24.752	-3.059
a_3	2.598	83.061	9.676
a_4	-4.112	-112.046	-13.110
a_5	2.425	55.212	5.969
$\tau_B^f = 1.0$			
a_0	1.002	0.194	0.925
a_1	0.122	4.000	0.393
a_2	-1.139	-33.452	-5.211
a_3	5.024	117.268	17.873
a_4	-8.032	-160.212	-25.941
a_5	4.653	77.956	13.052
$\tau_B^f = 2.0$			
a_0	1.026	0.727	0.842
a_1	-0.041	5.733	-0.142
a_2	1.345	-44.096	-0.664
a_3	-3.587	156.440	2.953
a_4	3.989	-218.542	-5.624
a_5	-1.016	107.254	3.783
$\tau_B^f = 4.0$			
a_0	1.099	1.718	0.729
a_1	0.141	5.685	-0.277
a_2	0.394	-37.795	1.157
a_3	-1.125	129.619	-3.232
a_4	2.309	-182.610	4.996
a_5	-1.065	91.756	-2.343
$\tau_B^f = 8.0$			
a_0	1.230	2.763	0.685
a_1	0.483	6.037	0.878
a_2	-1.827	-44.548	-7.585
a_3	6.694	144.855	27.851
a_4	-7.716	-197.911	-37.802
a_5	2.714	98.889	17.186
b_0	1.914	–	–

Table B.12: **Dust effects** $corr^{dust}$, as in Table B.11, but in V band.

Disk (Sérsic fits); V band

	$\frac{R_{app}}{R_i}$	ΔSB	n_{app}^{sers}
$\tau_B^f = 0.1$			
a_0	0.996	-0.073	1.002
a_1	0.030	2.129	-0.182
a_2	-0.271	-18.625	1.108
a_3	0.932	60.194	-3.893
a_4	-1.334	-80.297	5.541
a_5	0.714	38.186	-3.026
$\tau_B^f = 0.3$			
a_0	0.993	-0.063	0.993
a_1	0.045	2.638	-0.113
a_2	-0.395	-25.476	0.591
a_3	1.489	87.379	-2.464
a_4	-2.249	-119.994	3.709
a_5	1.297	58.553	-2.226
$\tau_B^f = 0.5$			
a_0	0.993	-0.040	0.979
a_1	0.043	2.347	0.090
a_2	-0.393	-21.559	-1.267
a_3	1.682	74.742	3.511
a_4	-2.686	-103.175	-4.456
a_5	1.634	51.468	1.726
$\tau_B^f = 1.0$			
a_0	0.995	0.027	0.953
a_1	0.143	3.812	0.320
a_2	-1.396	-30.914	-4.416
a_3	5.636	103.901	15.434
a_4	-8.588	-139.285	-22.605
a_5	4.738	67.656	11.295
$\tau_B^f = 2.0$			
a_0	1.014	0.405	0.889
a_1	-0.041	4.579	0.039
a_2	0.577	-37.239	-2.297
a_3	-0.384	134.507	8.525
a_4	-0.828	-187.320	-13.661
a_5	1.332	91.712	7.669
$\tau_B^f = 4.0$			
a_0	1.067	1.221	0.784
a_1	-0.117	6.442	-0.432
a_2	2.347	-48.673	2.099
a_3	-6.991	170.863	-6.111
a_4	9.211	-239.758	7.741
a_5	-3.855	118.370	-3.032
$\tau_B^f = 8.0$			
a_0	1.170	2.305	0.691
a_1	0.328	5.584	0.551
a_2	-0.744	-37.821	-5.302
a_3	2.194	125.151	18.248
a_4	-0.993	-174.691	-22.781
a_5	-0.404	88.842	9.689
b_0	1.734	–	–

Table B.13: **Dust effects** $corr^{dust}$, as in Table B.11, but in I band.

Disk (Sérsic fits); I band	$\frac{R_{app}}{R_i}$	ΔSB	n^{sers}_{app}
$\tau^f_B = 0.1$			
a_0	0.998	-0.044	1.001
a_1	0.005	0.836	-0.110
a_2	-0.065	-7.329	0.362
a_3	0.294	23.507	-1.198
a_4	-0.478	-30.968	1.583
a_5	0.285	14.771	-1.000
$\tau^f_B = 0.3$			
a_0	0.994	-0.102	1.000
a_1	0.022	2.777	-0.192
a_2	-0.185	-24.179	1.045
a_3	0.765	79.406	-3.402
a_4	-1.205	-107.268	4.523
a_5	0.723	51.710	-2.420
$\tau^f_B = 0.5$			
a_0	0.993	-0.108	0.991
a_1	0.038	3.564	-0.033
a_2	-0.284	-31.501	-0.197
a_3	1.153	103.483	0.219
a_4	-1.796	-138.234	-0.104
a_5	1.076	65.947	-0.299
$\tau^f_B = 1.0$			
a_0	0.991	-0.072	0.974
a_1	0.126	3.207	0.217
a_2	-1.006	-25.867	-2.983
a_3	3.742	85.774	10.048
a_4	-5.481	-115.619	-14.227
a_5	2.980	56.726	6.767
$\tau^f_B = 2.0$			
a_0	0.997	0.082	0.943
a_1	0.188	4.511	0.285
a_2	-1.357	-35.919	-4.521
a_3	5.193	121.950	16.264
a_4	-7.681	-164.960	-24.092
a_5	4.224	80.136	12.253
$\tau^f_B = 4.0$			
a_0	1.029	0.572	0.863
a_1	0.018	6.053	-0.058
a_2	0.893	-46.157	-0.692
a_3	-2.523	157.560	2.460
a_4	3.283	-213.748	-4.427
a_5	-1.132	102.909	2.974
$\tau^f_B = 8.0$			
a_0	1.103	1.514	0.762
a_1	0.206	6.497	0.022
a_2	0.087	-47.529	-0.630
a_3	-0.788	163.635	1.580
a_4	2.447	-228.405	-0.712
a_5	-1.548	113.085	-0.019
b_0	1.516	–	–

Table B.14: **Dust effects** $corr^{dust}$, as in Table B.11, but in J band.

Disk (Sérsic fits); J band	$\frac{R_{app}}{R_i}$	ΔSB	n^{sers}_{app}
$\tau^f_B = 0.1$			
a_0	0.990	-0.022	0.991
a_1	0.158	-0.132	0.143
a_2	-0.877	2.597	-1.399
a_3	2.098	-9.741	3.762
a_4	-2.243	13.065	-4.611
a_5	0.894	-5.539	1.840
$\tau^f_B = 0.3$			
a_0	0.989	-0.032	0.990
a_1	0.158	-0.149	0.018
a_2	-0.901	2.272	-0.361
a_3	2.280	-5.536	0.536
a_4	-2.572	3.323	-0.382
a_5	1.107	1.290	-0.155
$\tau^f_B = 0.5$			
a_0	0.989	-0.049	0.991
a_1	0.166	0.531	-0.049
a_2	-0.981	-3.416	0.150
a_3	2.622	12.386	-0.991
a_4	-3.094	-19.444	1.451
a_5	1.399	11.707	-0.931
$\tau^f_B = 1.0$			
a_0	0.996	-0.042	0.987
a_1	0.066	1.180	-0.046
a_2	-0.548	-9.131	-0.280
a_3	2.056	32.105	0.897
a_4	-2.975	-46.121	-1.467
a_5	1.599	24.969	0.546
$\tau^f_B = 2.0$			
a_0	0.986	-0.022	0.966
a_1	0.378	3.265	0.262
a_2	-2.632	-26.149	-3.543
a_3	8.165	87.412	12.589
a_4	-10.676	-118.301	-18.537
a_5	5.172	58.245	9.199
$\tau^f_B = 4.0$			
a_0	0.999	0.175	0.928
a_1	0.381	5.298	0.425
a_2	-2.277	-41.000	-4.877
a_3	6.996	133.928	16.352
a_4	-9.024	-176.144	-23.504
a_5	4.464	83.760	11.869
$\tau^f_B = 8.0$			
a_0	1.044	0.711	0.873
a_1	0.277	5.220	-0.141
a_2	-1.082	-36.255	0.056
a_3	3.213	121.875	0.205
a_4	-3.534	-164.571	-1.115
a_5	1.620	80.321	1.203
b_0	1.417	–	–

Table B.15: **Dust effects** $corr^{dust}$, as in Table B.11, but in K band.

Disk (Sérsic fits); K band

	$\frac{R_{app}}{R_i}$	ΔSB	n_{app}^{sers}
$\tau_B^f = 0.1$			
a_0	1.000	-0.004	1.000
a_1	-0.003	0.362	-0.018
a_2	0.016	-3.375	-0.756
a_3	-0.015	10.413	2.705
a_4	-0.012	-13.219	-4.034
a_5	0.019	6.028	1.867
$\tau_B^f = 0.3$			
a_0	1.000	-0.004	1.000
a_1	-0.005	0.336	-0.004
a_2	0.030	-2.616	-0.771
a_3	-0.019	7.521	2.427
a_4	-0.044	-9.168	-3.355
a_5	0.058	4.301	1.435
$\tau_B^f = 0.5$			
a_0	1.000	-0.013	0.998
a_1	-0.007	0.803	-0.065
a_2	0.044	-7.283	-0.100
a_3	-0.023	24.732	0.316
a_4	-0.076	-34.370	-0.758
a_5	0.097	16.966	0.322
$\tau_B^f = 1.0$			
a_0	1.001	-0.014	0.990
a_1	-0.007	1.452	0.051
a_2	0.044	-12.479	-0.999
a_3	0.072	40.648	2.865
a_4	-0.287	-55.139	-3.709
a_5	0.252	27.300	1.483
$\tau_B^f = 2.0$			
a_0	1.002	-0.002	0.990
a_1	0.016	1.973	-0.017
a_2	-0.151	-15.100	-0.740
a_3	0.865	47.400	2.539
a_4	-1.493	-62.524	-3.822
a_5	0.917	30.901	1.741
$\tau_B^f = 4.0$			
a_0	1.006	0.087	0.973
a_1	0.125	1.723	0.222
a_2	-1.087	-14.479	-3.569
a_3	4.214	53.737	13.137
a_4	-6.265	-78.279	-19.515
a_5	3.341	41.376	9.712
$\tau_B^f = 8.0$			
a_0	1.020	0.253	0.945
a_1	0.167	3.285	0.380
a_2	-1.142	-21.763	-4.948
a_3	4.410	71.740	17.391
a_4	-6.501	-97.370	-25.382
a_5	3.535	49.569	12.819
b_0	1.360	–	–

Table B.16: **Dust effects** $corr^{dust}$ on the derived photometric parameters of the **thin disk**: scale-lengths and central surface brightnesses. Results are listed as coefficients of polynomial fits a_k (Eq. 3.1.19) at different τ_B^f and at 912Å.

Thin Disk (exponential fits); 912Å

	$\frac{R_{app}}{R_i}$	ΔSB
$\tau_B^f = 0.1$		
a_0	1.025	0.238
a_1	0.612	-0.557
a_2	-5.679	5.783
a_3	20.339	-13.798
a_4	-29.505	12.592
a_5	15.288	-0.727
$\tau_B^f = 0.3$		
a_0	1.096	0.628
a_1	1.058	1.292
a_2	-9.435	-4.892
a_3	35.353	25.837
a_4	-53.075	-45.920
a_5	28.711	31.399
$\tau_B^f = 0.5$		
a_0	1.176	1.026
a_1	1.096	2.155
a_2	-9.227	-5.062
a_3	37.412	22.126
a_4	-59.843	-36.171
a_5	34.669	26.218
$\tau_B^f = 1.0$		
a_0	1.356	1.928
a_1	2.340	4.346
a_2	-19.238	-14.232
a_3	76.913	50.135
a_4	-123.527	-69.942
a_5	72.592	41.298
$\tau_B^f = 2.0$		
a_0	–	–
a_1	–	–
a_2	–	–
a_3	–	–
a_4	–	–
a_5	–	–
$\tau_B^f = 4.0$		
a_0	–	–
a_1	–	–
a_2	–	–
a_3	–	–
a_4	–	–
a_5	–	–
$\tau_B^f = 8.0$		
a_0	–	–
a_1	–	–
a_2	–	–
a_3	–	–
a_4	–	–
a_5	–	–

Table B.17: **Dust effects** $corr^{dust}$, as in Table B.16, but at 1350Å.

Thin Disk (exponential fits); 1350Å

	$\frac{R_{app}}{R_i}$	ΔSB
$\tau_B^f = 0.1$		
a_0	1.008	0.105
a_1	0.431	-1.436
a_2	-4.047	16.665
a_3	14.298	-55.731
a_4	-20.601	72.612
a_5	10.593	-30.452
$\tau_B^f = 0.3$		
a_0	1.043	0.297
a_1	0.791	-0.097
a_2	-7.440	6.649
a_3	27.333	-19.443
a_4	-40.348	20.507
a_5	21.340	-2.430
$\tau_B^f = 0.5$		
a_0	1.081	0.540
a_1	0.985	1.190
a_2	-8.997	-5.326
a_3	33.861	25.912
a_4	-50.891	-44.371
a_5	27.550	30.185
$\tau_B^f = 1.0$		
a_0	1.169	1.066
a_1	2.141	2.646
a_2	-19.501	-11.187
a_3	73.491	46.183
a_4	-111.042	-70.482
a_5	60.172	43.042
$\tau_B^f = 2.0$		
a_0	1.401	2.035
a_1	0.867	3.980
a_2	-1.995	-8.583
a_3	12.122	30.125
a_4	-25.331	-39.597
a_5	21.825	25.467
$\tau_B^f = 4.0$		
a_0	–	–
a_1	–	–
a_2	–	–
a_3	–	–
a_4	–	–
a_5	–	–
$\tau_B^f = 8.0$		
a_0	–	–
a_1	–	–
a_2	–	–
a_3	–	–
a_4	–	–
a_5	–	–

Table B.18: **Dust effects** $corr^{dust}$, as in Table B.16, but at 1500Å.

Thin Disk (exponential fits); 1500Å

	$\frac{R_{app}}{R_i}$	ΔSB
$\tau_B^f = 0.1$		
a_0	1.004	0.084
a_1	0.420	-1.226
a_2	-3.944	13.980
a_3	13.839	-46.445
a_4	-19.831	60.230
a_5	10.147	-24.922
$\tau_B^f = 0.3$		
a_0	1.033	0.237
a_1	0.753	-0.277
a_2	-7.137	6.660
a_3	26.201	-16.706
a_4	-38.639	14.387
a_5	20.393	0.912
$\tau_B^f = 0.5$		
a_0	1.066	0.432
a_1	0.920	1.220
a_2	-8.538	-5.787
a_3	32.204	26.737
a_4	-48.409	-44.493
a_5	26.155	29.551
$\tau_B^f = 1.0$		
a_0	1.159	0.933
a_1	0.986	0.839
a_2	-8.441	4.623
a_3	35.277	-5.468
a_4	-57.262	-2.005
a_5	33.608	11.352
$\tau_B^f = 2.0$		
a_0	1.357	1.789
a_1	0.780	4.164
a_2	-1.599	-11.377
a_3	10.129	41.498
a_4	-20.688	-57.003
a_5	17.851	34.224
$\tau_B^f = 4.0$		
a_0	–	–
a_1	–	–
a_2	–	–
a_3	–	–
a_4	–	–
a_5	–	–
$\tau_B^f = 8.0$		
a_0	–	–
a_1	–	–
a_2	–	–
a_3	–	–
a_4	–	–
a_5	–	–

Table B.19: **Dust effects** $corr^{dust}$, as in Table B.16, but at 1650Å.

Thin Disk (exponential fits); 1650Å

	$\frac{R_{app}}{R_i}$	ΔSB
$\tau_B^f = 0.1$		
a_0	1.001	0.064
a_1	0.406	-1.523
a_2	-3.797	15.694
a_3	13.237	-50.444
a_4	-18.896	64.151
a_5	9.640	-26.392
$\tau_B^f = 0.3$		
a_0	1.024	0.200
a_1	0.710	-0.296
a_2	-6.804	5.411
a_3	24.945	-13.128
a_4	-36.769	11.177
a_5	19.385	1.437
$\tau_B^f = 0.5$		
a_0	1.053	0.321
a_1	0.857	0.896
a_2	-8.095	-1.783
a_3	30.557	10.602
a_4	-45.916	-20.849
a_5	24.761	17.916
$\tau_B^f = 1.0$		
a_0	1.132	0.774
a_1	0.987	1.492
a_2	-8.724	-3.603
a_3	35.796	22.766
a_4	-57.094	-40.579
a_5	32.859	29.342
$\tau_B^f = 2.0$		
a_0	1.316	1.570
a_1	0.707	4.048
a_2	-0.006	-8.385
a_3	3.119	29.322
a_4	-9.095	-39.432
a_5	10.836	25.428
$\tau_B^f = 4.0$		
a_0	–	–
a_1	–	–
a_2	–	–
a_3	–	–
a_4	–	–
a_5	–	–
$\tau_B^f = 8.0$		
a_0	–	–
a_1	–	–
a_2	–	–
a_3	–	–
a_4	–	–
a_5	–	–

Table B.20: **Dust effects** *corr*^{dust}, as in Table B.16, but at 2000Å.

Thin Disk (exponential fits); 2000Å

	$\frac{R_{app}}{R_i}$	ΔSB
$\tau_B^f = 0.1$		
a_0	0.999	0.040
a_1	0.441	-1.159
a_2	-4.126	13.118
a_3	14.467	-43.311
a_4	-20.727	56.216
a_5	10.616	-23.116
$\tau_B^f = 0.3$		
a_0	1.023	0.230
a_1	0.764	-1.520
a_2	-7.235	14.229
a_3	26.621	-35.838
a_4	-39.324	35.887
a_5	20.812	-7.620
$\tau_B^f = 0.5$		
a_0	1.055	0.325
a_1	0.914	1.547
a_2	-8.474	-7.152
a_3	32.139	28.827
a_4	-48.450	-44.874
a_5	26.273	29.142
$\tau_B^f = 1.0$		
a_0	1.151	0.820
a_1	0.848	0.964
a_2	-6.903	6.136
a_3	30.565	-12.717
a_4	-51.311	11.037
a_5	31.110	3.928
$\tau_B^f = 2.0$		
a_0	1.388	1.828
a_1	1.070	4.501
a_2	-2.240	-9.516
a_3	11.543	31.803
a_4	-22.974	-42.024
a_5	19.749	26.735
$\tau_B^f = 4.0$		
a_0	–	–
a_1	–	–
a_2	–	–
a_3	–	–
a_4	–	–
a_5	–	–
$\tau_B^f = 8.0$		
a_0	–	–
a_1	–	–
a_2	–	–
a_3	–	–
a_4	–	–
a_5	–	–

Table B.21: **Dust effects** *corr*^{dust}, as in Table B.16, but at 2200Å.

Thin Disk (exponential fits); 2200Å

	$\frac{R_{app}}{R_i}$	ΔSB
$\tau_B^f = 0.1$		
a_0	1.000	0.058
a_1	0.480	-1.337
a_2	-4.478	14.927
a_3	15.732	-48.808
a_4	-22.541	62.773
a_5	11.546	-25.547
$\tau_B^f = 0.3$		
a_0	1.029	0.212
a_1	0.822	-0.640
a_2	-7.653	10.231
a_3	28.202	-26.585
a_4	-41.722	26.286
a_5	22.143	-3.584
$\tau_B^f = 0.5$		
a_0	1.067	0.416
a_1	0.971	0.855
a_2	-8.789	-2.116
a_3	33.499	17.848
a_4	-50.765	-35.186
a_5	27.721	26.628
$\tau_B^f = 1.0$		
a_0	1.183	0.952
a_1	0.662	1.392
a_2	-4.824	4.614
a_3	24.674	-8.654
a_4	-45.213	6.739
a_5	29.510	5.524
$\tau_B^f = 2.0$		
a_0	1.434	2.018
a_1	1.322	5.194
a_2	-3.768	-11.877
a_3	17.879	36.876
a_4	-34.457	-46.861
a_5	27.841	28.553
$\tau_B^f = 4.0$		
a_0	–	–
a_1	–	–
a_2	–	–
a_3	–	–
a_4	–	–
a_5	–	–
$\tau_B^f = 8.0$		
a_0	–	–
a_1	–	–
a_2	–	–
a_3	–	–
a_4	–	–
a_5	–	–

Table B.22: **Dust effects** *corr*^{dust}, as in Table B.16, but at 2500Å.

Thin Disk (exponential fits); 2500Å		
	$\frac{R_{app}}{R_i}$	ΔSB
$\tau^f_B = 0.1$		
a_0	0.992	0.008
a_1	0.401	-2.140
a_2	-3.752	21.033
a_3	13.031	-67.001
a_4	-18.536	84.758
a_5	9.433	-35.062
$\tau^f_B = 0.3$		
a_0	1.002	0.034
a_1	0.707	0.755
a_2	-6.727	-4.914
a_3	24.468	20.312
a_4	-35.873	-32.638
a_5	18.842	21.546
$\tau^f_B = 0.5$		
a_0	1.022	0.155
a_1	0.835	0.015
a_2	-7.878	2.954
a_3	29.564	-1.692
a_4	-44.193	-5.974
a_5	23.724	11.273
$\tau^f_B = 1.0$		
a_0	1.093	0.454
a_1	0.940	2.038
a_2	-7.505	-5.296
a_3	31.341	26.848
a_4	-50.467	-44.363
a_5	29.269	30.151
$\tau^f_B = 2.0$		
a_0	1.320	1.481
a_1	2.043	3.998
a_2	-14.879	-11.417
a_3	59.082	45.016
a_4	-94.459	-67.070
a_5	55.804	41.290
$\tau^f_B = 4.0$		
a_0	–	–
a_1	–	–
a_2	–	–
a_3	–	–
a_4	–	–
a_5	–	–
$\tau^f_B = 8.0$		
a_0	–	–
a_1	–	–
a_2	–	–
a_3	–	–
a_4	–	–
a_5	–	–

Table B.23: **Dust effects** *corr*^{dust}, as in Table B.16, but at 2800Å.

Thin Disk (exponential fits); 2800Å		
	$\frac{R_{app}}{R_i}$	ΔSB
$\tau^f_B = 0.1$		
a_0	0.988	-0.029
a_1	0.468	-1.246
a_2	-4.414	14.170
a_3	15.151	-48.559
a_4	-21.310	64.367
a_5	10.664	-27.452
$\tau^f_B = 0.3$		
a_0	0.994	-0.012
a_1	0.647	0.137
a_2	-6.224	0.884
a_3	22.485	0.041
a_4	-32.824	-5.379
a_5	17.154	8.639
$\tau^f_B = 0.5$		
a_0	1.007	0.076
a_1	0.759	-0.846
a_2	-7.325	10.043
a_3	27.334	-25.567
a_4	-40.679	25.306
a_5	21.704	-3.076
$\tau^f_B = 1.0$		
a_0	1.059	0.306
a_1	0.934	0.357
a_2	-7.758	7.293
a_3	31.384	-14.306
a_4	-49.226	10.369
a_5	27.730	4.661
$\tau^f_B = 2.0$		
a_0	1.262	1.153
a_1	1.438	3.819
a_2	-9.505	-12.382
a_3	38.355	48.800
a_4	-61.693	-73.241
a_5	37.055	44.461
$\tau^f_B = 4.0$		
a_0	–	–
a_1	–	–
a_2	–	–
a_3	–	–
a_4	–	–
a_5	–	–
$\tau^f_B = 8.0$		
a_0	–	–
a_1	–	–
a_2	–	–
a_3	–	–
a_4	–	–
a_5	–	–

Table B.24: **Dust effects** $corr^{dust}$, as in Table B.16, but at 3600Å.

Thin Disk (exponential fits); 3600Å

	$\frac{R_{app}}{R_i}$	ΔSB
$\tau_B^f = 0.1$		
a_0	1.014	0.175
a_1	0.272	-2.847
a_2	-2.475	27.088
a_3	8.762	-84.574
a_4	-12.570	106.574
a_5	6.415	-45.439
$\tau_B^f = 0.3$		
a_0	1.044	0.324
a_1	0.661	0.059
a_2	-5.910	4.178
a_3	21.100	-10.477
a_4	-30.519	8.858
a_5	15.773	0.805
$\tau_B^f = 0.5$		
a_0	1.075	0.569
a_1	0.918	-0.624
a_2	-8.058	10.348
a_3	29.073	-26.076
a_4	-42.463	25.554
a_5	22.254	-4.167
$\tau_B^f = 1.0$		
a_0	1.157	1.018
a_1	1.282	1.022
a_2	-10.829	1.968
a_3	40.590	0.493
a_4	-61.384	-8.681
a_5	33.574	12.854
$\tau_B^f = 2.0$		
a_0	1.321	1.837
a_1	1.640	3.299
a_2	-12.336	-10.668
a_3	48.887	42.317
a_4	-78.133	-63.644
a_5	46.195	39.124
$\tau_B^f = 4.0$		
a_0	–	–
a_1	–	–
a_2	–	–
a_3	–	–
a_4	–	–
a_5	–	–
$\tau_B^f = 8.0$		
a_0	–	–
a_1	–	–
a_2	–	–
a_3	–	–
a_4	–	–
a_5	–	–

Table B.25: **Dust effects** $corr^{dust}$, as in Table B.16, but in B band.

Thin Disk (exponential fits); B band

	$\frac{R_{app}}{R_i}$	ΔSB
$\tau_B^f = 0.1$		
a_0	0.989	-0.084
a_1	0.304	1.115
a_2	-2.820	-7.785
a_3	9.527	22.418
a_4	-13.308	-29.037
a_5	6.645	14.784
$\tau_B^f = 0.3$		
a_0	0.981	-0.072
a_1	0.705	-0.250
a_2	-6.821	4.195
a_3	23.819	-14.539
a_4	-33.896	17.742
a_5	17.152	-4.332
$\tau_B^f = 0.5$		
a_0	0.980	-0.107
a_1	1.030	1.152
a_2	-10.144	-9.028
a_3	35.941	33.109
a_4	-51.487	-49.928
a_5	26.155	29.625
$\tau_B^f = 1.0$		
a_0	1.008	-0.017
a_1	0.451	0.973
a_2	-4.428	-5.939
a_3	18.618	29.424
a_4	-29.290	-48.859
a_5	16.546	31.756
$\tau_B^f = 2.0$		
a_0	1.125	0.459
a_1	0.662	3.284
a_2	-3.270	-14.923
a_3	14.334	56.927
a_4	-23.998	-83.837
a_5	15.305	48.504
$\tau_B^f = 4.0$		
a_0	–	–
a_1	–	–
a_2	–	–
a_3	–	–
a_4	–	–
a_5	–	–
$\tau_B^f = 8.0$		
a_0	–	–
a_1	–	–
a_2	–	–
a_3	–	–
a_4	–	–
a_5	–	–

Table B.26: **Dust effects** *corr*^{dust}, as in Table B.16, but in V band.

Thin Disk (exponential fits); V band

	$\frac{R_{app}}{R_i}$	ΔSB
$\tau_B^f = 0.1$		
a_0	0.990	-0.090
a_1	0.227	2.042
a_2	-2.121	-18.066
a_3	7.176	59.015
a_4	-10.017	-80.836
a_5	4.996	39.924
$\tau_B^f = 0.3$		
a_0	0.980	-0.082
a_1	0.562	-0.652
a_2	-5.369	7.347
a_3	18.583	-25.571
a_4	-26.304	34.385
a_5	13.259	-13.553
$\tau_B^f = 0.5$		
a_0	0.976	-0.114
a_1	0.825	0.330
a_2	-8.006	-2.191
a_3	28.105	9.075
a_4	-40.081	-15.884
a_5	20.309	12.349
$\tau_B^f = 1.0$		
a_0	0.991	-0.222
a_1	0.324	7.145
a_2	-3.202	-67.282
a_3	13.186	235.223
a_4	-20.885	-331.860
a_5	12.005	166.771
$\tau_B^f = 2.0$		
a_0	1.043	0.101
a_1	1.040	2.673
a_2	-7.848	-11.694
a_3	30.160	45.596
a_4	-46.295	-69.664
a_5	25.748	42.168
$\tau_B^f = 4.0$		
a_0	–	–
a_1	–	–
a_2	–	–
a_3	–	–
a_4	–	–
a_5	–	–
$\tau_B^f = 8.0$		
a_0	–	–
a_1	–	–
a_2	–	–
a_3	–	–
a_4	–	–
a_5	–	–

Table B.27: **Dust effects** *corr*^{dust}, as in Table B.16, but in I band.

Thin Disk (exponential fits); I band

	$\frac{R_{app}}{R_i}$	ΔSB
$\tau_B^f = 0.1$		
a_0	0.994	-0.040
a_1	0.105	0.842
a_2	-1.084	-8.802
a_3	3.863	31.279
a_4	-5.539	-44.841
a_5	2.813	22.743
$\tau_B^f = 0.3$		
a_0	0.985	-0.018
a_1	0.316	-2.304
a_2	-3.140	19.246
a_3	11.102	-58.373
a_4	-15.875	72.471
a_5	8.052	-29.911
$\tau_B^f = 0.5$		
a_0	0.978	-0.070
a_1	0.520	-2.038
a_2	-5.059	19.207
a_3	17.823	-61.176
a_4	-25.443	78.691
a_5	12.894	-32.947
$\tau_B^f = 1.0$		
a_0	0.980	-0.153
a_1	0.286	0.133
a_2	-2.574	0.107
a_3	9.890	4.659
a_4	-15.242	-12.537
a_5	8.603	11.954
$\tau_B^f = 2.0$		
a_0	0.988	-0.149
a_1	0.535	1.272
a_2	-4.533	-7.869
a_3	17.616	35.119
a_4	-27.148	-57.414
a_5	15.239	36.215
$\tau_B^f = 4.0$		
a_0	–	–
a_1	–	–
a_2	–	–
a_3	–	–
a_4	–	–
a_5	–	–
$\tau_B^f = 8.0$		
a_0	–	–
a_1	–	–
a_2	–	–
a_3	–	–
a_4	–	–
a_5	–	–

Table B.28: **Dust effects** $corr^{dust}$, as in Table B.16, but in J band.

Thin Disk (exponential fits); J band	$\frac{R_{app}}{R_i}$	ΔSB
$\tau_B^f = 0.1$		
a_0	0.997	-0.026
a_1	0.037	0.277
a_2	-0.426	-3.052
a_3	1.630	12.543
a_4	-2.433	-19.996
a_5	1.271	10.933
$\tau_B^f = 0.3$		
a_0	0.993	-0.047
a_1	0.123	0.648
a_2	-1.333	-7.516
a_3	4.990	29.645
a_4	-7.367	-45.783
a_5	3.820	24.810
$\tau_B^f = 0.5$		
a_0	0.989	-0.028
a_1	0.219	-1.683
a_2	-2.287	14.309
a_3	8.444	-41.563
a_4	-12.367	49.316
a_5	6.376	-19.190
$\tau_B^f = 1.0$		
a_0	0.982	-0.066
a_1	0.481	-2.369
a_2	-4.764	22.219
a_3	17.193	-66.935
a_4	-24.848	82.261
a_5	12.685	-33.320
$\tau_B^f = 2.0$		
a_0	0.986	-0.098
a_1	0.296	-0.140
a_2	-2.644	1.152
a_3	10.382	5.930
a_4	-16.056	-17.966
a_5	9.019	15.560
$\tau_B^f = 4.0$		
a_0	0.998	-0.055
a_1	0.684	0.605
a_2	-5.693	-0.623
a_3	21.244	12.540
a_4	-31.888	-28.081
a_5	17.468	22.590
$\tau_B^f = 8.0$		
a_0	–	–
a_1	–	–
a_2	–	–
a_3	–	–
a_4	–	–
a_5	–	–

Table B.29: **Dust effects** $corr^{dust}$, as in Table B.16, but in K band.

Thin Disk (exponential fits); K band	$\frac{R_{app}}{R_i}$	ΔSB
$\tau_B^f = 0.1$		
a_0	0.999	-0.014
a_1	0.030	0.017
a_2	-0.254	0.771
a_3	0.854	-3.193
a_4	-1.188	4.237
a_5	0.591	-1.691
$\tau_B^f = 0.3$		
a_0	0.996	-0.040
a_1	0.085	0.998
a_2	-0.738	-8.630
a_3	2.502	28.676
a_4	-3.495	-39.329
a_5	1.743	19.170
$\tau_B^f = 0.5$		
a_0	0.994	-0.064
a_1	0.136	1.304
a_2	-1.193	-10.857
a_3	4.077	36.415
a_4	-5.720	-50.806
a_5	2.860	25.267
$\tau_B^f = 1.0$		
a_0	0.991	-0.092
a_1	0.246	1.400
a_2	-2.226	-10.228
a_3	7.742	34.169
a_4	-10.967	-48.803
a_5	5.520	25.370
$\tau_B^f = 2.0$		
a_0	0.989	-0.051
a_1	0.434	-2.004
a_2	-4.094	22.106
a_3	14.516	-70.488
a_4	-20.775	89.315
a_5	10.527	-37.422
$\tau_B^f = 4.0$		
a_0	0.991	-0.049
a_1	0.809	0.100
a_2	-7.737	3.641
a_3	27.605	-9.946
a_4	-39.618	9.338
a_5	20.102	0.334
$\tau_B^f = 8.0$		
a_0	1.019	0.046
a_1	0.439	1.840
a_2	-3.783	-13.813
a_3	15.089	58.069
a_4	-23.572	-91.974
a_5	13.345	52.943

Table B.30: **Dust effects** *corr*^{dust}, as in Table B.16, but for the $H\alpha$ line.

Thin Disk (exponential fits); $H\alpha$

	$\frac{R_{app}}{R_i}$	ΔSB
$\tau_B^f = 0.1$		
a_0	0.992	-0.072
a_1	0.181	1.590
a_2	-1.731	-14.576
a_3	5.928	48.566
a_4	-8.330	-67.275
a_5	4.174	33.452
$\tau_B^f = 0.3$		
a_0	0.982	-0.058
a_1	0.469	-1.275
a_2	-4.529	11.830
a_3	15.765	-37.929
a_4	-22.375	48.733
a_5	11.297	-19.716
$\tau_B^f = 0.5$		
a_0	0.977	-0.098
a_1	0.710	-0.562
a_2	-6.896	5.870
a_3	24.232	-17.391
a_4	-34.567	19.746
a_5	17.516	-4.715
$\tau_B^f = 1.0$		
a_0	0.987	-0.196
a_1	0.310	4.503
a_2	-2.966	-41.894
a_3	11.944	148.362
a_4	-18.759	-211.560
a_5	10.724	108.446
$\tau_B^f = 2.0$		
a_0	1.022	0.015
a_1	0.850	1.605
a_2	-6.599	-4.982
a_3	25.435	23.761
a_4	-39.081	-40.432
a_5	21.789	28.152
$\tau_B^f = 4.0$		
a_0	–	–
a_1	–	–
a_2	–	–
a_3	–	–
a_4	–	–
a_5	–	–
$\tau_B^f = 8.0$		
a_0	–	–
a_1	–	–
a_2	–	–
a_3	–	–
a_4	–	–
a_5	–	–

Table B.31: **Dust effects** $corr^{dust}$ on the derived photometric parameters of the **thin disk**: effective radius, central surface brightnesses and Sérsic index. Results are listed as coefficients of polynomial fits a_k (Eq. 3.1.19) at different τ_B^f and at 912Å.

Thin Disk (Sérsic fits); 912Å

	$\frac{R_{app}}{R_i}$	ΔSB	n_{app}^{sers}
$\tau_B^f = 0.1$			
a_0	1.009	0.277	0.964
a_1	0.378	-0.892	-0.254
a_2	-3.454	12.056	2.360
a_3	12.052	-33.435	-8.939
a_4	-17.179	34.303	13.209
a_5	8.743	-7.513	-7.054
$\tau_B^f = 0.3$			
a_0	1.042	0.801	0.892
a_1	0.481	0.757	-0.114
a_2	-4.122	5.509	-0.056
a_3	14.788	-14.876	-0.904
a_4	-21.350	17.520	1.820
a_5	11.141	-1.621	-1.525
$\tau_B^f = 0.5$			
a_0	1.078	1.370	0.826
a_1	0.481	0.697	-0.172
a_2	-4.122	10.704	-0.671
a_3	14.788	-27.731	2.002
a_4	-21.350	32.454	-3.182
a_5	11.141	-7.546	1.330
$\tau_B^f = 1.0$			
a_0	1.152	2.473	0.696
a_1	0.170	4.699	-0.610
a_2	0.596	-13.554	1.828
a_3	-1.009	50.192	-5.388
a_4	0.409	-71.104	6.447
a_5	0.798	40.843	-3.069
$\tau_B^f = 2.0$			
a_0	1.279	4.156	0.516
a_1	0.226	5.857	-0.857
a_2	1.218	-11.610	4.080
a_3	-4.399	35.626	-13.232
a_4	7.392	-46.473	18.242
a_5	-3.819	27.968	-9.272
$\tau_B^f = 4.0$			
a_0	–	–	–
a_1	–	–	–
a_2	–	–	–
a_3	–	–	–
a_4	–	–	–
a_5	–	–	–
$\tau_B^f = 8.0$			
a_0	–	–	–
a_1	–	–	–
a_2	–	–	–
a_3	–	–	–
a_4	–	–	–
a_5	–	–	–

Table B.32: **Dust effects** $corr^{dust}$, as in Table B.31, but at 1350Å.

Thin Disk (Sérsic fits); 1350Å

	$\frac{R_{app}}{R_i}$	ΔSB	n_{app}^{sers}
$\tau_B^f = 0.1$			
a_0	1.001	0.047	0.985
a_1	0.278	4.131	-0.301
a_2	-2.535	-38.595	3.022
a_3	8.708	134.298	-11.223
a_4	-12.362	-190.641	16.596
a_5	6.280	96.236	-8.710
$\tau_B^f = 0.3$			
a_0	1.018	0.422	0.945
a_1	0.298	-0.570	-0.322
a_2	-2.694	11.027	2.854
a_3	9.852	-31.606	-10.893
a_4	-14.577	35.591	15.755
a_5	7.807	-8.433	-8.230
$\tau_B^f = 0.5$			
a_0	1.037	0.679	0.912
a_1	0.251	0.640	-0.268
a_2	-2.051	4.335	1.413
a_3	7.875	-8.661	-5.879
a_4	-11.947	6.903	8.670
a_5	6.697	4.273	-4.800
$\tau_B^f = 1.0$			
a_0	1.081	1.398	0.821
a_1	0.246	1.126	-0.478
a_2	-1.451	9.271	2.014
a_3	5.914	-24.267	-7.227
a_4	-8.833	29.458	9.663
a_5	5.080	-6.507	-4.837
$\tau_B^f = 2.0$			
a_0	1.155	2.580	0.666
a_1	0.265	5.532	-0.586
a_2	0.231	-17.902	1.417
a_3	-0.679	63.611	-4.186
a_4	0.930	-88.919	5.082
a_5	0.216	49.377	-2.495
$\tau_B^f = 4.0$			
a_0	–	–	–
a_1	–	–	–
a_2	–	–	–
a_3	–	–	–
a_4	–	–	–
a_5	–	–	–
$\tau_B^f = 8.0$			
a_0	–	–	–
a_1	–	–	–
a_2	–	–	–
a_3	–	–	–
a_4	–	–	–
a_5	–	–	–

Table B.33: **Dust effects** *corr*^{dust}, as in Table B.31, but at 1500Å.

Thin Disk (Sérsic fits); 1500Å

	$\frac{R_{app}}{R_i}$	ΔSB	n^{sers}_{app}
$\tau^f_B = 0.1$			
a_0	1.001	0.064	0.984
a_1	0.150	1.670	-0.020
a_2	-1.264	-15.136	0.530
a_3	4.302	53.938	-3.148
a_4	-6.186	-78.692	5.618
a_5	3.272	41.979	-3.410
$\tau^f_B = 0.3$			
a_0	1.014	0.330	0.951
a_1	0.235	0.102	-0.010
a_2	-2.108	3.307	-0.190
a_3	7.840	-4.150	-0.883
a_4	-11.809	-3.059	2.577
a_5	6.480	9.980	-2.190
$\tau^f_B = 0.5$			
a_0	1.031	0.606	0.920
a_1	0.135	0.366	-0.159
a_2	-0.996	2.250	0.414
a_3	4.334	2.558	-2.265
a_4	-7.134	-11.701	3.493
a_5	4.407	14.170	-2.252
$\tau^f_B = 1.0$			
a_0	1.068	1.192	0.839
a_1	0.246	2.551	-0.372
a_2	-1.622	-6.502	0.918
a_3	6.604	29.512	-3.316
a_4	-9.941	-44.610	4.157
a_5	5.678	28.864	-2.181
$\tau^f_B = 2.0$			
a_0	1.137	2.325	0.687
a_1	0.123	5.650	-0.646
a_2	0.968	-19.041	1.967
a_3	-2.156	66.528	-6.326
a_4	2.028	-91.481	8.224
a_5	0.025	49.887	-4.020
$\tau^f_B = 4.0$			
a_0	1.257	4.058	0.491
a_1	0.443	8.584	-1.088
a_2	-0.154	-25.036	4.581
a_3	-0.139	67.987	-13.238
a_4	1.643	-83.571	17.536
a_5	-1.045	44.101	-8.748
$\tau^f_B = 8.0$			
a_0	–	–	–
a_1	–	–	–
a_2	–	–	–
a_3	–	–	–
a_4	–	–	–
a_5	–	–	–

Table B.34: **Dust effects** *corr*^{dust}, as in Table B.31, but at 1650Å.

Thin Disk (Sérsic fits); 1650Å

	$\frac{R_{app}}{R_i}$	ΔSB	n^{sers}_{app}
$\tau^f_B = 0.1$			
a_0	0.997	-0.006	0.997
a_1	0.236	3.877	-0.413
a_2	-2.098	-36.566	3.877
a_3	7.065	126.647	-13.712
a_4	-9.922	-179.338	19.641
a_5	5.027	90.341	-9.991
$\tau^f_B = 0.3$			
a_0	1.070	0.225	0.965
a_1	-0.802	0.333	-0.281
a_2	3.306	3.406	2.399
a_3	-4.236	-8.225	-9.338
a_4	0.181	4.178	13.927
a_5	2.107	6.227	-7.523
$\tau^f_B = 0.5$			
a_0	1.022	0.494	0.935
a_1	0.208	-0.234	-0.312
a_2	-1.822	9.213	2.023
a_3	7.190	-24.280	-7.916
a_4	-11.164	26.811	11.635
a_5	6.371	-4.537	-6.313
$\tau^f_B = 1.0$			
a_0	1.056	1.009	0.859
a_1	0.176	1.903	-0.403
a_2	-1.126	-3.370	1.545
a_3	4.973	22.405	-5.646
a_4	-7.808	-37.435	7.272
a_5	4.719	26.134	-3.581
$\tau^f_B = 2.0$			
a_0	1.113	2.096	0.710
a_1	0.137	5.286	-0.901
a_2	0.580	-12.481	2.473
a_3	-0.670	42.841	-6.338
a_4	-0.114	-60.495	7.596
a_5	1.085	36.223	-3.616
$\tau^f_B = 4.0$			
a_0	1.232	3.980	0.470
a_1	0.500	7.302	-0.876
a_2	-0.576	-21.113	3.245
a_3	1.231	63.224	-8.606
a_4	-0.437	-81.930	10.542
a_5	0.109	44.278	-5.049
$\tau^f_B = 8.0$			
a_0	–	–	–
a_1	–	–	–
a_2	–	–	–
a_3	–	–	–
a_4	–	–	–
a_5	–	–	–

Table B.35: **Dust effects** *corr^{dust}*, as in Table B.31, but at 2000Å.

Thin Disk (Sérsic fits); 2000Å

	$\frac{R_{app}}{R_i}$	ΔSB	n^{sers}_{app}
$\tau^f_B = 0.1$			
a_0	0.995	-0.008	0.997
a_1	0.285	3.753	-0.410
a_2	-2.580	-36.012	3.842
a_3	8.764	126.654	-13.620
a_4	-12.333	-180.907	19.483
a_5	6.230	91.874	-9.927
$\tau^f_B = 0.3$			
a_0	1.006	0.259	0.957
a_1	0.281	-0.401	-0.215
a_2	-2.520	9.726	1.933
a_3	9.237	-28.059	-8.078
a_4	-13.718	31.554	12.321
a_5	7.409	-6.765	-6.793
$\tau^f_B = 0.5$			
a_0	1.021	0.508	0.925
a_1	0.223	-0.019	-0.307
a_2	-1.830	7.585	2.088
a_3	7.189	-17.210	-8.384
a_4	-11.065	17.346	12.172
a_5	6.310	-0.188	-6.455
$\tau^f_B = 1.0$			
a_0	1.056	1.105	0.833
a_1	0.226	2.397	-0.417
a_2	-1.574	-3.441	1.099
a_3	6.782	21.158	-4.412
a_4	-10.387	-34.370	6.120
a_5	5.960	24.215	-3.195
$\tau^f_B = 2.0$			
a_0	1.115	2.436	0.629
a_1	0.676	6.757	-0.913
a_2	-3.137	-22.838	3.196
a_3	9.494	74.196	-8.392
a_4	-11.733	-100.796	9.906
a_5	5.777	54.414	-4.523
$\tau^f_B = 4.0$			
a_0	1.264	4.394	0.408
a_1	0.685	8.024	-0.803
a_2	-1.485	-27.229	3.987
a_3	3.175	83.257	-12.626
a_4	-2.169	-110.649	17.083
a_5	0.553	59.201	-8.446
$\tau^f_B = 8.0$			
a_0	–	–	–
a_1	–	–	–
a_2	–	–	–
a_3	–	–	–
a_4	–	–	–
a_5	–	–	–

Table B.36: **Dust effects** *corr^{dust}*, as in Table B.31, but at 2200Å.

Thin Disk (Sérsic fits); 2200Å

	$\frac{R_{app}}{R_i}$	ΔSB	n^{sers}_{app}
$\tau^f_B = 0.1$			
a_0	0.998	0.017	0.992
a_1	0.159	2.313	-0.112
a_2	-1.362	-21.335	0.776
a_3	4.696	77.046	-3.370
a_4	-6.775	-113.025	5.657
a_5	3.598	59.827	-3.446
$\tau^f_B = 0.3$			
a_0	1.009	0.301	0.942
a_1	0.188	0.322	0.144
a_2	-1.518	3.148	-1.499
a_3	5.785	-5.788	2.913
a_4	-8.854	2.372	-2.154
a_5	5.048	6.545	-0.099
$\tau^f_B = 0.5$			
a_0	1.027	0.587	0.909
a_1	0.132	1.147	-0.079
a_2	-0.783	-2.277	-0.330
a_3	3.561	16.310	-0.281
a_4	-5.948	-27.720	1.111
a_5	3.834	20.843	-1.194
$\tau^f_B = 1.0$			
a_0	1.066	1.268	0.811
a_1	0.271	3.389	-0.515
a_2	-1.760	-8.475	1.453
a_3	7.419	33.987	-4.639
a_4	-11.231	-48.892	5.726
a_5	6.344	30.469	-2.827
$\tau^f_B = 2.0$			
a_0	1.145	2.685	0.608
a_1	0.515	6.391	-0.854
a_2	-2.193	-16.420	2.707
a_3	7.357	50.803	-7.327
a_4	-9.451	-67.610	9.260
a_5	4.824	38.181	-4.563
$\tau^f_B = 4.0$			
a_0	1.290	4.693	0.387
a_1	0.745	8.583	-0.677
a_2	-1.610	-30.858	2.635
a_3	2.957	94.014	-7.925
a_4	-1.201	-124.039	10.701
a_5	-0.234	65.111	-5.477
$\tau^f_B = 8.0$			
a_0	–	–	–
a_1	–	–	–
a_2	–	–	–
a_3	–	–	–
a_4	–	–	–
a_5	–	–	–

Table B.37: **Dust effects** $corr^{dust}$, as in Table B.31, but at 2500Å.

Thin Disk (Sérsic fits); 2500Å

	$\frac{R_{app}}{R_i}$	ΔSB	n_{app}^{sers}
$\tau_B^f = 0.1$			
a_0	0.992	-0.079	0.999
a_1	0.222	3.395	-0.327
a_2	-1.995	-31.101	3.478
a_3	6.721	106.880	-12.913
a_4	-9.424	-151.494	18.877
a_5	4.775	77.064	-9.703
$\tau_B^f = 0.3$			
a_0	0.992	0.081	0.978
a_1	0.327	-0.570	-0.273
a_2	-2.831	8.717	2.463
a_3	9.881	-22.103	-9.851
a_4	-14.245	20.363	14.957
a_5	7.503	-0.546	-8.126
$\tau_B^f = 0.5$			
a_0	1.002	0.232	0.947
a_1	0.228	-0.165	-0.201
a_2	-1.946	8.304	1.548
a_3	7.420	-20.400	-7.064
a_4	-11.291	20.523	11.029
a_5	6.369	-1.054	-6.189
$\tau_B^f = 1.0$			
a_0	1.023	0.730	0.860
a_1	0.205	2.444	-0.335
a_2	-1.753	-4.652	-0.369
a_3	7.414	27.175	0.216
a_4	-11.188	-45.251	0.603
a_5	6.295	29.955	-0.870
$\tau_B^f = 2.0$			
a_0	1.079	2.133	0.628
a_1	0.621	4.914	-0.716
a_2	-2.478	-12.420	2.464
a_3	7.091	43.462	-6.766
a_4	-8.641	-61.328	8.030
a_5	4.444	36.551	-3.686
$\tau_B^f = 4.0$			
a_0	1.234	3.875	0.446
a_1	0.513	7.161	-0.629
a_2	-0.871	-23.633	2.581
a_3	2.335	75.669	-8.643
a_4	-2.201	-101.550	12.146
a_5	1.080	54.322	-6.208
$\tau_B^f = 8.0$			
a_0	–	–	–
a_1	–	–	–
a_2	–	–	–
a_3	–	–	–
a_4	–	–	–
a_5	–	–	–

Table B.38: **Dust effects** $corr^{dust}$, as in Table B.31, but at 2800Å.

Thin Disk (Sérsic fits); 2800Å

	$\frac{R_{app}}{R_i}$	ΔSB	n_{app}^{sers}
$\tau_B^f = 0.1$			
a_0	0.992	-0.081	1.002
a_1	0.142	2.049	-0.099
a_2	-1.222	-17.308	0.805
a_3	4.041	57.379	-3.302
a_4	-5.671	-80.248	5.370
a_5	2.935	41.373	-3.168
$\tau_B^f = 0.3$			
a_0	0.991	-0.039	0.983
a_1	0.182	2.222	0.043
a_2	-1.564	-17.944	-0.465
a_3	5.546	65.932	0.041
a_4	-8.177	-100.144	1.468
a_5	4.506	56.944	-1.705
$\tau_B^f = 0.5$			
a_0	0.996	0.122	0.964
a_1	0.186	-0.620	-0.009
a_2	-1.623	8.661	-0.470
a_3	6.199	-19.146	0.307
a_4	-9.508	16.618	0.600
a_5	5.436	1.371	-1.140
$\tau_B^f = 1.0$			
a_0	0.991	0.475	0.893
a_1	0.479	2.040	-0.334
a_2	-4.482	-2.496	-0.447
a_3	15.898	19.533	0.432
a_4	-22.856	-34.649	0.504
a_5	11.820	24.634	-0.909
$\tau_B^f = 2.0$			
a_0	1.055	1.762	0.659
a_1	0.251	4.375	-0.554
a_2	0.195	-10.180	1.524
a_3	0.147	35.434	-4.388
a_4	-1.426	-48.635	5.270
a_5	1.871	29.505	-2.495
$\tau_B^f = 4.0$			
a_0	1.196	3.417	0.489
a_1	0.470	5.597	-0.547
a_2	-0.801	-12.589	1.843
a_3	2.353	40.602	-5.712
a_4	-2.511	-52.808	7.049
a_5	1.381	29.884	-3.207
$\tau_B^f = 8.0$			
a_0	1.376	5.285	0.347
a_1	0.790	8.548	-0.918
a_2	-2.126	-28.904	4.933
a_3	5.129	86.346	-15.877
a_4	-4.762	-111.933	21.991
a_5	1.564	58.501	-11.152

Table B.39: **Dust effects** $corr^{dust}$, as in Table B.31, but at 3600Å.

Thin Disk (Sérsic fits); 3600Å

	$\frac{R_{app}}{R_i}$	ΔSB	n_{app}^{sers}
$\tau_B^f = 0.1$			
a_0	1.005	0.112	0.984
a_1	0.240	2.417	-0.240
a_2	-2.257	-22.913	2.424
a_3	7.868	81.680	-9.122
a_4	-11.132	-117.263	13.530
a_5	5.556	59.523	-7.037
$\tau_B^f = 0.3$			
a_0	1.020	0.457	0.955
a_1	0.450	-1.156	-0.297
a_2	-4.105	14.323	2.325
a_3	14.367	-39.806	-8.548
a_4	-20.399	43.268	12.561
a_5	10.272	-12.185	-6.730
$\tau_B^f = 0.5$			
a_0	1.035	0.665	0.921
a_1	0.534	0.254	-0.284
a_2	-4.716	7.190	1.664
a_3	16.577	-19.958	-5.993
a_4	-23.632	21.131	8.644
a_5	12.011	-2.850	-4.788
$\tau_B^f = 1.0$			
a_0	1.069	1.293	0.850
a_1	0.729	1.094	-0.183
a_2	-5.946	4.517	-0.328
a_3	20.450	-9.656	0.784
a_4	-28.585	9.771	-0.998
a_5	14.385	1.829	-0.028
$\tau_B^f = 2.0$			
a_0	1.144	2.295	0.729
a_1	0.347	3.082	-0.328
a_2	-1.697	-1.890	-0.033
a_3	6.809	10.353	0.087
a_4	-10.331	-16.644	-0.445
a_5	5.855	14.772	-0.036
$\tau_B^f = 4.0$			
a_0	1.263	3.793	0.570
a_1	0.452	5.965	-0.600
a_2	-1.766	-15.504	1.531
a_3	5.931	47.464	-4.589
a_4	-7.369	-59.379	6.065
a_5	3.644	31.722	-3.239
$\tau_B^f = 8.0$			
a_0	1.405	5.686	0.407
a_1	0.689	8.121	-0.921
a_2	-1.852	-25.809	3.991
a_3	4.623	76.490	-11.790
a_4	-4.297	-99.657	15.526
a_5	1.481	52.955	-7.748

Table B.40: **Dust effects** $corr^{dust}$, as in Table B.31, but in B band.

Thin Disk (Sérsic fits); B band

	$\frac{R_{app}}{R_i}$	ΔSB	n_{app}^{sers}
$\tau_B^f = 0.1$			
a_0	0.991	-0.107	1.003
a_1	0.207	2.751	-0.223
a_2	-1.884	-24.886	2.352
a_3	6.221	83.164	-8.472
a_4	-8.577	-115.570	12.209
a_5	4.238	57.476	-6.252
$\tau_B^f = 0.3$			
a_0	0.983	-0.093	0.995
a_1	0.439	0.848	-0.074
a_2	-4.071	-7.054	1.279
a_3	13.746	27.210	-6.406
a_4	-19.182	-44.258	10.890
a_5	9.579	27.854	-6.320
$\tau_B^f = 0.5$			
a_0	0.982	-0.048	0.985
a_1	0.420	-1.003	-0.063
a_2	-3.933	10.845	1.051
a_3	13.591	-29.587	-5.455
a_4	-19.296	30.622	9.153
a_5	9.868	-5.446	-5.407
$\tau_B^f = 1.0$			
a_0	0.987	0.039	0.963
a_1	0.308	0.328	-0.215
a_2	-3.136	3.427	1.272
a_3	11.627	-0.455	-7.250
a_4	-17.232	-6.626	11.480
a_5	9.332	10.809	-6.085
$\tau_B^f = 2.0$			
a_0	0.987	0.876	0.769
a_1	0.308	2.901	-0.352
a_2	-3.136	-2.187	-0.288
a_3	11.627	8.549	1.507
a_4	-17.232	-11.794	-2.585
a_5	9.332	11.483	1.130
$\tau_B^f = 4.0$			
a_0	1.101	2.201	0.607
a_1	0.688	4.862	-0.435
a_2	-3.269	-12.995	0.981
a_3	9.996	46.034	-3.102
a_4	-12.760	-63.563	3.549
a_5	6.409	36.644	-1.606
$\tau_B^f = 8.0$			
a_0	1.261	3.889	0.466
a_1	0.398	6.332	-0.807
a_2	-0.022	-13.992	3.220
a_3	-0.104	40.218	-8.834
a_4	1.007	-49.002	10.304
a_5	-0.539	27.453	-4.541

Table B.41: **Dust effects** $corr^{dust}$, as in Table B.31, but in V band.

Thin Disk (Sérsic fits); V band

	$\frac{R_{app}}{R_i}$	ΔSB	n_{app}^{sers}
$\tau_B^f = 0.1$			
a_0	0.993	-0.087	1.004
a_1	0.152	1.886	-0.259
a_2	-1.426	-17.304	2.662
a_3	4.772	57.824	-9.369
a_4	-6.618	-79.989	13.250
a_5	3.278	39.674	-6.635
$\tau_B^f = 0.3$			
a_0	0.984	-0.158	1.005
a_1	0.322	3.654	-0.292
a_2	-2.986	-34.389	2.882
a_3	10.055	118.403	-10.508
a_4	-14.024	-167.607	15.311
a_5	7.016	85.234	-7.964
$\tau_B^f = 0.5$			
a_0	0.980	-0.121	0.996
a_1	0.408	0.203	-0.088
a_2	-3.813	-0.117	1.253
a_3	13.037	4.624	-6.119
a_4	-18.355	-14.411	10.275
a_5	9.279	14.599	-5.991
$\tau_B^f = 1.0$			
a_0	0.980	-0.071	0.986
a_1	0.355	-0.654	-0.167
a_2	-3.396	9.504	1.243
a_3	12.204	-24.429	-5.989
a_4	-17.844	25.767	9.477
a_5	9.476	-3.724	-5.346
$\tau_B^f = 2.0$			
a_0	0.980	0.352	0.863
a_1	0.355	2.347	-0.677
a_2	-3.396	1.167	1.758
a_3	12.204	-3.939	-4.371
a_4	-17.844	5.003	5.112
a_5	9.476	3.690	-2.536
$\tau_B^f = 4.0$			
a_0	1.051	1.558	0.669
a_1	0.148	4.149	-0.357
a_2	0.644	-11.281	0.771
a_3	-0.416	41.440	-2.827
a_4	-1.507	-57.844	3.396
a_5	2.154	33.876	-1.606
$\tau_B^f = 8.0$			
a_0	1.199	3.069	0.537
a_1	0.123	6.042	-0.739
a_2	1.176	-16.817	2.934
a_3	-2.367	52.442	-8.421
a_4	2.356	-66.216	9.966
a_5	-0.413	35.395	-4.399

Table B.42: **Dust effects** $corr^{dust}$, as in Table B.31, but in I band.

Thin Disk (Sérsic fits); I band

	$\frac{R_{app}}{R_i}$	ΔSB	n_{app}^{sers}
$\tau_B^f = 0.1$			
a_0	0.996	-0.043	1.003
a_1	0.065	0.802	-0.205
a_2	-0.721	-9.124	2.101
a_3	2.588	33.814	-7.399
a_4	-3.723	-49.267	10.526
a_5	1.888	25.099	-5.310
$\tau_B^f = 0.3$			
a_0	0.990	-0.132	1.012
a_1	0.167	2.698	-0.319
a_2	-1.761	-25.408	2.856
a_3	6.309	87.455	-9.831
a_4	-9.089	-123.235	13.866
a_5	4.632	62.019	-7.025
$\tau_B^f = 0.5$			
a_0	0.985	-0.142	1.005
a_1	0.232	3.000	-0.278
a_2	-2.399	-31.168	2.581
a_3	8.604	113.106	-9.348
a_4	-12.413	-164.137	13.690
a_5	6.355	84.500	-7.207
$\tau_B^f = 1.0$			
a_0	0.977	-0.133	1.006
a_1	0.354	-0.449	-0.319
a_2	-3.398	5.159	2.312
a_3	12.064	-8.813	-8.210
a_4	-17.340	1.525	11.978
a_5	8.925	8.055	-6.485
$\tau_B^f = 2.0$			
a_0	0.973	-0.051	0.973
a_1	0.417	-0.489	-0.310
a_2	-3.780	9.253	1.736
a_3	13.520	-18.610	-6.907
a_4	-19.512	14.556	10.271
a_5	10.222	2.493	-5.598
$\tau_B^f = 4.0$			
a_0	0.971	0.702	0.788
a_1	0.728	2.126	-0.534
a_2	-5.732	0.644	1.753
a_3	20.197	3.109	-5.057
a_4	-28.523	-8.075	6.087
a_5	14.515	10.960	-2.901
$\tau_B^f = 8.0$			
a_0	1.074	1.947	0.628
a_1	0.665	4.144	-0.541
a_2	-2.733	-9.053	1.996
a_3	7.906	35.207	-6.125
a_4	-10.198	-51.156	7.329
a_5	5.430	31.511	-3.284

Table B.43: **Dust effects** *corr*^{dust}, as in Table B.31, but in J band.

Thin Disk (Sérsic fits); J band

	$\frac{R_{app}}{R_i}$	ΔSB	n^{sers}_{app}
$\tau^f_B = 0.1$			
a_0	0.998	-0.023	1.003
a_1	0.025	-0.099	-0.212
a_2	-0.302	0.802	2.146
a_3	1.155	-1.149	-7.436
a_4	-1.719	-0.483	10.375
a_5	0.892	1.465	-5.114
$\tau^f_B = 0.3$			
a_0	0.995	-0.048	1.003
a_1	0.059	0.317	-0.234
a_2	-0.733	-5.096	2.513
a_3	2.873	23.740	-9.132
a_4	-4.353	-39.637	13.103
a_5	2.294	22.493	-6.586
$\tau^f_B = 0.5$			
a_0	0.992	-0.079	1.003
a_1	0.097	1.572	-0.247
a_2	-1.142	-17.567	2.653
a_3	4.432	66.906	-9.689
a_4	-6.682	-99.598	13.957
a_5	3.515	51.868	-7.090
$\tau^f_B = 1.0$			
a_0	0.987	-0.144	1.004
a_1	0.175	2.832	-0.231
a_2	-1.935	-28.610	2.269
a_3	7.401	106.518	-8.793
a_4	-11.071	-157.063	13.291
a_5	5.812	81.679	-7.109
$\tau^f_B = 2.0$			
a_0	0.982	-0.062	0.999
a_1	0.296	-2.100	-0.489
a_2	-2.983	20.357	3.895
a_3	11.137	-54.545	-13.390
a_4	-16.414	58.711	18.701
a_5	8.573	-17.262	-9.479
$\tau^f_B = 4.0$			
a_0	0.980	0.005	0.967
a_1	0.417	0.419	-0.553
a_2	-3.719	5.381	3.340
a_3	13.581	-12.345	-10.585
a_4	-19.729	12.204	13.954
a_5	10.320	1.442	-6.997
$\tau^f_B = 8.0$			
a_0	0.984	0.597	0.830
a_1	0.723	2.650	-0.743
a_2	-5.800	-0.844	2.838
a_3	20.104	3.477	-7.220
a_4	-27.909	-5.171	8.132
a_5	14.058	8.814	-3.735

Table B.44: **Dust effects** *corr*^{dust}, as in Table B.31, but in K band.

Thin Disk (Sérsic fits); K band

	$\frac{R_{app}}{R_i}$	ΔSB	n^{sers}_{app}
$\tau^f_B = 0.1$			
a_0	0.999	-0.012	1.003
a_1	0.026	-0.212	-0.216
a_2	-0.207	2.728	2.207
a_3	0.666	-9.511	-7.703
a_4	-0.898	12.815	10.771
a_5	0.435	-5.761	-5.278
$\tau^f_B = 0.3$			
a_0	0.996	-0.031	1.002
a_1	0.065	0.369	-0.176
a_2	-0.548	-2.474	1.952
a_3	1.824	7.928	-7.273
a_4	-2.526	-11.265	10.641
a_5	1.247	6.154	-5.407
$\tau^f_B = 0.5$			
a_0	0.995	-0.066	1.002
a_1	0.100	1.455	-0.182
a_2	-0.848	-12.298	2.011
a_3	2.834	41.314	-7.463
a_4	-3.930	-57.482	10.847
a_5	1.944	28.442	-5.503
$\tau^f_B = 1.0$			
a_0	0.991	-0.113	1.004
a_1	0.171	2.614	-0.263
a_2	-1.472	-21.418	2.396
a_3	4.980	70.571	-8.475
a_4	-6.957	-97.000	12.220
a_5	3.466	47.851	-6.263
$\tau^f_B = 2.0$			
a_0	0.989	-0.136	0.997
a_1	0.247	3.446	-0.172
a_2	-2.234	-28.736	1.933
a_3	7.801	97.948	-7.857
a_4	-11.097	-138.172	12.112
a_5	5.610	69.999	-6.524
$\tau^f_B = 4.0$			
a_0	0.988	-0.044	0.985
a_1	0.325	0.237	-0.299
a_2	-3.043	3.473	2.709
a_3	10.972	-6.861	-10.124
a_4	-15.873	0.978	14.903
a_5	8.150	6.911	-7.878
$\tau^f_B = 8.0$			
a_0	0.995	0.130	0.953
a_1	0.377	-0.396	-0.121
a_2	-3.509	13.318	0.539
a_3	13.065	-39.085	-3.244
a_4	-19.214	46.028	5.827
a_5	10.062	-13.598	-3.779

Table B.45: **Dust effects** $corr^{dust}$, as in Table B.31, but for the $H\alpha$ line.

Thin Disk (Sérsic fits); $H\alpha$

	$\frac{R_{app}}{R_i}$	ΔSB	n^{sers}_{app}
$\tau^f_B = 0.1$			
a_0	0.994	-0.070	1.003
a_1	0.119	1.478	-0.238
a_2	-1.161	-14.233	2.451
a_3	3.954	48.815	-8.627
a_4	-5.535	-68.462	12.224
a_5	2.758	34.203	-6.136
$\tau^f_B = 0.3$			
a_0	0.986	-0.148	1.007
a_1	0.264	3.294	-0.302
a_2	-2.525	-31.016	2.872
a_3	8.649	106.780	-10.253
a_4	-12.173	-150.938	14.767
a_5	6.122	76.509	-7.610
$\tau^f_B = 0.5$			
a_0	0.982	-0.129	0.999
a_1	0.342	1.257	-0.160
a_2	-3.281	-11.825	1.753
a_3	11.373	45.529	-7.336
a_4	-16.125	-70.865	11.562
a_5	8.181	40.954	-6.449
$\tau^f_B = 1.0$			
a_0	0.979	-0.094	0.994
a_1	0.355	-0.576	-0.224
a_2	-3.397	7.857	1.646
a_3	12.156	-18.510	-6.826
a_4	-17.662	16.587	10.419
a_5	9.272	0.734	-5.775
$\tau^f_B = 2.0$			
a_0	0.973	0.200	0.904
a_1	0.437	1.279	-0.539
a_2	-4.025	4.203	1.750
a_3	15.025	-9.430	-5.326
a_4	-21.934	8.555	7.056
a_5	11.500	3.260	-3.689
$\tau^f_B = 4.0$			
a_0	1.023	1.229	0.714
a_1	0.255	3.797	-0.431
a_2	-0.670	-10.793	1.208
a_3	3.658	40.590	-3.897
a_4	-6.605	-57.795	4.726
a_5	4.382	34.185	-2.245
$\tau^f_B = 8.0$			
a_0	1.152	2.645	0.571
a_1	0.293	5.455	-0.653
a_2	0.057	-15.218	2.465
a_3	0.234	50.713	-7.143
a_4	-0.526	-67.472	8.371
a_5	0.854	37.433	-3.675

Table B.46: **Dust effects** $corr^{dust}$ on the derived effective radius and Sérsic index of **exponential bulges**. Results are listed as coefficients of polynomial fits a_k (Eq. 3.1.19) at different τ_B^f, for B band.

exponential bulges (Sérsic fits); B band

	$\frac{R_{app}}{R_i}$	n_{app}^{sers}
$\tau_B^f = 0.1$		
a_0	1.001	0.761
a_1	0.004	-0.067
a_2	0.105	0.692
a_3	-0.324	-2.486
a_4	0.420	3.620
a_5	-0.167	-1.831
$\tau_B^f = 0.3$		
a_0	1.010	0.763
a_1	-0.013	-0.235
a_2	0.493	2.460
a_3	-1.999	-8.929
a_4	3.247	13.134
a_5	-1.733	-6.712
$\tau_B^f = 0.5$		
a_0	1.018	0.762
a_1	0.007	-0.171
a_2	0.456	1.927
a_3	-1.971	-7.495
a_4	3.323	11.816
a_5	-1.847	-6.479
$\tau_B^f = 1.0$		
a_0	1.029	0.749
a_1	0.181	0.122
a_2	-1.421	-1.758
a_3	4.386	5.735
a_4	-5.055	-6.312
a_5	1.887	1.786
$\tau_B^f = 2.0$		
a_0	1.050	0.739
a_1	-0.060	-0.147
a_2	0.399	0.465
a_3	-0.364	0.523
a_4	-0.249	-2.295
a_5	0.208	0.939
$\tau_B^f = 4.0$		
a_0	1.057	0.728
a_1	-0.039	0.003
a_2	-0.072	-1.633
a_3	0.694	7.464
a_4	-1.076	-12.035
a_5	0.399	5.716
$\tau_B^f = 8.0$		
a_0	1.046	0.697
a_1	-0.043	0.093
a_2	0.548	-2.264
a_3	-2.581	9.270
a_4	5.339	-15.430
a_5	-3.843	7.973

Table B.47: **Dust effects** $corr^{dust}$, as in Table B.46, but in V band.

exponential bulges (Sérsic fits); V band

	$\frac{R_{app}}{R_i}$	n_{app}^{sers}
$\tau_B^f = 0.1$		
a_0	1.009	0.770
a_1	-0.049	-0.224
a_2	0.385	1.558
a_3	-1.067	-4.445
a_4	1.282	5.475
a_5	-0.527	-2.405
$\tau_B^f = 0.3$		
a_0	1.018	0.771
a_1	-0.093	-0.321
a_2	1.011	2.633
a_3	-3.423	-8.525
a_4	4.825	11.686
a_5	-2.318	-5.645
$\tau_B^f = 0.5$		
a_0	1.024	0.772
a_1	-0.039	-0.342
a_2	0.588	3.073
a_3	-2.123	-10.730
a_4	3.304	15.591
a_5	-1.745	-7.933
$\tau_B^f = 1.0$		
a_0	1.036	0.767
a_1	0.014	-0.089
a_2	0.243	0.635
a_3	-1.420	-3.341
a_4	2.899	6.954
a_5	-1.801	-4.657
$\tau_B^f = 2.0$		
a_0	1.054	0.761
a_1	-0.009	-0.193
a_2	-0.480	0.208
a_3	3.258	1.979
a_4	-5.666	-4.302
a_5	2.942	1.883
$\tau_B^f = 4.0$		
a_0	1.067	0.747
a_1	-0.109	-0.236
a_2	0.553	0.634
a_3	-0.973	0.693
a_4	0.664	-3.628
a_5	-0.232	2.032
$\tau_B^f = 8.0$		
a_0	1.063	0.729
a_1	-0.173	-0.075
a_2	1.136	-1.370
a_3	-3.829	7.179
a_4	6.316	-12.867
a_5	-3.938	6.722

Table B.48: **Dust effects** $corr^{dust}$, as in Table B.46, but in I band.

exponential bulges (Sérsic fits); I band	$\frac{R_{app}}{R_i}$	n_{app}^{sers}
$\tau_B^f = 0.1$		
a_0	1.003	0.760
a_1	0.029	0.000
a_2	-0.082	0.000
a_3	0.081	0.000
a_4	0.012	0.000
a_5	-0.020	0.000
$\tau_B^f = 0.3$		
a_0	1.009	0.762
a_1	0.033	-0.134
a_2	0.012	1.363
a_3	-0.334	-4.789
a_4	0.677	6.785
a_5	-0.347	-3.320
$\tau_B^f = 0.5$		
a_0	1.015	0.765
a_1	-0.010	-0.037
a_2	0.560	0.533
a_3	-2.371	-2.666
a_4	3.705	4.699
a_5	-1.876	-2.656
$\tau_B^f = 1.0$		
a_0	1.031	0.774
a_1	-0.079	-0.285
a_2	0.937	2.444
a_3	-3.209	-8.784
a_4	4.759	13.299
a_5	-2.458	-7.053
$\tau_B^f = 2.0$		
a_0	1.046	0.767
a_1	0.015	-0.063
a_2	0.026	0.168
a_3	-0.339	-1.424
a_4	1.122	4.026
a_5	-0.888	-3.222
$\tau_B^f = 4.0$		
a_0	1.065	0.761
a_1	-0.091	-0.243
a_2	0.235	0.916
a_3	0.673	-0.973
a_4	-1.908	0.109
a_5	1.036	-0.371
$\tau_B^f = 8.0$		
a_0	1.074	0.748
a_1	-0.144	-0.293
a_2	0.492	0.812
a_3	-0.462	-0.670
a_4	-0.237	-0.278
a_5	0.287	-0.397

Table B.49: **Dust effects** $corr^{dust}$, as in Table B.46, but in J band.

exponential bulges (Sérsic fits); J band	$\frac{R_{app}}{R_i}$	n_{app}^{sers}
$\tau_B^f = 0.1$		
a_0	1.005	0.769
a_1	-0.059	-0.210
a_2	0.450	1.412
a_3	-1.315	-3.922
a_4	1.636	4.759
a_5	-0.716	-2.087
$\tau_B^f = 0.3$		
a_0	1.010	0.771
a_1	-0.094	-0.343
a_2	0.826	2.725
a_3	-2.614	-8.447
a_4	3.453	11.085
a_5	-1.586	-5.162
$\tau_B^f = 0.5$		
a_0	1.014	0.773
a_1	-0.129	-0.475
a_2	1.202	4.038
a_3	-3.899	-12.972
a_4	5.241	17.412
a_5	-2.443	-8.238
$\tau_B^f = 1.0$		
a_0	1.022	0.770
a_1	-0.108	-0.291
a_2	1.045	2.310
a_3	-3.385	-7.342
a_4	4.609	10.013
a_5	-2.165	-4.882
$\tau_B^f = 2.0$		
a_0	1.035	0.772
a_1	-0.143	-0.430
a_2	1.486	3.754
a_3	-5.054	-12.603
a_4	7.323	17.854
a_5	-3.706	-9.001
$\tau_B^f = 4.0$		
a_0	1.053	0.770
a_1	-0.169	-0.261
a_2	1.667	2.315
a_3	-5.359	-8.810
a_4	7.433	13.870
a_5	-3.733	-7.730
$\tau_B^f = 8.0$		
a_0	1.068	0.757
a_1	-0.037	-0.002
a_2	0.087	-1.189
a_3	-0.037	4.209
a_4	0.225	-4.765
a_5	-0.382	1.136

Table B.50: **Dust effects** *corr*^{dust}, as in Table B.46, but in K band.

exponential bulges (Sérsic fits); K band

	$\frac{R_{app}}{R_i}$	n^{sers}_{app}
$\tau^f_B = 0.1$		
a_0	1.006	0.770
a_1	-0.011	-0.032
a_2	0.126	0.311
a_3	-0.392	-1.057
a_4	0.509	1.455
a_5	-0.236	-0.696
$\tau^f_B = 0.3$		
a_0	1.007	0.771
a_1	-0.025	-0.101
a_2	0.292	1.002
a_3	-0.980	-3.468
a_4	1.339	4.872
a_5	-0.637	-2.380
$\tau^f_B = 0.5$		
a_0	1.009	0.771
a_1	-0.036	-0.104
a_2	0.421	1.057
a_3	-1.444	-3.752
a_4	2.008	5.413
a_5	-0.966	-2.722
$\tau^f_B = 1.0$		
a_0	1.012	0.771
a_1	-0.008	-0.066
a_2	0.201	0.712
a_3	-0.761	-2.669
a_4	1.144	4.074
a_5	-0.578	-2.172
$\tau^f_B = 2.0$		
a_0	1.018	0.772
a_1	-0.022	-0.127
a_2	0.407	1.361
a_3	-1.547	-5.007
a_4	2.348	7.433
a_5	-1.199	-3.868
$\tau^f_B = 4.0$		
a_0	1.028	0.770
a_1	0.004	-0.036
a_2	0.269	0.583
a_3	-1.202	-3.072
a_4	2.063	5.606
a_5	-1.144	-3.358
$\tau^f_B = 8.0$		
a_0	1.043	0.773
a_1	0.013	-0.152
a_2	0.350	1.078
a_3	-1.775	-3.875
a_4	3.390	6.184
a_5	-2.120	-3.670

Table B.51: **Dust effects** *corr*^{dust} on the derived photometric parameters of **de Vaucouleurs bulges**: effective radius and Sérsic index. Results are listed as coefficients of polynomial fits a_k (Eq. 3.1.19) at different τ^f_B, for B band.

de Vaucouleurs bulges (Sérsic fits); B band

	$\frac{R_{app}}{R_i}$	n^{sers}_{app}
$\tau^f_B = 0.1$		
a_0	1.040	3.471
a_1	0.006	-0.072
a_2	-0.151	0.598
a_3	1.035	-0.981
a_4	-2.612	-0.978
a_5	2.174	1.375
$\tau^f_B = 0.3$		
a_0	1.041	3.310
a_1	0.051	0.042
a_2	-0.746	-1.209
a_3	3.683	8.354
a_4	-7.331	-19.540
a_5	5.060	13.095
$\tau^f_B = 0.5$		
a_0	1.030	3.220
a_1	-0.074	–
a_2	0.854	–
a_3	-2.969	–
a_4	3.018	–
a_5	0.274	–
$\tau^f_B = 1.0$		
a_0	1.095	3.303
a_1	-0.076	-0.296
a_2	0.928	3.450
a_3	-3.702	-11.970
a_4	5.501	14.094
a_5	-2.408	-8.427
$\tau^f_B = 2.0$		
a_0	1.126	2.885
a_1	–	-0.581
a_2	–	6.413
a_3	–	-25.091
a_4	–	27.521
a_5	–	-11.171
$\tau^f_B = 4.0$		
a_0	–	–
a_1	–	–
a_2	–	–
a_3	–	–
a_4	–	–
a_5	–	–
$\tau^f_B = 8.0$		
a_0	–	–
a_1	–	–
a_2	–	–
a_3	–	–
a_4	–	–
a_5	–	–

Table B.52: **Dust effects** $corr^{dust}$, as in Table B.51, but in V band.

de Vaucouleurs bulges (Sérsic fits); V band		
	$\frac{R_{app}}{R_i}$	n^{sers}_{app}
$\tau^f_B = 0.1$		
a_0	1.036	3.481
a_1	0.005	-0.120
a_2	-0.110	1.271
a_3	0.704	-4.055
a_4	-1.707	4.397
a_5	1.381	1.800
$\tau^f_B = 0.3$		
a_0	1.040	3.351
a_1	0.033	-0.095
a_2	-0.475	0.704
a_3	2.352	-0.374
a_4	-4.750	-4.055
a_5	3.377	3.832
$\tau^f_B = 0.5$		
a_0	1.029	3.230
a_1	0.083	0.082
a_2	-1.228	-1.837
a_3	6.016	11.714
a_4	-11.658	-26.833
a_5	7.856	18.614
$\tau^f_B = 1.0$		
a_0	1.002	3.301
a_1	0.118	-0.187
a_2	-0.085	2.236
a_3	0.307	-8.071
a_4	–	11.552
a_5	–	-7.655
$\tau^f_B = 2.0$		
a_0	1.066	3.286
a_1	0.031	-0.387
a_2	-0.308	-1.697
a_3	0.609	–
a_4	0.581	–
a_5	-0.962	–
$\tau^f_B = 4.0$		
a_0	–	–
a_1	–	–
a_2	–	–
a_3	–	–
a_4	–	–
a_5	–	–
$\tau^f_B = 8.0$		
a_0	–	–
a_1	–	–
a_2	–	–
a_3	–	–
a_4	–	–
a_5	–	–

Table B.53: **Dust effects** $corr^{dust}$, as in Table B.51, but in I band.

de Vaucouleurs bulges (Sérsic fits); I band		
	$\frac{R_{app}}{R_i}$	n^{sers}_{app}
$\tau^f_B = 0.1$		
a_0	1.024	3.490
a_1	0.041	-0.062
a_2	-0.543	0.552
a_3	2.453	-1.037
a_4	-4.487	-0.706
a_5	2.874	1.238
$\tau^f_B = 0.3$		
a_0	1.025	3.370
a_1	0.018	0.021
a_2	-0.201	-0.433
a_3	0.763	2.692
a_4	-1.304	-5.885
a_5	0.964	3.550
$\tau^f_B = 0.5$		
a_0	1.028	3.340
a_1	0.011	-0.102
a_2	-0.130	2.406
a_3	0.565	-13.826
a_4	-1.212	25.338
a_5	1.103	-15.648
$\tau^f_B = 1.0$		
a_0	1.022	3.143
a_1	0.027	-0.284
a_2	-0.436	2.664
a_3	2.367	-5.718
a_4	-5.260	0.309
a_5	4.117	3.877
$\tau^f_B = 2.0$		
a_0	0.981	3.201
a_1	0.263	-0.102
a_2	-0.309	0.575
a_3	0.383	0.320
a_4	–	-3.262
a_5	–	0.292
$\tau^f_B = 4.0$		
a_0	–	–
a_1	–	–
a_2	–	–
a_3	–	–
a_4	–	–
a_5	–	–
$\tau^f_B = 8.0$		
a_0	–	–
a_1	–	–
a_2	–	–
a_3	–	–
a_4	–	–
a_5	–	–

Table B.54: **Dust effects** $corr^{dust}$, as in Table B.51, but in J band.

de Vaucouleurs bulges (Sérsic fits); J band

	$\frac{R_{app}}{R_i}$	n^{sers}_{app}
$\tau^f_B = 0.1$		
a_0	1.011	3.460
a_1	-0.002	–
a_2	0.013	–
a_3	0.024	–
a_4	-0.240	–
a_5	0.296	–
$\tau^f_B = 0.3$		
a_0	1.000	3.348
a_1	0.050	–
a_2	-0.553	–
a_3	2.229	–
a_4	-3.811	–
a_5	2.367	–
$\tau^f_B = 0.5$		
a_0	0.997	3.310
a_1	0.136	–
a_2	-1.438	–
a_3	5.388	–
a_4	-8.445	–
a_5	4.798	–
$\tau^f_B = 1.0$		
a_0	1.002	3.235
a_1	0.144	-0.387
a_2	-1.544	3.685
a_3	5.920	-11.578
a_4	-9.600	13.990
a_5	5.700	-6.003
$\tau^f_B = 2.0$		
a_0	1.014	3.081
a_1	0.037	-0.036
a_2	-0.347	-0.372
a_3	1.263	4.406
a_4	-2.352	-10.317
a_5	1.921	5.965
$\tau^f_B = 4.0$		
a_0	1.172	3.776
a_1	0.026	-0.164
a_2	-0.145	-3.411
a_3	-0.209	5.554
a_4	1.412	2.182
a_5	-0.508	-7.747
$\tau^f_B = 8.0$		
a_0	–	–
a_1	–	–
a_2	–	–
a_3	–	–
a_4	–	–
a_5	–	–

Table B.55: **Dust effects** $corr^{dust}$, as in Table B.51, but in K band.

de Vaucouleurs bulges (Sérsic fits); K band

	$\frac{R_{app}}{R_i}$	n^{sers}_{app}
$\tau^f_B = 0.1$		
a_0	1.010	3.439
a_1	-0.002	–
a_2	0.064	–
a_3	-0.333	–
a_4	0.557	–
a_5	-0.253	–
$\tau^f_B = 0.3$		
a_0	0.992	3.359
a_1	0.008	–
a_2	-0.082	–
a_3	0.373	–
a_4	-0.810	–
a_5	0.651	–
$\tau^f_B = 0.5$		
a_0	0.985	3.330
a_1	0.017	–
a_2	-0.205	–
a_3	0.929	–
a_4	-1.833	–
a_5	1.313	–
$\tau^f_B = 1.0$		
a_0	0.986	3.301
a_1	0.070	–
a_2	-0.804	–
a_3	3.294	–
a_4	-5.658	–
a_5	3.491	–
$\tau^f_B = 2.0$		
a_0	0.998	3.234
a_1	0.125	–
a_2	-1.441	–
a_3	5.890	–
a_4	-9.992	–
a_5	6.040	–
$\tau^f_B = 4.0$		
a_0	1.090	3.350
a_1	0.153	3.239
a_2	–	-28.937
a_3	–	112.177
a_4	–	-173.207
a_5	–	89.894
$\tau^f_B = 8.0$		
a_0	1.095	3.292
a_1	0.204	2.851
a_2	–	-26.095
a_3	–	104.732
a_4	–	-172.223
a_5	–	95.467

Table B.56: **Dust effects** *corr*^{dust} on the effective radius of **de Vaucouleurs bulges**. Results are listed as coefficients of polynomial fits a_k (Eq. 3.1.19) at different τ_B^f and the effective wavelength of the B band.

de Vaucouleurs bulges (de Vaucouleurs fits) B band

	$\frac{R_{app}}{R_i}$
$\tau_B^f = 0.1$	
a_0	1.026
a_1	0.045
a_2	-0.676
a_3	2.808
a_4	-4.285
a_5	2.331
$\tau_B^f = 0.3$	
a_0	1.058
a_1	0.026
a_2	-0.673
a_3	4.281
a_4	-7.875
a_5	4.756
$\tau_B^f = 0.5$	
a_0	1.085
a_1	0.131
a_2	-2.090
a_3	10.459
a_4	-19.227
a_5	12.454
$\tau_B^f = 1.0$	
a_0	1.103
a_1	0.249
a_2	-4.402
a_3	25.009
a_4	-50.839
a_5	36.672
$\tau_B^f = 2.0$	
a_0	1.361
a_1	0.155
a_2	-1.500
a_3	6.354
a_4	-5.392
a_5	4.735
$\tau_B^f = 4.0$	
a_0	–
a_1	–
a_2	–
a_3	–
a_4	–
a_5	–
$\tau_B^f = 8.0$	
a_0	–
a_1	–
a_2	–
a_3	–
a_4	–
a_5	–

Table B.57: **Dust effects** *corr*^{dust}, as in Table B.56, but in V band.

de Vaucouleurs bulges (de Vaucouleurs fits) V band

	$\frac{R_{app}}{R_i}$
$\tau_B^f = 0.1$	
a_0	1.020
a_1	0.036
a_2	-0.502
a_3	1.834
a_4	-2.386
a_5	1.081
$\tau_B^f = 0.3$	
a_0	1.049
a_1	-0.032
a_2	0.075
a_3	1.202
a_4	-3.057
a_5	2.189
$\tau_B^f = 0.5$	
a_0	1.077
a_1	0.054
a_2	-0.955
a_3	4.866
a_4	-7.860
a_5	4.398
$\tau_B^f = 1.0$	
a_0	1.092
a_1	0.192
a_2	-2.526
a_3	10.123
a_4	-14.938
a_5	8.621
$\tau_B^f = 2.0$	
a_0	1.205
a_1	-0.375
a_2	3.183
a_3	-7.006
a_4	7.785
a_5	-0.532
$\tau_B^f = 4.0$	
a_0	–
a_1	–
a_2	–
a_3	–
a_4	–
a_5	–
$\tau_B^f = 8.0$	
a_0	–
a_1	–
a_2	–
a_3	–
a_4	–
a_5	–

Table B.58: **Dust effects** *corr*^{dust}, as in Table B.56, but in I band.

de Vaucouleurs bulges (de Vaucouleurs fits) I band

	$\frac{R_{app}}{R_i}$
$\tau_B^f = 0.1$	
a_0	1.013
a_1	–
a_2	–
a_3	–
a_4	–
a_5	–
$\tau_B^f = 0.3$	
a_0	1.032
a_1	-0.021
a_2	0.102
a_3	0.407
a_4	-1.098
a_5	0.712
$\tau_B^f = 0.5$	
a_0	1.058
a_1	0.027
a_2	-0.389
a_3	1.594
a_4	-1.680
a_5	0.615
$\tau_B^f = 1.0$	
a_0	1.092
a_1	0.076
a_2	-1.151
a_3	5.113
a_4	-7.487
a_5	3.930
$\tau_B^f = 2.0$	
a_0	1.112
a_1	-0.049
a_2	0.080
a_3	0.366
a_4	0.696
a_5	–
$\tau_B^f = 4.0$	
a_0	–
a_1	–
a_2	–
a_3	–
a_4	–
a_5	–
$\tau_B^f = 8.0$	
a_0	–
a_1	–
a_2	–
a_3	–
a_4	–
a_5	–

Table B.59: **Dust effects** *corr*^{dust}, as in Table B.56, but in J band.

de Vaucouleurs bulges (de Vaucouleurs fits) J band

	$\frac{R_{app}}{R_i}$
$\tau_B^f = 0.1$	
a_0	0.998
a_1	0.066
a_2	-0.894
a_3	3.336
a_4	-4.701
a_5	2.268
$\tau_B^f = 0.3$	
a_0	1.008
a_1	-0.032
a_2	0.192
a_3	0.275
a_4	-1.343
a_5	1.027
$\tau_B^f = 0.5$	
a_0	1.013
a_1	0.041
a_2	-0.702
a_3	3.862
a_4	-6.842
a_5	4.017
$\tau_B^f = 1.0$	
a_0	1.040
a_1	0.119
a_2	-1.684
a_3	8.008
a_4	-13.650
a_5	8.006
$\tau_B^f = 2.0$	
a_0	1.076
a_1	0.171
a_2	-2.295
a_3	10.676
a_4	-18.012
a_5	10.838
$\tau_B^f = 4.0$	
a_0	0.842
a_1	0.363
a_2	-0.083
a_3	0.564
a_4	–
a_5	–
$\tau_B^f = 8.0$	
a_0	1.044
a_1	0.547
a_2	-1.688
a_3	4.140
a_4	–
a_5	–

Table B.60: **Dust effects** $corr^{dust}$, as in Table B.56, but in K band.

de Vaucouleurs bulges (de Vaucouleurs fits) K band

	$\frac{R_{app}}{R_i}$
$\tau_B^f = 0.1$	
a_0	0.993
a_1	–
a_2	–
a_3	–
a_4	–
a_5	–
$\tau_B^f = 0.3$	
a_0	0.999
a_1	0.077
a_2	-0.974
a_3	3.508
a_4	-4.826
a_5	2.285
$\tau_B^f = 0.5$	
a_0	1.005
a_1	0.097
a_2	-1.195
a_3	4.330
a_4	-6.067
a_5	2.946
$\tau_B^f = 1.0$	
a_0	1.012
a_1	0.185
a_2	-2.158
a_3	8.008
a_4	-11.796
a_5	6.133
$\tau_B^f = 2.0$	
a_0	1.049
a_1	0.067
a_2	-0.801
a_3	3.408
a_4	-6.090
a_5	3.945
$\tau_B^f = 4.0$	
a_0	0.718
a_1	0.381
a_2	0.171
a_3	-0.327
a_4	–
a_5	–
$\tau_B^f = 8.0$	
a_0	0.811
a_1	0.123
a_2	0.652
a_3	–
a_4	–
a_5	–

Appendix C

The corrections for dust effects on decomposed disks and bulges

Table C.1: **Dust effects** $corr^{B/D}$ on the derived photometric parameters of **decomposed disks** and **exponential bulges** ($B/D = 0.25$): disk scale-lengths, bulge effective radii and Sérsic indices. Results are listed as coefficients of polynomial fits a_k (Eq. 3.1.19) at different τ^f_B and at the effective wavelength of the B band.

Fits with exponential + Sérsic functions; B band

	$\frac{R^{B/D}_{app,d}}{R_{app,d}}$	$\frac{R^{eff,B/D}_{app,b}}{R^{eff}_{app,b}}$	$n^{sers,B/D}_{app,b} - n^{sers}_{app,b}$
$\tau^f_B = 0.1$			
a_0	0.986	1.054	0.061
a_1	-0.058	-0.088	-0.073
a_2	0.251	0.821	0.788
a_3	-0.869	-3.251	-3.729
a_4	1.192	4.874	6.497
a_5	-0.557	-2.463	-3.688
$\tau^f_B = 0.3$			
a_0	0.980	1.047	0.054
a_1	-0.069	0.216	0.452
a_2	0.255	-2.461	-4.596
a_3	-0.845	9.046	15.946
a_4	0.866	-14.115	-23.125
a_5	-0.185	7.851	12.070
$\tau^f_B = 0.5$			
a_0	0.974	1.044	0.050
a_1	-0.087	0.133	0.217
a_2	0.276	-1.818	-2.129
a_3	-0.664	7.454	7.845
a_4	0.045	-13.221	-12.975
a_5	0.567	8.312	8.085
$\tau^f_B = 1.0$			
a_0	0.956	1.038	0.050
a_1	-0.008	0.057	-0.060
a_2	-0.744	-0.677	1.421
a_3	2.706	1.555	-7.045
a_4	-4.749	-2.417	11.459
a_5	2.862	1.493	-5.806
$\tau^f_B = 2.0$			
a_0	0.919	1.019	0.040
a_1	0.025	-0.107	0.056
a_2	-1.778	-0.156	-1.129
a_3	6.585	0.084	2.944
a_4	-10.052	-0.328	-3.961
a_5	5.490	0.660	2.542
$\tau^f_B = 4.0$			
a_0	0.882	0.984	0.013
a_1	-0.060	-0.130	-0.088
a_2	-0.217	0.820	1.692
a_3	1.455	-3.199	-8.677
a_4	-2.567	4.937	14.424
a_5	1.592	-2.265	-7.018
$\tau^f_B = 8.0$			
a_0	0.897	0.992	0.013
a_1	0.058	0.022	-0.010
a_2	-0.380	0.411	1.076
a_3	2.286	-0.598	-4.824
a_4	-4.076	-0.662	7.796
a_5	2.260	1.472	-3.252

Table C.2: **Dust effects** $corr^{B/D}$, as in Table C.1, but in V band.

Fits with exponential + Sérsic functions; V band

	$\frac{R^{B/D}_{app,d}}{R_{app,d}}$	$\frac{R^{eff,B/D}_{app,b}}{R^{eff}_{app,b}}$	$n^{sers,B/D}_{app,b} - n^{sers}_{app,b}$
$\tau^f_B = 0.1$			
a_0	0.987	1.045	0.043
a_1	-0.053	-0.027	0.016
a_2	0.179	0.424	0.774
a_3	-0.567	-2.075	-4.417
a_4	0.742	3.425	7.904
a_5	-0.337	-1.852	-4.545
$\tau^f_B = 0.3$			
a_0	0.982	1.041	0.041
a_1	-0.076	-0.006	0.170
a_2	0.392	0.150	-0.988
a_3	-1.433	-0.953	2.237
a_4	1.944	1.334	-2.350
a_5	-0.865	-0.444	1.073
$\tau^f_B = 0.5$			
a_0	0.977	1.036	0.038
a_1	-0.060	0.198	0.340
a_2	0.113	-2.174	-3.076
a_3	-0.261	8.171	10.561
a_4	-0.170	-13.358	-15.857
a_5	0.457	7.833	8.837
$\tau^f_B = 1.0$			
a_0	0.967	1.033	0.036
a_1	-0.175	-0.070	0.088
a_2	1.184	0.891	0.099
a_3	-4.188	-3.837	-1.976
a_4	5.432	5.242	3.496
a_5	-2.328	-2.131	-1.263
$\tau^f_B = 2.0$			
a_0	0.938	1.019	0.029
a_1	-0.013	0.008	0.376
a_2	-1.281	-0.672	-3.237
a_3	4.876	1.399	8.985
a_4	-7.926	-1.981	-11.170
a_5	4.536	1.296	5.391
$\tau^f_B = 4.0$			
a_0	0.895	0.989	0.013
a_1	-0.102	-0.237	0.032
a_2	-0.364	1.105	-0.203
a_3	2.056	-3.843	-1.737
a_4	-3.608	5.469	4.358
a_5	2.238	-2.370	-2.048
$\tau^f_B = 8.0$			
a_0	0.882	0.966	-0.009
a_1	0.036	0.102	0.163
a_2	-0.393	-0.294	0.167
a_3	1.986	0.717	-4.285
a_4	-3.236	-1.088	9.855
a_5	1.780	1.027	-5.547

Table C.3: **Dust effects** $corr^{B/D}$, as in Table C.1, but in I band.

Fits with exponential + Sérsic functions; I band

	$\frac{R^{B/D}_{app,d}}{R_{app,d}}$	$\frac{R^{eff,B/D}_{app,b}}{R^{eff}_{app,b}}$	$n^{sers,B/D}_{app,b} - n^{sers}_{app,b}$
$\tau^f_B = 0.1$			
a_0	0.988	1.047	0.051
a_1	-0.044	-0.091	-0.061
a_2	0.003	0.573	0.716
a_3	0.203	-1.969	-3.702
a_4	-0.482	2.852	6.884
a_5	0.315	-1.470	-4.155
$\tau^f_B = 0.3$			
a_0	0.985	1.046	0.050
a_1	-0.067	-0.124	0.020
a_2	0.235	0.836	-0.309
a_3	-0.737	-2.850	0.163
a_4	0.941	3.986	1.228
a_5	-0.408	-1.921	-1.265
$\tau^f_B = 0.5$			
a_0	0.981	1.043	0.047
a_1	-0.085	-0.073	-0.020
a_2	0.394	0.221	-0.142
a_3	-1.349	-0.448	0.742
a_4	1.780	0.068	-1.282
a_5	-0.771	0.358	0.861
$\tau^f_B = 1.0$			
a_0	0.973	1.031	0.040
a_1	-0.064	0.108	0.047
a_2	0.011	-1.489	-0.682
a_3	0.265	6.097	3.444
a_4	-1.145	-10.941	-7.121
a_5	1.079	7.008	5.160
$\tau^f_B = 2.0$			
a_0	0.956	1.026	0.036
a_1	-0.066	-0.115	-0.217
a_2	-0.161	1.006	2.990
a_3	0.819	-3.998	-12.069
a_4	-1.890	5.505	18.315
a_5	1.310	-2.510	-9.117
$\tau^f_B = 4.0$			
a_0	0.919	1.001	0.017
a_1	0.056	0.037	0.222
a_2	-1.726	-1.024	-2.159
a_3	6.170	2.491	6.296
a_4	-9.368	-3.418	-8.648
a_5	5.122	2.088	4.756
$\tau^f_B = 8.0$			
a_0	0.884	0.965	0.001
a_1	0.020	0.074	0.174
a_2	-0.741	-1.024	-1.331
a_3	2.631	2.814	3.153
a_4	-3.668	-3.493	-4.457
a_5	1.951	1.984	3.445

Table C.4: **Dust effects** $corr^{B/D}$, as in Table C.1, but in J band.

Fits with exponential + Sérsic functions; J band

	$\frac{R^{B/D}_{app,d}}{R_{app,d}}$	$\frac{R^{eff,B/D}_{app,b}}{R^{eff}_{app,b}}$	$n^{sers,B/D}_{app,b} - n^{sers}_{app,b}$
$\tau^f_B = 0.1$			
a_0	0.988	1.040	0.043
a_1	-0.027	0.022	0.105
a_2	-0.232	-0.397	-0.820
a_3	1.146	1.184	1.678
a_4	-1.953	-1.461	-0.645
a_5	1.103	0.603	-0.601
$\tau^f_B = 0.3$			
a_0	0.986	1.039	0.042
a_1	-0.046	-0.005	0.031
a_2	-0.088	-0.170	-0.238
a_3	0.654	0.406	0.044
a_4	-1.265	-0.363	1.298
a_5	0.763	0.073	-1.418
$\tau^f_B = 0.5$			
a_0	0.985	1.038	0.040
a_1	-0.069	-0.026	-0.027
a_2	0.099	0.001	0.532
a_3	-0.007	-0.186	-2.699
a_4	-0.317	0.447	4.913
a_5	0.292	-0.283	-2.961
$\tau^f_B = 1.0$			
a_0	0.979	1.033	0.037
a_1	-0.057	0.026	0.165
a_2	-0.057	-0.621	-1.344
a_3	0.413	2.191	3.719
a_4	-0.810	-3.388	-4.449
a_5	0.519	1.975	2.082
$\tau^f_B = 2.0$			
a_0	0.969	1.027	0.031
a_1	-0.064	-0.006	0.216
a_2	-0.165	-0.680	-1.849
a_3	1.038	3.513	5.775
a_4	-2.273	-7.363	-8.467
a_5	1.636	5.320	5.119
$\tau^f_B = 4.0$			
a_0	0.949	1.016	0.032
a_1	-0.025	-0.040	-0.075
a_2	-0.700	-0.228	0.308
a_3	2.775	0.797	-0.441
a_4	-4.488	-1.412	0.163
a_5	2.477	0.845	0.224
$\tau^f_B = 8.0$			
a_0	0.916	0.993	0.022
a_1	-0.027	-0.079	-0.141
a_2	-0.686	0.198	1.695
a_3	2.821	-0.542	-5.517
a_4	-5.009	-0.896	5.336
a_5	3.122	1.590	-0.953

Table C.5: **Dust effects** $corr^{B/D}$, as in Table C.1, but in K band.

Fits with exponential + Sérsic functions; K band

	$\frac{R^{B/D}_{app,d}}{R_{app,d}}$	$\frac{R^{eff,B/D}_{app,b}}{R^{eff}_{app,b}}$	$n^{sers,B/D}_{app,b} - n^{sers}_{app,b}$
$\tau^f_B = 0.1$			
a_0	0.987	1.034	0.036
a_1	-0.011	0.044	0.010
a_2	-0.462	-1.019	-0.602
a_3	2.062	3.826	1.891
a_4	-3.422	-5.666	-1.780
a_5	1.924	2.862	0.197
$\tau^f_B = 0.3$			
a_0	0.986	1.033	0.028
a_1	-0.006	0.041	0.166
a_2	-0.507	-1.003	-1.489
a_3	2.183	3.762	4.032
a_4	-3.569	-5.553	-4.089
a_5	1.987	2.796	1.113
$\tau^f_B = 0.5$			
a_0	0.985	1.033	0.028
a_1	-0.006	0.036	0.166
a_2	-0.511	-0.977	-1.682
a_3	2.183	3.670	4.960
a_4	-3.553	-5.411	-5.575
a_5	1.973	2.722	1.902
$\tau^f_B = 1.0$			
a_0	0.981	1.031	0.028
a_1	0.108	0.029	0.172
a_2	-1.662	-0.945	-1.955
a_3	6.063	3.554	6.187
a_4	-8.851	-5.228	-7.453
a_5	4.482	2.637	2.881
$\tau^f_B = 2.0$			
a_0	0.979	1.029	0.032
a_1	-0.057	-0.152	-0.111
a_2	-0.095	0.907	0.907
a_3	0.635	-3.193	-4.162
a_4	-1.219	4.637	7.491
a_5	0.759	-2.282	-4.412
$\tau^f_B = 4.0$			
a_0	0.970	1.024	0.029
a_1	-0.080	-0.196	-0.159
a_2	0.004	1.127	0.808
a_3	0.287	-3.466	-1.908
a_4	-0.789	3.922	1.676
a_5	0.651	-1.031	0.041
$\tau^f_B = 8.0$			
a_0	0.955	1.012	0.019
a_1	-0.187	-0.201	-0.001
a_2	0.814	0.842	-0.217
a_3	-2.299	-2.067	0.702
a_4	2.455	1.294	-1.347
a_5	-0.697	0.640	1.581

Table C.6: **Dust effects** $corr^{B/D}$, as in Table C.1, but for $B/D = 0.5$.

Fits with exponential + Sérsic functions; B band

	$\frac{R^{B/D}_{app,d}}{R_{app,d}}$	$\frac{R^{eff,B/D}_{app,b}}{R^{eff}_{app,b}}$	$n^{sers,B/D}_{app,b} - n^{sers}_{app,b}$
$\tau^f_B = 0.1$			
a_0	0.975	1.053	0.060
a_1	-0.148	-0.028	0.009
a_2	0.882	0.213	-0.135
a_3	-2.816	-0.887	-0.128
a_4	3.757	1.234	0.802
a_5	-1.716	-0.514	-0.556
$\tau^f_B = 0.3$			
a_0	0.967	1.050	0.059
a_1	-0.126	0.108	0.071
a_2	0.401	-1.361	-0.805
a_3	-0.702	5.424	3.409
a_4	-0.081	-9.121	-6.299
a_5	0.687	5.445	4.154
$\tau^f_B = 0.5$			
a_0	0.962	1.049	0.059
a_1	-0.286	-0.000	0.016
a_2	1.936	-0.285	-0.660
a_3	-5.988	1.775	4.042
a_4	7.093	-4.318	-8.656
a_5	-2.646	3.381	6.135
$\tau^f_B = 1.0$			
a_0	0.941	1.046	0.052
a_1	0.035	0.114	0.109
a_2	-1.281	-0.999	-0.161
a_3	4.626	2.699	-1.694
a_4	-7.772	-3.746	4.193
a_5	4.418	1.909	-2.450
$\tau^f_B = 2.0$			
a_0	0.910	1.041	0.051
a_1	-0.098	-0.041	0.265
a_2	-1.254	-0.400	-2.782
a_3	5.051	0.893	8.067
a_4	-8.409	-1.420	-10.475
a_5	4.931	1.081	5.384
$\tau^f_B = 4.0$			
a_0	0.866	1.022	0.041
a_1	-0.050	-0.071	-0.097
a_2	-0.828	0.475	1.809
a_3	3.678	-2.484	-9.367
a_4	-5.988	4.204	15.734
a_5	3.411	-2.041	-7.875
$\tau^f_B = 8.0$			
a_0	0.877	1.024	0.033
a_1	0.009	0.023	-0.101
a_2	-0.338	0.188	2.396
a_3	2.718	-0.023	-10.952
a_4	-5.596	-1.492	18.703
a_5	3.379	1.921	-9.977

Table C.7: **Dust effects** $corr^{B/D}$, as in Table C.1, but for $B/D = 0.5$, in V band.

Fits with exponential + Sérsic functions; V band

	$\frac{R^{B/D}_{app,d}}{R_{app,d}}$	$\frac{R^{eff,B/D}_{app,b}}{R^{eff}_{app,b}}$	$n^{sers,B/D}_{app,b} - n^{sers}_{app,b}$
$\tau^f_B = 0.1$			
a_0	0.975	1.044	0.042
a_1	-0.129	0.010	0.096
a_2	0.727	0.076	-0.208
a_3	-2.298	-0.678	-0.463
a_4	3.073	1.216	1.697
a_5	-1.414	-0.640	-1.202
$\tau^f_B = 0.3$			
a_0	0.968	1.040	0.041
a_1	-0.150	0.063	0.203
a_2	0.885	-0.538	-1.419
a_3	-2.863	1.794	4.325
a_4	3.628	-2.973	-6.063
a_5	-1.468	1.894	3.249
$\tau^f_B = 0.5$			
a_0	0.962	1.036	0.039
a_1	-0.079	0.267	0.291
a_2	-0.014	-2.821	-2.762
a_3	0.785	10.684	10.573
a_4	-2.455	-17.093	-17.184
a_5	2.045	9.725	9.961
$\tau^f_B = 1.0$			
a_0	0.951	1.038	0.036
a_1	-0.208	-0.096	0.075
a_2	1.435	1.432	0.669
a_3	-5.083	-6.078	-4.573
a_4	6.844	9.365	8.054
a_5	-3.207	-4.804	-4.110
$\tau^f_B = 2.0$			
a_0	0.924	1.032	0.040
a_1	0.044	0.097	0.279
a_2	-2.252	-1.124	-2.102
a_3	8.263	2.876	5.284
a_4	-12.975	-3.796	-6.223
a_5	7.126	1.968	2.983
$\tau^f_B = 4.0$			
a_0	0.883	1.022	0.033
a_1	-0.142	-0.126	-0.013
a_2	-0.665	0.466	0.139
a_3	3.237	-2.179	-2.154
a_4	-5.521	3.504	4.176
a_5	3.305	-1.595	-1.762
$\tau^f_B = 8.0$			
a_0	0.862	1.005	0.022
a_1	0.041	0.114	0.064
a_2	-0.832	-0.513	1.146
a_3	3.801	1.215	-8.380
a_4	-6.362	-1.758	16.574
a_5	3.557	1.358	-9.405

Table C.8: **Dust effects** $corr^{B/D}$, as in Table C.1, but for $B/D = 0.5$, in I band.

Fits with exponential + Sérsic functions; I band

	$\frac{R^{B/D}_{app,d}}{R_{app,d}}$	$\frac{R^{eff,B/D}_{app,b}}{R^{eff}_{app,b}}$	$n^{sers,B/D}_{app,b} - n^{sers}_{app,b}$
$\tau^f_B = 0.1$			
a_0	0.978	1.050	0.051
a_1	-0.161	-0.142	-0.090
a_2	0.774	0.956	1.085
a_3	-2.037	-2.907	-4.317
a_4	2.384	3.809	6.685
a_5	-0.982	-1.782	-3.536
$\tau^f_B = 0.3$			
a_0	0.973	1.048	0.048
a_1	-0.192	-0.136	0.087
a_2	1.148	0.806	-0.689
a_3	-3.578	-2.215	1.846
a_4	4.709	2.525	-2.178
a_5	-2.132	-0.931	1.014
$\tau^f_B = 0.5$			
a_0	0.968	1.045	0.044
a_1	-0.209	-0.035	0.167
a_2	1.288	-0.368	-1.825
a_3	-4.040	2.342	6.906
a_4	5.162	-4.684	-10.682
a_5	-2.188	3.082	5.878
$\tau^f_B = 1.0$			
a_0	0.958	1.035	0.036
a_1	-0.108	0.153	0.312
a_2	0.046	-2.074	-3.106
a_3	0.900	8.710	11.728
a_4	-2.996	-15.002	-18.769
a_5	2.511	9.068	10.846
$\tau^f_B = 2.0$			
a_0	0.940	1.032	0.042
a_1	0.004	0.053	-0.127
a_2	-1.104	-0.500	1.852
a_3	4.487	1.452	-7.337
a_4	-7.467	-2.071	10.966
a_5	4.057	0.973	-5.447
$\tau^f_B = 4.0$			
a_0	0.907	1.022	0.038
a_1	0.001	0.107	0.245
a_2	-1.599	-1.288	-2.852
a_3	5.735	3.324	9.345
a_4	-9.121	-4.486	-13.265
a_5	5.206	2.471	7.004
$\tau^f_B = 8.0$			
a_0	0.867	1.001	0.020
a_1	0.053	0.169	0.247
a_2	-1.451	-1.413	-1.429
a_3	4.945	3.181	2.237
a_4	-6.979	-3.181	-1.786
a_5	3.643	1.437	1.429

Table C.9: **Dust effects** $corr^{B/D}$, as in Table C.1, but for $B/D = 0.5$, in J band.

Fits with exponential + Sérsic functions; J band

	$\frac{R^{B/D}_{app,d}}{R_{app,d}}$	$\frac{R^{eff,B/D}_{app,b}}{R^{eff}_{app,b}}$	$n^{sers,B/D}_{app,b} - n^{sers}_{app,b}$
$\tau^f_B = 0.1$			
a_0	0.976	1.041	0.042
a_1	-0.095	-0.009	0.122
a_2	0.231	0.067	-0.757
a_3	-0.283	-0.452	1.133
a_4	-0.018	0.839	0.109
a_5	0.184	-0.492	-0.772
$\tau^f_B = 0.3$			
a_0	0.974	1.039	0.043
a_1	-0.129	-0.029	0.109
a_2	0.529	0.235	-0.626
a_3	-1.331	-1.006	0.695
a_4	1.481	1.576	0.642
a_5	-0.556	-0.810	-0.951
$\tau^f_B = 0.5$			
a_0	0.972	1.038	0.042
a_1	-0.166	-0.033	0.144
a_2	0.872	0.232	-1.266
a_3	-2.557	-0.916	3.522
a_4	3.235	1.300	-3.905
a_5	-1.411	-0.558	1.517
$\tau^f_B = 1.0$			
a_0	0.965	1.032	0.038
a_1	-0.217	0.104	0.149
a_2	1.334	-1.287	-1.586
a_3	-4.183	4.887	5.985
a_4	5.403	-7.830	-9.445
a_5	-2.329	4.546	5.384
$\tau^f_B = 2.0$			
a_0	0.950	1.028	0.039
a_1	0.022	0.127	0.079
a_2	-1.341	-1.730	-0.827
a_3	5.717	7.063	3.189
a_4	-9.594	-12.003	-5.662
a_5	5.738	7.332	3.912
$\tau^f_B = 4.0$			
a_0	0.933	1.023	0.032
a_1	-0.060	0.215	0.155
a_2	-0.568	-2.487	-1.340
a_3	2.453	8.771	4.336
a_4	-3.997	-12.548	-5.566
a_5	2.012	6.074	2.450
$\tau^f_B = 8.0$			
a_0	0.904	1.018	0.035
a_1	-0.132	-0.044	-0.115
a_2	0.010	0.256	1.610
a_3	0.834	-0.752	-5.263
a_4	-3.215	-0.683	4.990
a_5	2.713	1.435	-0.834

Table C.10: **Dust effects** $corr^{B/D}$, as in Table C.1, but for $B/D = 0.5$, in K band.

Fits with exponential + Sérsic functions; K band

	$\frac{R_{app,d}^{B/D}}{R_{app,d}}$	$\frac{R_{app,b}^{eff,B/D}}{R_{app,b}^{eff}}$	$n_{app,b}^{sers,B/D} - n_{app,b}^{sers}$
$\tau_B^f = 0.1$			
a_0	0.976	1.035	0.038
a_1	-0.076	-0.023	-0.127
a_2	-0.074	-0.160	0.643
a_3	0.937	0.726	-1.553
a_4	-1.910	-1.128	2.009
a_5	1.193	0.575	-1.140
$\tau_B^f = 0.3$			
a_0	0.975	1.035	0.038
a_1	-0.077	-0.032	-0.094
a_2	-0.069	-0.096	0.297
a_3	0.888	0.530	-0.310
a_4	-1.809	-0.860	0.199
a_5	1.131	0.447	-0.224
$\tau_B^f = 0.5$			
a_0	0.973	1.034	0.038
a_1	-0.081	-0.036	-0.092
a_2	-0.026	-0.066	0.258
a_3	0.706	0.412	-0.082
a_4	-1.519	-0.678	-0.265
a_5	0.975	0.358	0.081
$\tau_B^f = 1.0$			
a_0	0.970	1.033	0.029
a_1	-0.102	-0.043	0.075
a_2	0.187	-0.032	-0.604
a_3	-0.129	0.349	1.670
a_4	-0.245	-0.668	-1.900
a_5	0.317	0.419	0.736
$\tau_B^f = 2.0$			
a_0	0.967	1.029	0.026
a_1	-0.186	0.008	0.266
a_2	0.923	-0.654	-2.580
a_3	-2.700	2.792	8.270
a_4	3.413	-4.620	-11.094
a_5	-1.460	2.730	5.465
$\tau_B^f = 4.0$			
a_0	0.958	1.026	0.030
a_1	-0.308	-0.029	0.089
a_2	1.954	-0.587	-1.517
a_3	-6.049	3.573	6.674
a_4	7.581	-7.594	-11.651
a_5	-3.065	5.474	7.328
$\tau_B^f = 8.0$			
a_0	0.941	1.022	0.028
a_1	-0.299	-0.220	-0.134
a_2	1.787	1.570	1.110
a_3	-6.075	-5.450	-4.165
a_4	8.707	7.785	6.589
a_5	-4.403	-3.755	-3.286

Table C.11: **Dust effects** $corr^{B/D}$ on the derived photometric parameters of **decomposed disks** and **exponential bulges** ($B/D = 0.25$): disk and bulge bulge effective radii, disk and bulge Sérsic indices. Results are listed as coefficients of polynomial fits a_k (Eq. 3.1.19) at different τ_B^f and at the effective wavelength of the B band.

Fits with two Sérsic functions; B band

	$\frac{R_{app,d}^{B/D}}{R_{app,d}}$	$\frac{R_{app,b}^{eff,B/D}}{R_{app,b}^{eff}}$	$n_{app,d}^{sers,B/D} - n_{app,d}^{sers}$	$n_{app,b}^{sers,B/D} - n_{app,b}^{sers}$
$\tau_B^f = 0.1$				
a_0	0.992	1.034	0.062	0.048
a_1	-0.048	-0.029	0.361	0.158
a_2	0.241	-0.259	-1.440	-1.650
a_3	-0.745	1.365	1.840	4.969
a_4	1.192	-1.822	-1.553	-5.847
a_5	-0.554	0.950	0.726	2.453
$\tau_B^f = 0.3$				
a_0	0.990	1.030	0.074	0.046
a_1	-0.029	0.026	0.464	0.036
a_2	-0.053	-1.073	-2.495	-1.157
a_3	0.518	5.093	5.509	5.811
a_4	-0.955	-8.311	-7.243	-10.060
a_5	0.726	4.913	3.833	5.961
$\tau_B^f = 0.5$				
a_0	0.990	1.030	0.085	0.039
a_1	-0.077	-0.203	0.646	0.037
a_2	0.416	1.198	-4.488	-0.849
a_3	-1.076	-2.472	12.489	4.785
a_4	1.226	1.646	-17.035	-9.126
a_5	-0.310	0.662	8.376	6.039
$\tau_B^f = 1.0$				
a_0	0.993	1.032	0.102	0.039
a_1	-0.075	-0.262	0.308	-0.087
a_2	0.579	2.952	-2.983	2.109
a_3	-2.158	-12.106	11.415	-9.801
a_4	3.132	19.541	-19.330	16.358
a_5	-1.523	-10.302	10.783	-8.625
$\tau_B^f = 2.0$				
a_0	1.002	1.034	0.104	0.050
a_1	-0.121	-0.114	0.142	0.012
a_2	0.144	0.066	-0.141	-0.505
a_3	0.458	-0.861	1.427	0.832
a_4	-1.689	2.056	-5.019	-0.719
a_5	1.301	-1.111	3.819	0.747
$\tau_B^f = 4.0$				
a_0	0.993	1.032	0.073	0.041
a_1	0.036	0.155	-0.080	0.177
a_2	-0.789	-1.532	0.567	-0.540
a_3	3.263	4.752	-1.864	-1.226
a_4	-5.481	-6.410	1.554	4.025
a_5	3.153	3.312	0.064	-2.016
$\tau_B^f = 8.0$				
a_0	0.980	1.065	-0.046	0.062
a_1	-0.010	0.175	-0.196	0.024
a_2	0.023	-1.062	1.132	0.704
a_3	-1.335	5.205	-9.013	-3.353
a_4	3.227	-11.194	21.288	4.740
a_5	-1.902	7.813	-13.636	-1.318

Table C.12: **Dust effects** $corr^{B/D}$, as in Table C.11, but in V band.

Fits with two Sérsic functions; V band

	$\frac{R^{B/D}_{app,d}}{R_{app,d}}$	$\frac{R^{eff,B/D}_{app,b}}{R^{eff}_{app,b}}$	$n^{sers,B/D}_{app,d} - n^{sers}_{app,d}$	$n^{sers,B/D}_{app,b} - n^{sers}_{app,b}$
$\tau^f_B = 0.1$				
a_0	0.990	1.025	0.063	0.031
a_1	-0.040	0.021	0.353	0.240
a_2	0.190	-0.591	-1.480	-1.965
a_3	-0.584	2.371	2.044	6.015
a_4	1.032	-3.093	-1.669	-7.381
a_5	-0.516	1.492	0.657	3.168
$\tau^f_B = 0.3$				
a_0	0.987	1.017	0.083	0.018
a_1	-0.027	0.085	0.166	0.459
a_2	0.031	-1.208	-0.161	-4.219
a_3	0.025	4.675	-1.496	14.703
a_4	0.029	-6.651	1.702	-20.890
a_5	0.101	3.533	-0.203	10.508
$\tau^f_B = 0.5$				
a_0	0.986	1.021	0.093	0.018
a_1	0.007	-0.415	0.382	0.374
a_2	-0.380	3.786	-2.723	-3.799
a_3	1.704	-12.383	7.509	14.618
a_4	-2.717	16.829	-10.890	-22.548
a_5	1.655	-7.510	5.803	12.294
$\tau^f_B = 1.0$				
a_0	0.988	1.018	0.090	0.025
a_1	-0.118	-0.440	0.869	-0.142
a_2	1.154	5.018	-7.399	2.181
a_3	-4.314	-19.230	23.914	-8.309
a_4	6.629	29.833	-34.780	12.521
a_5	-3.400	-15.314	17.749	-5.996
$\tau^f_B = 2.0$				
a_0	0.990	1.018	0.100	0.030
a_1	0.048	0.038	0.317	0.292
a_2	-0.890	-0.722	-1.298	-2.131
a_3	3.078	0.919	4.454	4.630
a_4	-4.529	0.853	-9.046	-3.677
a_5	2.380	-1.166	5.851	1.033
$\tau^f_B = 4.0$				
a_0	0.992	1.025	0.087	0.031
a_1	0.019	-0.038	0.126	0.220
a_2	-0.802	-0.627	-0.758	-1.689
a_3	3.314	2.201	4.103	3.281
a_4	-5.368	-3.027	-9.052	-2.604
a_5	2.980	1.739	5.979	1.286
$\tau^f_B = 8.0$				
a_0	0.985	1.035	0.017	0.030
a_1	0.050	0.252	-0.485	0.309
a_2	-0.446	-1.373	3.830	-1.029
a_3	1.152	4.080	-14.750	0.367
a_4	-1.812	-6.106	22.807	1.585
a_5	1.205	3.521	-11.499	-0.521

Table C.13: **Dust effects** $corr^{B/D}$, as in Table C.11, but in I band.

Fits with two Sérsic functions; I band

	$\frac{R^{B/D}_{app,d}}{R_{app,d}}$	$\frac{R^{eff,B/D}_{app,b}}{R^{eff}_{app,b}}$	$n^{sers,B/D}_{app,d} - n^{sers}_{app,d}$	$n^{sers,B/D}_{app,b} - n^{sers}_{app,b}$
$\tau^f_B = 0.1$				
a_0	0.986	1.027	0.061	0.038
a_1	-0.066	-0.092	0.183	-0.116
a_2	0.342	0.013	0.005	0.365
a_3	-0.906	1.010	-2.536	-0.132
a_4	1.460	-1.672	4.233	-0.258
a_5	-0.753	0.926	-2.037	0.144
$\tau^f_B = 0.3$				
a_0	0.984	1.022	0.074	0.028
a_1	-0.065	-0.079	0.197	0.183
a_2	0.334	-0.163	-0.333	-1.906
a_3	-0.901	1.706	-1.465	6.632
a_4	1.469	-2.685	2.664	-8.969
a_5	-0.739	1.484	-1.122	4.263
$\tau^f_B = 0.5$				
a_0	0.982	1.018	0.083	0.023
a_1	-0.060	-0.101	0.225	0.192
a_2	0.276	0.009	-1.253	-2.141
a_3	-0.652	1.261	3.226	8.198
a_4	1.017	-2.278	-5.797	-12.158
a_5	-0.432	1.484	3.832	6.353
$\tau^f_B = 1.0$				
a_0	0.979	1.005	0.093	0.015
a_1	-0.016	0.137	0.502	0.377
a_2	-0.202	-2.111	-3.710	-3.679
a_3	1.225	9.068	10.701	13.990
a_4	-2.026	-14.591	-15.409	-21.680
a_5	1.309	8.577	8.083	12.039
$\tau^f_B = 2.0$				
a_0	0.980	1.012	0.092	0.024
a_1	-0.015	-0.443	0.958	-0.099
a_2	0.034	4.961	-9.456	2.222
a_3	-0.313	-19.363	34.130	-9.997
a_4	1.102	31.013	-52.622	16.873
a_5	-0.846	-16.651	27.945	-9.115
$\tau^f_B = 4.0$				
a_0	0.983	1.013	0.099	0.028
a_1	0.109	0.014	0.348	0.161
a_2	-1.613	-0.468	-3.077	-1.383
a_3	5.743	-0.200	13.037	3.144
a_4	-8.454	2.248	-22.820	-3.099
a_5	4.394	-1.633	13.084	1.472
$\tau^f_B = 8.0$				
a_0	0.985	1.020	0.069	0.031
a_1	0.095	0.147	-0.137	0.131
a_2	-1.460	-1.264	0.429	-0.286
a_3	5.527	2.384	1.087	-1.760
a_4	-8.529	-1.244	-5.072	4.124
a_5	4.577	-0.034	4.065	-1.699

Table C.14: **Dust effects** $corr^{B/D}$, as in Table C.11, but in J band.

Fits with two Sérsic functions; J band

	$\frac{R^{B/D}_{app,d}}{R_{app,d}}$	$\frac{R^{eff,B/D}_{app,b}}{R^{eff}_{app,b}}$	$n^{sers,B/D}_{app,d} - n^{sers}_{app,d}$	$n^{sers,B/D}_{app,b} - n^{sers}_{app,b}$
$\tau^f_B = 0.1$				
a_0	0.991	1.017	0.068	0.028
a_1	-0.234	0.004	0.139	0.128
a_2	1.244	-0.632	-0.344	-1.242
a_3	-2.855	2.806	-0.469	3.940
a_4	3.429	-3.785	1.034	-4.701
a_5	-1.508	1.814	-0.511	1.885
$\tau^f_B = 0.3$				
a_0	0.989	1.014	0.071	0.020
a_1	-0.226	0.004	0.114	0.284
a_2	1.194	-0.663	0.094	-2.149
a_3	-2.739	3.010	-2.116	6.265
a_4	3.326	-4.127	3.141	-7.465
a_5	-1.475	2.010	-1.355	3.141
$\tau^f_B = 0.5$				
a_0	0.989	1.014	0.070	0.021
a_1	-0.245	-0.044	0.204	0.226
a_2	1.306	-0.466	-0.520	-2.334
a_3	-3.022	2.730	-0.650	7.989
a_4	3.649	-4.025	1.616	-10.606
a_5	-1.603	2.076	-0.727	4.909
$\tau^f_B = 1.0$				
a_0	0.977	1.008	0.081	0.018
a_1	-0.082	-0.043	0.289	0.235
a_2	0.388	-0.420	-1.704	-2.434
a_3	-0.851	2.489	4.348	8.816
a_4	1.348	-3.634	-7.002	-12.676
a_5	-0.667	1.995	4.361	6.533
$\tau^f_B = 2.0$				
a_0	0.982	1.001	0.107	0.017
a_1	-0.220	-0.143	-0.011	0.224
a_2	1.145	0.929	0.546	-2.570
a_3	-2.692	-3.036	-2.666	10.149
a_4	3.306	5.036	2.334	-15.923
a_5	-1.354	-2.336	-0.254	9.080
$\tau^f_B = 4.0$				
a_0	0.980	1.000	0.114	0.021
a_1	-0.221	-0.254	-0.048	-0.078
a_2	1.446	2.656	-0.151	0.791
a_3	-4.535	-10.938	2.819	-2.927
a_4	6.982	19.211	-9.102	5.404
a_5	-3.868	-11.104	6.773	-3.192
$\tau^f_B = 8.0$				
a_0	0.977	1.008	0.084	0.033
a_1	-0.015	-0.238	0.513	-0.221
a_2	-0.221	2.330	-4.661	2.416
a_3	1.278	-8.169	16.201	-7.603
a_4	-2.758	10.669	-24.072	8.442
a_5	1.835	-4.589	12.447	-2.714

Table C.15: **Dust effects** $corr^{B/D}$, as in Table C.11, but in K band.

Fits with two Sérsic functions; K band

	$\frac{R^{B/D}_{app,d}}{R_{app,d}}$	$\frac{R^{eff,B/D}_{app,b}}{R^{eff}_{app,b}}$	$n^{sers,B/D}_{app,d} - n^{sers}_{app,d}$	$n^{sers,B/D}_{app,b} - n^{sers}_{app,b}$
$\tau^f_B = 0.1$				
a_0	0.976	1.009	0.060	0.020
a_1	-0.057	-0.036	0.286	-0.012
a_2	0.209	-0.610	-1.213	-0.801
a_3	-0.120	3.216	1.711	3.907
a_4	0.367	-4.609	-1.568	-5.811
a_5	-0.283	2.274	0.673	2.764
$\tau^f_B = 0.3$				
a_0	0.976	1.008	0.061	0.017
a_1	-0.055	-0.034	0.238	-0.003
a_2	0.191	-0.644	-0.830	-0.804
a_3	-0.066	3.370	0.646	4.035
a_4	0.296	-4.844	-0.316	-6.220
a_5	-0.250	2.395	0.144	3.069
$\tau^f_B = 0.5$				
a_0	0.975	1.007	0.063	0.017
a_1	-0.055	-0.033	0.325	-0.002
a_2	0.185	-0.662	-1.850	-0.843
a_3	-0.039	3.450	3.964	4.264
a_4	0.256	-4.971	-4.488	-6.685
a_5	-0.229	2.468	1.947	3.374
$\tau^f_B = 1.0$				
a_0	0.974	1.004	0.071	0.016
a_1	-0.053	-0.024	0.120	0.036
a_2	0.179	-0.761	-0.172	-1.193
a_3	-0.034	3.860	-1.243	5.349
a_4	0.262	-5.610	2.053	-8.160
a_5	-0.233	2.827	-0.861	4.146
$\tau^f_B = 2.0$				
a_0	0.972	1.000	0.069	0.015
a_1	-0.071	-0.035	0.342	0.103
a_2	0.353	-0.660	-2.006	-1.863
a_3	-0.649	3.583	4.710	7.693
a_4	1.142	-5.323	-6.281	-11.597
a_5	-0.654	2.815	3.365	6.057
$\tau^f_B = 4.0$				
a_0	0.973	1.002	0.072	0.018
a_1	-0.183	-0.310	0.698	-0.221
a_2	1.294	1.745	-5.315	0.646
a_3	-3.845	-4.537	16.435	0.764
a_4	5.715	6.155	-24.402	-3.729
a_5	-2.912	-2.667	13.434	3.247
$\tau^f_B = 8.0$				
a_0	0.970	0.997	0.091	0.008
a_1	-0.186	-0.415	0.162	-0.160
a_2	1.424	3.158	-0.792	1.525
a_3	-4.895	-11.033	2.111	-5.144
a_4	8.047	17.805	-5.017	8.105
a_5	-4.495	-9.490	3.509	-4.160

Table C.16: **Dust effects** $corr^{B/D}$, as in Table C.11, but for $B/D = 0.5$.

Fits with two Sérsic functions; B band

	$\frac{R^{B/D}_{app,d}}{R_{app,d}}$	$\frac{R^{eff,B/D}_{app,b}}{R^{eff}_{app,b}}$	$n^{sers,B/D}_{app,d} - n^{sers}_{app,d}$	$n^{sers,B/D}_{app,b} - n^{sers}_{app,b}$
$\tau^f_B = 0.1$				
a_0	0.972	1.038	0.054	0.049
a_1	0.080	-0.136	2.104	0.098
a_2	-0.723	0.633	-12.234	-1.012
a_3	1.864	-1.552	30.708	2.688
a_4	-1.871	2.198	-37.826	-2.604
a_5	0.814	-1.074	17.830	0.857
$\tau^f_B = 0.3$				
a_0	0.972	1.033	0.093	0.049
a_1	-0.011	-0.129	1.939	-0.251
a_2	-0.196	0.555	-11.377	2.018
a_3	0.603	-0.948	27.767	-5.956
a_4	-0.641	0.783	-33.698	7.518
a_5	0.486	0.078	15.686	-3.207
$\tau^f_B = 0.5$				
a_0	0.971	1.032	0.105	0.048
a_1	0.009	-0.181	2.226	-0.158
a_2	-0.491	0.850	-14.275	0.522
a_3	2.158	-1.091	36.735	0.896
a_4	-3.635	-0.416	-44.661	-4.247
a_5	2.360	1.586	19.925	3.731
$\tau^f_B = 1.0$				
a_0	0.965	1.018	0.146	0.051
a_1	0.081	0.010	1.461	-0.452
a_2	0.234	1.766	-12.794	5.115
a_3	-3.136	-10.098	44.755	-19.288
a_4	6.184	18.275	-68.310	28.872
a_5	-3.606	-10.348	36.167	-14.575
$\tau^f_B = 2.0$				
a_0	0.981	1.044	0.074	0.061
a_1	0.031	-0.135	1.646	-0.071
a_2	-0.686	-0.048	-4.774	-0.036
a_3	1.386	0.025	4.789	-0.926
a_4	-1.460	0.006	0.929	2.008
a_5	0.688	0.235	-3.144	-0.700
$\tau^f_B = 4.0$				
a_0	0.989	1.041	0.136	0.052
a_1	-0.097	0.058	-0.393	0.039
a_2	0.462	-0.740	5.034	0.439
a_3	-1.651	1.710	-18.223	-4.481
a_4	2.455	-2.145	28.229	8.423
a_5	-1.377	1.341	-15.655	-4.064
$\tau^f_B = 8.0$				
a_0	0.981	1.057	0.001	0.051
a_1	0.025	0.039	0.598	0.147
a_2	-0.797	-0.095	-5.859	0.282
a_3	2.809	1.272	16.112	-4.339
a_4	-3.575	-4.882	-12.027	9.062
a_5	1.411	4.553	0.397	-4.738

Table C.17: **Dust effects** $corr^{B/D}$, as in Table C.11, but for $B/D = 0.5$, in V band.

Fits with two Sérsic functions; V band

	$\frac{R^{B/D}_{app,d}}{R_{app,d}}$	$\frac{R^{eff,B/D}_{app,b}}{R^{eff}_{app,b}}$	$n^{sers,B/D}_{app,d} - n^{sers}_{app,d}$	$n^{sers,B/D}_{app,b} - n^{sers}_{app,b}$
$\tau^f_B = 0.1$				
a_0	0.978	1.024	0.135	0.030
a_1	-0.093	0.024	0.445	0.249
a_2	0.378	-0.471	-1.439	-1.797
a_3	-1.089	1.757	0.320	5.069
a_4	1.766	-2.110	0.484	-5.887
a_5	-0.864	0.923	0.159	2.432
$\tau^f_B = 0.3$				
a_0	0.973	1.022	0.156	0.021
a_1	-0.105	-0.224	0.546	0.245
a_2	0.404	2.037	-2.746	-2.074
a_3	-1.020	-7.056	4.983	7.272
a_4	1.431	10.450	-6.621	-10.477
a_5	-0.510	-5.176	3.906	5.420
$\tau^f_B = 0.5$				
a_0	0.971	1.017	0.175	0.019
a_1	-0.135	-0.084	0.639	0.302
a_2	0.671	0.856	-4.549	-2.831
a_3	-1.824	-3.599	12.153	10.409
a_4	2.444	6.618	-17.560	-15.454
a_5	-0.954	-3.785	9.383	8.193
$\tau^f_B = 1.0$				
a_0	0.973	1.020	0.173	0.025
a_1	-0.259	-0.361	1.234	-0.199
a_2	2.308	4.149	-11.314	2.996
a_3	-8.230	-15.905	37.567	-11.491
a_4	12.261	24.772	-55.886	17.199
a_5	-6.256	-12.870	29.118	-8.431
$\tau^f_B = 2.0$				
a_0	0.979	1.024	0.174	0.038
a_1	0.001	0.066	-0.318	0.166
a_2	-0.897	-1.123	6.955	-1.393
a_3	2.878	2.757	-25.779	3.072
a_4	-4.116	-2.616	35.040	-2.756
a_5	2.125	0.887	-16.623	1.078
$\tau^f_B = 4.0$				
a_0	0.986	1.033	0.134	0.043
a_1	-0.142	-0.028	0.015	0.034
a_2	0.459	-0.765	3.855	-0.220
a_3	-1.600	2.218	-14.969	-1.427
a_4	2.336	-2.860	22.085	3.572
a_5	-1.210	1.650	-11.812	-1.588
$\tau^f_B = 8.0$				
a_0	0.984	1.034	0.075	0.040
a_1	-0.061	0.170	-0.338	0.041
a_2	0.227	-1.002	3.263	1.361
a_3	-0.742	2.930	-13.577	-8.411
a_4	0.907	-5.089	25.760	14.889
a_5	-0.488	3.555	-16.385	-7.630

Table C.18: **Dust effects** $corr^{B/D}$, as in Table C.11, but for $B/D = 0.5$, in I band.

Fits with two Sérsic functions; I band

	$\frac{R^{B/D}_{app,d}}{R_{app,d}}$	$\frac{R^{eff,B/D}_{app,b}}{R^{eff}_{app,b}}$	$n^{sers,B/D}_{app,d} - n^{sers}_{app,d}$	$n^{sers,B/D}_{app,b} - n^{sers}_{app,b}$
$\tau^f_B = 0.1$				
a_0	0.974	1.029	0.099	0.039
a_1	-0.192	-0.123	0.868	-0.194
a_2	0.947	0.327	-3.837	1.128
a_3	-2.333	-0.066	6.021	-2.514
a_4	3.151	-0.224	-5.230	2.684
a_5	-1.493	0.185	2.141	-1.095
$\tau^f_B = 0.3$				
a_0	0.968	1.024	0.128	0.037
a_1	-0.170	-0.125	0.673	-0.013
a_2	0.772	0.398	-3.540	-0.710
a_3	-1.791	-0.400	7.144	3.772
a_4	2.418	0.369	-8.966	-6.093
a_5	-1.085	-0.101	4.919	3.258
$\tau^f_B = 0.5$				
a_0	0.961	1.022	0.152	0.027
a_1	-0.108	-0.299	0.593	-0.029
a_2	0.315	2.259	-4.396	0.007
a_3	-0.355	-7.167	13.571	1.062
a_4	0.376	10.278	-22.160	-2.522
a_5	0.023	-5.044	13.216	1.786
$\tau^f_B = 1.0$				
a_0	0.956	1.008	0.177	0.016
a_1	-0.072	0.070	0.480	0.250
a_2	-0.040	-1.208	-3.024	-2.268
a_3	1.061	5.407	6.687	8.677
a_4	-1.956	-8.874	-9.220	-13.644
a_5	1.382	5.425	4.793	7.774
$\tau^f_B = 2.0$				
a_0	0.961	1.016	0.168	0.025
a_1	-0.245	-0.416	0.875	-0.157
a_2	2.163	4.658	-8.357	2.685
a_3	-7.751	-17.916	29.428	-11.192
a_4	11.926	28.274	-46.563	18.085
a_5	-6.439	-15.169	25.453	-9.656
$\tau^f_B = 4.0$				
a_0	0.970	1.020	0.154	0.030
a_1	-0.011	0.076	0.216	0.209
a_2	-0.875	-1.190	0.141	-1.613
a_3	2.837	2.683	0.808	3.045
a_4	-4.259	-2.745	-4.347	-2.245
a_5	2.372	1.252	3.249	0.808
$\tau^f_B = 8.0$				
a_0	0.976	1.028	0.107	0.036
a_1	0.002	0.024	0.165	0.013
a_2	-0.988	-0.413	-0.177	1.095
a_3	3.793	-0.290	2.722	-7.468
a_4	-6.019	1.771	-6.248	13.165
a_5	3.298	-1.014	3.516	-6.578

Table C.19: **Dust effects** $corr^{B/D}$, as in Table C.11, but for $B/D = 0.5$, in J band.

Fits with two Sérsic functions; J band

	$\frac{R^{B/D}_{app,d}}{R_{app,d}}$	$\frac{R^{eff,B/D}_{app,b}}{R^{eff}_{app,b}}$	$n^{sers,B/D}_{app,d} - n^{sers}_{app,d}$	$n^{sers,B/D}_{app,b} - n^{sers}_{app,b}$
$\tau^f_B = 0.1$				
a_0	0.975	1.021	0.121	0.029
a_1	-0.353	-0.041	0.129	0.071
a_2	1.862	-0.199	0.836	-0.760
a_3	-4.388	1.394	-6.348	2.589
a_4	5.364	-1.973	9.530	-3.184
a_5	-2.423	0.935	-4.370	1.310
$\tau^f_B = 0.3$				
a_0	0.971	1.018	0.126	0.021
a_1	-0.349	-0.046	0.184	0.227
a_2	1.845	-0.186	0.344	-1.667
a_3	-4.353	1.438	-4.961	4.914
a_4	5.355	-2.085	7.770	-5.947
a_5	-2.423	1.019	-3.491	2.567
$\tau^f_B = 0.5$				
a_0	0.968	1.016	0.132	0.020
a_1	-0.339	-0.051	0.307	0.264
a_2	1.776	-0.154	-0.919	-2.035
a_3	-4.154	1.343	-0.875	6.217
a_4	5.109	-1.940	2.086	-7.894
a_5	-2.293	0.968	-0.565	3.634
$\tau^f_B = 1.0$				
a_0	0.953	1.008	0.149	0.023
a_1	-0.170	-0.083	0.511	0.072
a_2	0.917	0.537	-4.186	-0.823
a_3	-2.431	-1.867	13.810	3.182
a_4	3.711	3.536	-23.660	-4.598
a_5	-1.891	-2.041	14.699	2.468
$\tau^f_B = 2.0$				
a_0	0.954	1.000	0.189	0.021
a_1	-0.269	0.027	-0.270	-0.074
a_2	1.466	-0.494	2.759	0.729
a_3	-3.885	1.850	-10.365	-2.505
a_4	5.414	-2.337	12.328	3.818
a_5	-2.523	1.544	-4.954	-1.699
$\tau^f_B = 4.0$				
a_0	0.954	1.004	0.184	0.023
a_1	-0.260	-0.099	0.302	-0.197
a_2	1.548	1.038	-3.666	1.942
a_3	-4.884	-4.889	15.502	-6.600
a_4	7.988	9.891	-29.345	10.198
a_5	-4.783	-6.330	17.995	-5.528
$\tau^f_B = 8.0$				
a_0	0.959	1.016	0.143	0.034
a_1	-0.221	-0.242	0.912	-0.370
a_2	1.436	2.248	-7.840	4.188
a_3	-4.067	-7.436	25.261	-14.120
a_4	3.743	8.615	-33.623	17.567
a_5	-0.840	-3.093	15.496	-7.098

Table C.20: **Dust effects** $corr^{B/D}$, as in Table C.11, but for $B/D = 0.5$, in K band.

Fits with two Sérsic functions; K band

	$\frac{R^{B/D}_{app,d}}{R_{app,d}}$	$\frac{R^{eff,B/D}_{app,b}}{R^{eff}_{app,b}}$	$n^{sers,B/D}_{app,d} - n^{sers}_{app,d}$	$n^{sers,B/D}_{app,b} - n^{sers}_{app,b}$
$\tau^f_B = 0.1$				
a_0	0.958	1.015	0.102	0.019
a_1	-0.177	-0.093	0.355	0.092
a_2	0.731	-0.035	-0.951	-0.971
a_3	-1.063	1.307	-1.009	3.393
a_4	1.270	-2.188	2.991	-4.556
a_5	-0.636	1.143	-1.570	2.100
$\tau^f_B = 0.3$				
a_0	0.954	1.010	0.111	0.019
a_1	-0.126	-0.017	0.161	0.082
a_2	0.446	-0.480	0.302	-1.132
a_3	-0.389	2.423	-4.445	4.386
a_4	0.560	-3.418	7.108	-6.282
a_5	-0.361	1.641	-3.338	3.042
$\tau^f_B = 0.5$				
a_0	0.955	1.009	0.105	0.021
a_1	-0.149	-0.015	0.339	0.004
a_2	0.578	-0.496	-0.809	-0.761
a_3	-0.715	2.487	-1.805	3.677
a_4	0.925	-3.515	4.395	-5.631
a_5	-0.510	1.699	-2.306	2.818
$\tau^f_B = 1.0$				
a_0	0.952	1.007	0.121	0.021
a_1	-0.148	-0.016	0.134	-0.054
a_2	0.594	-0.514	0.196	-0.455
a_3	-0.799	2.608	-3.785	3.144
a_4	1.071	-3.738	5.823	-5.363
a_5	-0.580	1.851	-2.459	2.899
$\tau^f_B = 2.0$				
a_0	0.949	1.005	0.121	0.019
a_1	-0.175	-0.090	0.368	-0.128
a_2	0.895	0.257	-2.242	0.378
a_3	-1.961	-0.202	5.324	0.351
a_4	2.871	0.442	-8.539	-1.709
a_5	-1.509	-0.241	5.636	1.382
$\tau^f_B = 4.0$				
a_0	0.944	1.000	0.145	0.019
a_1	-0.231	-0.157	0.329	-0.143
a_2	1.701	0.982	-3.663	0.568
a_3	-5.826	-2.965	15.835	-0.322
a_4	9.941	4.571	-32.367	-0.873
a_5	-5.762	-2.100	22.328	1.270
$\tau^f_B = 8.0$				
a_0	0.943	1.001	0.143	0.008
a_1	-0.347	-0.379	0.579	-0.121
a_2	2.689	3.168	-4.344	1.484
a_3	-9.361	-11.521	13.545	-5.947
a_4	15.089	18.510	-21.712	10.133
a_5	-8.386	-9.903	12.003	-5.557

Table C.21: **Dust effects** $corr^{B/D}$ on the derived photometric parameters of **decomposed disks** and **de Vaucouleurs bulges** ($B/D = 0.25$): disk scale-lengths, bulge effective radii and Sérsic indices. Results are listed as coefficients of polynomial fits a_k (Eq. 3.1.19) at different τ^f_B and at the effective wavelength of the B band.

Fits with exponential + Sérsic functions; B band

	$\frac{R^{B/D}_{app,d}}{R_{app,d}}$	$\frac{R^{eff,B/D}_{app,b}}{R^{eff}_{app,b}}$	$n^{sers,B/D}_{app,b} - n^{sers}_{app,b}$
$\tau^f_B = 0.1$			
a_0	1.070	1.395	0.853
a_1	0.134	-0.642	-2.320
a_2	-1.364	4.199	11.096
a_3	5.414	-13.700	-30.568
a_4	-8.542	25.900	53.806
a_5	4.371	-19.215	-38.749
$\tau^f_B = 0.3$			
a_0	1.064	1.365	0.803
a_1	0.053	-0.566	-2.229
a_2	-0.883	1.224	6.411
a_3	3.916	0.204	-8.191
a_4	-6.780	-1.385	10.484
a_5	3.594	-1.716	-12.365
$\tau^f_B = 0.5$			
a_0	1.050	1.320	0.727
a_1	0.335	-0.839	-2.288
a_2	-4.166	2.654	4.895
a_3	15.531	-4.983	-3.697
a_4	-23.555	3.529	1.112
a_5	11.831	-2.377	-7.729
$\tau^f_B = 1.0$			
a_0	1.051	1.248	0.604
a_1	-0.137	-0.528	-1.083
a_2	-0.330	-2.975	-17.119
a_3	0.912	9.579	68.672
a_4	-2.942	-14.930	-117.677
a_5	2.383	8.920	71.827
$\tau^f_B = 2.0$			
a_0	0.978	1.012	0.076
a_1	0.182	-0.878	-2.714
a_2	-5.998	-3.648	-13.605
a_3	21.027	16.553	56.900
a_4	-29.071	-22.233	-70.425
a_5	14.130	10.385	31.500
$\tau^f_B = 4.0$			
a_0	0.983	–	–
a_1	-0.714	–	–
a_2	0.486	–	–
a_3	3.727	–	–
a_4	-8.233	–	–
a_5	4.886	–	–
$\tau^f_B = 8.0$			
a_0	1.037	–	–
a_1	-1.070	–	–
a_2	7.122	–	–
a_3	-20.169	–	–
a_4	23.727	–	–
a_5	-9.725	–	–

Table C.22: **Dust effects** $corr^{B/D}$, as in Table C.21, but in V band.

Fits with exponential + Sérsic functions; V band

	$\frac{R^{B/D}_{app,d}}{R_{app,d}}$	$\frac{R^{eff,B/D}_{app,b}}{R^{eff}_{app,b}}$	$n^{sers,B/D}_{app,b} - n^{sers}_{app,b}$
$\tau^f_B = 0.1$			
a_0	1.068	1.424	0.921
a_1	0.101	-1.102	-4.317
a_2	-1.105	7.678	25.559
a_3	4.590	-23.290	-69.399
a_4	-7.403	38.069	99.618
a_5	3.811	-25.144	-58.642
$\tau^f_B = 0.3$			
a_0	1.064	1.411	0.886
a_1	0.046	-0.970	-3.849
a_2	-0.742	4.847	20.365
a_3	3.449	-10.449	-50.378
a_4	-6.133	13.123	66.667
a_5	3.356	-9.114	-39.330
$\tau^f_B = 0.5$			
a_0	1.056	1.363	0.599
a_1	0.134	-0.539	1.968
a_2	-1.817	-0.003	-25.130
a_3	7.081	7.028	93.930
a_4	-11.154	-16.542	-139.143
a_5	5.631	8.973	67.337
$\tau^f_B = 1.0$			
a_0	1.038	1.287	0.702
a_1	-0.034	-1.544	-3.878
a_2	-0.784	8.860	17.194
a_3	3.634	-29.996	-50.132
a_4	-7.410	41.118	59.495
a_5	4.384	-20.963	-28.486
$\tau^f_B = 2.0$			
a_0	0.990	1.041	0.057
a_1	0.410	0.524	-0.792
a_2	-6.170	-13.996	-19.981
a_3	19.490	49.397	78.949
a_4	-26.032	-71.211	-124.478
a_5	12.428	37.202	72.903
$\tau^f_B = 4.0$			
a_0	1.003	–	–
a_1	-0.584	–	–
a_2	-1.444	–	–
a_3	9.879	–	–
a_4	-16.168	–	–
a_5	8.429	–	–
$\tau^f_B = 8.0$			
a_0	0.995	–	–
a_1	-0.732	–	–
a_2	2.334	–	–
a_3	-3.017	–	–
a_4	0.376	–	–
a_5	1.220	–	–

Table C.23: **Dust effects** $corr^{B/D}$, as in Table C.21, but in I band.

Fits with exponential + Sérsic functions; I band

	$\frac{R^{B/D}_{app,d}}{R_{app,d}}$	$\frac{R^{eff,B/D}_{app,b}}{R^{eff}_{app,b}}$	$n^{sers,B/D}_{app,b} - n^{sers}_{app,b}$
$\tau^f_B = 0.1$			
a_0	1.056	1.486	1.018
a_1	0.073	-0.997	-4.107
a_2	-0.904	7.862	25.624
a_3	3.859	-26.929	-75.916
a_4	-6.318	48.268	118.671
a_5	3.284	-33.255	-73.452
$\tau^f_B = 0.3$			
a_0	1.053	1.496	1.025
a_1	0.075	-0.865	-3.635
a_2	-1.041	4.867	18.952
a_3	4.443	-12.952	-48.032
a_4	-7.399	21.403	69.455
a_5	3.961	-16.060	-44.093
$\tau^f_B = 0.5$			
a_0	1.050	1.489	1.003
a_1	0.020	-0.932	-3.330
a_2	-0.551	4.101	14.121
a_3	2.701	-8.941	-28.595
a_4	-5.012	11.954	34.324
a_5	2.834	-9.003	-22.256
$\tau^f_B = 1.0$			
a_0	1.039	1.418	0.895
a_1	0.013	-1.228	-3.568
a_2	-0.674	4.478	13.614
a_3	2.739	-9.143	-28.817
a_4	-4.526	7.643	32.226
a_5	2.099	-3.724	-20.338
$\tau^f_B = 2.0$			
a_0	1.013	1.265	0.670
a_1	-0.056	-1.348	-3.254
a_2	-0.447	5.472	6.536
a_3	1.520	-19.658	-12.657
a_4	-3.751	26.989	-1.953
a_5	2.543	-12.964	11.009
$\tau^f_B = 4.0$			
a_0	1.011	–	–
a_1	0.149	–	–
a_2	-5.924	–	–
a_3	19.822	–	–
a_4	-25.736	–	–
a_5	11.661	–	–
$\tau^f_B = 8.0$			
a_0	0.985	–	–
a_1	-0.346	–	–
a_2	-3.124	–	–
a_3	15.567	–	–
a_4	-24.242	–	–
a_5	12.449	–	–

Table C.24: **Dust effects** $corr^{B/D}$, as in Table C.21, but in J band.

Fits with exponential + Sérsic functions; J band

	$\frac{R^{B/D}_{app,d}}{R_{app,d}}$	$\frac{R^{eff,B/D}_{app,b}}{R^{eff}_{app,b}}$	$n^{sers,B/D}_{app,b} - n^{sers}_{app,b}$
$\tau^f_B = 0.1$			
a_0	1.041	1.541	1.025
a_1	0.055	-0.108	0.300
a_2	-0.770	1.519	-15.752
a_3	3.296	-2.016	76.355
a_4	-5.468	–	-118.652
a_5	2.888	–	58.034
$\tau^f_B = 0.3$			
a_0	1.040	1.570	1.161
a_1	0.019	-0.009	-1.614
a_2	-0.597	0.727	-1.797
a_3	2.916	-1.327	32.802
a_4	-5.160	–	-62.225
a_5	2.840	–	32.225
$\tau^f_B = 0.5$			
a_0	1.039	1.575	1.177
a_1	0.015	-0.015	-2.503
a_2	-0.626	0.283	6.569
a_3	3.084	-0.915	2.656
a_4	-5.527	–	-19.900
a_5	3.098	–	11.702
$\tau^f_B = 1.0$			
a_0	1.033	1.563	1.140
a_1	0.098	-0.473	-2.944
a_2	-1.553	0.968	8.805
a_3	6.174	-1.552	-8.961
a_4	-9.797	–	–
a_5	5.159	–	–
$\tau^f_B = 2.0$			
a_0	1.019	1.425	0.940
a_1	0.229	-0.359	-2.780
a_2	-3.086	-0.497	6.604
a_3	11.441	-0.349	-8.027
a_4	-17.175	–	–
a_5	8.528	–	–
$\tau^f_B = 4.0$			
a_0	1.002	1.212	0.606
a_1	-0.026	1.032	2.665
a_2	0.595	-6.775	-18.470
a_3	-3.142	5.477	13.097
a_4	3.000	–	–
a_5	-0.658	–	- -
$\tau^f_B = 8.0$			
a_0	0.984	–	–
a_1	0.440	–	–
a_2	-6.674	–	–
a_3	19.893	–	–
a_4	-24.337	–	–
a_5	10.608	–	–

Table C.25: **Dust effects** $corr^{B/D}$, as in Table C.21, but in K band.

Fits with exponential + Sérsic functions; K band

	$\frac{R^{B/D}_{app,d}}{R_{app,d}}$	$\frac{R^{eff,B/D}_{app,b}}{R^{eff}_{app,b}}$	$n^{sers,B/D}_{app,b} - n^{sers}_{app,b}$
$\tau^f_B = 0.1$			
a_0	1.020	1.652	1.146
a_1	0.036	-0.113	-1.471
a_2	-0.629	0.881	5.680
a_3	2.641	-1.524	-5.524
a_4	-4.449	–	–
a_5	2.423	–	–
$\tau^f_B = 0.3$			
a_0	1.018	1.685	1.203
a_1	0.044	-0.094	-1.424
a_2	-0.698	0.663	5.519
a_3	2.855	-1.346	-5.542
a_4	-4.733	–	–
a_5	2.562	–	–
$\tau^f_B = 0.5$			
a_0	1.017	1.688	1.224
a_1	0.050	-0.080	-1.571
a_2	-0.770	0.478	5.823
a_3	3.095	-1.168	-5.837
a_4	-5.073	–	–
a_5	2.736	–	–
$\tau^f_B = 1.0$			
a_0	1.013	1.665	1.221
a_1	0.197	-0.062	-1.902
a_2	-2.246	0.084	6.562
a_3	8.137	-0.773	-6.637
a_4	-12.092	–	–
a_5	6.149	–	–
$\tau^f_B = 2.0$			
a_0	1.011	1.603	1.202
a_1	0.103	-0.323	-2.950
a_2	-1.432	0.395	9.061
a_3	5.425	-1.009	-9.115
a_4	-8.489	–	–
a_5	4.518	–	–
$\tau^f_B = 4.0$			
a_0	0.992	–	–
a_1	0.305	–	–
a_2	-3.528	–	–
a_3	14.060	–	–
a_4	-22.326	–	–
a_5	11.730	–	–
$\tau^f_B = 8.0$			
a_0	0.999	–	–
a_1	-0.246	–	–
a_2	2.245	–	–
a_3	-7.733	–	–
a_4	8.827	–	–
a_5	-3.377	–	–

Table C.26: **Dust effects** $corr^{B/D}$, as in Table C.21, but for $B/D = 0.5$.

Fits with exponential + Sérsic functions; B band

	$\frac{R^{B/D}_{app,d}}{R_{app,d}}$	$\frac{R^{eff,B/D}_{app,b}}{R^{eff}_{app,b}}$	$n^{sers,B/D}_{app,b} - n^{sers}_{app,b}$
$\tau^f_B = 0.1$			
a_0	1.181	1.377	0.825
a_1	0.086	-0.742	-2.375
a_2	-0.050	5.272	11.352
a_3	-0.294	-17.073	-30.390
a_4	0.000	30.379	52.066
a_5	0.000	-21.376	-37.383
$\tau^f_B = 0.3$			
a_0	1.166	1.358	0.784
a_1	0.007	-0.617	-2.134
a_2	0.167	2.324	7.026
a_3	-0.627	-3.883	-12.678
a_4	0.000	5.638	20.216
a_5	0.000	-6.086	-19.020
$\tau^f_B = 0.5$			
a_0	1.133	1.330	0.738
a_1	0.155	-0.829	-2.483
a_2	-0.394	3.387	8.172
a_3	-0.444	-7.999	-16.117
a_4	0.000	9.541	21.613
a_5	0.000	-6.721	-20.005
$\tau^f_B = 1.0$			
a_0	1.112	1.258	0.622
a_1	-0.391	-0.238	-0.544
a_2	1.496	-4.612	-20.219
a_3	-6.234	15.569	79.297
a_4	7.001	-24.970	-134.509
a_5	-2.605	14.531	80.787
$\tau^f_B = 2.0$			
a_0	1.039	1.097	0.205
a_1	0.495	-0.793	-2.277
a_2	-13.503	-5.607	-18.458
a_3	46.272	21.478	68.416
a_4	-62.552	-26.569	-80.694
a_5	29.755	11.464	34.335
$\tau^f_B = 4.0$			
a_0	1.051	–	–
a_1	-1.424	–	–
a_2	0.804	–	–
a_3	8.621	–	–
a_4	-18.910	–	–
a_5	11.158	–	–
$\tau^f_B = 8.0$			
a_0	1.200	–	–
a_1	-2.969	–	–
a_2	17.867	–	–
a_3	-49.919	–	–
a_4	59.773	–	–
a_5	-25.311	–	–

Table C.27: **Dust effects** $corr^{B/D}$, as in Table C.21, but for $B/D = 0.5$, in V band.

Fits with exponential + Sérsic functions; V band

	$\frac{R^{B/D}_{app,d}}{R_{app,d}}$	$\frac{R^{eff,B/D}_{app,b}}{R^{eff}_{app,b}}$	$n^{sers,B/D}_{app,b} - n^{sers}_{app,b}$
$\tau^f_B = 0.1$			
a_0	1.158	1.403	0.885
a_1	0.209	-1.207	-4.351
a_2	-2.131	8.843	26.338
a_3	9.674	-27.125	-72.623
a_4	-16.371	43.307	104.460
a_5	8.629	-27.758	-61.418
$\tau^f_B = 0.3$			
a_0	1.156	1.410	0.885
a_1	-0.010	-1.350	-4.277
a_2	-0.597	8.349	23.314
a_3	4.952	-22.039	-58.494
a_4	-10.514	30.361	77.282
a_5	6.116	-18.530	-44.763
$\tau^f_B = 0.5$			
a_0	1.145	1.373	0.606
a_1	0.077	-0.817	1.556
a_2	-1.801	2.766	-20.776
a_3	8.716	-2.111	78.928
a_4	-15.322	-2.472	-116.298
a_5	8.005	0.862	54.622
$\tau^f_B = 1.0$			
a_0	1.117	1.325	0.751
a_1	-0.154	-1.639	-3.935
a_2	-0.775	10.251	19.144
a_3	5.375	-34.326	-57.831
a_4	-12.721	47.427	72.905
a_5	7.847	-24.906	-37.491
$\tau^f_B = 2.0$			
a_0	1.041	1.108	0.166
a_1	0.964	0.994	-0.042
a_2	-12.999	-18.188	-25.744
a_3	39.377	61.346	92.665
a_4	-50.437	-86.315	-138.764
a_5	23.153	44.344	78.463
$\tau^f_B = 4.0$			
a_0	1.143	–	–
a_1	-1.491	–	–
a_2	-2.240	–	–
a_3	18.592	–	–
a_4	-30.174	–	–
a_5	15.192	–	–
$\tau^f_B = 8.0$			
a_0	1.101	–	–
a_1	-1.829	–	–
a_2	6.118	–	–
a_3	-9.288	–	–
a_4	3.770	–	–
a_5	1.528	–	–

Table C.28: **Dust effects** $corr^{B/D}$, as in Table C.21, but for $B/D = 0.5$, in I band.

Fits with exponential + Sérsic functions; I band

	$\frac{R^{B/D}_{app,d}}{R_{app,d}}$	$\frac{R^{eff,B/D}_{app,b}}{R^{eff}_{app,b}}$	$n^{sers,B/D}_{app,b} - n^{sers}_{app,b}$
$\tau^f_B = 0.1$			
a_0	1.132	1.466	0.981
a_1	0.154	-1.049	-3.984
a_2	-1.674	8.562	24.682
a_3	7.899	-29.059	-71.692
a_4	-13.678	50.891	110.382
a_5	7.304	-34.565	-68.439
$\tau^f_B = 0.3$			
a_0	1.127	1.480	0.999
a_1	0.159	-0.918	-3.685
a_2	-1.916	6.016	20.185
a_3	8.845	-17.404	-52.922
a_4	-15.339	28.925	77.263
a_5	8.343	-20.726	-48.853
$\tau^f_B = 0.5$			
a_0	1.123	1.480	0.986
a_1	0.043	-0.958	-3.361
a_2	-0.828	5.153	15.894
a_3	4.865	-13.076	-37.059
a_4	-9.663	19.355	49.977
a_5	5.563	-13.849	-32.354
$\tau^f_B = 1.0$			
a_0	1.105	1.432	0.915
a_1	-0.036	-1.134	-3.524
a_2	-0.291	4.502	14.146
a_3	1.793	-9.358	-31.205
a_4	-3.638	8.772	37.381
a_5	1.369	-5.130	-24.314
$\tau^f_B = 2.0$			
a_0	1.068	1.324	0.747
a_1	-0.181	-1.199	-2.809
a_2	0.382	4.815	3.647
a_3	-1.668	-17.487	-2.559
a_4	-0.614	22.761	-18.277
a_5	1.585	-10.391	19.878
$\tau^f_B = 4.0$			
a_0	1.117	–	–
a_1	0.380	–	–
a_2	-13.252	–	–
a_3	43.115	–	–
a_4	-54.002	–	–
a_5	23.483	–	–
$\tau^f_B = 8.0$			
a_0	1.128	–	–
a_1	-2.201	–	–
a_2	5.632	–	–
a_3	-9.867	–	–
a_4	11.988	–	–
a_5	-6.678	–	–

Table C.29: **Dust effects** $corr^{B/D}$, as in Table C.21, but for $B/D = 0.5$, in J band.

Fits with exponential + Sérsic functions; J band

	$\frac{R^{B/D}_{app,d}}{R_{app,d}}$	$\frac{R^{eff,B/D}_{app,b}}{R^{eff}_{app,b}}$	$n^{sers,B/D}_{app,b} - n^{sers}_{app,b}$
$\tau^f_B = 0.1$			
a_0	1.098	1.527	1.005
a_1	0.117	-0.078	0.335
a_2	-1.351	1.607	-15.833
a_3	6.410	-2.248	76.992
a_4	-11.272	–	-121.168
a_5	6.111	–	59.802
$\tau^f_B = 0.3$			
a_0	1.095	1.554	1.134
a_1	0.096	0.062	-1.224
a_2	-1.279	0.839	-4.877
a_3	6.235	-1.608	43.598
a_4	-11.155	–	-78.634
a_5	6.154	–	40.571
$\tau^f_B = 0.5$			
a_0	1.093	1.563	1.158
a_1	0.090	0.076	-2.043
a_2	-1.336	0.411	2.456
a_3	6.496	-1.237	17.777
a_4	-11.682	–	-42.884
a_5	6.529	–	23.431
$\tau^f_B = 1.0$			
a_0	1.088	1.564	1.128
a_1	0.013	-0.353	-2.567
a_2	-0.758	1.124	7.971
a_3	4.242	-1.883	-8.476
a_4	-8.282	–	–
a_5	4.782	–	–
$\tau^f_B = 2.0$			
a_0	1.063	1.494	0.998
a_1	0.544	-0.844	-2.880
a_2	-6.381	1.705	7.420
a_3	22.909	-2.534	-8.951
a_4	-33.257	–	–
a_5	15.924	–	–
$\tau^f_B = 4.0$			
a_0	1.096	1.308	1.182
a_1	-0.561	1.396	-1.100
a_2	5.223	-7.787	-8.196
a_3	-19.739	5.834	4.247
a_4	25.046	–	–
a_5	-10.813	–	–
$\tau^f_B = 8.0$			
a_0	1.061	–	–
a_1	0.825	–	–
a_2	-13.122	–	–
a_3	37.472	–	–
a_4	-43.375	–	–
a_5	17.780	–	–

Table C.30: **Dust effects** $corr^{B/D}$, as in Table C.21, but for $B/D = 0.5$, in K band.

Fits with exponential + Sérsic functions; K band

	$\frac{R^{B/D}_{app,d}}{R_{app,d}}$	$\frac{R^{eff,B/D}_{app,b}}{R^{eff}_{app,b}}$	$n^{sers,B/D}_{app,b} - n^{sers}_{app,b}$
$\tau^f_B = 0.1$			
a_0	1.048	1.647	1.192
a_1	0.069	-0.308	-1.300
a_2	-0.980	2.333	-6.953
a_3	4.631	-3.251	56.949
a_4	-8.304	–	-102.403
$\tau^f_B = 0.3$			
a_0	1.046	1.672	1.235
a_1	0.087	-0.274	-0.802
a_2	-1.137	2.175	-9.141
a_3	5.093	-3.133	59.540
a_4	-8.879	–	-102.449
a_5	4.895	–	52.536
$\tau^f_B = 0.5$			
a_0	1.044	1.675	1.249
a_1	0.109	-0.224	-0.892
a_2	-1.331	1.945	-7.806
a_3	5.696	-2.937	53.675
a_4	-9.675	–	-93.382
a_5	5.278	–	47.858
$\tau^f_B = 1.0$			
a_0	1.038	1.627	1.214
a_1	0.295	0.272	-1.500
a_2	-3.206	-0.211	5.392
a_3	12.083	-0.863	-5.932
a_4	-18.540	–	–
a_5	9.593	–	–
$\tau^f_B = 2.0$			
a_0	1.037	1.621	1.205
a_1	0.116	-0.122	-2.315
a_2	-1.619	0.250	7.178
a_3	6.731	-1.118	-7.737
a_4	-11.289	–	–
a_5	6.230	–	–
$\tau^f_B = 4.0$			
a_0	1.043	–	–
a_1	0.521	–	–
a_2	-5.734	–	–
a_3	21.983	–	–
a_4	-34.166	–	–
a_5	17.524	–	–
$\tau^f_B = 8.0$			
a_0	1.023	–	–
a_1	0.513	–	–
a_2	-5.488	–	–
a_3	21.657	–	–
a_4	-39.086	–	–
a_5	23.539	–	–

Table C.31: **Dust effects** $corr^{B/D}$ on the derived photometric parameters of **decomposed disks** and **de Vaucouleurs bulges** ($B/D = 0.25$): disk and bulge bulge effective radii, disk and bulge Sérsic indices. Results are listed as coefficients of polynomial fits a_k (Eq. 3.1.19) at different τ^f_B and at the effective wavelength of the B band.

Fits with two Sérsic functions; B band

	$\frac{R^{B/D}_{app,d}}{R_{app,d}}$	$\frac{R^{eff,B/D}_{app,b}}{R^{eff}_{app,b}}$	$n^{sers,B/D}_{app,d} - n^{sers}_{app,d}$	$n^{sers,B/D}_{app,b} - n^{sers}_{app,b}$
$\tau^f_B = 0.1$				
a_0	1.066	1.631	-0.088	1.129
a_1	0.014	-0.454	-0.093	-1.494
a_2	0.341	6.438	0.705	8.701
a_3	-1.054	-30.269	1.004	-43.730
a_4	1.839	56.178	-4.807	98.986
a_5	-1.420	-36.214	3.745	-73.478
$\tau^f_B = 0.3$				
a_0	1.065	1.584	-0.089	1.092
a_1	0.079	-1.400	0.432	-3.037
a_2	-0.685	8.973	-1.987	14.782
a_3	3.290	-34.215	5.800	-50.565
a_4	-5.539	60.692	-6.623	91.862
a_5	2.807	-39.761	2.181	-63.974
$\tau^f_B = 0.5$				
a_0	1.060	1.532	-0.068	1.021
a_1	0.301	-2.930	0.339	-4.997
a_2	-3.184	19.583	0.148	26.722
a_3	12.168	-68.001	-1.718	-85.062
a_4	-18.584	103.779	3.267	130.134
a_5	9.361	-58.159	-2.333	-78.905
$\tau^f_B = 1.0$				
a_0	1.057	1.353	-0.029	0.763
a_1	0.165	-0.969	0.534	-1.113
a_2	-1.963	-4.810	1.030	-26.127
a_3	6.319	13.043	-1.090	93.905
a_4	-9.505	-11.383	–	-140.535
a_5	4.982	2.745	–	77.504
$\tau^f_B = 2.0$				
a_0	1.070	1.194	-0.160	0.354
a_1	-1.042	-2.422	4.637	-4.688
a_2	7.581	-7.962	-2.470	-27.419
a_3	-14.122	45.854	-2.368	130.835
a_4	7.778	-69.077	–	-185.221
a_5	-0.128	34.624	–	90.536
$\tau^f_B = 4.0$				
a_0	1.072	–	-0.264	–
a_1	-0.931	–	3.398	–
a_2	5.125	–	-1.130	–
a_3	-5.009	–	-2.398	–
a_4	-4.277	–	–	–
a_5	5.280	–	–	–
$\tau^f_B = 8.0$				
a_0	–	–	–	–
a_1	–	–	–	–
a_2	–	–	–	–
a_3	–	–	–	–
a_4	–	–	–	–
a_5	–	–	–	–

Table C.32: **Dust effects** $corr^{B/D}$, as in Table C.31, but in V band.

Fits with two Sérsic functions; V band

	$\frac{R_{app,d}^{B/D}}{R_{app,d}}$	$\frac{R_{app,b}^{eff,B/D}}{R_{app,b}^{eff}}$	$n_{app,d}^{sers,B/D} - n_{app,d}^{sers}$	$n_{app,b}^{sers,B/D} - n_{app,b}^{sers}$
$\tau_B^f = 0.1$				
a_0	1.064	1.615	-0.071	1.085
a_1	0.129	-0.436	-0.141	-0.579
a_2	-0.995	6.249	1.537	8.160
a_3	4.145	-30.372	-2.683	-39.146
a_4	-6.371	59.343	1.682	75.787
a_5	3.098	-39.570	-0.476	-50.891
$\tau_B^f = 0.3$				
a_0	1.064	1.591	-0.066	1.127
a_1	0.085	-1.349	0.170	-4.215
a_2	-0.634	11.373	-0.468	27.362
a_3	2.948	-46.926	1.852	-93.069
a_4	-4.891	84.925	-2.192	153.494
a_5	2.490	-54.737	0.413	-95.445
$\tau_B^f = 0.5$				
a_0	1.061	1.544	-0.056	0.841
a_1	0.142	-1.906	0.496	0.226
a_2	-1.343	12.216	-3.157	-8.891
a_3	5.456	-41.143	10.723	27.793
a_4	-8.616	62.843	-14.232	-28.446
a_5	4.332	-36.369	6.012	3.623
$\tau_B^f = 1.0$				
a_0	1.055	1.409	0.002	0.866
a_1	0.117	-1.820	0.008	-3.947
a_2	-1.539	2.853	1.641	6.643
a_3	6.287	-2.738	-1.746	-7.814
a_4	-11.014	–	–	–
a_5	6.154	–	–	–
$\tau_B^f = 2.0$				
a_0	1.047	1.205	-0.041	0.314
a_1	0.136	-2.573	1.962	-5.328
a_2	-2.399	2.378	0.513	2.842
a_3	9.467	-0.037	-2.361	3.045
a_4	-14.433	–	–	–
a_5	7.283	–	–	–
$\tau_B^f = 4.0$				
a_0	1.090	–	-0.267	–
a_1	-1.177	–	3.281	–
a_2	7.370	–	-0.368	–
a_3	-17.439	–	-2.834	–
a_4	19.132	–	–	–
a_5	-8.466	–	–	–
$\tau_B^f = 8.0$				
a_0	1.081	–	-0.110	–
a_1	-0.771	–	3.575	–
a_2	9.759	–	-7.417	–
a_3	-34.237	–	4.460	–
a_4	44.895	–	–	–
a_5	-19.967	–	–	–

Table C.33: **Dust effects** $corr^{B/D}$, as in Table C.31, but in I band.

Fits with two Sérsic functions; I band

	$\frac{R^{B/D}_{app,d}}{R_{app,d}}$	$\frac{R^{eff,B/D}_{app,b}}{R^{eff}_{app,b}}$	$n^{sers,B/D}_{app,d} - n^{sers}_{app,d}$	$n^{sers,B/D}_{app,b} - n^{sers}_{app,b}$
$\tau^f_B = 0.1$				
a_0	1.056	1.618	-0.008	1.044
a_1	0.117	-0.754	-0.289	-3.142
a_2	-1.008	11.864	2.539	26.614
a_3	4.099	-61.707	-6.155	-110.511
a_4	-6.145	125.358	5.861	211.411
a_5	2.948	-84.015	-2.064	-140.754
$\tau^f_B = 0.3$				
a_0	1.055	1.543	-0.004	1.051
a_1	0.102	-0.282	-0.193	-3.129
a_2	-0.916	5.025	2.173	21.621
a_3	3.791	-29.180	-5.839	-82.672
a_4	-5.789	65.571	6.248	156.401
a_5	2.843	-47.487	-2.602	-106.076
$\tau^f_B = 0.5$				
a_0	1.054	1.452	0.002	1.030
a_1	0.053	-0.049	-0.090	-3.305
a_2	-0.450	1.446	1.303	19.890
a_3	2.109	-10.860	-3.099	-71.220
a_4	-3.425	28.807	2.927	130.001
a_5	1.709	-23.400	-1.310	-87.621
$\tau^f_B = 1.0$				
a_0	1.047	1.431	0.016	0.914
a_1	0.230	-1.702	0.126	-4.318
a_2	-2.481	9.535	0.403	21.126
a_3	9.285	-34.134	-0.805	-63.926
a_4	-13.809	56.947	–	99.602
a_5	6.786	-35.177	–	-62.701
$\tau^f_B = 2.0$				
a_0	1.042	1.247	0.052	0.635
a_1	-0.080	-1.343	0.321	-3.001
a_2	0.428	1.776	1.047	-1.931
a_3	-2.093	-10.487	-1.202	10.704
a_4	2.312	22.807	–	-22.449
a_5	-0.797	-15.322	–	15.674
$\tau^f_B = 4.0$				
a_0	1.054	–	-0.350	–
a_1	-0.095	–	4.772	–
a_2	-0.829	–	-6.409	–
a_3	3.223	–	2.364	–
a_4	-4.439	–	–	–
a_5	1.906	–	–	–
$\tau^f_B = 8.0$				
a_0	1.091	–	-0.218	–
a_1	-0.799	–	4.213	–
a_2	3.295	–	-4.129	–
a_3	-4.520	–	-0.013	–
a_4	0.677	–	–	–
a_5	1.206	–	–	–

Table C.34: **Dust effects** $corr^{B/D}$, as in Table C.31, but in J band.

Fits with two Sérsic functions; J band

	$\frac{R^{B/D}_{app,d}}{R_{app,d}}$	$\frac{R^{eff,B/D}_{app,b}}{R^{eff}_{app,b}}$	$n^{sers,B/D}_{app,d} - n^{sers}_{app,d}$	$n^{sers,B/D}_{app,b} - n^{sers}_{app,b}$
$\tau^f_B = 0.1$				
a_0	1.049	1.565	0.063	0.735
a_1	-0.103	-2.904	-0.309	3.338
a_2	0.189	11.541	2.842	-42.843
a_3	1.223	-9.350	-8.852	165.482
a_4	-3.010	–	10.081	-226.647
a_5	1.708	–	-3.923	100.983
$\tau^f_B = 0.3$				
a_0	1.048	1.578	0.066	0.852
a_1	-0.098	-2.700	-0.131	1.367
a_2	0.123	10.322	1.516	-27.623
a_3	1.406	-8.251	-5.211	116.807
a_4	-3.222	–	5.867	-162.753
a_5	1.813	–	-2.222	71.602
$\tau^f_B = 0.5$				
a_0	1.046	1.551	0.064	0.872
a_1	-0.097	-2.438	0.024	0.111
a_2	0.112	9.055	0.095	-16.401
a_3	1.372	-7.195	-0.435	77.899
a_4	-3.111	–	-0.428	-109.545
a_5	1.757	–	0.573	46.484
$\tau^f_B = 1.0$				
a_0	1.033	1.358	0.062	0.860
a_1	0.217	0.206	0.550	-2.177
a_2	-2.262	-6.056	-4.632	3.533
a_3	8.177	23.055	15.743	7.338
a_4	-11.434	-25.604	-23.055	-11.898
a_5	5.409	7.392	11.461	-0.296
$\tau^f_B = 2.0$				
a_0	1.039	1.258	0.097	0.688
a_1	-0.042	0.359	-0.259	-0.898
a_2	-0.686	-11.818	3.559	-16.378
a_3	3.646	45.254	-11.504	78.967
a_4	-5.762	-62.673	13.873	-121.304
a_5	2.698	28.445	-6.091	57.594
$\tau^f_B = 4.0$				
a_0	0.973	–	-0.121	–
a_1	-0.110	–	-0.997	–
a_2	2.151	–	12.580	–
a_3	-8.720	–	-53.397	–
a_4	14.455	–	87.439	–
a_5	-8.735	–	-46.390	–
$\tau^f_B = 8.0$				
a_0	1.043	–	-0.039	–
a_1	0.272	–	-3.766	–
a_2	-4.228	–	50.130	–
a_3	12.202	–	-149.514	–
a_4	-14.130	–	178.952	–
a_5	5.618	–	-76.917	–

Table C.35: **Dust effects** $corr^{B/D}$, as in Table C.31, but in K band.

Fits with two Sérsic functions; K band

	$\frac{R^{B/D}_{app,d}}{R_{app,d}}$	$\frac{R^{eff,B/D}_{app,b}}{R^{eff}_{app,b}}$	$n^{sers,B/D}_{app,d} - n^{sers}_{app,d}$	$n^{sers,B/D}_{app,b} - n^{sers}_{app,b}$
$\tau^f_B = 0.1$				
a_0	1.011	0.897	0.133	0.434
a_1	0.017	4.240	-0.238	2.820
a_2	-0.214	-44.283	2.442	-46.555
a_3	1.722	179.530	-10.574	210.455
a_4	-3.191	-253.801	14.421	-312.807
a_5	1.720	115.760	-6.287	147.602
$\tau^f_B = 0.3$				
a_0	1.010	0.940	0.134	0.476
a_1	0.028	3.152	-0.243	3.185
a_2	-0.326	-39.495	2.401	-47.348
a_3	2.091	170.531	-10.245	207.356
a_4	-3.664	-246.412	13.925	-303.818
a_5	1.933	113.438	-6.101	141.769
$\tau^f_B = 0.5$				
a_0	1.009	0.944	0.136	0.488
a_1	0.041	3.016	-0.210	3.249
a_2	-0.467	-37.588	1.981	-47.224
a_3	2.556	161.790	-8.924	203.663
a_4	-4.266	-232.377	12.387	-295.629
a_5	2.208	106.170	-5.519	136.770
$\tau^f_B = 1.0$				
a_0	1.006	0.928	0.144	0.497
a_1	0.166	3.658	-0.307	2.445
a_2	-1.736	-42.933	2.818	-40.191
a_3	6.851	175.820	-11.402	176.466
a_4	-10.096	-249.838	15.386	-254.745
a_5	4.967	114.928	-6.827	115.951
$\tau^f_B = 2.0$				
a_0	1.007	0.929	0.141	0.494
a_1	0.039	2.067	-0.241	0.645
a_2	-0.590	-24.280	2.487	-23.093
a_3	2.780	100.465	-9.652	107.812
a_4	-4.106	-138.181	12.198	-150.411
a_5	1.939	60.081	-5.144	62.603
$\tau^f_B = 4.0$				
a_0	0.986	–	-0.027	–
a_1	0.314	–	-0.512	–
a_2	-2.324	–	9.140	–
a_3	8.931	–	-32.828	–
a_4	-13.781	–	44.481	–
a_5	7.053	–	-21.007	–
$\tau^f_B = 8.0$				
a_0	1.024	–	0.081	–
a_1	-0.320	–	0.900	–
a_2	3.990	–	-10.987	–
a_3	-15.394	–	44.212	–
a_4	21.464	–	-66.859	–
a_5	-10.246	–	33.750	–

Table C.36: **Dust effects** $corr^{B/D}$, as in Table C.31, but for $B/D = 0.5$.

Fits with two Sérsic functions; B band

	$\frac{R^{B/D}_{app,d}}{R_{app,d}}$	$\frac{R^{eff,B/D}_{app,b}}{R^{eff}_{app,b}}$	$n^{sers,B/D}_{app,d} - n^{sers}_{app,d}$	$n^{sers,B/D}_{app,b} - n^{sers}_{app,b}$
$\tau^f_B = 0.1$				
a_0	1.124	1.630	-0.285	1.198
a_1	0.188	-0.445	-0.177	-2.232
a_2	0.242	0.856	2.645	5.551
a_3	-0.627	-1.093	-2.548	-5.053
a_4	–	–	–	–
a_5	–	–	–	–
$\tau^f_B = 0.3$				
a_0	1.125	1.617	-0.262	1.165
a_1	0.147	-1.076	-0.021	-3.181
a_2	0.279	2.536	2.458	8.485
a_3	-0.752	-2.873	-2.609	-8.654
a_4	–	–	–	–
a_5	–	–	–	–
$\tau^f_B = 0.5$				
a_0	1.108	1.541	-0.230	1.059
a_1	0.426	-1.154	0.493	-3.539
a_2	-0.844	1.533	1.399	8.703
a_3	-0.006	-1.734	-1.981	-9.973
a_4	–	–	–	–
a_5	–	–	–	–
$\tau^f_B = 1.0$				
a_0	1.076	1.480	-0.493	0.975
a_1	1.055	-2.266	6.290	-4.548
a_2	-3.140	-1.789	3.615	-5.318
a_3	1.539	4.116	-10.409	9.378
a_4	–	–	–	–
a_5	–	–	–	–
$\tau^f_B = 2.0$				
a_0	1.150	1.278	-0.270	0.526
a_1	0.941	-6.419	23.306	-13.447
a_2	-4.885	14.776	-53.915	27.544
a_3	3.767	-10.277	33.795	-15.832
a_4	–	–	–	–
a_5	–	–	–	–
$\tau^f_B = 4.0$				
a_0	1.052	–	-0.617	–
a_1	1.166	–	13.976	–
a_2	-3.538	–	-24.986	–
a_3	2.210	–	11.894	–
a_4	–	–	–	–
a_5	–	–	–	–
$\tau^f_B = 8.0$				
a_0	–	–	–	–
a_1	–	–	–	–
a_2	–	–	–	–
a_3	–	–	–	–
a_4	–	–	–	–
a_5	–	–	–	–

Table C.37: **Dust effects** $corr^{B/D}$, as in Table C.31, but for $B/D = 0.5$, in V band.

Fits with two Sérsic functions; V band

	$\frac{R^{B/D}_{app,d}}{R_{app,d}}$	$\frac{R^{eff,B/D}_{app,b}}{R^{eff}_{app,b}}$	$n^{sers,B/D}_{app,d} - n^{sers}_{app,d}$	$n^{sers,B/D}_{app,b} - n^{sers}_{app,b}$
$\tau^f_B = 0.1$				
a_0	1.125	1.649	-0.261	1.213
a_1	0.205	-0.507	-0.069	-2.557
a_2	0.155	0.990	2.266	6.855
a_3	-0.556	-1.088	-2.284	-6.080
a_4	–	–	–	–
a_5	–	–	–	–
$\tau^f_B = 0.3$				
a_0	1.124	1.638	-0.240	1.191
a_1	0.203	-0.845	-0.027	-3.018
a_2	0.052	1.921	2.319	8.295
a_3	-0.473	-2.157	-2.484	-8.079
a_4	–	–	–	–
a_5	–	–	–	–
$\tau^f_B = 0.5$				
a_0	1.120	1.582	-0.206	0.954
a_1	0.223	-0.972	0.105	-1.693
a_2	-0.111	1.760	2.164	4.333
a_3	-0.468	-2.143	-2.529	-5.737
a_4	–	–	–	–
a_5	–	–	–	–
$\tau^f_B = 1.0$				
a_0	1.100	1.493	0.016	1.007
a_1	0.515	-2.579	-1.528	-5.614
a_2	-1.832	5.200	8.052	12.660
a_3	0.787	-5.297	-5.001	-14.595
a_4	–	–	–	–
a_5	–	–	–	–
$\tau^f_B = 2.0$				
a_0	1.078	1.298	-0.677	0.469
a_1	0.876	-4.795	19.496	-9.160
a_2	-3.207	8.019	-34.880	11.824
a_3	1.829	-4.043	16.911	-2.725
a_4	–	–	–	–
a_5	–	–	–	–
$\tau^f_B = 4.0$				
a_0	1.137	–	-0.951	–
a_1	0.127	–	13.770	–
a_2	-1.842	–	-20.329	–
a_3	1.265	–	7.480	–
a_4	–	–	–	–
a_5	–	–	–	–
$\tau^f_B = 8.0$				
a_0	1.169	–	0.015	–
a_1	2.131	–	11.970	–
a_2	-7.900	–	-28.777	–
a_3	6.094	–	18.097	–
a_4	–	–	–	–
a_5	–	–	–	–

Table C.38: **Dust effects** $corr^{B/D}$, as in Table C.31, but for $B/D = 0.5$, in I band.

Fits with two Sérsic functions; I band

	$\frac{R^{B/D}_{app,d}}{R_{app,d}}$	$\frac{R^{eff,B/D}_{app,b}}{R^{eff}_{app,b}}$	$n^{sers,B/D}_{app,d} - n^{sers}_{app,d}$	$n^{sers,B/D}_{app,b} - n^{sers}_{app,b}$
$\tau^f_B = 0.1$				
a_0	1.124	1.654	-0.162	1.218
a_1	0.156	-0.746	0.420	-2.946
a_2	0.051	1.811	0.367	8.343
a_3	-0.384	-1.454	-0.883	-6.928
a_4	–	–	–	–
a_5	–	–	–	–
$\tau^f_B = 0.3$				
a_0	1.119	1.649	-0.137	1.208
a_1	0.198	-0.900	0.414	-3.181
a_2	-0.181	2.212	0.410	9.205
a_3	-0.149	-1.995	-1.014	-8.270
a_4	–	–	–	–
a_5	–	–	–	–
$\tau^f_B = 0.5$				
a_0	1.118	1.629	-0.113	1.170
a_1	0.143	-1.055	0.344	-3.269
a_2	-0.066	2.297	0.752	9.014
a_3	-0.246	-2.111	-1.390	-8.421
a_4	–	–	–	–
a_5	–	–	–	–
$\tau^f_B = 1.0$				
a_0	1.106	1.509	-0.054	1.014
a_1	0.146	-1.485	0.685	-4.011
a_2	-0.216	2.845	-0.060	10.370
a_3	-0.326	-2.689	-0.895	-10.558
a_4	–	–	–	–
a_5	–	–	–	–
$\tau^f_B = 2.0$				
a_0	1.093	1.281	0.052	0.631
a_1	-0.021	-1.052	-1.642	-0.909
a_2	-1.019	-4.966	26.558	-16.669
a_3	0.482	6.593	-28.082	18.436
a_4	–	–	–	–
a_5	–	–	–	–
$\tau^f_B = 4.0$				
a_0	1.165	–	-1.020	–
a_1	-0.730	–	19.200	–
a_2	0.371	–	-34.985	–
a_3	-0.335	–	17.646	–
a_4	–	–	–	–
a_5	–	–	–	–
$\tau^f_B = 8.0$				
a_0	1.190	–	-0.491	–
a_1	-1.072	–	16.066	–
a_2	0.806	–	-34.407	–
a_3	-0.354	–	20.179	–
a_4	–	–	–	–
a_5	–	–	–	–

Table C.39: **Dust effects** $corr^{B/D}$, as in Table C.31, but for $B/D = 0.5$, in J band.

Fits with two Sérsic functions; J band

	$\frac{R^{B/D}_{app,d}}{R_{app,d}}$	$\frac{R^{eff,B/D}_{app,b}}{R^{eff}_{app,b}}$	$n^{sers,B/D}_{app,d} - n^{sers}_{app,d}$	$n^{sers,B/D}_{app,b} - n^{sers}_{app,b}$
$\tau^f_B = 0.1$				
a_0	1.095	1.424	0.099	0.841
a_1	0.022	-0.739	0.158	-1.885
a_2	0.294	4.435	-0.649	8.882
a_3	-0.466	-4.229	0.237	-8.324
a_4	–	–	–	–
a_5	–	–	–	–
$\tau^f_B = 0.3$				
a_0	1.092	1.431	0.109	0.930
a_1	0.010	-0.664	0.208	-2.368
a_2	0.279	3.922	-0.750	9.727
a_3	-0.417	-3.752	0.245	-9.002
a_4	–	–	–	–
a_5	–	–	–	–
$\tau^f_B = 0.5$				
a_0	1.089	1.431	0.119	0.940
a_1	0.010	-0.747	0.213	-2.686
a_2	0.221	3.753	-0.647	10.360
a_3	-0.333	-3.511	0.076	-9.628
a_4	–	–	–	–
a_5	–	–	–	–
$\tau^f_B = 1.0$				
a_0	1.082	1.414	0.132	0.922
a_1	-0.032	-1.283	0.384	-3.624
a_2	0.304	4.594	-0.902	12.299
a_3	-0.397	-4.158	0.081	-11.568
a_4	–	–	–	–
a_5	–	–	–	–
$\tau^f_B = 2.0$				
a_0	1.088	1.292	0.173	0.660
a_1	-0.452	-1.636	0.905	-2.609
a_2	1.573	4.489	-2.250	6.626
a_3	-1.692	-4.150	1.065	-7.214
a_4	–	–	–	–
a_5	–	–	–	–
$\tau^f_B = 4.0$				
a_0	1.062	–	-0.164	–
a_1	0.808	–	-5.615	–
a_2	-3.444	–	30.152	–
a_3	2.258	–	-26.351	–
a_4	–	–	–	–
a_5	–	–	–	–
$\tau^f_B = 8.0$				
a_0	1.137	–	-0.522	–
a_1	-0.886	–	12.328	–
a_2	0.231	–	-17.554	–
a_3	0.069	–	5.238	–
a_4	–	–	–	–
a_5	–	–	–	–

Table C.40: **Dust effects** $corr^{B/D}$, as in Table C.31, but for $B/D = 0.5$, in K band.

Fits with two Sérsic functions; K band

	$\frac{R^{B/D}_{app,d}}{R_{app,d}}$	$\frac{R^{eff,B/D}_{app,b}}{R^{eff}_{app,b}}$	$n^{sers,B/D}_{app,d} - n^{sers}_{app,d}$	$n^{sers,B/D}_{app,b} - n^{sers}_{app,b}$
$\tau^f_B = 0.1$				
a_0	0.994	0.985	0.404	0.253
a_1	0.162	-0.225	-0.473	-1.028
a_2	0.073	6.864	-1.092	11.397
a_3	-0.269	-7.109	1.122	-11.563
a_4	–	–	–	–
a_5	–	–	–	–
$\tau^f_B = 0.3$				
a_0	0.993	1.005	0.405	0.309
a_1	0.155	-0.251	-0.450	-1.006
a_2	0.087	6.922	-1.067	11.349
a_3	-0.269	-7.145	1.039	-11.656
a_4	–	–	–	–
a_5	–	–	–	–
$\tau^f_B = 0.5$				
a_0	0.992	1.013	0.403	0.338
a_1	0.141	-0.342	-0.426	-1.202
a_2	0.115	7.037	-1.058	11.736
a_3	-0.277	-7.160	0.979	-11.960
a_4	–	–	–	–
a_5	–	–	–	–
$\tau^f_B = 1.0$				
a_0	0.979	1.015	0.414	0.346
a_1	0.338	-0.530	-0.416	-1.681
a_2	-0.589	7.072	-1.041	12.780
a_3	0.357	-6.975	0.900	-12.816
a_4	–	–	–	–
a_5	–	–	–	–
$\tau^f_B = 2.0$				
a_0	0.996	1.052	0.394	0.396
a_1	-0.097	-1.509	0.006	-3.378
a_2	0.775	8.964	-1.982	16.765
a_3	-0.737	-8.281	1.439	-16.138
a_4	–	–	–	–
a_5	–	–	–	–
$\tau^f_B = 4.0$				
a_0	0.972	–	-0.028	–
a_1	0.253	–	-0.491	–
a_2	0.209	–	2.094	–
a_3	-0.738	–	-1.941	–
a_4	–	–	–	–
a_5	–	–	–	–
$\tau^f_B = 8.0$				
a_0	1.026	–	0.199	–
a_1	0.640	–	-0.527	–
a_2	-2.643	–	2.767	–
a_3	1.645	–	-2.096	–
a_4	–	–	–	–
a_5	–	–	–	–

Appendix D

The corrections for dust effects on single Sérsic fits of galaxies

Table D.1: **Dust effects** $corr^{sS}$ on the derived sizes of galaxies with **exponential bulges** ($B/D = 0.25$), in B band.

Single Sérsic fits; B band

	$\frac{R^{eff}_{app,gal}}{R^{eff}_{app,d}}$
$\tau^f_B = 0.1$	
a_0	0.664
a_1	0.027
a_2	-0.350
a_3	1.560
a_4	-2.712
a_5	1.633
b_0	1.176
$\tau^f_B = 0.3$	
a_0	0.671
a_1	0.075
a_2	-0.706
a_3	3.061
a_4	-5.249
a_5	3.152
b_0	1.945
$\tau^f_B = 0.5$	
a_0	0.681
a_1	0.050
a_2	-0.458
a_3	2.332
a_4	-4.438
a_5	2.973
b_0	1.980
$\tau^f_B = 1.0$	
a_0	0.700
a_1	0.213
a_2	-2.046
a_3	7.603
a_4	-10.779
a_5	5.495
b_0	1.437
$\tau^f_B = 2.0$	
a_0	0.748
a_1	0.017
a_2	-0.207
a_3	2.315
a_4	-4.249
a_5	2.233
b_0	1.058
$\tau^f_B = 4.0$	
a_0	0.796
a_1	0.138
a_2	-1.541
a_3	5.898
a_4	-9.678
a_5	5.268
b_0	0.894
$\tau^f_B = 8.0$	
a_0	0.742
a_1	0.217
a_2	-2.508
a_3	6.582
a_4	-8.513
a_5	4.410
b_0	0.793

Table D.2: **Dust effects** $corr^{sS}$, as in Table D.1, but in V band.

Single Sérsic fits; V band

	$\frac{R^{eff}_{app,gal}}{R^{eff}_{app,d}}$
$\tau^f_B = 0.1$	
a_0	0.668
a_1	0.025
a_2	-0.298
a_3	1.273
a_4	-2.244
a_5	1.374
b_0	1.029
$\tau^f_B = 0.3$	
a_0	0.674
a_1	0.038
a_2	-0.320
a_3	1.468
a_4	-2.716
a_5	1.743
b_0	1.598
$\tau^f_B = 0.5$	
a_0	0.681
a_1	0.099
a_2	-0.982
a_3	4.047
a_4	-6.732
a_5	3.952
b_0	1.839
$\tau^f_B = 1.0$	
a_0	0.695
a_1	0.233
a_2	-2.212
a_3	8.014
a_4	-11.769
a_5	6.290
b_0	1.539
$\tau^f_B = 2.0$	
a_0	0.730
a_1	0.016
a_2	-0.238
a_3	2.061
a_4	-3.460
a_5	1.799
b_0	1.117
$\tau^f_B = 4.0$	
a_0	0.783
a_1	0.050
a_2	-0.699
a_3	3.834
a_4	-6.953
a_5	3.808
b_0	0.918
$\tau^f_B = 8.0$	
a_0	0.781
a_1	0.204
a_2	-2.134
a_3	6.108
a_4	-8.750
a_5	4.687
b_0	0.821

Table D.3: **Dust effects** $corr^{sS}$, as in Table D.1, but in I band.

Single Sérsic fits; I band

	$\frac{R^{eff}_{app,gal}}{R^{eff}_{app,d}}$
$\tau^f_B = 0.1$	
a_0	0.684
a_1	0.087
a_2	-0.885
a_3	3.170
a_4	-4.900
a_5	2.683
b_0	0.885
$\tau^f_B = 0.3$	
a_0	0.689
a_1	0.122
a_2	-1.265
a_3	4.624
a_4	-7.108
a_5	3.852
b_0	1.091
$\tau^f_B = 0.5$	
a_0	0.694
a_1	0.169
a_2	-1.784
a_3	6.583
a_4	-10.045
a_5	5.393
b_0	1.134
$\tau^f_B = 1.0$	
a_0	0.704
a_1	0.194
a_2	-2.118
a_3	8.083
a_4	-12.578
a_5	6.883
b_0	1.441
$\tau^f_B = 2.0$	
a_0	0.723
a_1	0.043
a_2	-0.434
a_3	1.608
a_4	-2.338
a_5	1.356
b_0	1.157
$\tau^f_B = 4.0$	
a_0	0.757
a_1	-0.028
a_2	-0.097
a_3	1.598
a_4	-3.053
a_5	1.597
b_0	0.926
$\tau^f_B = 8.0$	
a_0	0.790
a_1	0.052
a_2	-0.755
a_3	3.293
a_4	-6.093
a_5	3.518
b_0	0.829

Table D.4: **Dust effects** $corr^{sS}$, as in Table D.1, but in J band.

Single Sérsic fits; J band

	$\frac{R^{eff}_{app,gal}}{R^{eff}_{app,d}}$
$\tau^f_B = 0.1$	
a_0	0.702
a_1	0.068
a_2	-0.729
a_3	2.478
a_4	-3.762
a_5	2.057
b_0	0.825
$\tau^f_B = 0.3$	
a_0	0.705
a_1	0.081
a_2	-0.854
a_3	2.921
a_4	-4.408
a_5	2.390
b_0	0.877
$\tau^f_B = 0.5$	
a_0	0.708
a_1	0.101
a_2	-1.042
a_3	3.590
a_4	-5.393
a_5	2.904
b_0	0.957
$\tau^f_B = 1.0$	
a_0	0.713
a_1	0.148
a_2	-1.474
a_3	5.149
a_4	-7.728
a_5	4.149
b_0	1.164
$\tau^f_B = 2.0$	
a_0	0.721
a_1	0.176
a_2	-1.693
a_3	6.001
a_4	-9.086
a_5	4.934
b_0	1.210
$\tau^f_B = 4.0$	
a_0	0.737
a_1	-0.005
a_2	0.267
a_3	-1.132
a_4	1.510
a_5	-0.535
b_0	0.997
$\tau^f_B = 8.0$	
a_0	0.759
a_1	0.106
a_2	-0.991
a_3	3.486
a_4	-4.946
a_5	2.331
b_0	0.847

Table D.5: **Dust effects** $corr^{sS}$, as in Table D.1, but in K band.

Single Sérsic fits; K band

	$\frac{R^{eff}_{app,gal}}{R^{eff}_{app,d}}$
$\tau^f_B = 0.1$	
a_0	0.722
a_1	0.050
a_2	-0.555
a_3	1.797
a_4	-2.698
a_5	1.493
b_0	0.803
$\tau^f_B = 0.3$	
a_0	0.723
a_1	0.050
a_2	-0.564
a_3	1.831
a_4	-2.753
a_5	1.522
b_0	0.811
$\tau^f_B = 0.5$	
a_0	0.724
a_1	0.052
a_2	-0.585
a_3	1.910
a_4	-2.873
a_5	1.586
b_0	0.824
$\tau^f_B = 1.0$	
a_0	0.727
a_1	0.062
a_2	-0.691
a_3	2.311
a_4	-3.479
a_5	1.906
b_0	0.875
$\tau^f_B = 2.0$	
a_0	0.731
a_1	0.084
a_2	-0.969
a_3	3.399
a_4	-5.166
a_5	2.818
b_0	1.009
$\tau^f_B = 4.0$	
a_0	0.738
a_1	0.086
a_2	-1.044
a_3	3.793
a_4	-5.874
a_5	3.267
b_0	1.091
$\tau^f_B = 8.0$	
a_0	0.750
a_1	-0.011
a_2	-0.070
a_3	0.324
a_4	-0.694
a_5	0.559
b_0	0.955

Table D.6: **Dust effects** $corr^{sS}$, as in Table D.1, but for $B/D = 0.5$.

Single Sérsic fits; B band

	$\frac{R^{eff}_{app,gal}}{R^{eff}_{app,d}}$
$\tau^f_B = 0.1$	
a_0	0.323
a_1	0.092
a_2	-0.765
a_3	3.742
a_4	-6.197
a_5	3.458
b_0	0.992
$\tau^f_B = 0.3$	
a_0	0.331
a_1	0.220
a_2	-2.107
a_3	8.690
a_4	-13.564
a_5	7.290
b_0	1.296
$\tau^f_B = 0.5$	
a_0	0.339
a_1	0.125
a_2	-1.147
a_3	5.285
a_4	-8.742
a_5	4.964
b_0	1.114
$\tau^f_B = 1.0$	
a_0	0.349
a_1	0.070
a_2	-0.546
a_3	2.454
a_4	-3.486
a_5	1.710
b_0	0.726
$\tau^f_B = 2.0$	
a_0	0.353
a_1	-0.013
a_2	0.125
a_3	0.435
a_4	-1.391
a_5	0.895
b_0	0.534
$\tau^f_B = 4.0$	
a_0	0.325
a_1	0.084
a_2	-0.847
a_3	2.283
a_4	-3.029
a_5	1.590
b_0	0.458
$\tau^f_B = 8.0$	
a_0	0.242
a_1	0.220
a_2	-2.148
a_3	6.419
a_4	-8.209
a_5	3.974
b_0	0.411

Table D.7: **Dust effects** $corr^{sS}$, as in Table D.1, but for $B/D = 0.5$, in V band.

Single Sérsic fits; V band

	$\frac{R^{eff}_{app,gal}}{R^{eff}_{app,d}}$
$\tau^f_B = 0.1$	
a_0	0.336
a_1	0.068
a_2	-0.520
a_3	2.797
a_4	-4.771
a_5	2.712
b_0	0.868
$\tau^f_B = 0.3$	
a_0	0.344
a_1	0.162
a_2	-1.489
a_3	6.358
a_4	-10.068
a_5	5.465
b_0	1.213
$\tau^f_B = 0.5$	
a_0	0.350
a_1	0.190
a_2	-1.820
a_3	7.661
a_4	-12.133
a_5	6.610
b_0	1.190
$\tau^f_B = 1.0$	
a_0	0.361
a_1	0.053
a_2	-0.316
a_3	1.716
a_4	-2.797
a_5	1.631
b_0	0.842
$\tau^f_B = 2.0$	
a_0	0.370
a_1	-0.015
a_2	0.078
a_3	0.802
a_4	-1.779
a_5	0.991
b_0	0.589
$\tau^f_B = 4.0$	
a_0	0.358
a_1	0.051
a_2	-0.446
a_3	1.557
a_4	-2.574
a_5	1.466
b_0	0.488
$\tau^f_B = 8.0$	
a_0	0.294
a_1	0.312
a_2	-3.036
a_3	9.276
a_4	-12.170
a_5	5.868
b_0	0.440

Table D.8: **Dust effects** $corr^{sS}$, as in Table D.1, but for $B/D = 0.5$, in I band.

Single Sérsic fits; I band

	$\frac{R^{eff}_{app,gal}}{R^{eff}_{app,d}}$
$\tau^f_B = 0.1$	
a_0	0.380
a_1	0.042
a_2	-0.268
a_3	1.717
a_4	-3.074
a_5	1.802
b_0	0.724
$\tau^f_B = 0.3$	
a_0	0.387
a_1	0.077
a_2	-0.668
a_3	3.252
a_4	-5.433
a_5	3.060
b_0	0.932
$\tau^f_B = 0.5$	
a_0	0.392
a_1	0.102
a_2	-0.958
a_3	4.370
a_4	-7.160
a_5	3.992
b_0	1.064
$\tau^f_B = 1.0$	
a_0	0.402
a_1	0.084
a_2	-0.858
a_3	4.190
a_4	-7.142
a_5	4.115
b_0	0.988
$\tau^f_B = 2.0$	
a_0	0.412
a_1	-0.030
a_2	0.408
a_3	-0.927
a_4	1.064
a_5	-0.385
b_0	0.709
$\tau^f_B = 4.0$	
a_0	0.415
a_1	-0.015
a_2	0.015
a_3	0.827
a_4	-1.915
a_5	1.120
b_0	0.552
$\tau^f_B = 8.0$	
a_0	0.385
a_1	0.332
a_2	-3.128
a_3	10.195
a_4	-14.255
a_5	7.075
b_0	0.494

Table D.9: **Dust effects** $corr^{sS}$, as in Table D.1, but for $B/D = 0.5$, in J band.

Single Sérsic fits; J band

	$\frac{R^{eff}_{app,gal}}{R^{eff}_{app,d}}$
$\tau^f_B = 0.1$	
a_0	0.426
a_1	0.028
a_2	-0.145
a_3	1.114
a_4	-2.083
a_5	1.258
b_0	0.659
$\tau^f_B = 0.3$	
a_0	0.430
a_1	0.047
a_2	-0.315
a_3	1.692
a_4	-2.919
a_5	1.687
b_0	0.737
$\tau^f_B = 0.5$	
a_0	0.433
a_1	0.072
a_2	-0.545
a_3	2.491
a_4	-4.098
a_5	2.307
b_0	0.828
$\tau^f_B = 1.0$	
a_0	0.438
a_1	0.113
a_2	-0.888
a_3	3.669
a_4	-5.873
a_5	3.277
b_0	0.970
$\tau^f_B = 2.0$	
a_0	0.445
a_1	0.115
a_2	-0.811
a_3	3.291
a_4	-5.318
a_5	3.031
b_0	0.890
$\tau^f_B = 4.0$	
a_0	0.454
a_1	-0.022
a_2	0.671
a_3	-2.206
a_4	2.838
a_5	-1.203
b_0	0.669
$\tau^f_B = 8.0$	
a_0	0.454
a_1	0.082
a_2	-0.540
a_3	1.891
a_4	-2.932
a_5	1.527
b_0	0.554

Table D.10: **Dust effects** $corr^{sS}$, as in Table D.1, but for $B/D = 0.5$, in K band.

Single Sérsic fits; K band	$\frac{R^{eff}_{app,gal}}{R^{eff}_{app,d}}$
$\tau^f_B = 0.1$	
a_0	0.479
a_1	0.015
a_2	-0.037
a_3	0.611
a_4	-1.283
a_5	0.829
b_0	0.642
$\tau^f_B = 0.3$	
a_0	0.480
a_1	0.017
a_2	-0.049
a_3	0.650
a_4	-1.341
a_5	0.860
b_0	0.657
$\tau^f_B = 0.5$	
a_0	0.481
a_1	0.019
a_2	-0.079
a_3	0.756
a_4	-1.499
a_5	0.944
b_0	0.678
$\tau^f_B = 1.0$	
a_0	0.484
a_1	0.033
a_2	-0.239
a_3	1.337
a_4	-2.371
a_5	1.404
b_0	0.751
$\tau^f_B = 2.0$	
a_0	0.489
a_1	0.064
a_2	-0.600
a_3	2.700
a_4	-4.467
a_5	2.535
b_0	0.876
$\tau^f_B = 4.0$	
a_0	0.495
a_1	0.044
a_2	-0.445
a_3	2.194
a_4	-3.823
a_5	2.288
b_0	0.878
$\tau^f_B = 8.0$	
a_0	0.503
a_1	-0.023
a_2	0.238
a_3	-0.430
a_4	0.296
a_5	0.027
b_0	0.704

Bibliography

Allen, P.D., Driver, S.P., Graham, A.W. et al. 2006, MNRAS, 371, 2

Arnaboldi, M., Rejkuba, M., Retzlaff, J. et al. 2012, Msngr, 149, 7

Baes, M., Davies, J. I., Dejonghe, H. et al. 2003, MNRAS, 343, 1081

Baes, M., van Hese, E. 2011, A&A 534, A69

Baes, M., Gentile, G. 2011, A&A 525, A136

Bamford, S. P., Aragón-Salamanca, A., Milvang-Jensen, B. 2006, MNRAS, 366, 308

Bamford, S.P. et al. 2013, submitted

Benson, A., Džanović, D., Frenk, C. S., Sharples, R. 2007, MNRAS 379, 841

Bernardi, M., Meert, A., Vikram, V. et al. 2012, MNRAS submitted, arXiv:1211.6122

Boissier, S., Boselli, A., Buat, V. et al. 2004, A&A, 424, 465

Bourne, N., Maddox, S. J., Dunne, L. et al. 2012, MNRAS 421, 3027

Bruce, V. A., Dunlop, J. S., Cirasuolo, M., McLure, R. J., Targett, T. A et al. 2012, MNRAS 427, 1666

Byun Y. I., Freeman K. C., Kylafis N. D. 1994, ApJ, 432, 114

Cameron, E., Driver, S., Grahah, A. W., Liske, J. 2009, ApJ 699, 105

CHAPTER D

Cimatti, A. & Scaramella, R. 2012, MSAIS, 19, 31

Ciotti, L. & Bertin, G. 1999, A&A, 352, 447

Courteau, S. & Rix, H.-W. 1999, ApJ, 513, 561

Courteau, S., Andersen, D. R., Bershady, M. A., MacArthur, L. A., Rix, H.-W. 2003, ApJ, 594, 208

Cunow B. 2001, MNRAS, 323, 130

Evans R. 1994, MNRAS, 266, 511

de Jong, J.T.A., Verdoes Kleijn, G.A., Kuijken, K.H. & Valentijn, E.A. 2012, ExA 35, 25

de Vaucouleurs, G. 1948, Annales d'Astrophysique 11, 247

Dale, D. A., Aniano, G., Engelbracht, C. W. et al. 2012, ApJ, 2012, 745, 95

Dariush, A., Cortese, L., Eales, S. et al. 2011, MNRAS, 418, 64

Draine, B.T. & Li, A. 2007, ApJ, 657, 810

Driver, S. P., Popescu, C. C., Tuffs, R. J. et al. 2007, MNRAS, 379, 1022

Driver, S.P., Hill, D.K., Kelvin, L.S. et al. 2011, MNRAS, 413, 971

Dwek, E. 1998, ApJ, 501, 643

Emerson, J.P. & Sutherland, W.J. 2010, SPIE, 7733, 4

Fabricius, M. H., Saglia, R. P., Fisher, D. B. et al. 2012, ApJ 754, 67

Fisher, David B., Drory, Niv 2008, ApJ 136, 773

Gadotti, A. D. 2008, MNRAS, 384, 420

Gadotti, A. D. 2009, MNRAS, 393, 1531

CHAPTER D

Gadotti A. D., Baes M., Falony S. 2010, MNRAS, 403, 2053

Graham, A.W. & Driver, S.P. 2005, PASA, 22, 118

Graham, A.W. & Worley, C.C. 2008, MNRAS, 388, 1708

Graham, A.W. 2013, in “Planets, Stars and Stellar Systems”, Vol. 6, 91, eds. T.D.Oswalt & W.C.Keel, Springer Publishing

Grootes, M., Tuffs, R.J., Popescu, C.C., Pastrav, B., Andrae, E. et al. 2013, ApJ 766, 59

Häußler, B., Bamford, S.P., Vika, M. et al. 2013, MNRAS 430, 330

Hoyos, C., den Brok, M., Verdoes, K.G. et al. 2011, MNRAS, 411, 2439

Hubble E. 1926, ApJ, 64, 321

Jouvel, S. Kneib, J.-P., Bernstein, G. et al. 2011, A&A, 532, 25

Kelvin, L.S., Driver, S.P., Robotham, A.S.G. et al. 2012, MNRAS, 421, 1007

Koopmann, R. A., Kenney, J. D. P. 2004, ApJ 613, 851

Koopmann, R. A., Kenney, J. D. P. 2004, ApJ 613, 866

Kylafis, N. D. & Bahcall, J. N. 1987, ApJ, 317, 637

Lackner, C. N, Gunn, J. E. 2012, MNRAS, 421, 2277

Laureijs, R.J., Duvet, L., Escudero S.I. et al. 2010, SPIE, 7731, 40

Maltby, D. T., Hoyos, C., Gray, M. E., Aragón-Salamanca, A., Wolf, C. 2012, MNRAS, 420, 2475

Martinelli, M., Calabrese, E., de Bernardis, F. et al. 2011, Phys. Rev. D, 83, 023012

Misiriotis, A., Popescu, C. C., Tuffs, R., Kylafis, N. D. 2001, A&A, 372, 775

Mo, H., Mao, S., White, S. D. M. 1998, MNRAS, 295, 319

Möllenhoff, C., Appenzeller, I., Gässler, W. et al. 1999, A&A 352, L5

Möllenhoff, C., Heidt, J. 2001, A&A 368, 16

Möllenhoff, C. 2004, A&A 415, 63

Möllenhoff, C., Popescu, C. C., Tuffs, R. J. 2006, A&A, 456, 941

Pastrav, B. A., Popescu, C. C., Tuffs, R. J., Sansom, A. E. 2012, in Proceedings of the IAU Symp. 284: The Spectral Energy Distribution of Galaxies, eds. R. J. Tuffs & C. C. Popescu, 306

Pastrav, B. A., Popescu, C. C., Tuffs, R. J., Sansom, A. E. 2013, A&A 553, A80

Pastrav, B. A., Popescu, C. C., Tuffs, R. J., Sansom, A. E. 2013, A&A submitted

Peacock, J.. 2008, in “A Decade of Dark Energy”, eds N. Pirzkal and H. Ferguson

Peng, C. Y., Ho, L. C., Impey, C. D., Rix 2002, H.-W., AJ, 124, 266

Peng, C. Y., Ho, L. C., Impey, C. D., Rix 2010, H.-W., AJ, 139, 2097

Pierini D., Gordon K. D., Witt A. N., Madsen G. J. 2004, ApJ, 617, 1022

Popescu, C. C., Misiriotis, A., Kylafis, N. D., Tuffs, R. J. & Fischera, J. 2000, A&A, 362, 138

Popescu, C.C., Tuffs, R.J., Vlk, H.J., Pierini, D., Madore, B.F. 2002, ApJ, 567, 221

Popescu, C. C., Tuffs, R. J., Kylafis, N. D., Madore, B. F. 2004, A&A, 414, 45

Popescu, C. C., Tuffs, R. J., Madore, B. F. et al. 2005, ApJ, 619, L75

Popescu, C. C., Tuffs, R. J. 2005, in “The Spectral Energy Distributions of Gas-Rich Galaxies: Confronting Models with Data”, eds. C. C. Popescu & R. J. Tuffs, AIP Conference Proceedings, vol. 761

Popescu, C. C., Tuffs, R. J., Dopita, M. A. et al. 2011, A&A, 527, A109

Rowlands, K., Dunne, L., Maddox, S., et al. 2012, MNRAS, 419, 2545

Sérsic, J. L. 1968, Atlas de galaxias australes (Cordoba, Argentina: Observatorio Astronomico, 1968)

Simard, L., Willmer, C.N.A., Vogt, N.P. et al. 2002, ApJS, 142, 1

Simard, L., Mendel, J.T, Patton, D.R. et al. 2011, ApJS, 196, 11

Stickel, M., Lemke, D., Klaas, U. et al. 2000, A&A, 359, 865

Stickel, M., Lemke, D., Klaas, U., Krause, O., & Egner, S. 2004, A&A, 422, 39

The Dark Energy Survey Collaboration 2005, arXiv:astro-ph/0510346

Tuffs, R.J., Popescu, C.C., Pierini, D. et al. 2002, ApJS, 139, 37

Tuffs, R. J., Popescu, C. C., Völk, H. J., Kylafis, N. D., Dopita, M. A. 2004, A&A, 419, 821

Vlahakis, C., Dunne, L. & Eales, S. 2005, MNRAS, 364, 1253

Weingartner, J.C. & Draine, B.T. 2001, ApJ, 548, 296

York, D. G., Adelman, J., Anderson, J. E. Jr. et al. 2000, AJ, 120, 1579